Inaugural - Dissertation

zur Erlangung der Doktorwürde der
Naturwissenschaftlich-Mathematischen Gesamtfakultät der
Ruprecht-Karls-Universität
Heidelberg

Development of Frozen-Density Embedded Algebraic Diagrammatic Construction Schemes for Excited States and Quantum-Chemical Investigation of Photophysical Properties of Tetrathiaheterohelicenes

Vorgelegt von
Stefan H. Prager, Master of Science Chemie
aus Hanau

Mai 2017

Development of Frozen-Density Embedded Algebraic Diagrammatic Construction Schemes for Excited States and Quantum-Chemical Investigation of Photophysical Properties of Tetrathiaheterohelicenes

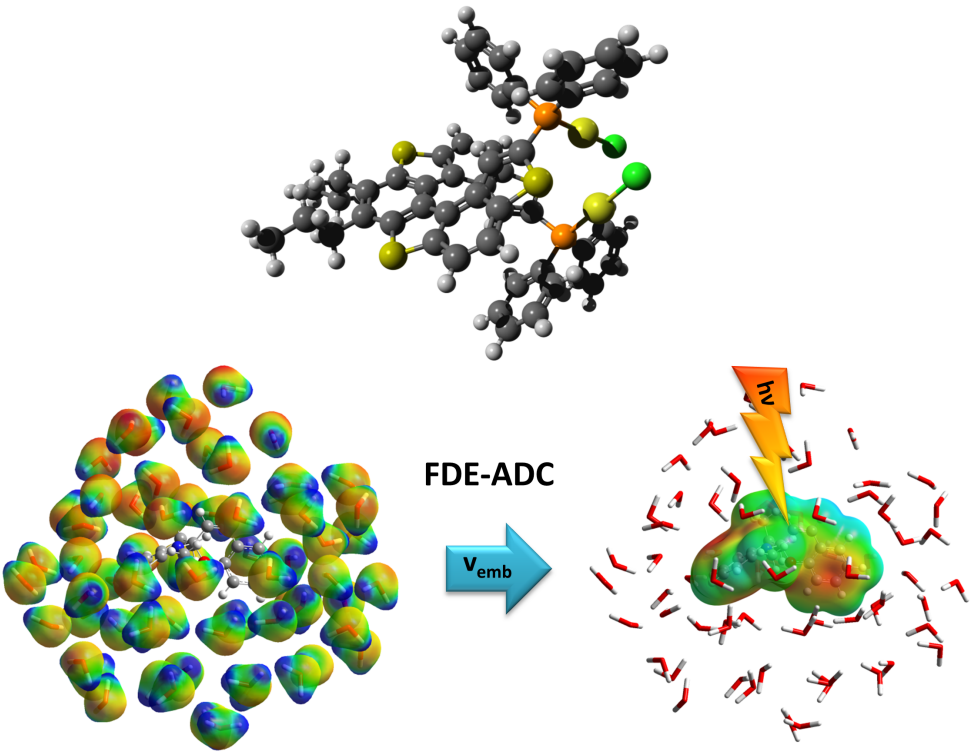

Stefan H. Prager

Referees:
Prof. Dr. Andreas Dreuw
Prof. Dr. Peter Comba

Submitted: 23.05.2017
Oral examination: 05.07.2017

Für meine Familie

Preface

Abstract

Theoretical chemistry has become an important branch of modern chemistry. Theoretical investigations improve our understanding of chemical problems and can predict properties or reaction pathways. Especially in photochemistry, quantum chemical calculations are used along with spectroscopy to analyze the interactions of molecules with light. In recent years, new methods like time-dependent density functional theory (TD-DFT) and the algebraic diagrammatic construction scheme for the polarization propagator (ADC) have been developed allowing calculations of excited states of molecules of chemical relevant size with an accuracy directly comparable with experimental results. These methods allow not only for the calculation of excitation energies, but also of excited state properties, electron densities, absorption strengths and even photoreaction pathways can be calculated. This paves the way for the theoretical investigation of all photochemical processes. Typically, however, chemical reactions and spectroscopic measurements are performed in solution. Unlike in gas phase, molecules in solution are comparatively close together, leading to an interaction between the solvent and solute molecules. In biochemistry, reactions often take place in the active center of a protein and in technical photochemical applications such as organic light emitting diodes (OLEDs) the chromophore is packed in a matrix. Hence, for comparable quantum mechanical calculations, the influence of the environment has to be considered as well. Since a direct treatment of the full environment is generally not feasible due to the computational demand of quantum chemical methods, an approximative treatment of the interaction using specific environment models is made.

In my dissertation, I focused on two main topics involving both the application of existing theoretical methods, and the development of new theoretical methods.

In the first part, I investigated the photochemical and electrochemical properties of various phosphorus-tetrathia-[7]heterohelicenes. The ground and several excited states of tetrathia-[7]heterohelicene-dialkylphosphane-borane (TTH-DAPB) and tetrathia-[7]heterohelicene-diphenylphosphane-gold(I)-chloride (TTH-DPP-Au(I)) have been analyzed using DFT, TD-DFT and RI-CC2. These molecules belong to the the class of helicenes, which are characterized by multiple annelated aromatic rings forming a helical structure which induces chirality. The optimized ground state equilibrium structures were compared with experimental structures determined by X-ray crystallography and showed generally good agreement. The eight energetically lowest excited singlet states have been calculated. Employing a constant shift accounting for environment effects and intrinsic errors of the

applied method, the calculated spectra almost perfectly resemble the experimental absorption and circular dichroism spectra. In both molecules, both the S_1 and S_2 state contribute to the first absorption band. Therefore, vibrationally resolved absorption spectra have been calculated for these two states for both molecules. It could be shown that only the first excited state determines the absorption band. The second excited state exhibits a very broad band due to many normal modes contributing to the vibronic excitation. In general, the TTH backbone dominates the photochemical properties and the phosphorus and gold atoms exhibit only minor influences.

In addition, electrochemical properties of the phosphine-oxide TTH derivatives TTH-$(PO(n\text{–}Bu)_2)_2$, TTH-$(PO(Ph)_2)_2$ and TTH-$PO(Ph)_2$ as well as of the two phosphine-selenide TTH derivatives TTH-$(PSe(Ph)_2)_2$ and TTH-$PSe(Ph)_2$ have been calculated. Ionization energies and electron affinities have been computed both in gas phase and solution. In solution, all first electron detachments and attachments are localized on the TTH moiety with only minor influence of the substituents. Each process is qualitatively determined in all molecules by a single frontier orbital, which has been verified by difference density analysis. For the phosphine-oxide TTH derivatives the gas phase results resemble the results in solution. The phosphine-selenides, however, show a different picture. The lone-pairs are shifted higher in energy without stabilization of the environment, leading to an ionization localized at the selenium atom in the gas phase.

The second focus of my dissertation was the development, implementation, and testing of a new method for including environment interaction in the excited state of a central molecule. To this end, I combined frozen density embedding thoery (FDET) with the ADC method to develop the new FDE-ADC method. This method is implemented in the quantum chemical program package `Q-Chem` as the module `fdeman`, which manages the FDE-ADC calculation. In FDET, the supersystem is divided in two subsystems: the embedded system (A) and the environment (B). The name "embedded system" comes from the fact that it is embedded in the electron density of the environment. The influence of the environment is expressed in an embedding potential, which depends on both electron densities of A and B. In `fdeman`, the whole FDE-ADC calculation is performed in a four step process: ***a)*** generation of the electron density of the embedded system $\rho_A(\vec{r})$, ***b)*** generation of the electron density of the environment $\rho_B(\vec{r})$, ***c)*** calculation of the embedding potential $v_{emb}^{lin}(\vec{r})$ and finally ***d)*** applying $v_{emb}^{lin}(\vec{r})$ in an FDE-ADC calculation by adding it to the Fock matrix during the SCF

followed by an ADC calculation using the orbitals influenced by the environment.

While the straight-forward implementation of FDE-ADC uses a supermolecular basis to express both density matrices and the embedding potential, an approximate variant named re-assembling of density matrix (RADM) has been introduced in which the density matrix of A is built together from MP(2) and HF based density matrices like a patchwork. The created embedding potential is subsequently cut to the monomer basis which features an FDE-ADC calculation using only the basis functions of the embedded system. This can be done since in the contraction of the density of A with the embedding potential, only the values of the block in the density matrix representing the embedded system contribute.

FDE-ADC has been benchmarked up to third order perturbation theory employing three test systems, designed to exhibit an increasing strength of environment interaction. The test systems are ***1)*** benzene with a hydrogen fluoride molecule in plane with the benzene ring, ***2)*** benzaldehyde with a hydrogen-bonded water dimer and ***3)*** uracil surrounded by five hydrogen-bonded water molecules. In the benchmark, the FDE-ADC results have been compared with supermolecular ADC calculations. The deviation from the reference calculation in excitation energies and oscillator strengths determines the accuracy of FDE-ADC. For SE-FDE-ADC(2) and RADM-FDE-ADC(2), mean absolute errors (MAEs) of 0.025 eV and 0.040 eV in excitation energies have been determined, respectively. For RADM-FDE-ADC(3), an MAE of 0.029 eV has been calculated. These errors are well below the intrinsic error of the underlying ADC methods, thus demonstrating the performance of FDE-ADC. This is furthermore demonstrated in three representative applications. First, the excited states of benzoquinone in 42 methanol molecules has been investigated. Next, the vertical photochemical properties of the photoswitch spiropyran in 100 water molecules have been investigated. In the last application, the core-valence excited states of carbon monoxide inside a C_{60}-cage have been calculated.

Using a frozen environment neglects the influence of the embedded system on the environment. This is called environment polarization and can be added following two different approaches. In the first variant referred to as pre-polarization, the ground state influence of the embedded system on the environment is treated by an electrostatic potential which is applied during the calculation of the environment density. This way, $\rho_B(\vec{r})$ is not calculated in the gas phase but instead in the presence of A. In the second variant, referred to as excitation-induced environment polarization, the influence of an electronic excitation of A on the environment

is considered. Therefore, the subsystems are interchanged and alternatingly embedded in each other until self-consistency (freeze and thaw). Here, two approximate variants to include excitation-induced environment polarization are introduced. In the first variant, named state-specific iteration (SSI), the alternate embedding is performed once, which prevents changes in the order of the excited states. In the second variant called difference density polarization potential (DDPP), the environment is embedded consecutively in the ground and excited state density of system A. The electron difference density describing the polarization of the environment is used to create a potential which is employed to calculate an energy correction for the excitation energy of the excited state of A. Both SSI and DDPP as well as the pre-polarization are implemented in the module `fdeman` in `Q-Chem`. In tests, both the pre-polarization and SSI could increase the accuracy of FDE-ADC. In the case of SSI, up to 35 % increased accuracy is observed. DDPP currently does not improve the results.

In total, the FDE-ADC method is a promising approach for considering environmental effects on electronically excited states. The error of this method is lower than the intrinsic error of the employed ADC method. Using the RADM approximation, explicit treatment of extended environments is directly feasible, making FDE-ADC a "black box" method for the calculation of excited states in complex environments.

Zusammenfassung

Die theoretische Chemie stellt heute ein wichtiges Teilgebiet der Chemie dar. Theoretische Untersuchungen helfen, chemische Fragestellungen zu beantworten und können Eigenschaften oder Reaktionen vorhersagen. Besonders in der Photochemie werden quantenchemische Berechnungen zusammen mit der Spektroskopie verwendet, um die Wechselwirkungen von Molekülen mit Licht zu analysieren. In den letzten Jahren wurden neue Methoden wie die zeitabhängige Dichtefunktionaltheorie (engl. *time-dependent density functional theory*, TD-DFT) oder das algebraisch-diagrammatische Konstruktionsschema für den Polarisationspropagator (engl. *algebraic diagrammatic construction scheme*, ADC) entwickelt, die die Berechnung von elektronisch angeregten Zuständen in Molekülen von chemisch relevanter Größe mit einer Genauigkeit ermöglicht, die einen direkten Vergleich mit experimentellen Ergebnissen zulässt. Mit diesen Methoden können nicht nur Anregungsenergien, sondern auch weitere Eigenschaften angeregter Zustände, wie etwa Elektronendichten, Absorptionsstärken und sogar Photoreaktionswege, berechnet werden. Dies ermöglicht theoretische Untersuchungen aller photochemischen Prozesse. In der Regel werden jedoch chemische Reaktionen und spektroskopische Messungen in Lösung durchgeführt. Anders als in der Gasphase sind in Lösungen Moleküle eng zusammen, was zu einer Wechselwirkung der Moleküle von Solvent und Lösemittel führt. Auch in der Biochemie geschehen Reaktionen oft im aktiven Zentrum innerhalb eines Proteins und in technischen photochemischen Anwendungen wie organischen lichtemittierenden Dioden (OLEDs) wird der Chromophor in eine Matrix eingebettet. Für vergleichbare quantenmechanische Berechnungen ist daher auch der Einfluss der Umgebung zu berücksichtigen. Da eine direkte Behandlung der vollen Umgebung aufgrund der zeitlichen und technischen Anforderungen quantenchemischer Methoden meist nicht möglich ist, wird eine approximative Behandlung der Interaktion in sog. Umgebungsmodellen durchgeführt.

In meiner Dissertation habe ich vor allem auf zwei verschiedenen Themen gearbeitet, die in die Anwendung bestehender theoretischer Methoden einerseits und die Entwicklung neuer theoretischer Methoden andererseits kategorisiert werden können.

Im ersten Teil habe ich die photochemischen und elektrochemischen Eigenschaften verschiedener Phosphor-Tetrathia-[7]heterohelicene untersucht. Der Grund- und mehrere angeregte Zustände von Tetrathia-[7]heterohelicen-dialkylphosphan-boran (TTH-DAPB) und Tetrathia-[7]heterohelicen-diphenylphosphan-gold(I)-chlorid (TTH-DPP-Au(I)) wurden unter Verwendung von DFT, TD-DFT und RI-CC2

berechnet. Diese Moleküle gehören zu den Helicenen, die durch mehrere annelierte aromatische Ringe gekennzeichnet sind. Sie bilden eine helicale Struktur, die eine Chiralität bewirkt. Die optimierten Gleichgewichtsstrukturen wurden mit denen durch Röntgenkristallographie ermittelten experimentellen Strukturen verglichen und zeigten eine gute Übereinstimmung. Die acht energetisch niedrigsten angeregten Singulettzustände wurden berechnet. Nach Addition einer konstanten Verschiebung, die Fehler aufgrund von Umgebungswechselwirkungen und intrinsischen Fehlern der angewandten Methode korrigiert, stimmen die berechneten Spektren nahezu perfekt mit den experimentellen Absorptions- und Circulardichroismusspektren überein. Da in beiden Molekülen die beiden energetisch niedrigsten angeregten Zustnde zur ersten Absorptionsbande beitragen könnten, wurden für diese in beiden Molekülen vibrationsaufgelöste Absorptionsspektren berechnet. Es konnte gezeigt werden, dass nur der erste angeregte Zustand die Absorptionsbande bestimmt. Der zweite angeregte Zustand weist eine sehr breite Bande aufgrund vieler Normalmoden auf, die zur vibronischen Anregung beitragen. Im Allgemeinen dominiert das TTH-Rückgrat die photochemischen Eigenschaften und die Phosphor- und Goldatome zeigen nur geringe Einflüsse.

Darüber hinaus sind die elektrochemischen Eigenschaften der Phosphinoxid-TTH-Derivate TTH-$(PO(n{-}Bu)_2)_2$, TTH-$(PO(Ph)_2)_2$ und TTH-$PO(Ph)_2$ sowie der beiden Phosphin-Selenid-TTH-Derivate TTH-$(PSe(Ph)_2)_2$ und TTH-$PSe(Ph)_2$ berechnet worden. Ionisierungsenergien und Elektronenaffinitäten wurden sowohl in der Gasphase als auch in Lösung berechnet. In Lösung sind alle ersten Elektronenabgaben und -aufnahmen auf dem TTH-Ring lokalisiert, wobei die Substituenten nur einen geringen Einfluss zeigen. Jeder dieser Prozesse wird qualitativ in allen Molekülen durch ein einziges Grenzorbital bestimmt. Dies konnte durch Analyse der Differenzdichten verifiziert wurde. Während für die Phosphinoxid-TTH-Derivate die Gasphasen-Ergebnisse den Ergebnissen in Lösung ähneln, zeigen die Phosphin-Selenide ein anderes Bild. Die ungebundenen Elektronenpaare werden ohne eine Stabilisierung durch die Umgebung energetisch nach oben verschoben, was in der Gasphase zu einer am Selenatom lokalisierten Ionisation führt.

Im zweiten Teil habe ich eine neue Methode entwickelt, um den Einfluss der Wechselwirkung mit Molekülen der Umgebungen auf die angeregten Zustände eines zentralen Moleküls zu berücksichtigen. Deshalb habe ich die Umgebungsmethode Einbettung in eine gefrorene Dichte (engl. *frozen density embedding theory*, FDET) mit der ADC-Methode kombiniert, um die neue FDE-ADC-Methode zu entwickeln. Diese Methode wurde im quantenchemischen Programmpaket `Q-Chem` als Modul

`fdeman` implementiert, das die FDE-ADC-Berechnung verwaltet. In FDET ist das Supersystem in zwei Subsysteme, namentlich das eingebettete System (A) und die Umgebung (B), aufgeteilt. Das eingebettete System wird, seinem Namen entsprechend, in die Elektronendichte der Umgebung eingebettet. Der Einfluss der Umgebung wird in einem Potential (engl. *embedding potential*) ausgedrückt, das sowohl von der Elektronendichte von A als auch von B abhängt. In `fdeman` wird die gesamte FDE-ADC-Berechnung in einem vierstufigen Prozess durchgeführt: ***a)*** Erzeugung der Elektronendichte des eingebetteten Systems $\rho_A(\vec{r})$, ***b)*** Erzeugung der Elektronendichte der Umgebung $\rho_B(\vec{r})$, ***c)*** Berechnung des Potentials $v_{emb}^{lin}(\vec{r})$ und schließlich ***d)*** Anwendung von $v_{emb}^{lin}(\vec{r})$ in einer FDE-ADC-Berechnung durch Hinzufügen zur Fock-Matrix während des SCF. Dies ist gefolgt von einer ADC-Berechnung, die die von der Umgebung beeinflussten Orbitale nutzt.

Während die direkte Implementierung von FDE-ADC eine supermolekulare Basis verwendet, um sowohl die Dichtematrizen als auch das Potential auszudrücken, wurde eine genäherte Variante namens Neu-Zusammensetzung der Dichtematrix (engl. *Re-assembling of density matrix*, RADM) eingeführt, in der die Dichtematrix von A zusammengebaut wird aus MP(2)- und HF-basierten Dichtematrizen ähnlich eines Flickwerks. Das erzeugte Potential wird anschließend auf die Größe der Monomerbasis zugeschnitten, was eine FDE-ADC-Berechnung in lediglich den Basisfunktionen des eingebetteten Systems ermöglicht. Dies ist erlaubt, da bei der Kontraktion der Dichte von A mit dem Potential nur die Werte beitragen, die das eingebettete System selbst repräsentieren.

FDE-ADC wurde bis zur dritten Ordnung Störungstheorie getested, wobei drei Testsysteme eingesetzt wurden, die eine zunehmende Stärke der Umgebungseinflüsse aufweisen sollen. Die Testsysteme sind ***1)*** Benzol mit einem Wasserstofffluoridmolekül in der Ebene des Benzolrings, ***2)*** Benzaldehyd mit einem wasserstoffbrückengebundenem Wasser-Dimer und ***3)*** Uracil, umgeben von fünf wasserstoffbrückengebundenen Wassermolekülen. In dem Test wurden die FDE-ADC-Ergebnisse mit supermolekularen ADC-Berechnungen verglichen. Die Abweichung von den Anregungsenergien der Referenzberechnung bestimmt die Genauigkeit von FDE-ADC. Für SE-FDE-ADC(2) und RADM-FDE-ADC(2) werden mittlere absolute Fehler (engl. *mean absolute error*, MAEs) von 0,025 eV bzw. 0,040 eV bestimmt. Für RADM-FDE-ADC(3) wurde ein MAE von 0,029 eV berechnet. Diese Fehler liegen weit unter dem intrinsischen Fehler der zugrunde liegenden ADC-Methoden und zeigen somit die Leistung von FDE-ADC. Dies wurde auch in drei repräsentativen Anwendungen gezeigt. Zuerst sind die angeregten Zustände

von Benzochinon in 42 Methanolmolekülen untersucht worden. Als nächstes sind die vertikalen photochemischen Eigenschaften des Photoschalters Spiropyran in 100 Wassermolekülen untersucht worden. Zuletzt wurden die Kern-Valenz-angeregten Zustände von Kohlenmonoxid innerhalb eines C_{60}-Käfigs berechnet.

Die Verwendung einer gefrorenen Umgebung vernachlässigt den Einfluss des eingebetteten Systems auf die Umgebung. Dies wird als Umgebungspolarisation bezeichnet und kann durch zwei verschiedene Ansätze miteinbezogen werden. In der ersten Variante, die als Vorpolarisation bezeichnet wird, wird der Einfluss des Grundzustands des eingebetteten Systems auf die Umgebung durch ein elektrostatisches Potential berücksichtigt, das bei der Berechnung der Umgebungsdichte angewendet wird. Auf diese Weise wird $\rho_B(\vec{r})$ nicht in der Gasphase berechnet, sondern in Gegenwart von A. In der zweiten Variante, die als anregungsinduzierte Umgebungspolarisation bezeichnet wird, wird der Einfluss einer elektronischen Anregung von A auf die Umgebung berücksichtigt. Daher werden die Subsysteme vertauscht und abwechselnd ineinander eingebettet bis Selbstkonsistenz erreicht is (Einfrieren und Auftauen). Hier werden zwei Näherungsverfahren zur Berechnung der anregungsinduzierte Umgebungspolarisation eingeführt. In der ersten Variante namens zustandsspezifischer Iteration (engl. *state-specific iteration*, SSI) wird die gegenseitige Einbettung einmal durchgeführt, was Änderungen in der Reihenfolge der angeregten Zustände verhindert. In der zweiten Variante, die Differenzdichten-Polarisationspotential (engl. *difference density polarization potential*, DDPP) genannt wird, wird die Umgebung nacheinander in die Elektronendichte des Grund- und angeregten Zustands von System A eingebettet. Die Differenzdichte, die die Polarisation der Umgebung beschreibt, wird verwendet, um ein Potential zu erzeugen, das zur Berechnung einer Energiekorrektur für die Anregungsenergie von A verwendet wird. Sowohl SSI als auch DDPP sowie Vorpolarisation sind im Modul `fdeman` in `Q-Chem` implementiert. Bei Tests konnten sowohl die Vorpolarisation als auch SSI die Genauigkeit von FDE-ADC um bis zu 35% im letzteren Fall erhöhen. DDPP verbessert derzeit nicht die Ergebnisse.

Insgesamt ist die FDE-ADC-Methode ein vielversprechender Ansatz für die Berücksichtigung des Einflusses von Umgebungswechselwirkungen auf elektronisch angeregte Zustände. Der Fehler dieser Methode ist niedriger als der intrinsische Fehler der verwendeten ADC-Methode und unter Verwendung der RADM-Approximation ist eine explizite Behandlung von größeren Umgebungen direkt möglich. Dies macht FDE-ADC zu einer *„Black Box“* Methode für die Berechnung von elektronisch angeregten Zuständen in komplexen Umgebungen.

Contents

Chapter 1

Introduction

"Science is not only a disciple of reason
but, also, one of romance and passion."
Stephen Hawking

Photochemistry, I would call it *"the bright side of chemistry"*, is a special part of chemistry dealing with the interaction of molecules with light.[1,2] Photochemical processes are involved in important biological processes like photosynthesis and vision.[3] But photochemical processes are also important for technical aspects or development of new materials. This ranges from the stability of colors upon irradiation from the sun[4] to the reduction of photolability in drugs.[5,6] In additoin, photochemistry in the field of organic electronics is essential to design new organic solar cells or organic light-emitting diods (OLEDs).[7–10] Because of this diversity of photochemical applications, quantum chemical methods became more and more important since they provide an important tool to investigate and understand chemical and photochemical aspects.

Typically and without any external influence, a molecule occupies its energetically lowest state, the *electronic ground state*. Absorption of a photon can lead to an excitation to an energetically higher state, an *excited state*. This excitation is accomplished by an electron, which is transferred from an occupied molecular orbital to an energetically higher-lying unoccupied (or virtual) molecular orbital. Photoexcitations are very fast processes leading to a *vertical* excitation and thus also to an excitation of the vibrational states in the excited state according to the overlap of the vibrational wavefunction. This is referred to as the *Franck-Condon Principle*.[11,12] It is followed by relaxation to the vibrational ground state of the excited state from which flourescence can occur. As an alternative to fluorescence, the molecule can undergo a chemical reaction in the excited state referred to as

a *photochemical reaction*. In many cases, these photochemical reactions proceed barrierless and can can lead to different products than ground state reactions can achieve. Mostly, this is accompanied by a *conical intersection* (CI), a crossing of two electronic states. Hence, the previously excited state can become the electronic ground state in the photoproduct. It is also possible for the system to undergo an *inter-system crossing* (ISC) from the singlet excited state to an triplet state from which phosphorescence can occur (Fig. 1.1). If the energy of the absorbed photon is very high (like in X-rays), an electron is not excited to an excited state but instead completely removed and the system becomes ionized. The energy difference between absorption and flourescence is called the *Stokes shift* and is a result of the geometrical relaxation in the excited state.[11]

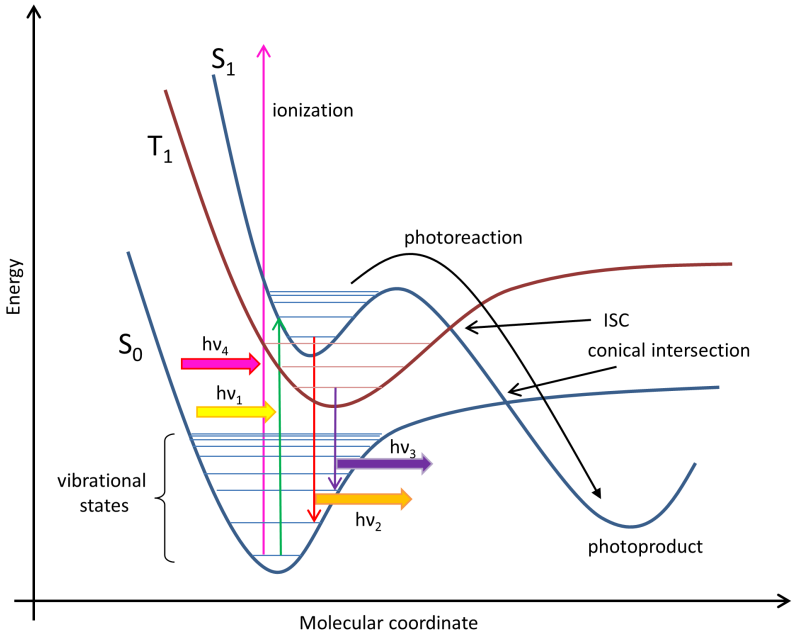

Figure 1.1: Jablonski-diagram illustrating various possible electronic transitions. The vertical arrows in green, red, purple and pink indicate absorption, fluorescence, phosphorescence and ionization, respectively. The horizontal arrows indicate absorbed and emitted photons. A photoreaction can occur from the S_1 state through a conical intersection to a new photoproduct. Relaxatation through an inter-system crossing populates the triplet state T_1.

In larger molecules, the excited state processes are more complex and in addition to the common ($\pi \mapsto \pi^*$) and ($n \mapsto \pi^*$) states, new kinds of excited states might arise. One example is the *charge-transfer state*, in which an electron is moved in space due to the excitation. This leads to a charge separation in the excited

state.[13] In order to analyze excited states properly, reliable quantum chemical methods have to be employed. Since various approximations are included in the methods, it is important to know which method in suited for the investigation of a certain problem. In Chapter 2 I will give an introduction into quantum chemistry and review several methods I have used in my dissertation.

In many chemical researches, different investigative techniques are combined. The three "cornerstones" of chemistry, preparative chemistry, which covers the synthesis of new compounds, analytical or spectroscopical chemistry, measuring and analyzing chemical and physical properties, and the theoretical chemistry, which simulates chemical reactions and properties, all work together to obtain a complete picture. Observed data can be compared with theoretical results and simulations on reaction pathways suggesting new ways of synthesis.

In the first part of my dissertation, I have performed various excited state analyses of larger molecules belonging to the class of tetrathiaheterohelicenes. In Chapter 3 I will show an detailed study on these molecules with close comparison to experimental results.

In recent years, the development of highly accurate quantum chemical methods has become ever more important to improve understanding of complicated chemical problems. These methods reach accuracies for either geometry, energies or other properties that allow direct comparison with experimental results. However, due to the computational demand, these accuracies are only achievable for small molecules in the gas phase. One of these highly accurate methods is the *Algebaic-diagrammatic construction scheme for the polarization propagator* (ADC),[14] which I will explain in Sec. 2.3.4.

As stated by the famous ancient Greek philosopher Aristotle (384-322 B.C.): *"Compounds do not react unless fluid or if dissolved"*[15,16] since the solvent increases the mobility of the solute and provides in most cases a stabilizing effect on the reactants. This quote demonstrates how important solvents or in general environments are for chemical reactions and properties.[17,18] But not only chemical reactions depend on the solvent, also excited states are mainly influenced by environment interaction. A well-known phenomenon is the shift of excitation energies due to various solvents. This is referred to as *solvatochromism*.[18–21]

In most cases, the absorption bands of a chromophor and its environment are clearly separated. As a consequence, photons of a wavelength absorbable by the chromophore will not interact with the environment molecules. This can be used to introduce the approximation of a separable system into photoactive compound,

e.g. the chromophore, and the environment. In this approximation, only the chromophore is electronically excited by absorption of light while the environment remains in the electronic ground state. After the instantaneous absorption of light, the following photochemical processes can be divided into three steps due to their intrinsic timescale. Within femtoseconds after the absorption, the electron density of the chromophore gets polarized. However, the electron densities of the environment molecules, which are arranged around the chromophore, were adapted to its ground state electron density. Since this electron density now changes, it induces a change in the environment electron densities as well. This is a mutual interaction which equilibrates. The excited state electron density of the chromophore is self-consistent with the ground state electron densities of the environment molecules. This mutual interaction between chromophore and environment influences the excitation properties like excitation energy or oscillator strength. Thus is is important to include these interactions in the calculation of absorption spectra.

In a second process on a picosecond timescale, the chromophore adapts geometrically to the new electronic structure of the excited state. Also the environment molecules rearrange which can again be described as a mutual interaction. This geometric relaxation and the interaction with the environment is important for the calculation of emission processes like fluorescence which an occur from the equilibrated structure of the system. This also lays the path to photochemical reactions in the excited state like photodissociation. These processes are illustrated in Fig. 1.2.

Hence it is obvious that interaction with the chemical environment should also be included in the theoretical investigations of molecules. However, a detailed description of large environments is not feasible due to computational demands. Therefore, new models have to be introduced to include the interaction with the chemical environment without including the environment itself. This kind of modeling was also awarded 2013 with the Nobel prize for chemistry to M. Karplus, M. Levitt and A. Warshel for *"the development of multiscale models for complex chemical systems"*.[22]

One of these models is the *Frozen density embedding theory* (FDET), which is reviewed in detail in Sec. 2.4.5. In the second part of my dissertation, I developed a new method for including environment interactions and their effects on electronically excited states by combining the FDET with the ADC-method resulting in the *FDE-ADC* method. This is implemented in the the quantum

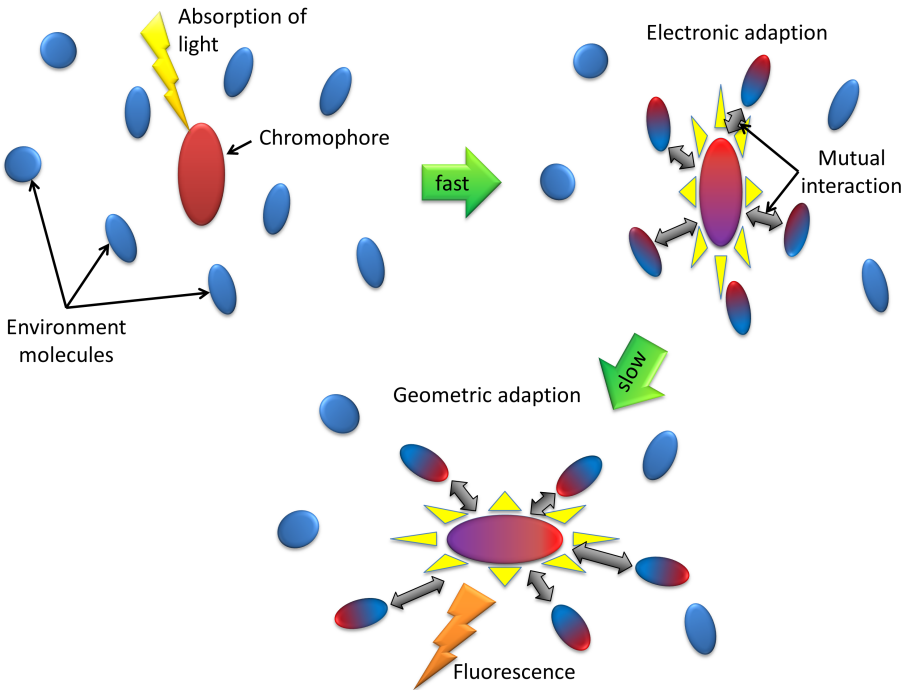

Figure 1.2: Illustration of the interaction of a chromophore (red) with its environment molecules (blue) after excitation by light. The electron density of the chromophore gets polarized (top right) in the excited state (indicated by the yellow beams) which iduces a polarization in the environment electron densities as well. This leads to a mutual interaction. In a slower timescale both the chromophore and the environment relaxes geometrically (bottom) which can lead to fluorescence or photochemical reactions.

chemical program package `Q-Chem`[23] in the new module called `fdeman`. It is closely linked with the implementation of ADC in `Q-Chem` in the module `adcman`.[24] The implementation is described in Chapter 4. The FDE-ADC method is thoroughly benchmarked in Chapter 5 and representative applications of FDE-ADC demonstrating its features and capabilities are shown in Chapter 6. Standard FDE-ADC includes only the influence of the environment onto the central system i.e. the chromophore but not the influence of the excitation of the central system onto the environment which might change the interaction between both subsystems. This influence of the chromophore onto the environment is referred to as *environment polarization*. In Chapter 7, I introduce two variants of environment polarization, describe their implementation in `fdeman` and present some test results of the effect of environment polarization on the excited states of the chromophore. Finally, I provide a summary and conclusion with a brief

outlook in Chapter 8.

All pictures of molecules, orbitals or electron densities in this thesis have been created using the programs Avogadro 1.1.0.[25], POV-Ray 3.7.0.RC6,[26] Jmol 13.0.14[27] or GaussView 5.0.8[28]

It should be noted that most of the results and developments described in this dissertation have already been published by myself and by my coauthors in peer-review journals.[29–34] These publications are listed below in chronological order:

- **Gold(I) Complexes of Tetrathiaheterohelicene Phosphanes**
  Silvia Cauteruccio, Annette Loos, Alberto Bossi, Maria C. Blanco Jaimes, Davide Dova, Frank Rominger, Stefan Prager, Andreas Dreuw, Emanuela Licandro and A. Stephen K. Hashmi
  Inorganic Chemistry, 52 (2013), pages 7995-8004

- **Ultrafast C_{Spiro}-O Dissociation via a Conical Intersection Drives Spiropyran to Merocyanine Photoswitching**
  Stefan Prager, Irene Burghardt and Andreas Dreuw
  The Journal of Physical Chemistry A, 118 (2014), pages 1339-1349

- **Chiral Thiahelicene-Based Alkyl Phosphine-Borane Complexes: Synthesis, X-ray Characterization, and Theoretical and Experimental Investigations of Optical Properties**
  Davide Dova, Silvia Cauteruccio, Stefan Prager, Andreas Dreuw, Claudia Graiff and Emanuela Licandro
  The Journal of Organic Chemistry, 80 (2015), pages 3921-3928.

- **Tetrathia[7]helicene Phosphorus Derivatives: Experimental and Theoretical Investigations of Electronic Properties, and Preliminary Applications as Organocatalysts**
  Davide Dova, Lucia Viglianti, Patrizia R. Mussini, Stefan Prager, Andreas Dreuw, Arnaud Voituriez, Emanuela Licandro and Silvia Cauteruccio
  Asian Journal of Organic Chemistry, 5 (2016), pages 537-549

- **First time combination of frozen density embedding theory with the algebraic diagrammatic construction scheme for the polarization propagator of second order**
  Stefan Prager, Alexander Zech, Francesco Aquilante, Andreas Dreuw and Tomasz A. Wesolowski
  The Journal of Chemical Physics, 144 (2016,) page 204103

- **Implementation and application of the frozen density embedding theory with the algebraic diagrammatic construction scheme for the polarization propagator up to third order**
  Stefan Prager, Alexander Zech, Tomasz A. Wesolowski and Andreas Dreuw
  submitted for publication, (2017)

Chapter 2

Theoretical Methods

"If quantum mechanics hasn't profoundly shocked
you, you haven't understood it yet."
Niels Bohr

In this chapter, I would like to introduce the basic concepts of quantum chemistry and review the various methods I used for my research projects. In the first part, I will discuss some of the fundamental theories like the *Schrödinger equation*, which are prerequisites for all further theories.

The starting point for quantum chemical investigations is typically the electronic ground state. It represents the energetically lowest electronic state and is generally the populated electronic state in most chemical systems. It determines most of the chemical and physical properties of a substance and most chemical reactions occur in it. From electronic ground state calculations, equilibrium geometries, reaction pathways and barriers, dipole moments, vibrational modes and many more properties and observables can be obtained.[11] In the second section, I will elaborate on some important quantum chemical ground state methods.

However, the investigation of photochemical processes or spectroscopic analysis on a quantum chemical level requires the calculation of the electronically excited state. These states are energetically higher than the ground state and can become occupied by electrons if an appropriate amount of energy, typically in form of a photon, is absorbed.[11,35,36] Excited state methods are based on ground state methods. Hence, a proper description of the electronic ground state is essential for reliable excited state calculations. In the third section, I will discuss some methods to calculate electronically excited states.

In the last section of this chapter, I would like to introduce methods and approximations to include environment effects on the chemical and physical prop-

erties of molecules. Since molecules generally interact with other neighboring molecules, this has to be considered in quantum chemical investigations as well. Also, a major part of this thesis deals with the development of a new method to include environment effects in the calculation of electronically excited states.

However, as will be shown in Sec. 2.1.1, the electronic structure of many-electron systems cannot be solved analytically. Therefore, various approximations have to be introduced ranging from very accurate to unpredictable with respect to the obtained results. Unfortunately, good approximations demand significant computational resources, thereby limiting the size of the systems able to be investigated. If a larger system is to be investigated, larger errors have to be accepted. A sketch in Fig. 2.1 illustrates the relation between employed level of approximation, feasible system size and error in describing electronic states.

In this chapter, I will focus on single reference *ab initio* and density based

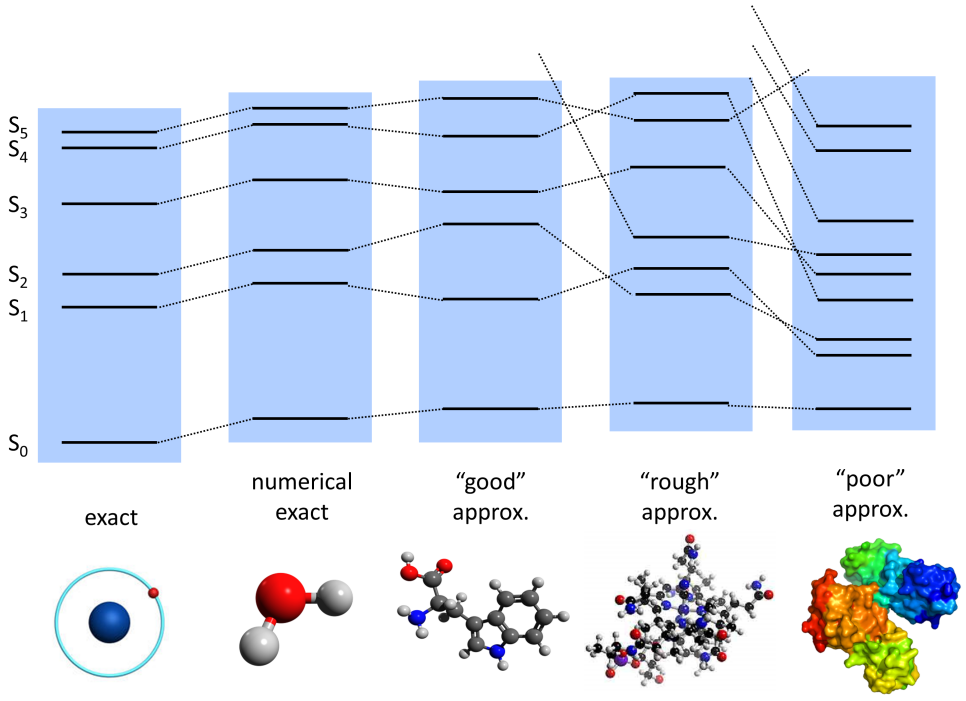

Figure 2.1: Schematic Sketch of the approximations introduced in quantum chemistry to calculate molecules of increasing size. The horizontal lines indicate the electronic states and the dotted lines indicate the error incorporated when more approximations are included. For each level of approximation, an example molecule is given to illustrate what system size can be treated on a reasonable timescale.

methods. Therefore, I will exclude multireference methods like *complete active space self-consistent field* (CASSCF) as well as semi-empirical approaches. For these methods, I would like to refer to Ref 37 and Ref 38, respectively.

In this work, atomic units are used for all equations. In atomic units, the Planck constant $\hbar$, the elementary charge ϵ, the electron mass m_e and the speed of light c is set to 1. If not otherwise stated, the orbital indices p, q, r, s corresponds to general orbitals, while the indices i, j, k, l and a, b, c, d correspond to occupied and virtual orbitals, respectively. Matrices are typically written using bold letters while vectors are indicated by an arrow above the symbol.

2.1 Basic concepts of quantum chemistry

I would like to begin with the basic concepts of quantum chemistry since all the following theories are based on these. The content of this section is, unless otherwise stated, taken from the books: *"Modern Quantum Chemistry"* by *A. Szabo and N. S. Ostlund,*[39] *"Introduction to Computational Chemistry"* by *F. Jensen*[40] and *"Molecular Electronic-Structure Theory"* by *T. Helgaker, J. Olsen and P. Jørgensen,*[41] to which I would like to refer for further reading.

2.1.1 Schrödinger equation

The basic equation for all quantum chemical theories is the Schrödinger equation.[42–45] The non-relativistic time-independent Schrödinger equation (SE) is given as

$$\hat{H}\Psi = E\Psi \tag{2.1}$$

for an N-electron system. $\hat{H}$ is the Hamilton operator and depends both on the coordinates of electrons, indicated by position vectors $\vec{r} = \vec{r_1}, \vec{r_2}...\vec{r_N}$ and nuclei, indicated by position vectors $\vec{R} = \vec{R_1}, \vec{R_2}...\vec{R_M}$. The SE is a partial differential eigenvalue equation and its eigenvalue E represents the energy of a given system. The Hamilton operator comprises all possible interactions contributing to the total energy E and reads

$$\hat{H} = \underbrace{-\sum_{i=1}^{N}\frac{1}{2}\nabla_i^2}_{\text{kinetic energy of electrons}} - \underbrace{\sum_{A=1}^{M}\frac{1}{2M_A}\nabla_A^2}_{\text{kinetic energy of nuclei}} - \underbrace{\sum_{i=1}^{N}\sum_{A=1}^{M}\frac{Z_A}{\left|\vec{r_i}-\vec{R}_A\right|}}_{\text{Coulomb attraction electron - nuclei}} + \underbrace{\sum_{i=1}^{N}\sum_{j>i}^{N}\frac{1}{|\vec{r_i}-\vec{r_j}|}}_{\text{Coulomb repulsion electron - electron}} + \underbrace{\sum_{A=1}^{M}\sum_{B>A}^{M}\frac{Z_A Z_B}{\left|\vec{R}_A-\vec{R}_B\right|}}_{\text{Coulomb repulsion nuclei - nuclei.}} \tag{2.2}$$

In Eq. 2.2 M_A is the ratio of the mass of nucleus A to the mass of an electron and Z_A is the atomic number of nucleus A. The Laplacian operators ∇_i^2 and ∇_A^2 indicate the second derivative with respect to the spatial coordinates of the i^{th} electron and A^{th} nucleus. The five individual terms of the Hamilton operator correspond to the kinetic energy of the electrons, the kinetic energy of the nuclei, the Coulomb attraction between electrons and nuclei, the Coulomb repulsion between electrons and the Coulomb repulsion between nuclei, respectively.

The wavefunction Ψ is the exact eigenstate of the Hamilton operator and depends both on the spatial coordinates of electrons and nuclei. Hence, the probability of finding an electron in a given position in space is

$$\left|\Psi(\vec{r},\vec{R})\right|^2. \tag{2.3}$$

For any kind of property, the SE (Eq. 2.1) has to be solved. However, analytic solutions for the SE are only possible for a few simple one-electron systems, since the wavefunction describes the correlated motion of N+M interacting particles. For any many-electron system, approximations have to be included.

2.1.2 Born-Oppenheimer approximation

The first approximation made to solve the SE is called the Born-Oppenheimer approximation. Generally, the Hamilton operator can be split in two parts: An nuclear Hamiltonian $\hat{H}_{nuc}$, containing all the parts depending on the nuclei, and an electronic part $\hat{H}_{el}$, containing the remaining terms including the electron-nuclei interaction:

$$\hat{H}_{nuc} = \sum_{A=1}^{M} \frac{1}{2M_A}\nabla_A^2 + \sum_{A=1}^{M}\sum_{B>A}^{M} \frac{Z_A Z_B}{\left|\vec{R}_A - \vec{R}_B\right|} \tag{2.4}$$

and

$$\hat{H}_{elec} = -\sum_{i=1}^{N}\frac{1}{2}\nabla_i^2 - \sum_{i=1}^{N}\sum_{A=1}^{M}\frac{Z_A}{\left|\vec{r}_i - \vec{R}_A\right|} + \sum_{i=1}^{N}\sum_{j>i}^{N}\frac{1}{|\vec{r}_i - \vec{r}_j|} + V_{nuc}(R). \tag{2.5}$$

As can be seen from Eq. 2.4, the kinetic energy T is inversely proportional to the mass of the nuclei. This also explains why quantum effects are less important for particles with larger mass. Since the nuclei are about 2000 times heavier than electrons, their movement is also much slower. As a result, the kinetic energy of the nuclei can be neglected, or, in other words, the position of the nuclei is fixed. Additionally, the Coulomb repulsion between the nuclei becomes a constant. As a consequence, the total wavefunction Ψ of a system can be separated into two parts: the electronic part, depending only parametrically on the spatial position of the nuclei, and the nuclear wavefunction. Eventually, this leads to the electronic SE

$$\hat{H}_{elec}(\vec{r},\{\vec{R}\})\Psi_{elec}(\vec{r},\{\vec{R}\} = E_{elec}(\{\vec{R}\})\Psi_{elec}(\vec{r},\{\vec{R}\}). \tag{2.6}$$

The only remaining many-body term is the electron-electron Coulomb repulsion. Thus, even the electronic SE in the Born-Oppenheimer approximation is not analytically solvable for many-electron systems. Finding appropriate approximations for this term is subject to contemporary quantum chemical development. From the parametric dependence of an electronic state on the positions of the nuclei,the concept of a potential energy surface (PES) emerges. The PES is a multi-dimensional hypersurface with 3M dimensions where M is the number of nuclei in the system. The PES can be plotted as energies at certain molecular geometries along a certain intermolecular axes. A well-known example is the so called Morse potential. It represents a model of the potential energy depending on an intermolecular coordinate, i.e. the distance between two atoms. An example of the Morse potential for the dissociation of H_2 is shown in Fig. 2.2

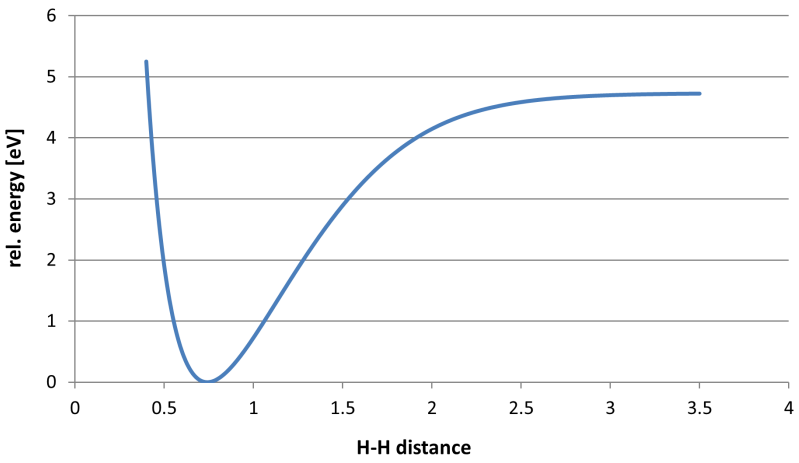

Figure 2.2: The Dissociation of H_2 resembles the Morse potential (calculated at Full-CI/cc-pVQZ level of theory).

The Born-Oppenheimer approximation is valid for systems in which the motion of the electrons and nuclei is separable. In well separated electronic states, this is mostly the case. But in cases with small energetic differences between the electronic states, like in conical intersections and avoided crossings, the electron and nuclei motion couple. Hence, in these cases the Born-Oppenheimer approximation is not valid any more.

2.1.3 Geometry optimization

Building the first derivative of the energy with respect to the nuclear coordinates yields the gradient $\vec{g}$, the second derivatives result in the Hesse matrix **H**

$$g = \begin{pmatrix} \frac{\partial E}{\partial R_1} \\ \frac{\partial E}{\partial R_2} \\ \vdots \\ \frac{\partial E}{\partial R_{3M}} \end{pmatrix} \tag{2.7}$$

$$\mathbf{H} = \begin{pmatrix} \frac{\partial^2 E}{\partial R_1^2} & \frac{\partial^2 E}{\partial R_2 \partial R_1} & \cdots & \frac{\partial^2 E}{\partial R_{3M} \partial R_1} \\ \frac{\partial^2 E}{\partial R_1 \partial R_2} & \frac{\partial^2 E}{\partial R_2^2} & \cdots & \frac{\partial^2 E}{\partial R_{3M} \partial R_2} \\ \vdots & \vdots & \ddots & \vdots \\ \frac{\partial^2 E}{\partial R_1 \partial R_{3M}} & \frac{\partial^2 E}{\partial R_2 \partial R_{3M}} & \cdots & \frac{\partial^2 E}{\partial R_{3M}^2} \end{pmatrix} \tag{2.8}$$

with M as the number of nuclei with 3 spatial coordinates each. At a stationary point the gradient g equals zero. If $\vec{g} \neq 0$ the current geometry is not a stationary point on the PES. The gradient g points in this case in the direction of the steepest increase in energy. If the geometry with a minimal energy should be found, the atomic displacement vector $\vec{d}$ is defined as

$$\vec{d} = -\vec{g}. \tag{2.9}$$

At the new geometry, a new gradient is calculated until the convergence criteria i.e. $\vec{g} \approx 0$ is reached. This method is called *steepest descent*. However, although convergence is guaranteed, the method tends to oscillate around the minimum structure and thus taking many steps to converge. A better way to choose the step $\vec{d}$ improves this issue. It is called the *Newton-Raphson technique*. The energy at a certain point on the PES is given as $E(\vec{x}_0)$. The energy of an nearby point $\vec{x} = \vec{x}_0 + \vec{d}$ can be expanded in a Taylor series

$$E(\vec{x}_0 + \vec{d}) = E(\vec{x}_0) + \vec{d}^t \frac{dE(\vec{x}_0)}{d\vec{x}} + \frac{1}{2}\vec{d}^t \frac{d^2E(\vec{x}_0}{d\vec{x}_1\vec{x}_2}\vec{d} + \dots. \tag{2.10}$$

Since only the lowest few derivations of E are known, step $\vec{d}$ is estimated by differentiating the Taylor series with respect to $\vec{d}$ and only the first two terms are kept.

$$\frac{E(\vec{x}_0 + \vec{d})}{d\vec{d}} \approx \frac{dE(\vec{x}_0)}{d\vec{x}} + \frac{d^2E(\vec{x}_0)}{d\vec{x}_1\vec{x}_2}\vec{d}. \tag{2.11}$$

Setting the left hand side of Eq. 2.11 to zero as it is in a stationary point yields

$$\vec{d} = -\mathbf{H}^{-1}\vec{g}. \tag{2.12}$$

This is referred to as the *Newton-Raphson step*. Eq. 2.12 can be rewritten in a diagonal Hessian representation as

$$\vec{d} = \sum_i \frac{-F_i}{b_i}\vec{u}_i \tag{2.13}$$

with $\vec{u}_i$ and b_i as the eigenvectors and eigenvalues of the Hesse matrix $\mathbf{H}$ and $F_i = \vec{u}_i^t g$ as the component of $\vec{g}$ along the eigenmode $\vec{u}_i$. The Newton-Raphson step can be considered as minimizing along all directions of $\vec{u}_i$ exhibiting positive eigenvalues while maximizing along the directions with negative eigenvalues. Since in most cases the Hesse matrix is too expensive to calculate in terms of computational cost, an approximate Hessian is used instead. This is referred to as *quasi Newton-Raphson step*.

2.1.4 The electronic wavefunction

In this section, I would like to elaborate how the electronic wavefunction in the electronic SE is defined. In the first part, I illustrate how the wavefunction obeys the Pauli exclusion principle. In the second part, I introduce the representation of the wavefunction in a basis set.

2.1.4.1 Slater determinants

Until now, the electronic Hamiltonian and the wavefunction were considered to only depend on spatial coordinates. But electrons hold a further quantum mechanic quantity: the spin (s). The spin can occupy one of two spin states denoted as up ($\alpha(s)$) and down ($\beta(s)$). The spin functions are orthogonal:

$$\langle\alpha(s)|\alpha(s)\rangle = \langle\beta(s)|\beta(s)\rangle = 1 \tag{2.14}$$

$$\langle\alpha(s)|\beta(s)\rangle = \langle\beta(s)|\alpha(s)\rangle = 0. \tag{2.15}$$

Since the Hamiltonian is a sum of one-particle Hamiltonians, the most simple way to construct a many-body wavefunction for N particles from N one-particle

wavefunctions is the Hartree product.

$$\Psi_{HP}(r_1, r_2, \ldots, r_N) = \chi_1(r_1)\chi_2(r_2)\ldots\chi_N(r_N). \tag{2.16}$$

However, the Hartree product does not obey the Pauli exclusion principle for fermions which says
"a many-electron wave function must be antisymmetric with respect to the interchange of the coordinate r of any two electrons,

$$\Psi_n(r_1, r_2, ..., r_i, r_j, ..., r_N) = -\Psi_n(r_1, r_2, ..., r_j, r_i, ..., r_N)".^{[39]} \tag{2.17}$$

As a consequence, the Hartree product must be antisymmetrized. Including the spin using

$$\psi(r) = \begin{cases} \chi(r)\alpha(s) \\ \chi(r)\beta(s) \end{cases} \tag{2.18}$$

where ψ correspond to singe-electron wavefunctions with separated spin (spin orbitals). As a result, one yields the so called *Slater determinant* which is defined as

$$\Psi_n(r_1, r_2, ..., r_N) = \frac{1}{\sqrt{N!}} \begin{vmatrix} \psi_i(r_1) & \psi_j(r_1) & \ldots & \psi_k(r_1) \\ \psi_i(r_2) & \psi_j(r_2) & \ldots & \psi_k(r_2) \\ \vdots & \vdots & \ddots & \vdots \\ \psi_i(r_N) & \psi_j(r_N) & \ldots & \psi_k(r_N) \end{vmatrix} \tag{2.19}$$

with $\frac{1}{\sqrt{N!}}$ as the normalization factor. In the Slater determinant, the rows are labeled by the electrons (x_1, x_2, etc.) while the columns are labeled by the spin orbitals (ψ_i, ψ_j, etc.). If two electrons in two orbitals are interchanged, the two corresponding columns in the Slater determinant are interchanged which leads to an change of the sign. The same holds for interchanging the coordinates of two electrons since the corresponding rows in the Slater determinant are interchanged. In summary, the Slater determinant is an appropriate way to construct the many-body wavefunction.

2.1.4.2 Gaussian basis sets

As mentioned before, the SE is only solvable for one-electron systems like the hydrogen atom. In these cases no Coulombic electron repulsion occurs. In this case,

I will stick to the hydrogen atom example. The electronic Hamiltonian reduces to

$$\begin{aligned} \hat{H}_{elec} &= \hat{T}(\vec{r}) + \hat{V}(\vec{r}, \vec{R}) \\ &= \frac{1}{2}\nabla^2_{\vec{r}} - \frac{Z}{|r_i - R_A|} \end{aligned} \tag{2.20}$$

with $\hat{T}(\vec{r})$ as the kinetic energy operator of the electron and $\hat{V}(\vec{r}, \vec{R})$ as the Coulomb attraction potential between electron and nucleus. Solving the electronic SE for this Hamiltonian yields the so called *Slater-type orbitals (STO)* as eigenfunctions of the Hamiltonian. The STOs are generally defined as

$$\phi^{\mathrm{STO}}_{nlm}(d, \Lambda, \Theta) = R_n(d, \zeta) Y_{lm}(\Lambda, \Theta) \tag{2.21}$$

with d as the distance between electron and nucleus defined as $d = |r_i - R_A|$, an radial part $R_n(d, \zeta)$ and the angular part $Y_{lm}(\Lambda, \Theta)$. The letters n, l, and m correspond to the principal quantum number (n), the orbital angular momentum quantum number (l) and the magnetic quantum number (m), respectively. The radial part $R_n(d, \zeta)$ is defined as

$$R_n(d, \zeta) = \frac{(2\zeta)^{\frac{3}{2}}}{\sqrt{(2n)!}} (2\zeta d)^{n-1} e^{-\zeta d} \tag{2.22}$$

with ζ corresponding to the compactness of the orbital. The angular part of Eq. 2.21 is based on spherical harmonics (see Fig. 2.3) and is defined as

$$Y_{lm}(\Lambda, \Theta) = \sqrt{\frac{2l+1}{4\pi} \frac{(l-m)!}{(l+m)!}} P^m_l(\cos(\Lambda) e^{(im\Theta)} \tag{2.23}$$

with P^m_l as the so called *Legendre polynomials*.

Although the STOs provide a good basis describing molecular wavefunctions the integration of these functions, which is needed for typical types of quantum chemical approaches is computationally very demanding. Hence, a further approximation is made. The STOs are resembled by *Gaussian-type functions (GTOs)*. GTOs can be integrated much easier than STOs and can therefore reduce the computational cost. The general form of the GTO is

$$\phi^{\mathrm{GTO}}_{nlm}(d, \Lambda, \Theta) = R_{nl}(d, \alpha) Y_{lm}(\Lambda, \Theta) \tag{2.24}$$

and is therefore very similar to the form of the STO as defined in Eq. 2.21. The

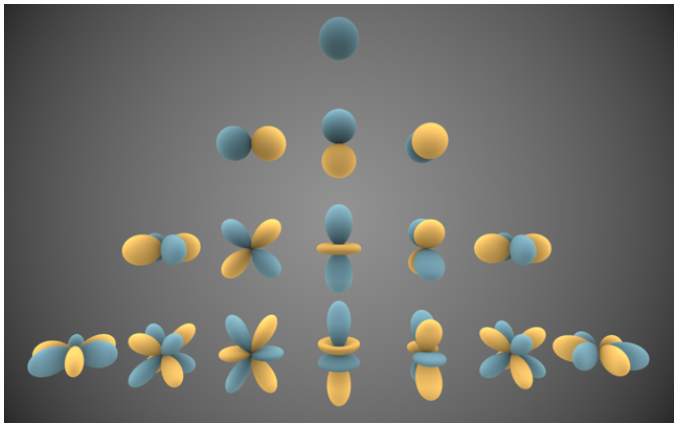

Figure 2.3: Visual representations of the first few real spherical harmonics. Blue portions represent regions where the function is positive, and yellow portions represent where it is negative. The distance of the surface from the origin indicates the value of $Y_{lm}(\Lambda, \Theta)$ in angular direction (Λ, Θ). Picture generously provided by Inigo Quilez [46]

same separation of the radial and angular part is noticeable. However, the radial part itself differs compared to the STO definition. The radial part for the GTO is given as

$$R_{nl}(d,\alpha)^{\mathrm{GTO}} = \sqrt[4]{\frac{2(2\alpha)^3}{\pi}}\sqrt{\frac{2^{2n-l-2}}{(4n-2l-3)!!}}\left(\sqrt{2\alpha}d\right)^{2n-l-2}e^{-\alpha d^2}. \tag{2.25}$$

It depends on the principle quantum number n, the angular momentum quantum number l in spherical harmonics and the orbital exponent α. Using variable exponents and rewriting the sperical harmonics in term of real solid harmonics yields the final equations for real-valued spherical-harmonic GTOs:

$$\phi^{\mathrm{GTO}}_{lm\alpha}(d,x,y,z) = N^{\mathrm{GTO}}_{lm\alpha}S_{lm}(x,y,z)e^{-\alpha d^2} \tag{2.26}$$

which is independent of n. In Eq. 2.26, $N^{\mathrm{GTO}}_{lm\alpha}$ is the normalization constant and $S_{lm}(x,y,z)$ corresponds to the real solid harmonics. A linear combination of GTOs is fitted to a STO according to

$$\phi^{\text{STO-kG}} = \sum_{i=1}^{k} C_i\phi^{\mathrm{GTO}}(\alpha_i). \tag{2.27}$$

In Eq. 2.27, k indicates the number of used GTOs to fit a STO. Since a GTO differs mainly in the nucleus-near and outer sphere region from a STO, many GTO

are used to fit one STO. Although a multiple of STOs is used in total in GTOs, it is still beneficial in computation time since a typical integration procedure on an STO is four orders of magnitude more demanding. The resemblance of GTOs to an STO is illustrated in Fig 2.4.

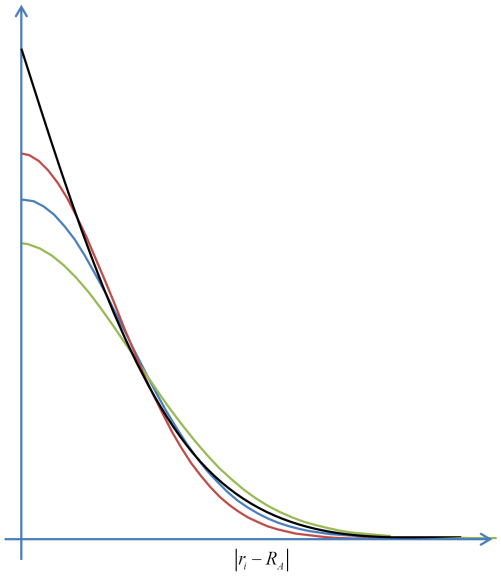

Figure 2.4: Schematic illustration of the fit of up to three GTOs to one STO.

Typically, the coefficients of the linear combination of GTOs is fixed in a basis set. The individual GTOs are called *primitive* Gaussian functions (primitive GFs), the resulting fitted STO is called *contracted* Gaussian function (contracted GF). If each STO is represented by only one contracted GF, the basis set is labeled as *minimal*. However, the minimal basis set resembles the STOs of the hydrogen atom quite well. For other elements, however, the description is getting poorer. The basis functions lack flexibility to adapt to the different electronic structure of heavier elements. Introducing more contracted GFs to resemble the same STO increases the accuracy since the various functions can adapt better to the exact form of the STO. This redundancy is referred to as the ζ- (zeta) level. In a double-ζ basis set, the STO is represented by two individual and independent contracted GFs. Since especially the valence region in an atom profits from more contracted GFs because of the interaction with other atoms, the basis set is split. A single-ζ basis is used to describe the core region and an n-ζ basis is used for the valence region. These types of basis sets are called *split valence* or *split valence n-ζ* basis sets with n as double, triple, etc.. A famous family of basis sets, introduced by

John A. Pople[47–53] is introduced here to analyze the contents of a typical basis set. These basis sets share the same syntax in the description. It is always $x - yG$ with x as the amount of primitive GFs used to form a contracted GF for the core region. The hyphen indicates the splitting of core- and valence region and the y indicate the amount of primitive GFs used for each contracted GF while the digits indicate the ζ level. I would like to illustrate the example of 6-311++G** in more detail.

- **6:** The number 6 indicates that six primitive GFs are used to construct one contracted GF for the core region.
- **-:** The hyphen separates the core and valence region.
- **311:** The three digits indicate a triple-ζ basis. Each contracted GF is constructed from n primitive GFs while n is indicated by the number at the specific digit. In this case, the first contracted GF is formed using three primitive GFs. The second and third contracted GF are identical to the primitive GF, since only one primitive GF is used.
- **++:** The plus sign requests additional diffuse functions. A diffuse function is defined as function with the same spatial orientation but a larger distribution. In that way, long range effects or electronic excitations with high excitation energies can be treated better. The resulting MOs might be spatially delocalized or occupy outer regions of the molecular system. In this case diffuse functions are requested for both hydrogen and heavy atoms (double plus sign).
- **G:** The letter G indicates the use of GTOs to resemble a STO.
- ****:** The asterisk request additional polarization functions. A polarization function is an additional function of higher order to polarize the electron distribution. For example, the p-orbital is polarized using a d-function. In this case, the double asterisk indicates polarization for both the hydrogen atoms as well as the second row elements Li to F using p- and d functions, respectively.

Other families of basis sets were introduced by e.g. Dunning et. al.[54–56] or Ahlrichs et. al.[57,58] Although they use different schemes for naming the basis sets, the mathematical construction using GTOs is comparable. The Dunning basis sets comprise the form cc-pVXZ with X=D, T, Q, etc. for the ζ level. The

letters are the abbreviation for *correlation-consistent polarized X-zeta*. These basis sets are constructed in a way that allows extrapolation to the complete basis set limit. The third family from Ahlrichs et. al. share names like TZVP for triple-zeta valence polarized and are similar to the aforementioned basis sets.

The atomic basis functions $\phi_\mu(\vec{r})$ are finally used to construct single-electron wavefunctions (i.e. molecular orbitals MOs)$\psi_n(\vec{r})$. This is done by a linear combination of atomic orbitals (LCAO).

$$\psi_n(\vec{r}) = \sum_\mu C_{\mu n}\phi_\mu(\vec{r}) \tag{2.28}$$

The coefficients of this linear combination are optimized in a special procedure. This is described in Section 2.2.1.

2.1.5 Second quantization

Up to now, I used the standard notation of quantum mechanics which represents observables as operators and states as functions. Here, I would like to introduce a further way of notation referred to as *second quantization* in which the wavefunction is also expressed in terms of operators. At first let me introduce the Dirac notation for vectors, matrices and two-electron integrals which will be used from now on.

- A state is represented as a *ket* vector $|\alpha\rangle$.
- The complex conjugate is represented by the bra vector $\langle\alpha|$.
- The inner (scalar) product is defined as $\langle\alpha|\beta\rangle$
- State vectors and operators:[59]

$$|a\rangle = \sum_i |\alpha_i\rangle\langle\alpha_i|\alpha\rangle = \sum_i a_i|\alpha_i\rangle \quad \rightarrow \quad (\alpha_1, \alpha_2, ...)^T \tag{2.29}$$

$$\hat{A} = \sum_{ij} A_{ij}|\alpha_i\rangle\langle\alpha_j| \tag{2.30}$$

$$\langle a|a\rangle = \sum_i a_i^\star a_i = \sum_i |a_i|^2 \tag{2.31}$$

- One- and two-electron integrals:[59]

$$\langle p|\hat{o}|q\rangle = \langle \psi_p|\hat{o}|\psi_q\rangle = \int dr_1 \psi_p^\star(r_1) o(x_1) \psi_q(r_1) \tag{2.32}$$

$$\langle pq|rs\rangle = \langle \psi_p\psi_q|\psi_r\psi_s\rangle = \int dr_1 dr_2 \frac{\psi_p^\star(r_1)\psi_q^\star(r_2)\psi_r(r_1)\psi_s(r_2)}{|x_1 - x_2|} \tag{2.33}$$

$$\langle pq||rs\rangle = \langle pq|rs\rangle - \langle pq|sr\rangle \tag{2.34}$$

$$\langle pq||rs\rangle = \langle rq||ps\rangle \tag{2.35}$$

For the second quantization, an abstract linear vector space is constructed, the *Fock space*. In this Fock space, each determinant of a Slater determinant (Eq. 2.19) can be represented by an *occupation number (ON) vector*, $|\mathbf{n}\rangle$, which is defined as

$$|\mathbf{n}\rangle = |n_1, n_2, ..., n_M\rangle \quad \text{with} \quad n_i = \begin{cases} 1 & \text{if one-particle state } \psi_i \text{ is occupied} \\ 0 & \text{if one-particle state } \psi_i \text{ is } \underline{\text{not}} \text{ occupied} \end{cases}. \tag{2.36}$$

Thus, the occupation number n_i indicates whether ψ_i is present (= 1) or absent (= 0) in the determinant. The inner product of two ON vectors $\langle\mathbf{n}|$ and $\langle\mathbf{m}|$ is defined as

$$\langle \mathbf{n}|\mathbf{m}\rangle = \delta_{n,m} = \prod_{p=1}^{M} \delta_{n_p m_p} \tag{2.37}$$

with M as the size of the basis. The vacuum state is defined as a state without any electrons:

$$|vac\rangle = |0_1, 0_2, \ldots, 0_M\rangle. \tag{2.38}$$

In contrast to the standard formulation of quantum mechanics, in the second quantization the number of particles is not conserved. Special operators are introduced to modifiy the number of particles in a system: the creation ($c_P^\dagger$) and annihilation (c_p) operators which create or destruct a particle in the state they are working on. The creation operator is defined by the relations

$$\hat{c}_p^\dagger |n_1, n_2, \ldots, 0_p, \ldots, n_M\rangle = \prod_{q=1}^{p-1} (-1)^{k_q} |n_1, n_2, \ldots, 1_p, \ldots, n_M\rangle \tag{2.39}$$

$$\hat{c}_p^\dagger |n_1, n_2, \ldots, 1_p, \ldots, n_M\rangle = 0. \tag{2.40}$$

with p and q as general spin-orbitals. The annihilation operator is defined as:

$$\hat{c}_p|n\rangle = \delta_{n_p 1} \prod_{q=1}^{p-1} (-1)^{k_q} |n_1, n_2, \ldots, 0_p, \ldots, n_M\rangle. \tag{2.41}$$

This means, that the creation operator can only create a particle in ψ_p if it is unoccupied and the annihilation operator can only destruct a particle in ψ_p if it is occupied. Otherwise, the operation yields zero. The creation operator increases the ON by one while the annihilation operator decreases the ON by one. Creation and annihilation operators can be combined as in the ON operator

$$\hat{N}_p = \hat{c}_p^\dagger \hat{c}_p \tag{2.42}$$

which simply counts the number of electrons in the spin-orbital p:

$$\hat{N}_p|\mathbf{n}\rangle = \hat{c}_p^\dagger \hat{c}_p|\mathbf{n}\rangle = \delta_{n_p 1}|\mathbf{n}\rangle = n_p|\mathbf{n}\rangle. \tag{2.43}$$

A second important example for combinations of creation and annihilation operators is the excitation operator

$$\hat{C}_i^a = \hat{c}_a^\dagger \hat{c}_i \tag{2.44}$$

This operator moves an electron from the orbital i to orbital a. When combining creation and annihilation operators, the anti-commutation relations have to be considered since the order of the operators is important. These are:

$$[\hat{c}_p^\dagger, \hat{c}_q^\dagger]_+ = 0 \tag{2.45}$$

$$[\hat{c}_p, \hat{c}_q]_+ = 0 \tag{2.46}$$

$$[\hat{c}_p, \hat{c}_q^\dagger]_+ = \delta_{pq} \tag{2.47}$$

with

$$[\hat{X}, \hat{Y}]_+ = \hat{X}\hat{Y} + \hat{Y}\hat{X}. \tag{2.48}$$

Using the creation and annihilation operators it is possible to represent any physical operator in the framework of second quantization. A general one-particle operator in first-quantization form is given as

$$\hat{O} = \sum_{i=1}^{N} \hat{o}(i) \tag{2.49}$$

with $\hat{o}(i)$ acting only on particle i. The same operator in the language of second quantization is

$$\hat{O} = \sum_{p,q} \langle \psi_p | \hat{o} | \psi_q \rangle \hat{c}_p^\dagger \hat{c}_q. \tag{2.50}$$

For two- or more-particle operators, a similar representation can be found. A general two-particle operator

$$\hat{G} = \frac{1}{2} \sum_{i \neq j=1}^{N} \hat{g}(i,j) \tag{2.51}$$

is given in second quantized form as

$$\hat{G} = \frac{1}{2} \sum_{p,q,r,s} \langle \psi_p \psi_q | \hat{g} | \psi_r \psi_s \rangle \hat{c}_p^\dagger \hat{c}_q^\dagger \hat{c}_s \hat{c}_r. \tag{2.52}$$

In combination, the molecular electronic Hamiltonian can be written in second quantization:

$$\hat{H} = \sum_{pq} h_{pq} \hat{c}_p^\dagger \hat{c}_q + \frac{1}{2} \sum_{pqrs} V_{pqrs} \hat{c}_p^\dagger \hat{c}_q^\dagger \hat{c}_s \hat{c}_r + \hat{H}_{nuc} \tag{2.53}$$

with

$$\begin{aligned} h_{pq} &= \langle \psi_p | -\frac{1}{2}\nabla^2 - \sum_A \frac{Z_A}{x_A} | \psi_q \rangle \qquad (2.54) \\ &= \int \psi_p^*(\vec{x} \left(-\frac{1}{2}\nabla^2 - \sum_A \frac{Z_A}{\vec{x_A}} \right) \psi_q(\vec{x}) \\ V_{pqrs} &= \langle \psi_p \psi_q | \frac{1}{x_{12}} | \psi_r \psi_s \rangle \qquad (2.55) \\ &= \int \int \frac{\psi_p^*(\vec{x_1}) \psi_q^*(\vec{x_2}) \psi_r(\vec{x_1}) \psi_s(\vec{x_2})}{x_{12}} d\vec{x_1} d\vec{x_2} \\ \hat{H}_{nuc} &= \frac{1}{2} \sum_{A \neq B} \frac{Z_A Z_B}{x_{AB}} \qquad (2.56) \end{aligned}$$

where x_A as the electron-nuclear distance, x_{12} as the electron-electron distance and x_{AB} as the nuclear-nuclear distance.

2.1.6 Slater-Condon rules

In this section I would like to briefly summarize the Slater-Condon rules for integrals of one- and two-body operators and wavefunctions constructed as Slater determinants. The Slater Condon rules are given here without derivation. For

further explanation I would like to refer the book "Modern Quantum Chemistry" by A. Szabo and N. S. Ostlund.[39]
As already shown in Eq. 2.49 a one-body operator in an N-particle system is defined as

$$\hat{O} = \sum_{i=1}^{N} \hat{o}(i). \tag{2.57}$$

The integrals for a generic one-body operator are given as:

$$\langle \Psi | \hat{O} | \Psi \rangle = \sum_{i=1}^{N} \langle \psi_i | \hat{f} | \psi_i \rangle \tag{2.58}$$

$$\langle \Psi | \hat{O} | \Psi_i^a \rangle = \langle \psi_i | \hat{f} | \psi_a \rangle \tag{2.59}$$

$$\langle \Psi | \hat{O} | \Psi_{ij}^{ab} \rangle = 0 \tag{2.60}$$

with Ψ_i^a as a wavefunction with an electron from orbital i excited to a and Ψ_{ij}^{ab} as a wavefunction with two electrons from orbitals i and j excited to orbitals a and b.

In other words: If the bra- and ket wavefunction differ by more than one electron, the expectation value vanishes. For a generic two-body operator, which is as shown in Eq. 2.51 composed as:

$$\hat{G} = \frac{1}{2} \sum_{i=1}^{N} \sum_{j \leq i}^{N} \hat{g}(i,j) \tag{2.61}$$

the Slater-Condon rules are given as:

$$\langle \Psi | \hat{G} | \Psi \rangle = \sum_{i=1}^{N} \sum_{j \leq i}^{N} \left(\langle \psi_i \psi_j | \hat{g} | \psi_i \psi_j \rangle - \langle \psi_i \psi_j | \hat{g} | \psi_j \psi_i \rangle \right) \tag{2.62}$$

$$\langle \Psi | \hat{G} | \Psi_i^a \rangle = \sum_{j=1}^{N} \left(\langle \psi_i \psi_j | \hat{g} | \psi_a \psi_j \rangle - \langle \psi_i \psi_j | \hat{g} | \psi_j \psi_a \rangle \right) \tag{2.63}$$

$$\langle \Psi | \hat{G} | \Psi_{ij}^{ab} \rangle = \langle \psi_i \psi_j | \hat{g} | \psi_a \psi_b \rangle - \langle \psi_i \psi_j | \hat{g} | \psi_b \psi_a \rangle. \tag{2.64}$$

Any integral of a two-body operator with wavefunctions differing in three or more orbitals results in zero.

2.2 Electronic ground state methods

In this Section I would like to elaborate some important methods used to describe the electronic ground state of a molecular system. As said before, the electronic SE is not solvable analytically due to the many-body electron-electron repulsion. Various methods were introduced approximating this term. I will start with the Hartree-Fock (HF) theory, the most common *ab initio* method. *"Ab initio"*, meaning "from the beginning", refers to the fact that nothing other than physical constraints are needed for the formulation of the theory. It serves also as the fundamental theory for a family of method denoted as post-Hartree-Fock theories since the are based on the HF solution. Out of these post-HF methods I would like to review the configuration interaction (CI) method, which is the most simple extension to HF, the Møller-Plesset (MP) perturbation theory as a second post-HF variant and coupled cluster as an alternative to CI. In the last part of this section I would like to introduce the density functional theory as an alternative to the HF and post-HF theories using a different ansatz.

The reviewed theories and methods in this section are again, if not otherwise stated, taken from the books: *"Modern Quantum Chemistry"* by *A. Szabo and N. S. Ostlund*,[39] *"Introduction to Computational Chemistry"* by *F. Jensen*[40], *"Essentials of Computational Chemistry: Theories and Models"* by *C. Cramer*[60] and *"Molecular Electronic-Structure Theory"* by *T. Helgaker, J. Olsen and P. Jørgensen*[41] to which I would like to refer for further reading.

2.2.1 Hartree-Fock theory

In Hartree-Fock (HF) the only further approximation made is that the total wavefunction Ψ consists of only one Slater determinant. Therefore, HF belongs to the singe-determinant methods in contrast to multi-determinant methods which will not be covered in this thesis. The neglect of electron correlation is a direct consequence from this approximation. The HF theory is derived via the variation principle. This principle states that if a normalized wave function Ψ with the boundary condition to vanish at infinity is given, the expectation value of the Hamiltonian is an upper bound to the exact ground state energy.

$$\frac{\langle \Psi | \hat{H} | \Psi \rangle}{\langle \Psi | \Psi \rangle} \geq E_0 \tag{2.65}$$

In other words: Using an approximate wavefunction, the energy is always lower than the exact energy of the Hamiltonian. A better wavefunction results in a lower energy while the exact wavefunction yields the minimal energy. Therefore, the trail wavefunction is varied to minimize the expectation value. This is done by varying the coefficients of the LCAO ansatz (Eq. 2.28) The minimization is under the side condition that the orbitals be orthogonal

$$\int \psi_i^*(\vec{x})\psi_j(\vec{x})d\vec{x} = \delta_{ij} \tag{2.66}$$

and results in the Hartree-Fock equation:

$$\hat{f}_i|\psi(\vec{x}_i)\rangle = \epsilon_i|\psi(\vec{x}_i)\rangle \tag{2.67}$$

with the Lagrange multiplier ϵ_i corresponding to the orbital energies as eigenvalues and the MOs $\psi_i(\vec{x}_i)$ as the eigenfunctions of the Fock operator $\hat{f}_i$ which is defines as:

$$\begin{aligned}\hat{f}_i &= \hat{h}_i + \hat{v}_i^{HF} \\ &= -\frac{1}{2}\nabla_i^2 - \sum_{A=1}\frac{Z_A}{\vec{x}_{iA}} + \sum_j(\hat{J}_j(i) - \hat{K}_j(i)).\end{aligned} \tag{2.68}$$

In Eq. 2.68, the operator $\hat{h}_i$ represents the one-electron interactions while $\hat{v}_i^{HF}$ describes the electron-electron interaction in terms of Coulomb $\hat{J}_j(i)$ and exchange $\hat{K}_j(i)$. The latter two operators are defined as

$$\hat{J}_j(1)\psi_i(1) = \left(\int d\vec{x}_2 \frac{\psi_j^\star(2)\psi_j(2)}{\vec{x}_{12}}\right)\psi_i(1) \tag{2.69}$$

$$\hat{K}_j(1)\psi_i(1) = \left(\int d\vec{x}_2 \frac{\psi_j^\star(2)\psi_i(2)}{\vec{x}_{12}}\right)\psi_j(1). \tag{2.70}$$

In second quantization, the Fock operator can be written as

$$\begin{aligned}\hat{f} &= \hat{h} + \hat{V}^{HF} \\ &= \sum_{pq}\langle\psi_p| - \frac{1}{2}\nabla^2 - \sum_A \frac{Z_A}{\vec{x}_{iA}}|\psi_q\rangle\hat{c}_p^\dagger\hat{c}_q + \sum_{pqi}(v_{pqii} - v_{piiq})\end{aligned} \tag{2.71}$$

with

$$v_{pqrs} = \langle pq|\frac{1}{\vec{x}_{12}}|rs\rangle. \tag{2.72}$$

As can be seen in Eqs 2.68 - 2.70 the electron i is treated in the mean field

of all other electrons. Therefore, HF is referred to as a *mean-field theory*. The direct electron-electron interaction, the *electron correlation* is neglected in Hartree Fock. The HF equation 2.67 is a non-linear differential eigenvalue equation. This means that for the calculation of the mean field of all other electrons, the solution of the equation itself is needed, since the orbitals are part of the operator itself. Therefore, the HF equation needs to be solved iteratively using an initial guess for the MOs in the first cycle. This iterative procedure is called *self-consistent cield (SCF)* and converges when the difference in orbital energies and wavefunction between two cycles is smaller than a given threshold. Eq. 2.67 results in the HF ground state energy which is defined as:

$$\begin{aligned} E_{HF} =& \langle \Psi_0^{HF} | \hat{H} | \Psi_0^{HF} \rangle \\ =& \sum_i \int \psi_i^*(\vec{x_1}) \hat{h}_i \psi_i(\vec{x_1}) d\vec{x}_1 \\ &+ \frac{1}{2} \Bigg(\sum_{ij} \int \frac{\psi_i^*(\vec{x_1}) \psi_j^*(\vec{x_2}) \psi_i(\vec{x_1}) \psi_j(\vec{x_2})}{|x_1 - x_2|} d(\vec{x_1}) d(\vec{x_2}) \\ &- \sum_{ij} \int \frac{\psi_i^*(\vec{x_1}) \psi_j^*(\vec{x_2}) \psi_j(\vec{x_1}) \psi_i(\vec{x_2})}{|x_1 - x_2|} d(\vec{x_1}) d(\vec{x_2}) \Bigg) \end{aligned} \tag{2.73}$$

which can be written as

$$\begin{aligned} E_{HF} &= \sum_i \langle i | \hat{h}_i | i \rangle + \frac{1}{2} \sum_{ij} \left(\langle ij | ij \rangle - \langle ij | ji \rangle \right) \\ &= \sum_i \langle i | \hat{h}_i | i \rangle + \frac{1}{2} \sum_{ij} \langle ij || ij \rangle. \end{aligned} \tag{2.74}$$

We introduce an atomic basis and expand the MOs in the basis functions of atomic orbitals (AOs)

$$\psi_n(\vec{x}) = \sum_\mu C_{\mu n} \phi_\mu(\vec{x}) \tag{2.75}$$

which is known as the LCAO anstz and already shown in Eq 2.28. Inserting Eq. 2.75 into the HF equation 2.67 yields

$$\hat{f}_i \sum_\mu C_{\mu i} \phi_{\mu i} = \epsilon_i \sum_\mu C_{\mu i} \phi_{\mu i}. \tag{2.76}$$

Multiplying from the left by a basis function $\phi_{\lambda i}^*$ and integrating yields the *Roothan-*

Hall equations, which are simply the HF equations in the atomic orbital basis.

$$\sum_{\mu} \mathbf{F}_{\mu\lambda}\mathbf{C}_{\mu i} = \epsilon_i \sum_{\mu} \mathbf{S}_{\mu\lambda}\mathbf{C}_{\mu i} \tag{2.77}$$

with

$$\begin{aligned} \mathbf{F}_{\mu\lambda} &= \langle\phi_\mu|\mathbf{F}|\phi_\lambda\rangle \\ \mathbf{S}_{\mu\lambda} &= \langle\phi_\mu|\phi_\lambda\rangle. \end{aligned} \tag{2.78}$$

Closely connected to the Roothan-Hall equation is the *density matrix*.[39] When a spatial wavefunction $\Psi_n(\vec{r})$ is given, the probability of finding an electron in the volume element $d(\vec{r})$ is defined by

$$\begin{aligned} \rho(\vec{r}) &= 2\sum_{n}^{N/2} |\Psi_n(\vec{x})|^2 \\ &= 2\sum_{a}^{N/2} \Psi_n^*(\vec{x})\Psi_n(\vec{x}). \end{aligned} \tag{2.79}$$

Inserting the LCAO ansatz from Eq. 2.75 into Eq. 2.79 yields the electron density in the AO basis:

$$\begin{aligned} \rho(\vec{r}) &= 2\sum_{n}^{N/2}\sum_{\nu} C_{\nu n}^*\phi_\nu^*(\vec{r})\sum_{\mu} C_{\mu n}\phi_\mu(\vec{x}) \\ &= \sum_{\mu\nu} P_{\mu\nu}\phi_\mu(\vec{x})\phi_\nu^*(\vec{x}) \end{aligned} \tag{2.80}$$

with

$$P_{\mu\nu} = 2\sum_{n}^{N/2} C_{\mu n}C_{\nu n}^* \tag{2.81}$$

as the density matrix. Multiplying this density matrix with a set of known basis functions ϕ_μ yields the electron density $\rho(\vec{r})$.

According to Eq. 2.68, the orbital energy ϵ_i of a occupied orbital i is defined as

$$\begin{aligned} \epsilon_i = \langle\psi_i|f|\psi_i\rangle &= \langle\psi_i|\hat{h}_i + \sum_j \hat{J}_j(i) - \hat{K}_j(i)|\psi_i\rangle \\ &= \langle\psi_i|\hat{h}_i|\psi_i\rangle + \sum_j \langle\psi_i|\hat{J}_j(i)|\psi_i\rangle - \langle\psi_i|\hat{K}_j(i)|\psi_i\rangle \\ &= \langle i|\hat{h}_i|i\rangle + \sum_j \langle ij||ij\rangle \end{aligned} \tag{2.82}$$

while for a virtual orbital a the orbital energy ϵ_a is defined as

$$\epsilon_a = \langle a|\hat{h}_a|a\rangle + \sum_j \langle aj||aj\rangle. \tag{2.83}$$

Since $\langle ii||ii\rangle = 0$ Eq. 2.82 can be rewritten as

$$\epsilon_i = \langle i|\hat{h}_i|i\rangle + \sum_{j\neq i} \langle ij||ij\rangle. \tag{2.84}$$

Comparison of Eqs. 2.83 and 2.84 shows that the occupied orbital i is exposed to the field created by all other orbitals since its artificial interaction with itself cancels out. In contrast, the virtual orbital a is calculated in the field of all occupied orbitals. Thus, the occupied orbitals represent the N-particle system while the virtual orbitals are calculated for the (N+1) particle system, i.e. an additional electron. This property of HF is utilized in an approximation estimating the electron affinity (EA) and the ionization potential (IP) referred to as *Koopmans' theorem*. It states, that the EA is the negative energy of the lowest unoccupied molecular orbital (LUMO) while the IP corresponds to the negaive energy of the highest occupied molecular orbital (HOMO).

The consequences from the approximation made in the HF theory is that it neglects completely the specific interactions between individual electrons, referred to as *electron correlation*. The correlation energy is defined as the difference of the HF energy from the exact energy E_0:

$$E_{corr} = E_0 - E_{HF}. \tag{2.85}$$

Although the contribution of the correlation energy to the total energy of a state is rather small ($< 5\%$) it is essential for chemical properties and especially electronic excitations. The post-HF methods were developed to calculate the electron correlation based on the HF results.

HF typically scales cubically (N^3) for the diagonalization of the Fock-matrix $\mathbf{F}$ with N as the number of basis functions.

2.2.2 Configuration interaction

The Configuration Interaction (CI) is based on the HF solution. Its main idea is to build a wavefunction not from only one Slater determinant (SD) but from a linear combination of multiple different Slater determinants. Therefore, based on the

HF solution, further SDs were created with electrons excited to virtual orbitals. These excited SDs however use the converged single-particle wavefunction (MOs) of HF without any modification. The excited determinants are constructed by excitation operators acting on the ground state SD. Using this ansatz, it is possible to calculate both ground and excited states. For now, I will concentrate on the ground state; for calculation of excited states please see section 2.3.1

$$|\Phi_{CI}\rangle = \sum_{\omega=0}^{N} k_\omega \hat{C}_N |\Psi_0\rangle \tag{2.86}$$

with

$$\hat{C}_N = \left\{ \mathbf{1};\ \hat{c}_a^\dagger \hat{c}_i;\ \hat{c}_a^\dagger \hat{c}_b^\dagger \hat{c}_i \hat{c}_j, a<b, i<j;\ \hat{c}_a^\dagger \hat{c}_b^\dagger \hat{c}_c^\dagger \hat{c}_i \hat{c}_j \hat{c}_k, a<b<c, i<j<k;\ ... \right\}. \tag{2.87}$$

The SDs are sorted by their level of excitation. SDs containing only one excited electron are called singles (S), two excited electrons are doubles(D) then triples(T) and so on.

$$\begin{aligned} |\Phi_{CI}\rangle &= k_0|\Psi_0\rangle + \left(\frac{1}{1!}\right)^2 \sum_{ai} k_i^a \hat{C}_i^a |\Psi_0\rangle \\ &\quad + \left(\frac{1}{2!}\right)^2 \sum_{abij} k_{ij}^{ab} \hat{C}_{ij}^{ab} |\Psi_0\rangle + \left(\frac{1}{3!}\right)^2 \sum_{abcijk} k_{ijk}^{abc} \hat{C}_{ijk}^{abc} |\Psi_0\rangle + ... \\ &= k_0|\Psi_0\rangle + k_S|\Psi_S\rangle + k_D|\Psi_D\rangle + k_T|\Psi_T\rangle + ... \end{aligned} \tag{2.88}$$

The CI coefficients k_ω are then optimized using the variation principle (see Eq. 2.65) as

$$0 = \frac{\partial}{\partial k_\omega} \frac{\langle \Phi_0 | \hat{H} | \Phi_0 \rangle}{\langle \Phi_0 | \Phi_0 \rangle}. \tag{2.89}$$

Sorting the multi-determinant wavefunction into its components of only singles (Ψ^S), doubles (Ψ^D), etc. results in the CI matrix. To obtain the exact ground state energy and wavefunction, this matrix has to be diagonalized. The resulting lowest eigenvalue represents the ground state energy while the corresponding eigenfunction represents the ground state wavefunktion. As stated by the Brillouin's theorem[39,60] the matrix elements for $\langle \Psi_S | \hat{H} | \Psi_0 \rangle$ and $\langle \Psi_0 | \hat{H} | \Psi_S \rangle$ vanish since they give no correction to the HF energy. Also, as stated by the Slater-Condon rules (see section 2.1.6), any expectation value calculated from wavefunctions that differ in more than two orbitals yields zero.

If all possible combinations of excitations are considered it is called *Full-CI*.

Table 2.1: Structure of the full CI matrix.

	$\|\Psi_0\rangle$	$\|\Psi_S\rangle$	$\|\Psi_D\rangle$	$\|\Psi_T\rangle$	$\|\Psi_Q\rangle$	...
$\langle\Psi_0\|$	$\langle\Psi_0\|\hat{H}\|\Psi_0\rangle$	0	$\langle\Psi_0\|\hat{H}\|\Psi_D\rangle$	0	0	...
$\langle\Psi_S\|$	0	$\langle\Psi_S\|\hat{H}\|\Psi_S\rangle$	$\langle\Psi_S\|\hat{H}\|\Psi_D\rangle$	$\langle\Psi_S\|\hat{H}\|\Psi_T\rangle$	0	...
$\langle\Psi_D\|$	$\langle\Psi_D\|\hat{H}\|\Psi_0\rangle$	$\langle\Psi_D\|\hat{H}\|\Psi_S\rangle$	$\langle\Psi_D\|\hat{H}\|\Psi_D\rangle$	$\langle\Psi_D\|\hat{H}\|\Psi_T\rangle$	$\langle\Psi_D\|\hat{H}\|\Psi_Q\rangle$	...
$\langle\Psi_T\|$	0	$\langle\Psi_T\|\hat{H}\|\Psi_S\rangle$	$\langle\Psi_T\|\hat{H}\|\Psi_D\rangle$	$\langle\Psi_T\|\hat{H}\|\Psi_T\rangle$	$\langle\Psi_T\|\hat{H}\|\Psi_Q\rangle$	...
$\langle\Psi_Q\|$	0	0	$\langle\Psi_Q\|\hat{H}\|\Psi_D\rangle$	$\langle\Psi_Q\|\hat{H}\|\Psi_T\rangle$	$\langle\Psi_Q\|\hat{H}\|\Psi_Q\rangle$	...
⋮	⋮	⋮	⋮	⋮	⋮	⋱

Full-CI is the numerically exact solution of the SE in the given basis. However, Full-CI, exhibiting an exponential scaling (e^N) with N as the number of basis functions, is computationally so expensive that on current computer systems only very small systems like H_2O can be calculated. Hence, not all possible excited determinants are considered. The CI expansion (Eq. 2.88) is truncated after a specific level of excitation operator. If only singles are considered in addition to the HF wavefunction, the method is referred to as CI-singles or CIS. If singles and doubles are included, it is called CI-singles and doubles (CISD). Unfortunately, except CIS, which is identical to HF for the electronic ground state and Full CI, all truncated CI methods suffer from size-inconsistency. That means that the result of a system of two non-interacting subsystems differs from the sum of the individually calculated subsystems, which is non-physical. Therefore, besides for benchmark calculations employing Full CI, the truncated CI methods are not used in contemporary ground state calculations any more.

2.2.3 Coupled cluster approach

The Coupled Cluster (CC) approach is similar to CI. It was designed to overcome the size-inconsistency of truncated CI methods. Similar to CI, the HF wavefunction is taken as the zero order reference. The coupled cluster wavefunction is expanded in a product form:

$$\Phi_{CC} = \prod_{\omega}(1 + t_\omega \hat{C}_\omega)|\Psi_0\rangle \tag{2.90}$$

with the generalized excitation operator

$$\hat{C}_\omega = \left\{\hat{c}_a^\dagger \hat{c}_i;\ \hat{c}_a^\dagger \hat{c}_b^\dagger \hat{c}_i \hat{c}_j, a<b, i<j;\ \hat{c}_a^\dagger \hat{c}_b^\dagger \hat{c}_c^\dagger \hat{c}_i \hat{c}_j \hat{c}_k, a<b<c, i<j<k;\ ...\right\} \tag{2.91}$$

and the excitation probabilities t_ω as coupled cluster amplitudes. In combination, they form the cluster operator

$$\hat{T} = \sum_{\omega}^{M} t_\omega \hat{C}_\omega \tag{2.92}$$

which can be ordered depending on the excitation class:

$$\hat{T} = \hat{T}_S + \hat{T}_D + \hat{T}_T + \ldots + \hat{T}_M. \tag{2.93}$$

M corresponds to the number of maximum possible excitations. CC can be truncated like CI (see section 2.2.2. In this case, M defines the truncation. The CCSD method is obtained if the cluster operator is truncated after double excitations. For a better algebraic usability, the product ansatz (Eq. 2.90) is reformulated in an exponential form using the relations $(\hat{C}_\omega)^2 = 0$ and $[\hat{C}_\omega, \hat{C}_\mu] = 0$ (See Eqs 2.45 - 2.48)

$$\begin{aligned} 1 + \hat{T}_\omega = 1 + \hat{T}_\omega + \frac{1}{2!}\hat{T}_\omega^2 + \frac{1}{3!}\hat{T}_\omega^3 + ... = e^{\hat{T}_\omega} \\ |\Phi_{CC}\rangle = \prod_{\omega}(1 + t_\omega \hat{C}_\omega)|\Psi_0\rangle = e^{\hat{T}}|\Psi_0\rangle. \end{aligned} \tag{2.94}$$

The CC wavefunction cannot be optimized using the variation principle since this results in an intractable set of nonlinear equations. A different approach is used instead which projects the HF state and those determinants that enter the CC state with connected amplitudes

$$\langle\mu| = \langle\Psi_o|\hat{O}_\omega^\dagger \tag{2.95}$$

against the CC Schrödinger equaition

$$\hat{H}e^{\hat{T}}|\Psi_0\rangle = E_{CC}e^{\hat{T}}|\Psi_0\rangle \tag{2.96}$$

yielding the projected CC equations

$$\langle\mu|\hat{H}e^{\hat{T}}|\Psi_0\rangle = E_0^{CC}\langle\mu|e^{\hat{T}}|\Psi_0\rangle \tag{2.97}$$

which can be written by left-multiplying with $e^{-\hat{T}}$ as

$$\langle\mu|e^{-\hat{T}}\hat{H}e^{\hat{T}}|\Psi_0\rangle = 0 \tag{2.98}$$

and the projected CC energy equation

$$E_0^{CC} = \langle \Psi_0 | e^{-\hat{T}} \hat{H} e^{\hat{T}} | \Psi_0 \rangle. \tag{2.99}$$

These projected CC equations are coupled and have to be solved iteratively.

Since the CC approach is not variational, the resulting energy can be lower than the exact energy of the system. The only exception is Full-CC which yields the same results as Full-CI. Another drawback is the the fact that CC is non-hermitian, resulting in different left-hand and right-hand eigenvectors. To obtain other properties than energies, the CC equations have to be solved twice. Although CC is very demanding in terms of computational cost, the results are very accurate. The truncated method CCSD(T), which treats the triples perturbatively, has become the "gold standard" of quantum chemistry.[61,62]

In addition to the normal truncated CC methods, further approximate CC methods were developed. The CC2 method contains the doubles only on first order, the CC3 method contains similar approximations for the triples.[63,64] The order of energy correction and typical scaling factors of several truncated and approximate CC methods are given in Table 2.2.

Table 2.2: Orders of energy correction and scaling factors for the coupled cluster methods CCS, CC2, CCSD, CC3 and CCSDT. The scaling factor is given as a function of N with N as the number of basis functions. Possible pre-factors are omitted.

Method	order of energy correction	Scaling $[N^x]$
CCS	1	4
CC2	2	5
CCSD	3	6
CC3	4	7
CCSDT	4	8

2.2.4 Perturbation theory

In this section I want to elaborate the perturbative correction of the Hartree-Fock solution to count for correlation energies. Therefore, in the first step the general Rayleigh-Schrödinger terturbation theory (RSPT) is introduced. In the following step this is applied to the HF solution, which is referred to as Møller-Plesset perturbation theory (MPPT).[65] The information reviewed in this section is taken

from Refs. 41 and 59.

2.2.4.1 Rayleigh-Schrödinger perturbation theory

Perturbative approaches are regularly used techniches in the sciences to approximate an exact solution of a quantity. In perturbation theory (PT), this quantity is separated into a known part and an unknown rest, referring to the latter as a *perturbation*. In RSPT, the Hamiltonian is split into two parts:

$$\hat{H} = \hat{H}_0 + \hat{U}. \tag{2.100}$$

with $\hat{H}_0$ as a zeroth-order Hamiltonian, which is known and the perturbation $\hat{U}$, which is defined as

$$\hat{U} = \hat{H} - \hat{H}_0. \tag{2.101}$$

To solve the exact SE

$$\hat{H}|0\rangle = E|0\rangle \tag{2.102}$$

the exact wavefunction and its energy is expanded in orders of perturbation

$$|0\rangle = \sum_{k=0}^{\infty} |0^{(k)}\rangle \tag{2.103}$$

$$E = \sum_{k=0}^{\infty} E^{(k)}. \tag{2.104}$$

The zeroth-order term resembles the exact solution for $\hat{H}_0$

$$\hat{H}_0|0^{(0)}\rangle = E^{(0)}|0^{(0)}\rangle \tag{2.105}$$

with $|0^{(0)}\rangle$ as a set of orthonormal eigenvectors and $E_0^{(0)}$ as the corresponding eigenvalues. The higher order terms are resolved by inserting Eqs. 2.103 and 2.104 into Eq. 2.102. These higher-order terms represent the corrections to the zeroth-order terms. It yields

$$(\hat{H}_0 + \hat{U}) \sum_{k=0}^{\infty} |0^{(k)}\rangle = \sum_{k=0}^{\infty} E^{(k)} \sum_{k=0}^{\infty} |0^{(k)}\rangle. \tag{2.106}$$

Introducing a truncation n of this expansion for considering only corrections up to a given level yields

$$(\hat{H}_0 - E^{(0)})|0^{(n)}\rangle = -\hat{U}|0^{(n-1)}\rangle + \sum_{i=0}^{n} E^{(i)}|0^{(n-i)}\rangle. \tag{2.107}$$

As can be seen, Eq. 2.107 is a recursive equation i.e. the solution for all lower order corrections is needed to calculate the correction of order n. The corrections are set to be orthogonal to the zeroth-order wavefunction:

$$\langle 0^{(0)}|0^{(k)}\rangle = 0,\ k > 1 \tag{2.108}$$

which is equivalent to the requirement that $|0\rangle$ is intermediately normalized:

$$\langle 0^{(0)}|0\rangle = \sum_{i=0}^{\infty}\langle 0^{(0)}|0^{(i)}\rangle = \langle 0^{(0)}|0^{(0)}\rangle = 1. \tag{2.109}$$

The expressions for the perturbative correction of the energy are yielded by multiplying equation 2.107 from the left by the zeroth-order wavefunction $\langle 0^{(0)}|$, resulting in

$$E^{(n)} = \langle 0^{(0)}|\hat{U}|0^{(n-1)}\rangle,\ n > 0 \tag{2.110}$$

The zeroth-order energy is obtained analogously by multiplying equation 2.105 from the left by the zeroth-order wavefunction $\langle 0^{(0)}|$:

$$E^{(0)} = \langle 0^{(0)}|\hat{H}_0|0^{(0)}\rangle. \tag{2.111}$$

In these energy correction terms in RSPT, the perturbation U itself remains unspecified. As can be seen in Eq. 2.110 the energy correction of n^{th}-order requires the $(n-1)^{\mathrm{th}}$-order corrected wavefunction $|0^{(n-1)}\rangle$. The n^{th}-order wavefunction is obtained by multiplying equation 2.107 from the left by $(\hat{H}_0 - E_0^{(0)})^{-1}$:

$$|0^{(n)}\rangle = -\frac{\hat{U}|0^{(n-1)}\rangle - \sum_{k=0}^{n} E^{(k)}|0^{(n-k)}\rangle}{\hat{H}_0 - E^{(0)}}. \tag{2.112}$$

Using the projection operator $\hat{P}$

$$\hat{P} = 1 - |0^{(0)}\rangle\langle 0^{(0)}| \tag{2.113}$$

equation 2.112 can be reformulated in the advantageous form:

$$|0^{(n)}\rangle = -\frac{\hat{P}\left(\hat{U}|0^{(n-1)}\rangle - \sum_{k=0}^{n-1} E^{(k)}|0^{(n-k)}\rangle\right)}{\hat{P}\left(\hat{H}_0 - E^{(0)}\right)}. \tag{2.114}$$

This leads to the annihilation of the zeroth-order wavefunction from the last term of Eq. 2.114. The n$^{\text{th}}$-order wavefunction correction is now determined as a function of all lower order corrections. This is shown in Eqs. 2.115-2.117:

$$|0^{(1)}\rangle = -\frac{\hat{P}\hat{U}|0^{(0)}\rangle}{\hat{P}\big(\hat{H}_0 - E^{(0)}\big)} \tag{2.115}$$

$$|0^{(2)}\rangle = -\frac{\hat{P}\big(\hat{U} - E^1\big)|0^{(1)}\rangle}{\hat{P}\big(\hat{H}_0 - E^{(0)}\big)} \tag{2.116}$$

$$|0^{(3)}\rangle = -\frac{\hat{P}\big[\big(\hat{U} - E^1\big)|0^{(2)}\rangle - E^2|0^{(1)}\rangle\big]}{\hat{P}\big(\hat{H}_0 - E^{(0)}\big)}. \tag{2.117}$$

In the following part, the Hamiltonian and the perturbation will be specified which leads to the Møller-Plesset perturbation theory

2.2.4.2 Møller-Plesset perturbation theory

In section 2.2.4.1, the Rayleigh-Schrödinger perturbation theory (RSPT) was introduced. In this chapter, it is adapted to correct the HF energy and wavefunction for the electron correlation. This is accomplished by taking the HF solution, which can be solved exactly, as the zeroth-order reference. By doing so, the Fock operator $\hat{f}$ is taken as the unperturbed Hamiltonian $\hat{H}_0$ and the perturbation itself is defined as the difference between the full Hamiltonian and the Fock operator:

$$\hat{U} = \hat{H} - \hat{f}. \tag{2.118}$$

The diagonal Fock operator is given as

$$\hat{f} = \sum_p \epsilon_p \hat{c}_p^\dagger \hat{c}_p \tag{2.119}$$

and the full Hamiltonian is, as defined in Eq. 2.53, given as:

$$\hat{H} = \sum_{pq} h_{pq} \hat{c}_p^\dagger \hat{c}_q + \frac{1}{2} \sum_{pqrs} V_{pqrs} \hat{c}_p^\dagger \hat{c}_q^\dagger \hat{c}_s \hat{c}_r. \tag{2.120}$$

Consequential, the perturbation is defined as:

$$\hat{U} = \hat{H} - \hat{f} = \hat{V}_{pqrs} - \hat{V}^{HF} = \frac{1}{2}\sum_{pqrs}\langle pq|rs\rangle c_p^\dagger c_q^\dagger c_s c_r - \sum_{pq}\sum_{i}\langle pi||qi\rangle c_p^\dagger c_q. \quad (2.121)$$

Taking the HF wavefunction $|\Psi_0^{HF}\rangle$ as the zeroth-order wavefunction $|0^{(0)}\rangle$ and inserting Eq. 2.121 in Eqs. 2.110 and 2.111 yields the expressions for the zeroth- (MP(0)) and first-order (MP(1)) MP energy corrections

$$E^{(0)} = \langle 0^{(0)}|\hat{H}_0|0^{(0)}\rangle = \langle 0^{(0)}|\hat{f}|0^{(0)}\rangle = \sum_{i}^{n}\epsilon_i \quad (2.122)$$

and

$$\begin{aligned} E^{(1)} &= \langle 0^{(0)}|\hat{U}|0^{(0)}\rangle = \langle 0^{(0)}|\hat{H} - \hat{f}|0^{(0)}\rangle = \langle 0^{(0)}|\hat{H}|0^{(0)}\rangle - \langle 0^{(0)}|\hat{f}|0^{(0)}\rangle \\ &= -\frac{1}{2}\sum_{ij}\langle ij||ij\rangle. \end{aligned} \quad (2.123)$$

As can be seen in Eq. 2.122 the zeroth-order MP correction is simply the sum of the occupied HF orbital energies. The first-order MP correction represents the difference of the Fock- and Hamilton operator expectation values. In combination, they resemble the HF energy. As a consequence, the first correction to the HF result is obtained from the second-order MP correction. For the calculation of the second-order energy correction, the first-order wavefunction has to be calculated according to Eq. 2.115. In order to reformulate this expression, excited determinants have to be introduced which are created analogously to the CI expansion as shown in Sec. 2.2.2. A N-tuply excited determinant is defined as

$$|\Psi^N\rangle = \hat{C}_N|0^{(0)}\rangle \quad (2.124)$$

with $\hat{C}_N$ as the excitation operator as defined in Eq. 2.87. All excited determinants and the HF ground state constitute an orthonormal set of states and the excited determinants are eigenfunctions of the Fock operator:

$$\hat{f}|\Psi^N\rangle = E_N^{(0)}|\Psi^N\rangle = (E_{MP}^{(0)} + \epsilon_N)|\Psi^N\rangle \quad (2.125)$$

with ϵ_N as the orbital energy differences of the N-tuply excited determinant. In the case of a double excited determinant, ϵ_N is defined as

$$\epsilon_D = \epsilon_a + \epsilon_b - \epsilon_i - \epsilon_j. \tag{2.126}$$

Invoking the resolution of the identity $|\Psi^N\rangle\langle\Psi^N|$ for the projection operator $\hat{P}$ in Eq. 2.115 and using both the Brillouin's theorem [39,60] and the Slater-Condon rules (see Sec. 2.1.6) yields

$$|0^{(1)}\rangle = -\sum_D \frac{|\Psi^D\rangle\langle\Psi^D|\hat{H}|0^{(0)}\rangle}{\epsilon_D}. \tag{2.127}$$

Alternatively, Eq. 2.127 can be expressed as an perturbation operator acting on the HF state:

$$|0^{(1)}\rangle = \hat{T}_2^{(1)}|0^{(0)}\rangle \tag{2.128}$$

with

$$\hat{T}_2^{(1)} = \sum_D t_D^{(1)}\hat{\tau}_D = \sum_{a<b,i<j} t_{ij}^{ab(1)}\hat{c}_a^\dagger\hat{c}_b^\dagger\hat{c}_i\hat{c}_j \tag{2.129}$$

with $t_{ij}^{ab(1)}$ as the first-order amplitude defined as

$$\begin{aligned} t_{ij}^{ab(1)} &= -\frac{\langle 0^{(0)}|[\hat{c}_a^\dagger\hat{c}_b^\dagger\hat{c}_i\hat{c}_j, \hat{H}]|0^{(0)}\rangle}{\epsilon_a + \epsilon_b - \epsilon_i - \epsilon_j} \\ &= -\frac{\langle ab||ij\rangle}{\epsilon_a + \epsilon_b - \epsilon_i - \epsilon_j}. \end{aligned} \tag{2.130}$$

Inserting the amplitude expression in Eq. 2.130 into the wavefunction expression in Eq. 2.128 yields the final expression for the first-order wavefunction:

$$\begin{aligned} |0^{(1)}\rangle &= -\sum_{a<b,i<j} \frac{\langle ab||ij\rangle}{\epsilon_a + \epsilon_b - \epsilon_i - \epsilon_j}|\Psi^D\rangle \\ &= -\sum_{a<b,i<j} t_{ij}^{ab}|\Psi^D\rangle \end{aligned} \tag{2.131}$$

which is identical to inserting the explicit Hamiltonian into Eq. 2.127. The second-order MP energy correction is then given as

$$\begin{aligned} E^{(2)} &= \langle 0^{(0)}|\hat{U}|0^{(1)}\rangle = -\frac{1}{4}\sum_{abij}\frac{|\langle ab||ij\rangle|^2}{\epsilon_a+\epsilon_b-\epsilon_i-\epsilon_j} \\ &= -\frac{1}{4}\sum_{abij} t_{ij}^{ab}\langle ab||ij\rangle. \end{aligned} \tag{2.132}$$

The total MP(2) energy is defined as the sum of all contributing corrections.

$$E^{MP2} = E^{(0)} + E^{(1)} + E^{(2)} = E^{HF} + E^{(2)} \tag{2.133}$$

The third-order energy correction expressions are derived analogously and are given as:

$$\begin{aligned} E^{(3)} &= \langle 0^{(0)}|\hat{U}|0^{(2)}\rangle \\ &= \frac{1}{8}\sum_{abijkl}\langle ij||kl\rangle t_{abij}t_{abkl} + \frac{1}{8}\sum_{abcdij} t_{cdij}t_{abij}\langle ab||cd\rangle \quad - \sum_{abcijk} t_{abij}t_{acik}\langle kb||jc\rangle. \end{aligned} \tag{2.134}$$

However, it is noteworthy to emphasize that MPPT is not a variational theory but a perturbative correction of the energy up to a certain order and thus the total energy can be lower than the exact solution of the SE. Especially MP(2) is an established method for correlated calculations since it provides a good accuracy to computational cost ratio with a scaling factor of N^5, where N as the number of basis functions. Also, all orders of MPPT are size-consistent.

2.2.5 Density functional theory

The density functional theory (DFT) [40,66] is a different approach to solve the electronic SE. Instead of a wavefunction, as it is in HF and post-HF theories, the electron density is the main quantity describing the system. First attempts were made by L. H. Thomas and E. Fermi in the Thomas-Fermi model treating electons as a uniform electron gas. [67–69] In this model, electrons are placed inside a positively charged volume. A further approximation was made stating that the electrons are distributed uniformly in a given volume ΔV In the TF-model, the kinetic energy of the electrons is defined as

$$T = \frac{3}{10}\left(3\pi^2\right)^{\frac{2}{3}}\int\left(\rho(\vec{r})\right)^{\frac{5}{3}}d^3\vec{r}. \tag{2.135}$$

The nuclear-electron attraction and the electron-electron repulsion were expressed classically. The resulting total energy of an atom is defined:

$$E_{TF} = \frac{3}{10}\left(3\pi^2\right)^{\frac{2}{3}} \int \left(\rho(\vec{r})\right)^{\frac{5}{3}} d^3\vec{r} - Z \int \frac{\rho(\vec{r})}{r} d\vec{r} + \frac{1}{2} \int \int \frac{\rho(\vec{r_1})\rho(\vec{r_2})}{r_{12}} d\vec{r_1} d\vec{r_2}. \tag{2.136}$$

The main problem was the expression of the kinetic energy of the electrons. Using this approximation, no chemical bond could be modeled. Also, both the electron correlation and exchange are missing.

The base for modern DFT is laid by *Hohenberg* and *Kohn* in their work on inhomogeneous electron gas with the introduction of the two *Hohenberg-Kohn theorems.*[70] The first theorem (HK I) sates that the ground state electronic energy is determined by the electron density ρ which means an mutual one-to-one mapping between both. It can be proven by *reductio ad absurdum*: An arbitrary ground state wavefunction Ψ_1, a Hamiltonian H_1 and a potential $V_1(\vec{r})$ given. E is defined as

$$E_1 = \langle \Psi_1 | \hat{H}_1 | \Psi_1 \rangle = \int V_1(\vec{r}) \rho(\vec{r}) d^3(\vec{r}). \tag{2.137}$$

Is is to be disproved that there is a second potential V_2 yielding the same electron density. Thus, a second wavefunction Ψ_2 with the corresponding Hamiltonian H_2 are introduced.

$$V_1 \Rightarrow \hat{H}_1 \Rightarrow \Psi_1 \Rightarrow \rho(\vec{r}) \Leftarrow \Psi_2 \Leftarrow \hat{H}_2 \Leftarrow V_2 \tag{2.138}$$

Taking Ψ_2 as a trail function for H and vice versa yields:

$$\begin{aligned} E_1 &< \langle \Psi_2 | \hat{H}_1 | \Psi_2 \rangle \\ E_1 &< \langle \Psi_2 | \hat{H}_2 | \Psi_2 \rangle + \langle \Psi_2 | \hat{H}_1 - \hat{H}_2 | \Psi_2 \rangle \\ E_1 &< E_2 + \langle \Psi_2 | V_1 - V_2 | \Psi_2 \rangle \\ E_1 &< \int \rho(\vec{r}) \big(V_1 - V_2\big) d(\vec{r}) + E_2 \end{aligned} \tag{2.139}$$

and

$$E_2 < \int \rho(\vec{r}) \big(V_1 - V_2\big) d(\vec{r}) + E_1. \tag{2.140}$$

By adding Eqs 2.138 and 2.139 one yields

$$E_2 + E_1 > E_2 + E_1 \tag{2.141}$$

which is obviously wrong. Hence, the statement is disproved and the HK I is

confirmed.

The second Hohenberg-Kohn theorem (HK II) serves as the density-based counterpart of the variational principle. At this point it shall be given without further proof or derivation as

$$E_0 \leq E[\tilde{\rho}] = T[\tilde{\rho}] + E_{Ne}[\tilde{\rho}] + E_{ee}[\tilde{\rho}] \tag{2.142}$$

with E_0 as the exact energy, $\tilde{\rho}$ as a trial density, T, E_{Ne} and E_{ee} as the kinetic energy, electron-nuclear attraction and electron-electron repulsion, respectively. It states that the energy obtained from the functional using a trial density represents an upper bound to the exact ground state energy E_0.

Although the Hohenberg-Kohn theorems represent the basis of contemporary DFT, no improvement for the problems encountered in the TF model were made. This was done in the Kohn-Sham approach (KS).[71] In this approach, a fictitious system of non-interacting particles is introduced. This system shall generate the same density as the real, interacting system. The kinetic energy of a non-interacting system can be solved exactly by introducing orbitals. The kinetic energy is then given as

$$T_s = -\frac{1}{2}\sum_{i}^{N}\langle\psi_i|\nabla^2|\psi_i\rangle. \tag{2.143}$$

Since the kinetic energy of the non-interacting system differs from the exact kinetic energy, a effective potential is introduced to account for that difference. This new potential is called the *exchange-correlation functional* (xc-functional), since it depends on the electron density $\rho(\vec{r})$. This energy functional contains the electron correlation, exchange interaction and the residual part of the true kinetic energy and is defined as

$$E_{xc}[\rho(\vec{r})] = \big(T[\rho(\vec{r})] - T_s[\rho(\vec{r})]\big) + \big(E_{ee}[\rho(\vec{r})] - J[\rho(\vec{r})]\big) \tag{2.144}$$

with $J[\rho(\vec{r})]$ as the Coulomb potential and $E_{ee}[\rho(\vec{r})]$ as the electron-electron interaction. In other words: Everything, that is not known exactly is put into the xc-functional. The total energy expression for Kohn-Sham DFT is then given as

$$\begin{aligned} E_{KS-DFT}[\rho(\vec{r})] = &\sum_i \langle\psi_i| - \frac{1}{2}\nabla_i^2|\psi_i\rangle - \sum_i\sum_A \langle\psi_i|\frac{Z_A}{|\vec{r}_i - \vec{R}_A|}|\psi_i\rangle \\ &+ \sum_i \langle\psi_i|\frac{1}{2}\int\frac{\rho(\vec{r}_2)}{|\vec{r}_i - \vec{r}_2|}d\vec{r}_2|\psi_i\rangle + E_{xc}[\rho(\vec{r})]. \end{aligned} \tag{2.145}$$

Minimizing E_{KS-DFT} using the variational principle with respect to single-particle orbitals yields the Kohn-Sham equation

$$\Big(-\frac{1}{2}\nabla^2 + \sum_A \frac{Z_A}{\vec{r}_A} + \int \frac{\rho(\vec{r}_2)}{\vec{r}_{12}} d\vec{r}_2 + v_{xc} \Big) \psi_i = \epsilon_i \psi_i \tag{2.146}$$

with

$$v_{xc} = \frac{\partial E_{xc}[\rho(\vec{r})]}{\partial[\rho(\vec{r})]}. \tag{2.147}$$

The Kohn-Sham equation 2.146 is very similar to the HF equation 2.67. Therefore, like HF, it has to be solved iteratively in an SCF procedure. With N^3 DFT exhibits the same scaling as HF. However, Koopmans's theorem is not valid for DFT orbitals. Since DFT contains no exact exchange but instead approximates it by a potential, the self-interaction is not canceled and both the occupied and virtual orbitals are described for the same N-electron system. As a consequence, the virtual orbitals do not correspond to an electron attachment but instead the orbital energy difference $(\epsilon_a - \epsilon_i)$ is more related to an optical excitation.

Since the exact xc-functinoal is not known, suitable approximations for E_{xc} have to be made. Finding better approximations for the xc-functional is still one of the main research topics in contemporary DFT development. Typically, the parameters defining the xc-functional are empirically fitted. The various approximate functionals are categorized into five rungs denoted as "Jacob's Ladder" of functionals as proposed by John Perdew [72] referring to a staircase to heaven from a dream of Jacob described in the Old Testament. In this case, the "heaven" would be the exact xc-functional.

First rung

Functionals of the first rung depend only on the (spin-)density $\rho(\vec{r})$ and are therefore denoted as *local spin-density approximation* (LSDA). These type of functionals suffer from problems describing systems containing significant inhomogeneity of the electron density.

An example LSDA xc-functional is the combination Slater [69] / VWN5 [73]

Second rung

In the second rung, the functionals depend not only on the local spin-density, but also on its gradient $\hat{\nabla}\rho(\vec{r})$ to account for the inhomogeneities in the electronic density. Functionals of this rung are denoted as *generalized gradient approximation* (GGA)

Examples for GGA functionals are BLYP,[74,75] PBE,[76] BP86,[74,77] PW91[78] or SOGGA11.[79]

Third rung

The third rung contains the so called *meta-GGA functionals*. These functionals can either include further improvements of the density by including the Laplacian $\hat{\nabla}^2\rho(\vec{r})$ or account for the kinetic energy density, $\tau(\vec{r}) = \frac{1}{2}\sum_i^{n_{occ}} |\nabla\psi_i|^2$. Meta-GGA functionals show improvement in areas such as thermochemistry, kinetics or non-covalent interactions.

Two examples of meta-GGA functionals are M06-L[80] and TPSS[81]

Fourth rung

The fort rung are *hybrid density functionals*. In these functionals, the exchange is (partly) calculated by means of exact Hartree-Fock exchange. This can be combined with any of the above mentioned classes of functionals. However, GGA and meta-GGA functionals are commonly used. Currently, two types of hybrid functionals are established:

Global hybrid functinoals

Global hybrid (GH) functionals contain a constant factor of exact HF exchange. Various functionals have been desinged with nearly any possible amount of HF exchange. Generally, GH functionals are defined as

$$E_{xc}^{GH} = c_x E_x^{HF} + (1 - c_x)E_x^{DFT} + E_c^{DFT} \tag{2.148}$$

with c_x as the amount of exact HF exchange.

Some examples of GH functionals are B3LYP,[82] PBE0,[83] M06-2X[84] and TPSSh.[85]

Range-separated hybrid functionals

The range-separated hybrid (RSH) functionals further improve the concept of hybrid functionals by separating the amount of exact exchange into a short-range component and a long-range component by means of the error function (erf):

$$\frac{1}{r_{12}} = \frac{\big(1 - \mathrm{erf}(\omega r_{12})\big)}{r_{12}} + \frac{\mathrm{erf}(\omega r_{12})}{r_{12}} \tag{2.149}$$

The first term on the right hand side of Eq. 2.149 is singular but

short-range, and decays to zero for $r_{12} \approx 1/\omega$, while the second term constitutes a non-singular, long-range background. A general RSH functional can be expressed as

$$\begin{aligned} E_{xc}^{RSH} &= c_{x,SR} E_{x,SR}^{HF} + c_{x,LR} E_{x,LR}^{HF} \\ &\quad + (1 - c_{x,SR}) E_{x,SR}^{DFT} + (1 - c_{x,LR}) E_{x,LR}^{DFT} + E_c^{DFT} \end{aligned} \tag{2.150}$$

where the short-range and long-range parts of the Coulomb operator are used to evaluate the exact HF exchange $E_{x,SR}^{HF}$ and $E_{x,LR}^{HF}$, respectively. The rate at which local DFT exchange is turned off and the exact exchange is turned on is defined by the parameter ω.

Typical examples of RSH functionals are ωB97X-D3 [86] and M11 [87]

Hybrid functionals exhibit improvements over classical DFT functionals since the DFT-inherent self-interaction error is at least partially corrected in the hybrid functionals. As self-interaction error is defined the artificial Coulomb repulsion of an electron with itself. In HF theory, this wrong self-interaction is completely corrected by exchange interaction. But since DFT approximates the exchange by a potential, the self-interaction is not completely canceled. This leads to various problems e.g. calculating bond lengths or ionization energies.

Fifth rung

Currently the last rung of Jacobs ladder of functionals before reaching the "heaven" of the exact xc-functional are the *double hybrid* (DH) functionals. [88–92] This class of functionals also contains correlation terms via MP(2) to improve the description of the virtual orbitals. Similar to the fourth rung functionals, the double hybrid functionals can be separated into global double hybrid (GDH) and range-separate double hybrid (RSDH) functionals.

Examples for DGH and RSDH functionals are XYG3 [88] and ωB97X-2(LP), [93] respectively.

Nowadays, DFT is a wildly used method in theoretical chemistry. It yields good results in the electronic ground state at moderate cost. However, the results strongly depend on the choice of the applied xc-functional.

2.3 Calculating electronically excited states

In this section, I would like to introduce different methods to calculate electronically excited states. These methods are based on the ground state methods elaborated in Sec. 2.2. In this section, I will mainly refer to three review articles by *A. Dreuw et. al.*.[13,14,94] Excited state methods are necessary for calculating spectroscopic properties and investigating photochemical reactions. As for the ground state, there is a large variety of methods to describe electronic excitations. At first I would like to introduce the CIS method based on the configuration interaction scheme. Next, I will introduce the linear response methods based on HF and DFT. In the following subsection, I would like to give an introduction to the algebraic diagrammaic construction scheme. Finally, I want to elaborate how to calculate vibrationally resolved absorption spectra.

2.3.1 Configuration interaction singles for excited states

As shown in Sec. 2.2.2 the configuration interaction scheme is a possibility to include electron correlation in the calculation of the ground state. Truncating the CI expansion after the singles yields the configuration interaction singles (CIS) method. As shown in Sec. 2.2.2 CIS contains no correction to the electronic ground state due to Brillouin's theorem. However, CIS can be used to calculate electronically excited states.[94]
As shown in Tab. 2.1 the CIS matrix is defined as

$$\mathbf{M}^{CIS} = \langle \Psi^S | \hat{H} | \Psi^S \rangle \tag{2.151}$$

with the matrix elements

$$M^{CIS}_{ia,jb} = \langle \Psi^a_i | \hat{H} | \Psi^a_i \rangle. \tag{2.152}$$

Using a Hamiltonian shifted by the HF ground state energy $\hat{H} - E_0^{HF}$ yields

$$M^{CIS}_{ia,jb} = \langle \Psi^a_i | \hat{H} - E_0^{HF} | \Psi^a_i \rangle = \big(\epsilon_a - \epsilon_i\big)\delta_{ij}\delta_{ab} + \langle ij||ab\rangle. \tag{2.153}$$

The corresponding eigenvalue problem is given as

$$\mathbf{M}^{CIS}\mathbf{X} = \mathbf{\Omega}\mathbf{X} \tag{2.154}$$

with $\mathbf{X}$ as the matrix of CIS expansion coefficients and $\mathbf{\Omega}$ as the matrix of eigenvalues, i.e. the excitation energies. Diagonalization of the CIS matrix directly

yields the excitation energies and expansion coefficients. Typically, diagonalization of the full matrix is unnecessary since in most cases only the few energetically lowest excited states are of interest. Therefore, iterative diagonalization schemes like the Davidson algorithm [95] are employed yielding the N lowest eigenvalues and eigenvectors. Although CIS is a computaionally rather cheap method to calculate electronically excited states, its accuracy is with an intrinsinc error of 0.5 - 2 eV too large for reliable results or comparison with experimental data. In general, the excitation energies are overestimated since electron correlation is generally neglected within CIS and the HF orbitals represent an not optimal basis for the expansion of the correlated excited state wavefunction. The leading term of Eq. 2.153, i.e. the orbital energy difference, is a poor estimate for excitation energies, since the virtual orbitals are calculated for the $(N+1)$ electron system (see Sec. 2.2.1).

2.3.2 Time-dependent density functional theory

Based on ground state DFT (Sec 2.2.5), there are two possible ways to calculate excitation energies and oscillator strengths. The first one is to propagate the time-dependent Kohn-Sham wavefunction in time (real-time TD-DFT). The other, more convenient way is to obtain the excitation energies from the linear time-dependent response of the time-independent ground-state electron density to a time-dependent external electric field. This is denoted as *linear response TD-DFT*. This is derived in this section. As reference, I would like to mention the review articles by *A. Dreuw et al.* [94] and *M. E. Casida et al.* [96].

The linear response TD-DFT starts at the electronic ground state, determined by the time-independent Kohn-Sham equation as defined in Eq. 2.146. The time-dependent analogue is the time-dependent Kohn-Sham equation which is derived from the time-dependent Schrödinger equation:

$$i\frac{\partial}{\partial t}\psi_i\left(r,t\right) = \left(-\frac{1}{2}\nabla_i^2 + \upsilon(r,t) + \int d^3r' \frac{\rho\left(r',t\right)}{|r-r'|} + \frac{\delta A_{XC}\left[\rho\right]}{\delta\rho\left(r,t\right)}\right)\psi_i\left(r,t\right) \quad (2.155)$$

Eq. 2.146 can be expressed in matrix notation in a basis of M single-particle wavefunctions $\phi_i(\vec{r})$ with

$$\psi_p(\vec{r}) = \sum_j^M c_{pj}\phi_j(\vec{r}) \quad (2.156)$$

resulting in

$$\sum_q \left\{ F_{pq}^{(0)} P_{qr}^{(0)} - P_{pq}^{(0)} F_{qr}^{(0)} \right\} = 0 \tag{2.157}$$

with the idempotency condition

$$\sum_p P_{pq}^{(0)} P_{qr}^{(0)} = P_{pr}^{(0)}. \tag{2.158}$$

In Eq. 2.157 $F_{pq}^{(0)}$ and $P_{pq}^{(0)}$ refers to the Kohn-Sham Hamiltonian and the density matrix of the unperturbed ground state, respectively. $F_{pq}^{(0)}$ is defined as

$$F_{pq}^{(0)} = \int d^3 r \psi_p^* (r) \left\{ -\frac{1}{2}\nabla^2 - \sum_{K=1}^{M} \frac{Z_K}{|r - R_K|} + \int d^3 r' \frac{\rho (r')}{|r - r'|} + \frac{\delta E_{XC}}{\delta \rho (r)} \right\} \psi_q (r) \tag{2.159}$$

and $P_{pq}^{(0)}$ as

$$\rho (r) = \sum_{p,q}^{M} P_{pq} \phi_p (r) \phi_q^* (r) \tag{2.160}$$

In a basis of orthonormal unperturbed single-particle orbitals of the ground state, they can be simply written as:

$$F_{pq}^{(0)} = \delta_{pq} \epsilon_p \tag{2.161}$$

$$\begin{aligned} P_{ij}^{(0)} &= \delta_{ij} \\ P_{ia}^{(0)} &= P_{ai}^{(0)} = P_{ab}^{(0)} = 0 \end{aligned} \tag{2.162}$$

the matrix notation for the time-dependent Kohn-Sham equation (Eq. 2.155) is given as

$$\sum_q \left\{ F_{pq} P_{qr} - P_{pq} F_{qr} \right\} = i \frac{\partial}{\partial t} P_{pr} \tag{2.163}$$

For the calculation of excited states, an oscillating time-dependent external field is added and the first order response (=linear response) to this perturbation is analyzed. In time-dependent perturbation theory, as in general perturbation theory, the perturbed wavefunction is a combination of the unperturbed ground state and the time-dependent change (i.e. the perturbation). In this case the wavefunction is represented by the density matrix

$$P_{pq} = P_{pq}^{(0)} + P_{pq}^{(1)}. \tag{2.164}$$

The same scheme is applied to the Kohn-Sham Hamiltonian. It is constructed as

a combination of the ground state Kohn-Sham Hamiltonian and the first order time-dependent change.

$$F_{pq} = F_{pq}^{(0)} + F_{pq}^{(1)} \tag{2.165}$$

Inserting Eq. 2.164 and 2.165 in Eq. 2.163 and considering only first order terms yields:

$$\sum_{q} \left\{ F_{pq}^{(0)} P_{qr}^{(1)} - P_{pq}^{(1)} F_{qr}^{(0)} + F_{pq}^{(1)} P_{qr}^{(0)} - P_{pq}^{(0)} F_{qr}^{(1)} \right\} = i \frac{\partial}{\partial t} P_{pr}^{(1)} \tag{2.166}$$

In this Eq. 2.166, $F_{pq}^{(1)}$ corresponds to the first-order change of the Kohn-Sham Hamiltonian which is defined as

$$F_{pq}^{(1)} = g_{pq} + \Delta F_{pq}^{(0)} \tag{2.167}$$

and $P_{pq}^{(1)}$ as the change of the density matrix. (see Eq. 2.170) As can be seen in Eq. 2.167, the change of the Kohn-Sham Hamiltonian consists of two parts. g_{pq} is the applied time-dependent electric field itself and $\Delta F_{pq}^{(0)}$ corresponds to the reaction of the Kohn-Sham Hamiltonian on the change of the density matrix due to the perturbation. The time-dependent electric field is defined as

$$g_{pq} = \frac{1}{2} \left(f_{pq} e^{-i\omega t} + f_{qp}^{*} e^{i\omega t} \right) \tag{2.168}$$

with f_{pq} corresponding to a one-electron operator describing the amplitude of the external field. The reaction of the Kohn-Sham Hamiltonian is given as

$$\Delta F_{pq}^{(0)} = \sum_{st} \frac{\partial F_{pq}^{(0)}}{\partial P_{st}} P_{st}^{(1)} \tag{2.169}$$

with $P_{pq}^{(1)}$ as the change of the density matrix, which is defined as

$$P_{pq}^{(1)} = \frac{1}{2} \left(d_{pq} e^{-i\omega t} + d_{pq}^{*} e^{i\omega t} \right). \tag{2.170}$$

with d_{pq} representing perturbation densities. Inserting again Eqs 2.167 - 2.170 in

Eq. 2.166 and considering only terms multiplied by $e^{-i\omega t}$ yields

$$\sum_q \left[F_{pq}^{(0)} d_{qr} - d_{pq} F_{qr}^{(0)} + \left(f_{pq} + \sum_{st} \frac{\partial F_{pq}^{(0)}}{\partial P_{st}} d_{st} \right) P_{qr}^{(0)} - P_{pq}^{(0)} \left(f_{qr} + \sum_{st} \frac{\partial F_{qr}^{(0)}}{\partial P_{st}} d_{st} \right) \right] = \omega d_{pr}. \tag{2.171}$$

The terms multiplied by $e^{i\omega t}$ yield the complex conjugate of Eq. 2.171. Considering the idempotency condition in Eq. 2.158, the first order change of the densitiy matrix can be written as

$$P_{pr}^{(1)} = \sum_q \left\{ P_{pq}^{(0)} P_{qr}^{(1)} + P_{pq}^{(1)} P_{qr}^{(0)} \right\} \tag{2.172}$$

This restricts the matrix d_{pq} from Eq. 2.171 to only occupied-virtual (d_{ia}) and virtual-occupied (d_{ai}) blocks, because all occupied-occupied (d_{ii}) and virtual-virtual (d_{aa}) blocks equal 0. Considering that the unperturbed Kohn-Sham Hamiltonian and density matrices are diagonal, these both equations are obtained:

$$F_{aa}^{(0)} x_{ai} - x_{ai} F_{ii}^{(0)} + \left(f_{ai} + \sum_{bj} \left(\frac{\partial F_{ai}}{\partial P_{bj}} x_{bj} + \frac{\partial F_{ai}}{\partial P_{jb}} y_{bj} \right) \right) P_{ii}^{(0)} = \omega x_{ai} \tag{2.173}$$

$$F_{ii}^{(0)} y_{ai} - y_{ai} F_{aa}^{(0)} - P_{ii}^{(0)} \left(f_{ia} + \sum_{bj} \left(\frac{\partial F_{ia}}{\partial P_{bj}} x_{bj} + \frac{\partial F_{ia}}{\partial P_{jb}} y_{bj} \right) \right) = \omega y_{ai}. \tag{2.174}$$

In these Eqs. 2.173 and 2.174, the symbol of the matrix d_{ai} has been replaced by the symbol x_{ai} and the matrix d_{ia} by y_{ai}. Assuming $f_{ai} = f_{ia} = 0$, because the excitation energies do not depend on the amplitude of the external field and considering Eqs. 2.161 and 2.162, one obtains the TD-DFT equation:

$$\begin{pmatrix} \mathbf{A} & \mathbf{B} \\ \mathbf{B}^\star & \mathbf{A}^\star \end{pmatrix} \begin{pmatrix} \mathbf{X} \\ \mathbf{Y} \end{pmatrix} = \omega \begin{pmatrix} 1 & 0 \\ 0 & -1 \end{pmatrix} \begin{pmatrix} \mathbf{X} \\ \mathbf{Y} \end{pmatrix} \tag{2.175}$$

with $\mathbf{X}$ and $\mathbf{Y}$ as the TD-DFT excitation and "de-excitation" amplitudes and ω

as the excitation energy. The matrix elements of **A** and **B** are given as:

$$\begin{aligned} A_{ia,jb} &= \delta_{ij}\delta_{ab}(\epsilon_a - \epsilon_i) + \int\int \psi_i^\star(1)\psi_a(1)\frac{1}{x_{12}}\psi_j^\star(2)\psi_b(2)d1d2 \\ &\quad + \int\int \psi_i^\star(1)\psi_a(1)f_{xc}\psi_j^\star(2)\psi_b(2)d1d2 \\ &= \delta_{ij}\delta_{ab}(\epsilon_a - \epsilon_i) + \langle ij|ab\rangle + \langle ij|f_{xc}|ab\rangle \end{aligned} \tag{2.176}$$

$$\begin{aligned} B_{ia,jb} &= \int\int d1d2\ \psi_i^\star(1)\psi_a(1)\frac{1}{x_{12}}\psi_b^\star(2)\psi_j(2) \\ &\quad + \int\int d1d2\ \psi_i^\star(1)\psi_a(1)f_{xc}\psi_b^\star(2)\psi_j(2) \\ &= \langle ib|aj\rangle + \langle ib|f_{xc}|aj\rangle. \end{aligned} \tag{2.177}$$

The matrices **A** and **B** can be referred to as excitation and de-excitation terms as well as the matrices **X** and **Y** refer to excitation and de-excitation amplitudes, respectively

In the *adiabatic local density approximation* (ALDA) the non-local (in time) time-dependent xc-kernel is replaced by a time-independent local functional. This approximation can be made, because the electron density varies very slowly in time. Using ALDA, normal ground state functionals can be used for TD-DFT. Using ALDA, f_{xc} of Eqs. 2.176 and 2.177 can be written as

$$f_{xc} = \frac{\delta^2 E_{xc}}{\delta\rho(1)\delta\rho(2)}. \tag{2.178}$$

which is the second functional derivative of the xc-kernel.

An further approximation can be made to Eq. 2.175 known as the *Tamm-Dancoff approximation*. In this approximation the B-Matrix is considered zero resulting in the neglect of the de-excitation amplitudes **Y** and yielding the following equation for Eq. 2.175:

$$\mathbf{AX} = \omega\mathbf{X}. \tag{2.179}$$

Diagonalization of the matrices in Eqs. 2.175 or 2.179 yields the excitation energies and excited states transition vectors.

2.3.3 Comparison of TD-DFT and TD-HF

The linear response formalism can also applied to HF yielding the TD-HF equation, which has an identical form as the TD-DFT equation 2.175. However, since HF contains exact exchange instead of an exchange-correlation functional, the matrices **A** and **B** are different:

$$A_{ij,ab} = \delta_{ij}\delta_{ab}(\epsilon_a - \epsilon_i) + \langle ij||ab\rangle \tag{2.180}$$

$$B_{ij,ab} = \langle ib||aj\rangle \tag{2.181}$$

It can be seen, that the only difference of the TD-HF and the TD-DFT equations arises from the xc-functional f_{xc}. As for TD-DFT, the the Tamm-Dancoff approximation can also be applied to TD-HF. Setting $\mathbf{B} = 0$ yields the same expression as the CIS equation 2.154 with $\mathbf{A} = \mathbf{M}^{CIS}$ from Eq. 2.153. In other words: The CIS expression can be obtained either via the CI formalism or as an approximation in the linear response theory. However, in DFT the TDA can not be derived through the CI formalism. The reason is that in HF, the molecular Hamiltonian contains the Coulomb operator $\sum \frac{1}{(\vec{r}_1 - \vec{r}_2)}$) and the projection of this operator yields terms which are equivalent to the response of the HF-exchange and Coulomb potential. In TD-DFT in contrast, the response of the xc-potential contains the second derivative of the xc functional, as can be seen in Eq. 2.178. The relations of the various methods is illustrated in a sketch in Fig. 2.5

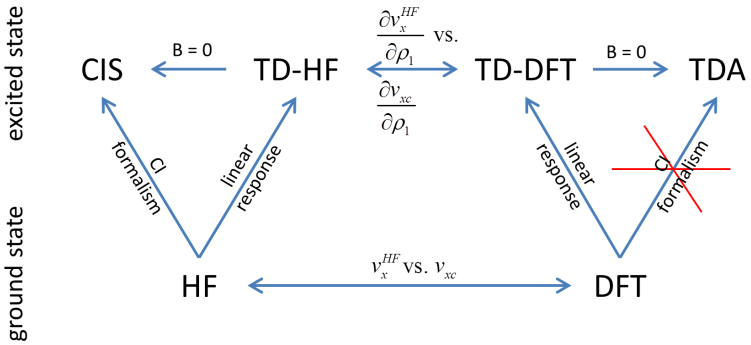

Figure 2.5: Sketch of the relations between HF, DFT, TD-HF, TD-DFT, CIS and TDA.

TD-DFT is a rather cheap method for calculation of electronically excited states which make is applicable for systems of up to several hundred atoms. However, as

DFT, TD-DFT suffers from the electron self-interaction error resulting in a wrong description of charge-transfer, extended π systems and Rydberg states.[97–101] Hence it is necessary to include exact HF exchange as well as to properly benchmark the chosen functional against high-level wavefunction-based methods to obtain reliable results.

2.3.4 Algebraic diagrammatic construction scheme

The algebraic diagrammatic construction scheme for the polarization propagator (ADC) is a quantum chemical excited state method based on perturbation theory.[102–106] It originates from the polarization propagator in many-body Green's function theory and uses the typical Møller-Plesset partitioning of the Hamiltonian operator. This also explains the name, since diagrammatic schemes were used to construct algebraic expressions of the polarization propagator. Hence, ADC can be seen as "perturbation theory for excited states". ADC is size-extensive, Hermitian and well-known for its robust structure. In this section, I will refer to a review article by *A. Dreuw et al.*[14] and the dissertations of *J. Wenzel*[59] and *M. Wormit.*[107]

2.3.4.1 Derivation using the polarization propagator

The polarization propagator evolves the polarization of a many-electron system in time. This can be considered as the time-dependent fluctuations of the ground state wavefunction upon an external perturbation. The spectral representation of the polarization propagator in matrix form is given as:

$$\Pi_{pq,rs}(\omega) = \sum_{n\neq 0} \left(\frac{\langle \Psi_0 | \hat{c}_p^\dagger \hat{c}_q | \Psi_n \rangle \langle \Psi_n | \hat{c}_r^\dagger \hat{c}_s | \Psi_0 \rangle}{\omega - (E_n - E_0)} - \frac{\langle \Psi_0 | \hat{c}_r^\dagger \hat{c}_s | \Psi_n \rangle \langle \Psi_n | \hat{c}_p^\dagger \hat{c}_q | \Psi_0 \rangle}{\omega + (E_n - E_0)} \right) \tag{2.182}$$

with Ψ_0 and Ψ_n as the ground and n^{th} excited state wavefunction with the corresponding energy E, respectively. The poles of the polarization propagator are the vertical excitation energies since the denominator contains the energy difference between ground and excited state. The transition amplitudes can be obtained from the expression in the numerator. The transition moment T_m of an m^{th} excited state is defined as

$$T_m = \sum_{pq} O_{pq} \langle \Psi_0 | \hat{c}_p^\dagger \hat{c}_q | \Psi_m \rangle \tag{2.183}$$

with $\hat{O}$ as an arbitrary single-particle operator. Eq. 2.182 can be written in diagonal form as

$$\Pi_{pq,rs}(\omega) = \mathbf{x}_{pq}^{\dagger} \left(\mathbf{1}\omega - \mathbf{\Omega}\right)^{-1} \mathbf{x}_{rs}. \tag{2.184}$$

Since neither the exact ground state nor any excited state wavefunction are known, approximations have to be included to the polarization propagator formalism. The existence of a non-diagonal form is postulated in an perturbation series using Feynman-Goldstone diagrams:

$$\Pi^{+}(\omega) = \mathbf{F}^{\dagger} \left(\mathbf{1}\omega - \mathbf{M}\right)^{-1} \mathbf{F} \tag{2.185}$$

with $\mathbf{M}$ as the ADC matrix and $\mathbf{F}$ as the matrix of transition moments. These are expanded using diagrammatic perturbation theory:

$$\mathbf{M} = \mathbf{M}^{(0)} + \mathbf{M}^{(1)} + \mathbf{M}^{(2)} + \ldots \tag{2.186}$$

$$\mathbf{F} = \mathbf{F}^{(0)} + \mathbf{F}^{(1)} + \mathbf{F}^{(2)} + \ldots. \tag{2.187}$$

Truncation of these expansions at a specific order of perturbation theory (n) yields the corresponding order in the ADC approximation scheme (ADC(n)). This results in the Hermitian eigenvalue equation

$$\mathbf{MX} = \mathbf{X\Omega}, \qquad \mathbf{X}^{\dagger}\mathbf{X} = \mathbf{1}. \tag{2.188}$$

with $\mathbf{X}$ as the matrix of eigenvectors, corresponding to the excited states and $\mathbf{\Omega}$ as the matrix of eigenvalues, corresponding to the excitation energies, which both are obtained by diagonalization of $\mathbf{M}$.

2.3.4.2 Derivation using the intermediate state representation

Beside the aforementioned derivation, a alternative way to derive ADC has been found.[102,105] The intermediate state representation (ISR) shows similarities to CI and defines the previously only proposed non-diagonal representation of the polarization propagator. In this formalism, a complete set of orthonormalized intermediate states $|\tilde{\Psi}_J\rangle$ is constructed by applying creation and annihilation operators $\hat{C}_J = \in \{\hat{c}_a^{\dagger}\hat{c}_i; \hat{c}_a^{\dagger}\hat{c}_b^{\dagger}\hat{c}_i\hat{c}_j; ...\}$ to the exact ground state wavefunction. The excitation operators can be divided into excitation classes of single, double, etc. excitations. The first class is referred to as *particle-hole (p-h)*, the second class as

two-particle-two-hole (2p-2h), etc. This yields the precursor states

$$|\Psi_J^{\#}\rangle = \hat{C}_J|\Psi_0\rangle - |\Psi_0\rangle\langle\Psi_0|\hat{C}_J|\Psi_0\rangle. \tag{2.189}$$

which are then orthogonalized to the ground state and all other underlying excited states using Gram-Schmidt orthogonalization technique

$$|\tilde{\Psi}_J\rangle = \sum_I |\Psi_I^{\#}\rangle \left(S^{-\frac{1}{2}}\right)_{I,J}. \tag{2.190}$$

and

$$\begin{aligned} S_{I,J} &= \langle\Psi_I^{\#}|\Psi_J^{\#}\rangle \\ &= \left(\langle\Psi_0|\hat{C}_I^{\dagger} - \langle\Psi_0|\hat{C}_I^{\dagger}|\Psi_0\rangle\langle\Psi_0|\right)\left(\hat{C}_J|\Psi_0\rangle - |\Psi_0\rangle\langle\Psi_0|\hat{C}_J|\Psi_0\rangle\right) \\ &= \langle\Psi_0|\hat{C}_I^{\dagger}\hat{C}_J|\Psi_0\rangle - 2\langle\Psi_0|\hat{C}_I^{\dagger}|\Psi_0\rangle\langle\Psi_0|\hat{C}_J|\Psi_0\rangle \\ &\quad + \langle\Psi_0|\hat{C}_I^{\dagger}|\Psi_0\rangle\langle\Psi_0|\Psi_0\rangle\langle\Psi_0|\hat{C}_J|\Psi_0\rangle \\ &= \langle\Psi_0|\hat{C}_I^{\dagger}\hat{C}_J|\Psi_0\rangle - \langle\Psi_0|\hat{C}_I^{\dagger}|\Psi_0\rangle\langle\Psi_0|\hat{C}_J|\Psi_0\rangle \end{aligned} \tag{2.191}$$

as the overlap between two precursor states I and J.[102,105] The exact excited states $|\Psi_n\rangle$ can now be expressed in these intermediate states according to

$$|\Psi_n\rangle = \sum_J X_{nJ}|\tilde{\Psi}_J\rangle. \tag{2.192}$$

This basis is used to express the Hamilton-Operator shifted by the exact ground state energy E_0

$$M_{IJ} = \langle\tilde{\Psi}_I|\hat{H} - E_0|\tilde{\Psi}_J\rangle, \tag{2.193}$$

which can be formulated using Eq. 2.190 as

$$M_{IJ} = \sum_{K,L}\left(S^{-\frac{1}{2}}\right)_{I,K}\left(\langle\Psi_K^{\#}|\hat{H} - E_0|\Psi_L^{\#}\rangle\right)\left(S^{-\frac{1}{2}}\right)_{L,J}. \tag{2.194}$$

The expectation value of the shifted Hamilton matrix can be written analogously to Eq. 2.191 as

$$\begin{aligned}\langle\Psi_I^{\#}|\hat{H}-E_0|\Psi_J^{\#}\rangle = &\langle\Psi_0|\hat{C}_I^{\dagger}\left(\hat{H}-E_0\right)\hat{C}_J|\Psi_0\rangle \\ &-\langle\Psi_0|\hat{C}_I^{\dagger}\left(\hat{H}-E_0\right)|\Psi_0\rangle\langle\Psi_0|\hat{C}_J|\Psi_0\rangle \\ &-\langle\Psi_0|\hat{C}_I^{\dagger}|\Psi_0\rangle\langle\Psi_0|\left(\hat{H}-E_0\right)\hat{C}_J|\Psi_0\rangle \\ &+\langle\Psi_0|\hat{C}_I^{\dagger}|\Psi_0\rangle\langle\Psi_0|\left(\hat{H}-E_0\right)|\Psi_0\rangle\langle\Psi_0|\hat{C}_J|\Psi_0\rangle.\end{aligned} \tag{2.195}$$

This leads to the Hermitian eigenvalue problem

$$\mathbf{MX}=\mathbf{X\Omega}, \qquad \mathbf{X}^{\dagger}\mathbf{X}=\mathbf{1}, \tag{2.196}$$

with $\mathbf{X}$ as the matrix of eigenvectors, corresponding to the excited states and $\mathbf{\Omega}$ as the matrix of eigenvalues, corresponding to the excitation energies. Eq. 2.196 can be solved by diagonalizing $\mathbf{M}$. Since typically only the energetically lowest eigenvalues are desired, iterative diagonalization schemes like the Davidson algorithm [95] are applied.

The transition moments T_n in the general form

$$T_n = \langle\Psi_n|\hat{D}|\Psi_0\rangle \tag{2.197}$$

can be derived analogously using the one-particle operator e.g. dipole operator

$$\hat{D}=\sum_{r,s} d_{rs}\hat{c}_r^{\dagger}\hat{c}_s, \tag{2.198}$$

with d_{rs} as the matrix elements associated with $\hat{D}$. In the ISR formalism the transition moments F_J and the corresponding transition amplitudes $f_{J,rs}$ with respect to $\hat{D}$ can be constructed as

$$F_J=\langle\tilde{\Psi}_J|\hat{D}|\Psi_0\rangle=\sum_{r,s} f_{J,rs}d_{rs}=\sum_{r,s}\langle\tilde{\Psi}_J|\hat{c}_r^{\dagger}\hat{c}_s|\Psi_0\rangle d_{rs}. \tag{2.199}$$

Combining Eq. 2.199 with the eigenvector $X_{n,J}$ in the intermediate state basis yields the final transition moment of excited state n:

$$T_n=\sum_J X_{nJ}F_J. \tag{2.200}$$

This can be done analogously for any one-particle operator to obtain excited state properties e.g. dipole moments. The general one-particle operator $\hat{D}$ and its corresponding property D_n of the n$^{\text{th}}$ excited state are defined as

$$D_n = \langle \Psi_n | \hat{D} | \Psi_n \rangle \qquad \text{with} \qquad \hat{D} = \sum_{r,s} d_{rs} \hat{c}_r^\dagger \hat{c}_s. \tag{2.201}$$

This expression 2.201 can be formulated as

$$\langle \Psi_n | \hat{D} | \Psi_m \rangle = \langle \Psi_n | \sum_{r,s} d_{rs} \hat{c}_r^\dagger \hat{c}_s | \Psi_m \rangle = \sum_{r,s} d_{rs} \langle \Psi_n | \hat{c}_r^\dagger \hat{c}_s | \Psi_m \rangle = \sum_{r,s} d_{rs} \rho_{rs}, \tag{2.202}$$

demonstrating the calculation of both excited state densities for the case $n = m$ and transition densities between two states for the case $n \neq m$ Using the ISR, the properties related to the operator $\hat{D}$ is defined as

$$D_n = \langle \vec{X}_n^\dagger | \tilde{\mathbf{D}} | \vec{X}_n \rangle, \tag{2.203}$$

with $\vec{X}_n$ as the n$^{\text{th}}$ eigenvector and $\tilde{\mathbf{D}}$ the representation of $\hat{D}$ in the ISR basis according to

$$\tilde{D}_{IJ} = \langle \tilde{\Psi}_I | \hat{D} | \tilde{\Psi}_J \rangle. \tag{2.204}$$

2.3.4.3 The ADC matrix

Unfortunately, ADC equations 2.194 cannot be solved directly, since neither the exact ground state wavefunction nor the exact ground state energy are known. Hence, the ADC matrix $\mathbf{M}$, the transition amplitude matrix $\mathbf{F}$ and the general one-particle property matrix $\tilde{\mathbf{D}}$ are expanded using perturbation theory and typical Møller-Plesset partitioning yields

$$\begin{aligned} \mathbf{M} &= \mathbf{M}^{(0)} + \mathbf{M}^{(1)} + \mathbf{M}^{(2)} + \ ... \\ \mathbf{F} &= \mathbf{F}^{(0)} + \mathbf{F}^{(1)} + \mathbf{F}^{(2)} + \ ... \\ \tilde{\mathbf{D}} &= \tilde{\mathbf{D}}^{(0)} + \tilde{\mathbf{D}}^{(1)} + \tilde{\mathbf{D}}^{(2)} + \ ... \ . \end{aligned} \tag{2.205}$$

Applying this expansion scheme to Eq. 2.194 yields

$$M_{IJ}^{(k+l+m)} \lambda^{(k+l+m)} = \sum_{K,L} \left(S_{I,K}^{-\frac{1}{2}} \right)^{(k)} \lambda^k \left(\langle \Psi_K^{\#} | \hat{H} - E_0 | \Psi_L^{\#} \rangle \right)^{(l)} \lambda^l \left(S_{L,J}^{-\frac{1}{2}} \right)^{(m)} \lambda^m, \tag{2.206}$$

with $\lambda = 1$ as an auxiliary index to sort the expressions depending on the order of perturbation theory, indicated by the indices k, l and m. For a given maximal order of perturbation defining the truncation of the MP expansion, and also defining the order or ADC (ADC(n)), only m-fold excitation classes (mp-mh) are maximally needed according to

$$m\frac{1}{2}n + 1, \qquad n \text{ even} \tag{2.207}$$

$$m\frac{1}{2}(n-1) + 1, \qquad n \text{ odd} \tag{2.208}$$

Hence, ADC(1) stays in the p-h picture. For ADC(2) and ADC(3), the ADC matrix consist of four different blocks: [p-h,p-h]; [p-h,2p-2h]; [2p-2h,p-h] and [2p-2h,2p-2h]. The first inclusion of triple excitation classes would occur in ADC(4). The individual blocks of the ADC matrix are treated in different order of perturbation theory. The ADC matrix and its subdivision in the individual blocks as well as the applied order of perturbation theory on each block is illustrated in Fig. 2.6. It can be shown that ADC(1) is identical to CIS [59] and therefore does not

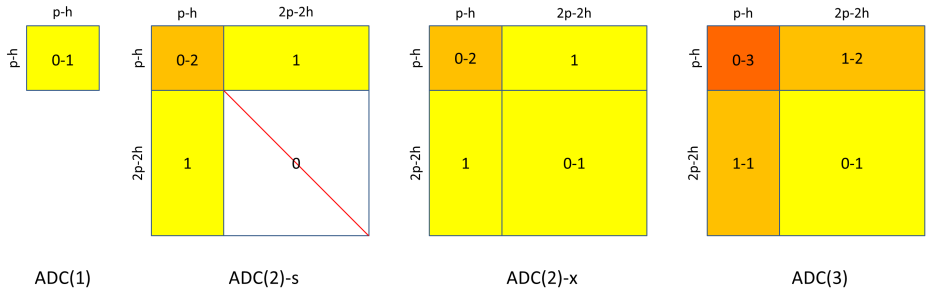

Figure 2.6: Structures of the ADC matrices for ADC(1), ADC(2)-s, ADC(2)-x and ADC(3) (from left to right) as well as the individual order of perturbation for each block of the matrix. (white: zeroth order, yellow: first order, orange: second order and red: third order) The red line in zeroth order indicates diagonal form of this block.

contain any electron correlation. It scales N^4. The ADC(2)-s matrix contains only orbital energy differences on the diagonal of the [2p-2h,2p-2h] block. It represents the direct result of applying the ISR scheme to an MP(2) ground state. The *ad hoc* extension of the [2p-2h,2p-2h] block to first order perturbation theory results in the ADC(2)-x scheme. It has been designed to improve the description of double-excited states. However, since the individual blocks are not treated on a

balanced level any more leading to a lowering of the excitation energies.[14] This is improved in the ADC(3) scheme which again contains a balanced treatment of the individual blocks and enhances thereby the description of the coupling between singles and doubles. It is yielded by applying the ISR scheme to an MP(3) ground state. The formal scaling for ADC(2)-s is N^5 and is increased to N^6 for ADC(2)-x since a diagonalization of the [2p-2h,2p-2h] block is needed. Fortunately, the scaling does not further increase for ADC(3) which exhibits also N^6 scaling.

ADC is a size-consistent method for any order of perturbation theory. As a consequence, the ADC scheme is systematically improvable. Also, the ADC matrix is Hermitian which provides direct access to excited state properties and densities without solving the eigenvalue problem twice. It is also worth mentioning that ADC is more compact than CI or CC. As indicated by Eqs. 2.207 and 2.208, the maximal needed excitation class is, except for zeroth order, less or equal than the desired order of perturbation. Hence, ADC(3) does not require triple excitations.

ADC is well known for its accuracy and reliability. For singlet valence-excited states, ADC(2)-s exhibits an accuracy for excitation energies of 0.22 ± 0.38 eV. At ADC(2)-x and ADC(3) level, the accuracy for excitation energies is -0.70 ± 0.37 eV and 0.12 ± 0.28 eV, respectively.[108]

2.3.5 Vibrationally resolved excited states

Typically, electronic transitions are instantaneous in comparison with the movement of nuclei. Thus, in absorption processes, the nuclear can be considered fixed. However, an electronic transition is most likely to happen, when also the vibrational wavefunction of the initial state overlaps with the vibrational wavefunction of the final state. This is, for absorption out of the electronic and vibrational ground state, most likely the case for vibrational excited states of the electronically excited state. This is known as the *Franck-Condon principle*[109–111] with the overlap integral over the initial and final vibrational wavefunctions as the *Franck-Condon factors*. The combination of vibrational and electronic transition is referred to as *vibronic transition*. This is illustrated in Fig. 2.7. Calculation of the Franck-Condon factors allows the generation of vibrationally resolved absorption and emission spectra. For the following explanation, I would like to refer to an article by *V. Barone et al.*[112]

In the Born-Oppenheimer approximation, the total wavefunction (Ψ) of each state can be separated into a nuclear- (ψ_n) and electronic (ψ_e) wavefunction. The same can be applied to the electric dipole moment operator yielding an electronic-

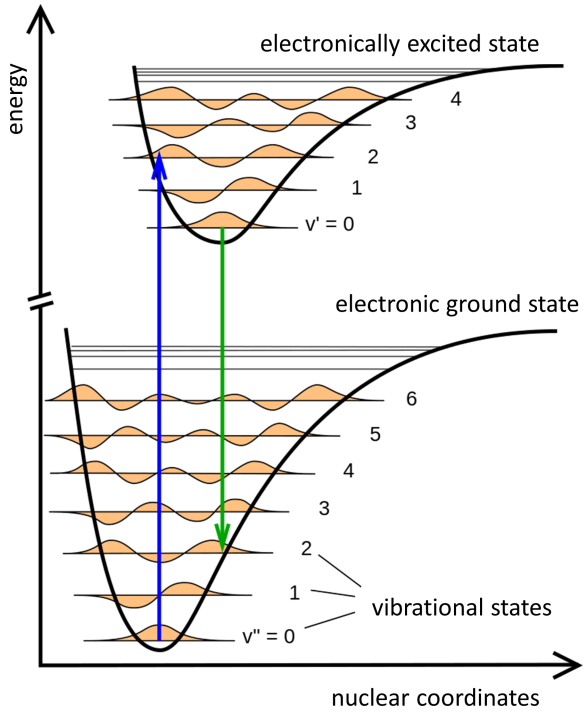

Figure 2.7: Illustration of a vibronic excitation (blue arrow) and relaxation (green arrow) in the Franck-Condon picture.

($\hat{\mu}_e$) and nuclear ($\hat{\mu}_n$) part. Hence, the transition dipole moment from initial- (Ψ_i) to final (Ψ_f) state can be formulated as

$$\langle \Psi_i | \mu | \Psi_f \rangle = \langle \psi_n \psi_e | \hat{\mu}_e | \psi'_e \psi'_n \rangle + \langle \psi_n \psi_e | \hat{\mu}_n | \psi'_e \psi'_n \rangle. \tag{2.209}$$

Due to the orthogonality of the electronic wavefunction of different electronic states the second term vanishes and Eq. 2.209 can be written as

$$\langle \Psi_i | \mu | \Psi_f \rangle = \langle \psi_n | \hat{\mu}_{if} | \psi'_n \rangle \tag{2.210}$$

with $\hat{\mu}_{if} = \langle \psi_e | \hat{\mu}_e | \psi'_e \rangle$ as the electronic transition moment. Unfortunately, no analytical expression for the electronic transition moment exists. Hence, it has to be approximated in a Taylor series of the normal coordinates with the Franck-Condon principle as the zeroth order assuming an unchanged transition dipole moment upon excitation. Higher order terms are needed in case of weakly allowed or dipole-forbidden states. The normal coordinates can either correspond to the

initial state (Q) or the final state (Q'), The Taylor series is given as

$$\mu_{if}(Q') \approx \mu_{if}(Q'_0) + \sum_{k=1}^{N} \frac{\partial \mu_{if}}{\partial Q'_k} Q'_k + \frac{1}{2} \sum_{k_1}^{N} \sum_{l=1}^{N} \left(\frac{\partial^2 \mu_{if}}{\partial Q'_k \partial Q'_l} \right)_0 Q'_k Q'_l + \dots \quad (2.211)$$

with Q'_0 as the equilibrium geometry of the final state and N as the number of normal modes. The first order term of the Taylor series corresponds to the *Herzberg-Teller approximation* which also considers a small change in the structure during the transition. Inserting Eq. 2.211 in Eq. 2.210 results

$$\begin{aligned} \langle \Psi_i | \mu | \Psi_f \rangle = \mu_{if}(Q'_0) \langle \psi_n | \psi'_n \rangle + \sum_{k=1}^{N} \frac{\partial \mu_{if}}{\partial Q'_k} \langle \psi_n | Q'_k | \psi'_n \rangle \\ + \frac{1}{2} \sum_{k_1}^{N} \sum_{l=1}^{N} \left(\frac{\partial^2 \mu_{if}}{\partial Q'_k \partial Q'_l} \right)_0 \langle \psi_n | Q'_k Q'_l | \psi'_n \rangle \end{aligned} \quad (2.212)$$

with $\langle \psi_n | \psi'_n \rangle$ corresponding to the Franck-Condon factors and $\langle \psi_n | Q'_k | \psi'_n \rangle$ corresponding to Herzberg-Teller factors. Typically, a harmonic approximation is used for the vibrational wavefunction. However, the vibrational states of both initial and final state have to be expressed in a common basis. This is accomplished by a transformation proposed by Duschinsky.[113] In this transformation, the normal modes of the final state are expressed as a linear combination of the modes of the initial state according to

$$Q' = JQ + K' \quad (2.213)$$

with J as the Duschinsky matrix describing the projection of the normal coordinates of the final state on those of the initial state and K' as the shift vector corresponding to the displacements of the normal modes.

2.3.6 Excited states analysis

In investigations of the photochemical properties of any system, the excited states have to be characterized. The character of an excited state is defined by its orbital transition pattern. In that way, e.g. charge transfer states can be identified or a ($n \mapsto \pi^*$) state can be distinguished from a ($\pi \mapsto \pi^*$) state. However, as mentioned in Sec. 2.2.1, in some cases the MOs are an inappropriate basis to express the correlated excited state. In HF the unoccupied orbitals are calculated for the N+1 electron system and thus represent an additional electron rather than an electronic excitation. This results in many different orbital transitions

contributing to the total excitation. In these cases, a characterization of the excitation based on the MO transitions can be different to impossible. One has to employ different techniques to determine the character of an excited state which are not based on the MO picture. The main two properties used for analysis is the transition density and the difference density.[94,114,115]

2.3.6.1 Transition density analysis

The one-electron transition density couples the electronic ground state with the excited state of interest and is in general given as[94]

$$T(\vec{r}) = N \int |\Psi_I(\vec{r}_1, \vec{r}_2, \ldots, \vec{r}_n)\rangle\langle\Psi_0(\vec{r}_1, \vec{r}_2, \ldots, \vec{r}_n)| d\vec{r}_2, \ldots, d\vec{r}_n \tag{2.214}$$

with Ψ_I and Ψ_0 as the wavefunction of the electronic I^{th} excited state and electronic ground state, respectively. In the quantum chemical picture, a excitation can be described as a electron and a hole. Therefore, $\vec{r}_H$ and $\vec{r}_E$ are defined as the coordinates to the center of the hole and electron, respectively. Their correlated motion is described by the wavefunction $\chi_{exc}(\vec{r}_H, \vec{r}_E)$. The hole and particle (or excess electron) density can be formulated as[114]

$$\rho_H(\vec{r}_H) = \int \chi_{exc}(\vec{r}_H, \vec{r}_E)^2 d\vec{r}_E \tag{2.215}$$

$$\rho_E(\vec{r}_E) = \int \chi_{exc}(\vec{r}_H, \vec{r}_E)^2 d\vec{r}_H \tag{2.216}$$

which indicate the density of the electron, which is "removed" (hole density) and again "added" (particle density) to create the excited state. Typically, these densities have a form corresponding to the MOs contributing to the excitation. Further, it is useful to analyze the transition density matrix, which is given in the molecular orbital basis as[94]

$$T_{ia} = \langle\psi_i|\hat{T}(\vec{r})|\psi_a\rangle \tag{2.217}$$

The transition density matrix (TDM) can not directly be diagonalized, since it is non-symmetric. Instead, a singular value decomposition is performed yielding *natural transition orbitals* (NTOs) as the eigenfunctions of the TDM.[116–118]

$$\mathbf{D}^{0I}_{|MO|} = \mathbf{U}\mathrm{diag}\left(\sqrt{\lambda_1}, \sqrt{\lambda_2}, \ldots\right)\mathbf{V}^T \tag{2.218}$$

with **U** and **V** as unitary matrices. The matrix **U** is used to generate the hole NTOs, while the matrix **V** yields the particle NTOs.[114] These NTOs are specific for one excitation and describe the electron transition itself. They are always pairs (particle and hole) sharing the same eigenvalue which corresponds to the contribution of this pair to the total excitation. In most cases, an excitation can be described by less than three NTO pairs. Using NTOs, the characterization of an excited state is facilitated dramatically. Charge-transfer states exhibit clearly localized orbitals on different moieties of a molecule. Also, artificial contributions to the excitation of various MOs (e.g. Rydberg orbitals, d-orbitals of transition metals, etc.) can clearly be identified and excluded.

2.3.6.2 Difference density analysis

In contrast to the transition density is the difference density defined as the difference of the full relaxed excited state density minus the equilibrated ground state density. The difference density differs from the transition density by including double-excited configurations and orbital relaxation effects.[119] Beside visualizing the difference density directly, it is possible to create *attachment* and *detachment* densities from the difference density matrix by diagonalization. Considering only the negative eigenvalues yields the detachment density by back-transformation to the initial orbital basis. Analogously, the attachment density is created by the positive eigenvalues.[114] The detachment density is that part of the total electron density that is removed upon excitation and replaced by the attachment density.

Analogously to the NTOs, *natural difference orbitals* (NDOs) can be created from the difference density matrix as its eigenfunctions. Like the difference density, the NDOs include effects of orbital relaxation which can be identified by comparison with the corresponding NTOs.[114,115]

2.3.6.3 Total density analysis

Finally, also the total density of an correlated (ground or excited) state can be analyzed. While the direct visualization does not provide much information in most cases, the eigenfunctions of the density matrix obtained by diagonalization can provide additional information. These eigenfunctions are referred to as *natural orbitals*.[114,115] A possible application is the identification of spin polarization in radicals.[115]

2.4 Environment methods

All of the here reviewed methods are used to calculate isolated molecules or small groups of few molecules. This is referred to as gas phase calculations since the molecules are simulated in the vacuum without any interaction beside interaction among themselves. However, most chemical reactions are carried out and most physical and chemical properties of molecules are observed in solution or solid phase. These different conditions influence the reactions and properties since the observed molecule interacts with its environment. An typical example of this kind of influence is the shift of the excitation energies of chromophores due to the solvent. This phenomenon is known as *solvatochromism.*[19] Including the environment in the quantum chemical calculation is only feasible for only small molecules with very few environment molecules due to the high scaling factors of the employed methods. Larger system can not, if even possible at all, be treated in a reasonable time scale.

To include the effects of the environments in the quantum chemical calculations, various approximations based on the separation between investigated system (e.g. the chromophore) and its environment have been introduced. The molecule of interest or a small group of molecules, which can be treated on the desired level of theory in reasonable time is selected as the *core system*, its surrounding molecules are defined as the *environment*. This is illustrated in Fig. 2.8. This separation

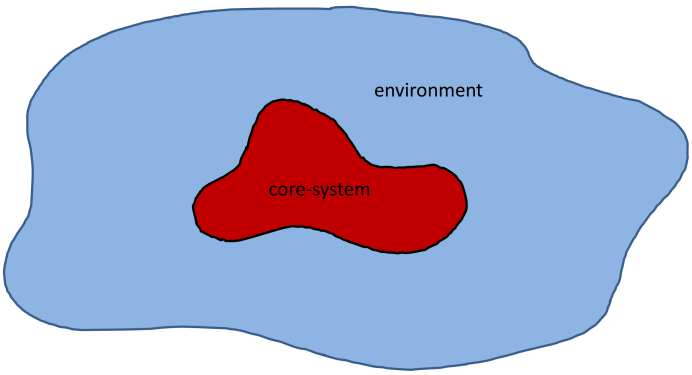

Figure 2.8: Schematic illustration of the separation between a central region i.e. the investigated molecule, defined as core-system, and its environment.

of the systems and the interaction between them can be accomplished in many ways. Generally, environment models are categorized in two classes: the *implicit* and *explicit* solvent models. In the implicit models, of which the polarizable

continuum model (PCM) constitutes the most prominent one, the molecules of the environment are not calculated explicitly, but rather are modeled by a electric field. In contrast, environment molecules are treated explicitly in the class of explicit models, as ther name suggests.

In this section I would like to introduce different implicit and explicit environment methods. However, I would like to concentrate on the frozen density embedding theory as the model I used for the development of FDE-ADC, which will be introduced later in this thesis.

2.4.1 Polarizable continuum model

The polarizable continuum model belongs to the class of implicit environment models and comprises actually a set of models which are closely related to another. It was originally developed by *S. Miertus et al.*.[120] The basic idea is to approxiate the core-environment interactions as electrostatic interactions of a molecule with an isotropic environment. Therefore the molecule is embedded in an cavity within an continuous solvent. The solvent itself is only described by macroscopic properties.

In this section I will mainly refer to the chapter "The polarizable continuum model for (bio)molecular electrostatics: Basic theory and recent advances for macromolecules and simulations" in the book "Many-Body Effects and Electrostatics in Biomolecules" by *J. M. Herbert and A. W. Lange*[121] and review articles by *J. Tomasi, B. Mennucci and R. Cammi*[122] and *B. Mennucci*[123]

The cavity around the molecule is formally created by combining the van-der-Waals spheres of all atoms and moving a artificial sphere with the given radius $\vec{r}$ over the van-der-Waals surface. The surface traced by the center of this artificial sphere is referred to as the *solvent accessible surface* (SAS) and defines the cavity. This creates the physical problem: A solvent continuum with dielectric permitivity (ϵ) outside of a charge density in a cavity ($\rho_M(\vec{r})$). This is formulated in the Poisson equation which is given as

$$-\vec{\nabla} * [\epsilon(\vec{r})\vec{\nabla}V(\vec{r})] = 4\pi\rho_M(\vec{r}) \tag{2.219}$$

with $V(\vec{r})$ defined as the potential created by an apparent charge distribution $\sigma(\vec{s})$ on the surface of the cavity Γ plus the potential created by $\rho_M(\vec{r})$. The former one is defined as

$$V_\sigma(\vec{r}) = \int_\Gamma \frac{\sigma(\vec{s})}{|\vec{r} - \vec{s}|} d^2s \tag{2.220}$$

and the apparent charge distribution is defined as

$$\sigma(\vec{s}) = \frac{f_\epsilon}{2\pi}\frac{\partial}{\partial n}(V_M + V_\sigma)_{\vec{s}} \tag{2.221}$$

with

$$f_\epsilon = \frac{\epsilon - 1}{\epsilon + 1}. \tag{2.222}$$

Eq. 2.221 can be rewritten as

$$\left(\mathbf{1} - \frac{f_\epsilon}{2\pi}\frac{\partial}{\partial n}\right)\sigma(\vec{s}) = \frac{f_\epsilon}{2\pi}\frac{\partial}{\partial n}(V_M) \tag{2.223}$$

In the PCM framework, the apparent charge is approximated by individual point charges $\alpha(\vec{s})$ on the cavity surface. The operator $\hat{S}$ is introduced acting on functions $f(\vec{s})$ defined on Γ and is given as

$$\hat{S}f(\vec{s}) = \int_\Gamma \frac{f(\vec{s}')}{|\vec{s} - \vec{s}'|}d\vec{s}' \tag{2.224}$$

Using this approximation, Eq. 2.223 can be written as:

$$\mathbf{K}\tilde{\sigma}(\vec{s}) = \mathbf{R}V_M \tag{2.225}$$

with $\tilde{\sigma}(\vec{s}) = \sigma(\vec{s}) + \alpha(\vec{s})$. As mentioned before, there are various types of PCM. They all have Eq. 2.225 as a basis, but differ in the definition of $\hat{K}$ and $\hat{R}$. An overview is given in Table 2.3.

Table 2.3: Definitions of various types of PCM. Definitions of **S**, **A** and **D** in the text. Note that COSMO and C-PCM differ also by an additional outlying charge correction, which is not included in Eq. 2.225

Model	**K**	**R**	f_ϵ
COSMO[124]	$\mathbf{S}$	$-f_\varepsilon\mathbf{1}$	$\frac{\epsilon-1}{\epsilon+1/2}$
C-PCM[125,126]	$\mathbf{S}$	$-f_\epsilon\mathbf{1}$	$\frac{\epsilon-1}{\epsilon}$
IEF-PCM[127,128]	$\mathbf{S} - \frac{f_\epsilon}{2\pi}\mathbf{DAS}$	$-f_\epsilon\left(\mathbf{1} - \frac{1}{2\pi}\mathbf{DA}\right)$	$\frac{\epsilon-1}{\epsilon+1}$
SS(V)PE[127,129]	$\mathbf{S} - \frac{f_\epsilon}{4\pi}\left(\mathbf{DAS} + \mathbf{SAD}^\dagger\right)$	$-f_\epsilon\left(\mathbf{1} - \frac{1}{2\pi}\mathbf{DA}\right)$	$\frac{\epsilon-1}{\epsilon+1}$

The matrices $\mathbf{D}$ and $\mathbf{D}^\dagger$ are defined as

$$\mathbf{D}f(\vec{s}) = \int_\Gamma f(\vec{s}') \frac{\partial}{\partial n} \frac{1}{|\vec{s} - \vec{s}'|} d\vec{s}' \tag{2.226}$$

$$\mathbf{D}^\dagger f(\vec{s}) = -\int_\Gamma f(\vec{s}') \frac{\partial}{\partial n'} \frac{1}{|\vec{s} - \vec{s}'|} d\vec{s}'. \tag{2.227}$$

The matrix $\mathbf{A}$ is diagonal and contains the surface areas of the cavity discretization elements, the matrix $\mathbf{1}$ is the identity matrix.

Because of its simple description of the solute-solvent interaction and the direct applicability in quantum chemical calculations, PCMs are by far the most often used variant to consider the environment. Also the computation time is only negligibly increase by including PCM. However, PCM is only capable of describing an uniform environment with unspecific interactions with the solute.

2.4.2 Combining quantum mechanics and molecular mechanics

In molecular mechanics (MM), the interactions of all electrons and nuclei are treated using classical mechanics instead of quantum mechanics (QM).[40] The potential energies are calculated using *force fields*. An classical harmonic oscillator is used to describe the potential energy in atom-atom distances i.e. chemical bonds or angles between atoms while periodic functions similar to a sinus function are used to describe dihedral angles. Dispersion or van-der-Waals interactions are modeled using the Lennard-Jones potential.[130] The parameters for these force fields are either empirically fitted to experimental data or obtained from quantum-chemical calculations. One of the main drawbacks of MM is the impossibility to describe chemical reactions since chemical bonds are defined beforehand instead of being the result of the calculation as it is in QM. Using the harmonic approximation for bond lengths, neither bond breaking nor creation of new bonds is possible. However, since the computational efford for MM is much lower than for QM calculations, MM offers to possibility to model extremely large molecules like whole proteins.[40]

In the QM/MM approach, both QM and MM calculations were combined using the aforementioned separation scheme. A small part, which is in the focus of the investigation is treated on QM level of theory while the environment, e.g. a protein is modeled using MM. This was firstly introduces by *Arieh Warshel* and *Michael Levitt*.[131] In the QM/MM method, the total Hamiltonian is split in three parts.

$$\hat{H}_{total} = \hat{H}_{QM} + \hat{H}_{MM} + \hat{H}_{QM/MM} \tag{2.228}$$

While $\hat{H}_{QM}$ and $\hat{H}_{MM}$ represent the typical Hamilton operators for the QM and MM system, respectively, $\hat{H}_{QM/MM}$ accounts for the interaction between core system and environment. Hence, the most important part for a realistic embedding of the QM region in the MM part is finding good approximations for the third term of Eq. 2.228.[60]

The most basic variant to treat the interaction is referred to as *mechanical embedding.*[40] It includes the steric and bonded interactions between the two subsystems. The QM atoms can include additional forces generated by the MM region and vice versa. However, no electrostatic interaction between the two regions is included. The interaction between the QM and MM part can be modeled as van-der-Waals interaction described by the Lennard-Jones potential and a point-charge-like interactions originating from population analysis:

$$\hat{H}_{QM/MM}^{mechanical} = \sum_{A}^{N_{MM-atoms}} \sum_{B}^{N_{QM-atoms}} \left[\frac{Q_A Q_B}{R_{AB}} + \left(\left(\frac{C_{12}^{AB}}{R_{AB}} \right)^{12} - \left(\frac{C_6^{AB}}{R_{AB}} \right)^{6} \right) \right]. \tag{2.229}$$

In Eq. 2.229, Q_A and Q_B correspond to the partial charge of atom A and B, respectively. The constants C_{12}^{AB} and C_6^{AB} correspond to empirical repulsion and attraction parameters depending on the type of atoms for A and B, respectively, while R_{AB} indicates the distance between atom A and B. As can readily seen from Eq. 2.229, the orbitals of the QM part are not affected by the interaction.

This is included in the next level of QM/MM denoted as *electronic embedding* or *electrostatic embedding.*[40,60] The interaction Hamiltonian is split between electrons and nuclei of the core system and an additional term is added describing the interaction between the electrons and the partial charge of an atom in the MM region:

$$\begin{aligned} \hat{H}_{QM/MM}^{mechanical} = & \sum_{i}^{N_{QM-electrons}} \sum_{A}^{N_{MM-atoms}} \frac{Q_A}{r_{iA}} \\ & + \sum_{A}^{N_{MM-atoms}} \sum_{B}^{N_{QM-nuclei}} \left[\frac{Q_A Z_B}{R_{AB}} + \left(\left(\frac{C_{12}^{AB}}{R_{AB}} \right)^{12} - \left(\frac{C_6^{AB}}{R_{AB}} \right)^{6} \right) \right] \end{aligned} \tag{2.230}$$

with Z_B as the nuclear charge and r_{iA} as the distance between electron i and atom A. This additional first part of Eq. 2.230 can be added to the molecular Hamiltonian of the QM region. The orbitals are then calculated including the point-charge-like Coulomb interaction with the environment.

The third and highest level of QM/MM includes the mutual polarization of QM and MM region and is therefore called *polarizable embedding.*[40,60] An additional polarizability tensor $\bar{\alpha}$ is added to the force field on each atom or molecule of the MM part. The induced dipole at each center is determined according to

$$\mu^{ind} = \bar{\alpha}\mathbf{E} \tag{2.231}$$

with $\mathbf{E}$ as the total electric field arising from all atomic point charges and all induced dipoles. Hence, an iterative procedure is required to determine μ^{ind}. The interaction of the induced dipoles with the partial charges of the atoms in the MM part is determined by

$$V = \frac{1}{2} \sum_{A}^{N_{MM-atoms}} \sum_{j}^{N_{MM-dipol}} \frac{Q_A \mu_j^{ind} r_{Aj}}{r_{ij}^3}. \tag{2.232}$$

This and the mutual interaction of the induced dipoles is added to the Hamiltonian of the MM part. Additionally, the interaction of the induced dipoles in the MM part with both the nuclei in the QM part, which is defined equivalently to Eq. 2.232, and the electronic wavefunction is added to the QM Hamiltonian. The latter is defined analogously to Eq. 2.232 but the partial charge Q_A is replaced by the wavefunction of electron i. The total interaction has to be solved iteratively using macrocycles. Hence, the QM/MM calculation using polarizable embedding can be quite demanding in computational resources and time. In addition, the use of a polarizable force field is essential, which are not yet very common nowadays.[60]

QM/MM is an established and frequently applied method to include explicit environment interaction. In most cases, the electronic embedding variant is employed. Using appropiate force fields and methods, also photochemical processes in large proteins can be investigated.[132]

2.4.3 Effective fragment potential

The effective fragment potential is quite related to the QM/MM approach. However, instead of a force field, the environment molecules are treated in a distributed multipole expansion.[133,134] It was originally developed by *Mark Gordon et al.*[135,136]

The environment is further separated into fragments. Typcally, each environment molecule is considered an individual fragment. The core system is as in the QM/MM approach treated on QM level of theory. The total energy of the system consisting of the core system and all fragments is defined as the energy of the

core system in the field of the fragments and the fragment-fragment interaction (E^{ef-ef}). The latter is defines as:

$$E^{ef-ef} = E_{Coul} + E_{pol} + E_{disp} + E_{ex-rep} \tag{2.233}$$

with E_{Coul}, E_{pol}, E_{disp} and E_{ex-rep} as the Coulomb, polarization, dispersion and exchange-repulsion energy contribution, respectively. The Coulomb and polarization interaction of the fragments on the QM calculation is modeled by a potential, which is added to the Hamiltonian

$$\hat{H}'_{pq} = \hat{H}_{pq} + \langle p|\hat{V}^{Coul} + \hat{V}^{pol}|q\rangle \tag{2.234}$$

while the dispersion and exchange-repulsion QM-EF interactions are applied as a total energy correction.
The fragments itself are modeled by [133]

- a multipole expansion up to octupoles obtained from a Stone's distributed multipolar analysis [137] located at atomic centers and bond midpoints for the Coulomb and polarization terms,
- static polarizability tensors centered at localized molecular orbital (LMO) centroids for the polarization term,
- dynamic polarizability tensors, also centered on the LMOs, for the dispersion calculation, and
- the Fock matrix, basis set, and localized orbitals needed for the exchange-repulsion term.

These data can be calculated for various molecules in beforehand and provided in a database. In an EFP calculation, the position of each environment molecule has to be defined to project the fragment data on this position. In this perspective, the EFP method can be considered as an QM/MM analog without empirical parameters.

Since the data for the environment is mostly provided in a database and the potential added to the Hamiltonian is only a one-particle operator, the demand in computational resources for an EFP calculation is comparable to the demand of the corresponding calculation of the isolated core system on the same level of theory.

2.4.4 Fragment molecular orbital

In the fragment molecular orbital theory (FMO), the system is not only divided in the two parts core and environment, but rather into multiple fragments, ideally one fragment per molecule.[138,139] The total energy of the complete system is expressed in a many-body expansion. This means that, in addition to the monomer fragments, dimers, trimers, ..., n-mers are created from the monomers to count for the fragment interactions. This expansion converges to the exact energy of the full system at the given level of theory since all lower interaction terms cancel. However, the expansion is truncated after a certain level of expansion, typically after dimers or trimers, determining the order of FMO.[140,141] If only monomer and dimer fragments are considered, the method is referred to as FMO2. FMO3 is employed, when also trimers are considered. The total energy for FMO2 is given as

$$E^{FMO2} = \sum_{I}^{N} E_I + \sum_{I>J}^{N} (E_{IJ} - E_I - E_J) \tag{2.235}$$

and for FMO3 as

$$\begin{aligned} E^{FMO3} = E^{FMO2} + \sum_{I>J>K}^{N} \big[&(E_{IJK} - E_I - E_J - E_K) - (E_{IJ} - E_I - E_J) \\ &- (E_{JK} - E_J - E_K) - (E_{KI} - E_K - E_I) \big] \end{aligned} \tag{2.236}$$

Each fragment is calculated in the electrostatic potential (ESP) of all other fragments. This is achieved by adding two extra terms to the Hamilton operator describing the Coulomb interaction with both the nuclei and electron density of all other fragments.[140,141] In the case of Hartree-Fock, the interaction terms can simply be added to the one-particle operator:

$$f_i^X(\vec{r}_i) = \tilde{h}_i^X(\vec{r}_i) + \sum_{i}^{N_X/2} \left(2J_i^X(\vec{r}_i) - K_i^X(\vec{r}_i)\right) \tag{2.237}$$

with

$$\tilde{h}_i^X(\vec{r}_i) = h_i^X(\vec{r}_i) + \sum_{K\neq X}^{N*N_Z} \left(-\frac{Z_K}{|\vec{r}_i - R_K|}\right) + \sum_{K\neq X}^{N} \sum_{i\in X} \int \frac{\rho_K(\vec{r}')}{|\vec{r}_i - \vec{r}'|} d\vec{r}' \tag{2.238}$$

where X indicates the fragment.[141] The first term in Eq. 2.238 is the one-electron operator as it is defined in Hartree-Fock theory. The second term corresponds to

the electron-nuclear attraction and runs over all atoms not part of the fragment X. The last term corresponds to the electrostatic repulsion of the electrons in fragment X with the electron density of all other fragments. The monomer fragments are calculated iteratively in the field of all other densities until self-consistency is reached. This macrocycle is called self-consistent charge (SCC).[141] After the SCF in each loop, a post-Hartree-Fock method and / or a excited state calculation is applicable to include electron correlation or electronically excited states. In principle, this can be chosen individually for each fragment. An illustration of the procedure in the case of FMO2 is shown in Fig. 2.9. It can be shown[141] that no

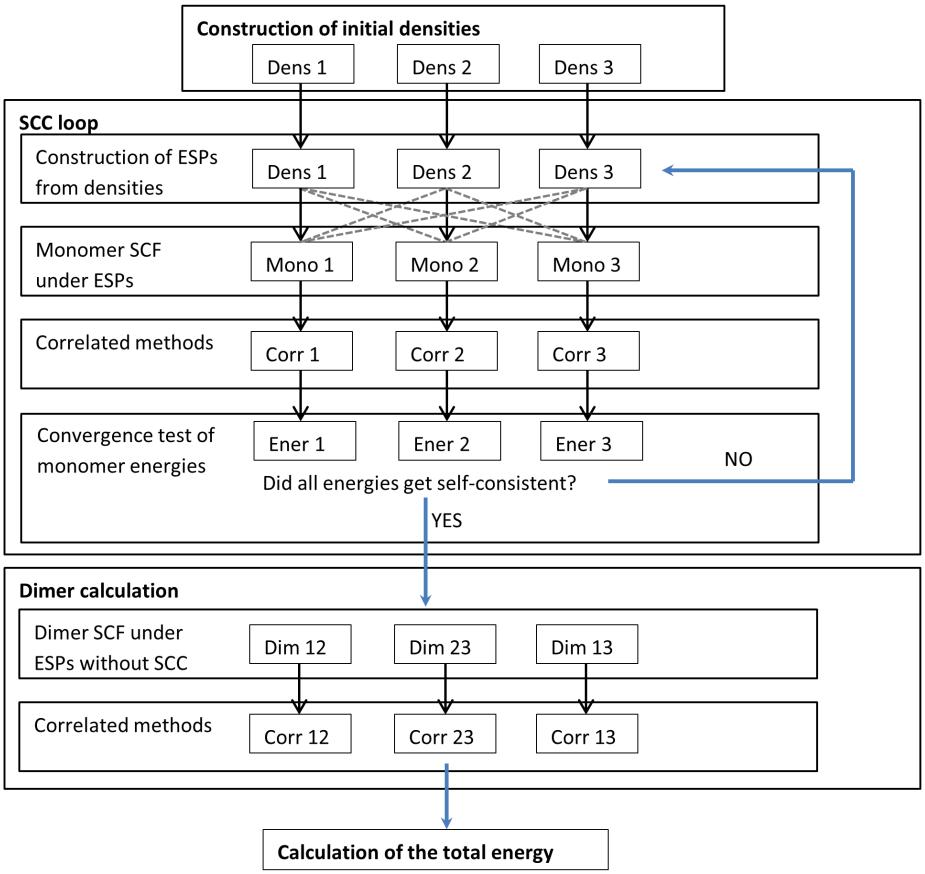

Figure 2.9: Illustration of the FMO2 total energy calculation scheme.[141]

double counting of the Coulomb interactions occurs, since these terms cancel out. The exchange and correlation interaction between the fragments is considered in the dimer calculations.

The main advantage of this method is, that the calculation of the individual fragments can perfectly be parallelized on suited computational infrastructure. However, the advantage gained from the parallelization vanishes if the fragments are of different size or different levels of theory are applied on the the individual fragment calculations.

2.4.5 Frozen density embedding theory

Frozen density embedding theory (FDET) belongs to the explicit environment methods, in which the supersystem is divided into core fragment and environemnt. The core fragment is embedded in the electron density of the environment, which is kept unchanged (*frozen*).[142,143] FDET was originally developed for DFT-in-DFT embedding by *T. Wesolowski et al*[144] since the electron density is divisible. Later developments introduced the wavefunction-based density embedding.[142,145–147] This was done first by *Carter et al.*.[148,149] Employing wavefunction based methods for the calculation of the embedded system is especially useful for the calculation of electronically excited states, since DFT methods have known limitations.[99–101]

Density embedding can be applied in various fashions like using for the independent variables the supersystem density and the core fragment density, as done by *Carter et al.*[148,149] This type of methods are collectively called *ONIOM strategy.*[150] Here, I would like to concentrate on the variant using the density of the core system and the environment as the independent quantities following the formal framework of FDET.[143,144,151]

FDET is designed for systems with non-covalently bound environments like systems amenable for QM/MM type of embedding methods. Hence, if electron transfer between core system and environment might occur, the system should not be modeled using FDET. In FDET, the core (or embedded) fragment is considered system A, while the environment is referred to as system B. The total energy of the supersystem AB in FDET has the form of a functional $E_{AB}^{EWF}[\Psi_A, \rho_B]$ since it depends both on the embedded wavefunction (EWF) and the environment electron density $\rho_B(\vec{r})$. Hence, the Euler-Lagrange equation

$$\frac{\delta E_{AB}^{EWF}[\Psi_A^I, \rho_B]}{\delta \Psi_A^I} - \lambda^I \Psi_A^I = 0 \tag{2.239}$$

can be employed to find stationary many-electron wave functions with λ^I as the Lagrange multiplier associated with the normalization. As indicated by the index I not only the lowest-energy, but also higher-energy solutions corresponding to

electronically excited states are concerned. The total energy of the supersystem is defined as

$$\begin{aligned} E_{AB}^{EWF}[\Psi_A, \rho_B] =& \langle \Psi_A | \hat{H}_A | \Psi_A \rangle + V_B^{nuc}[\rho_A] + J_{int}[\rho_A, \rho_B] \\ &+ E_{xc,T}^{nad}[\rho_A, \rho_B] + E_{v_B}^{HK}[\rho_B] + V_A^{nuc}[\rho_B], \end{aligned} \tag{2.240}$$

with

$$J_{int}[\rho_A, \rho_B] = \int \int \frac{\rho_A(\vec{r})\rho_B(\vec{r}')}{|\vec{r} - \vec{r}'|} \mathrm{d}\vec{r}\mathrm{d}\vec{r}' \tag{2.241}$$

$$V_A^{nuc}[\rho_B] = \int \rho_B(\vec{r}) v_A(\vec{r}) \mathrm{d}\vec{r} \tag{2.242}$$

$$V_B^{nuc}[\rho_A] = \int \rho_A(\vec{r}) v_B(\vec{r}) \mathrm{d}\vec{r} \tag{2.243}$$

$$E_{xc,T}^{nad}[\rho_A, \rho_B] = E_{xc}^{nad}[\rho_A, \rho_B] + T_s^{nad}[\rho_A, \rho_B] + \Delta F^{MD}[\rho_A]. \tag{2.244}$$

These terms describe the interaction between the embedded species A and the environment B. $J_{int}[\rho_A, \rho_B]$, $V_A^{nuc}[\rho_B]$ and $V_B^{nuc}[\rho_A]$ correspond to Coulombic electron-electron repulsion, attraction between electron density of B with nuclei of A and attraction between electron density of A with nuclei of B, respectively. $E_{xc,T}^{nad}[\rho_A, \rho_B]$ describes a non-additive energy bifunctional and comprises terms for exchange-, correlation- and kinetic density functionals. Typically, the ρ_A-dependent functional $\Delta F^{MD}[\rho_A]$ is neglected in practice since its contributions are usually small.[152] The non-additive energy bifunctional is defined as:

$$E^{nad}[\rho_A, \rho_B] = E[\rho_A + \rho_B] - (E[\rho_A] + E[\rho_B])\,. \tag{2.245}$$

It describes the interaction terms of the divided densities with respect to the employed functional and is a result of the divisibility of the density, but not of the functional. It is defined as the sum of the exchange-correlation and kinetic energy functional:

$$E_{xc,T}^{nad}[\rho_A, \rho_B] = E_{xc}^{nad}[\rho_A, \rho_B] + E_T^{nad}[\rho_A, \rho_B]. \tag{2.246}$$

The embedding is accomplished by creating an *embedding potential* v_{emb} as the functional derivative of the total energy functional (Eq. 2.240) with respect $\rho_A(\vec{r})$. The embedding potential depends on the functions $\rho_A(\vec{r})$, $\rho_B(\vec{r})$and v_B and is

defined as:

$$v_{emb}[\rho_A, \rho_B, v_B](\vec{r}) = v_B(\vec{r}) + \int \frac{\rho_B(\vec{r}')}{\left|\vec{r} - \vec{r}'\right|} \mathrm{d}\vec{r}' + \frac{\delta E_{xc,T}^{nad}[\rho_A, \rho_B]}{\delta \rho_A(\vec{r})}. \tag{2.247}$$

It is added to the Hamiltonian of the embedded system yielding the following Schrödinger-like equation as the neccesary condition for the stationary wavefunction:

$$\left(\hat{H}_A + \hat{v}_{emb}\right) \Psi_A = \epsilon_A \Psi_A \tag{2.248}$$

Two variants were introduced to carry out a FDE calculation which are referred to as *conventional FDET* and the approximated version *linearized FDET*.[153,154]

2.4.5.1 Conventional FDET

The embedding potential depends, beside the nuclear potential v_B on both the electron densities of system A and B. However, the electron density of system B is kept frozen resulting $\rho_B(\vec{r})$ to be constant. The embedding potential still depends on the electron density of system A, which is the solution of the eigenvalue problem in Eq. 2.248. This leads to an non-linear problem which has to be solved iteratively in macrocycles until convergence is achieved. The embedding potential has to be reconstructed using the updated electron density $\rho_A(\vec{r})$ from the previous step and solving the eigenvalue problem again using the newly generated embedding potential.[146,147,155,156] This has to be done for each total density of state I of system A. As a consequence, the embedding potential is state-specific for each electronic state of A.

This is not only very unfavorable because the iterative procedure converging the embedding potential in self-consistency with the embedded wavefunction has to be applied N times where N is the number of calculated excited states. It also results in non-orthogonal excited states. This prohibits the calculation of reliable excited state properties like oscillator strengths. Further problems might occur by interchanging excited states due to the embedding.

2.4.5.2 Linearized FDET

In contrast to the conventional FDET, an approximation is introduced by replacing the state-specific density $\rho_A(\vec{r})$ with a fixed reference density $\rho_A^{ref}(\vec{r})$.[146,156–159] This approximation overcomes the state-dependency and the iterative scheme to construct the embedding potential. However, this leads to an inconsistency

between the energy and the embedded wavefunction.[154] The state Ψ_A^I is calculated employing an embedding potential which is not evaluated at the corresponding electron density $\rho_A^I(\vec{r})$. Recently, a further approach was developed using the fixed reference density $\rho_A^{ref}(\vec{r})$ but maintains consistency between wavefunction and energy. This is referred to as *linearized FDET*.[153,154]

The non-additive energy functional $E_{xc,T}^{nad}[\rho_A, \rho_B]$ is approximated by a functional linear in $\rho_A(\vec{r})$. The approximation is constructed as a Taylor-expansion of the non-additive energy functional around the reference density $\rho_A^{ref}(\vec{r})$ with the series being truncated after the linear term:[154]

$$\begin{aligned} E_{xc,T}^{nad}[\rho_A, \rho_B] \approx & E_{xc,T}^{nad}[\rho_A^{ref}, \rho_B] + \int \left(\rho_A(\vec{r}) - \rho_A^{ref}(\vec{r})\right) \frac{\delta E_{xc,T}^{nad}[\rho_A^{ref}, \rho_B]}{\delta \rho_A^{ref}(\vec{r})} \mathrm{d}\vec{r} \\ = & E_{xc,T}^{nad}[\rho_A^{ref}, \rho_B] + \Delta^{lin}[\rho_A, \rho_A^{ref}, \rho_B]. \end{aligned} \tag{2.249}$$

The total energy expression in linearized FDET is now linear in $\rho_A(\vec{r})$ and reads:

$$\begin{aligned} E_{AB}^{LinFDET}[\Psi_A, \rho_B, \rho_A^{ref}] = & \\ & \langle \Psi_A | \hat{H}_A | \Psi_A \rangle + \int \rho_A(\vec{r}) v_B(\vec{r}) \mathrm{d}\vec{r} + \int \rho_B(\vec{r}) v_A(\vec{r}) \mathrm{d}\vec{r} \\ & + \int\int \frac{\rho_A(\vec{r}) \rho_B(\vec{r}')}{\left|\vec{r} - \vec{r}'\right|} \mathrm{d}\vec{r} \mathrm{d}\vec{r}' + E_{v_B}^{HK}[\rho_B] \\ & + E_{xc}^{nad}[\rho_A^{ref}, \rho_B] + T_s^{nad}[\rho_A^{ref}, \rho_B] + \Delta^{lin}[\rho_A, \rho_A^{ref}, \rho_B] \end{aligned} \tag{2.250}$$

with

$$\Delta^{lin}[\rho_A, \rho_A^{ref}, \rho_B] = \int \left(\rho_A(\vec{r}) - \rho_A^{ref}(\vec{r})\right) \frac{\delta E_{xc,T}^{nad}[\rho_A^{ref}, \rho_B]}{\delta \rho_A^{ref}(\vec{r})}. \tag{2.251}$$

The linearized embedding potential v_{emb}^{lin} is obtained as the functional derivative of Eq. 2.250:

$$v_{emb}^{lin}[\rho_A^{ref}, \rho_B, v_B](\vec{r}) = v_B(\vec{r}) + \int \frac{\rho_B(\vec{r}')}{\left|\vec{r} - \vec{r}'\right|} \mathrm{d}\vec{r}' + \frac{\delta E_{xc,T}^{nad}[\rho_A^{ref}, \rho_B]}{\delta \rho_A^{ref}(\vec{r})}. \tag{2.252}$$

This embedding potential is universal for each state of A since it contains no state-specific parameters.

For the evaluation of the total energy it has to be considered that in the

calculation of the expectation value of the Hamiltonian of A also the expectation value of the embedding potential is included, which includes all electrostatic and part of the non-electrostatic terms of Eq. 2.250. The expectation value of the embedding potential is given as:

$$\langle \Psi_A | \hat{v}_{emb}^{lin} | \Psi_A \rangle = V_B^{nuc}[\rho_A] + J_{int}[\rho_A, \rho_B] + \int \rho_A(\vec{r}) \frac{\delta E_{xc,T}^{nad}[\rho_A^{ref}, \rho_B]}{\delta \rho_A^{ref}(\vec{r})} \mathrm{d}\vec{r} \tag{2.253}$$

As a consequence, the total energy expression in Eq. 2.250 can be rewritten as:[154]

$$\begin{aligned} E_{AB}^{LinFDET}[\Psi_A, \rho_B, \rho_A^{ref}] = \\ \langle \Psi_A | \hat{H}_A + \hat{v}_{emb}^{lin}(\vec{r}) | \Psi_A \rangle + \int \rho_B(\vec{r}) v_A(\vec{r}) \mathrm{d}\vec{r} \\ + E_{v_B}^{HK}[\rho_B] + E_{xc,T}^{nad}[\rho_A^{ref}, \rho_B] - \int \rho_A^{ref}(\vec{r}) \frac{\delta E_{xc,T}^{nad}[\rho_A^{ref}, \rho_B]}{\delta \rho_A^{ref}(\vec{r})} \mathrm{d}\vec{r} \end{aligned} \tag{2.254}$$

As can readily be seen, after evaluation of the Hamiltonian including the embedding potential, only constant, state-independent terms have to be added. Thus, the excitation energy, which is defined as the energy difference between different states, simplifies to:

$$\Delta E_{IJ} = \langle \Psi_A^J | \hat{H}_A + \hat{v}_{emb}^{lin} | \Psi_A^J \rangle - \langle \Psi_A^I | \hat{H}_A + \hat{v}_{emb}^{lin} | \Psi_A^I \rangle. \tag{2.255}$$

because all other terms cancel exactly.[154] A comparison between conventional FDET and linearized FDET is shown in Fig. 2.10

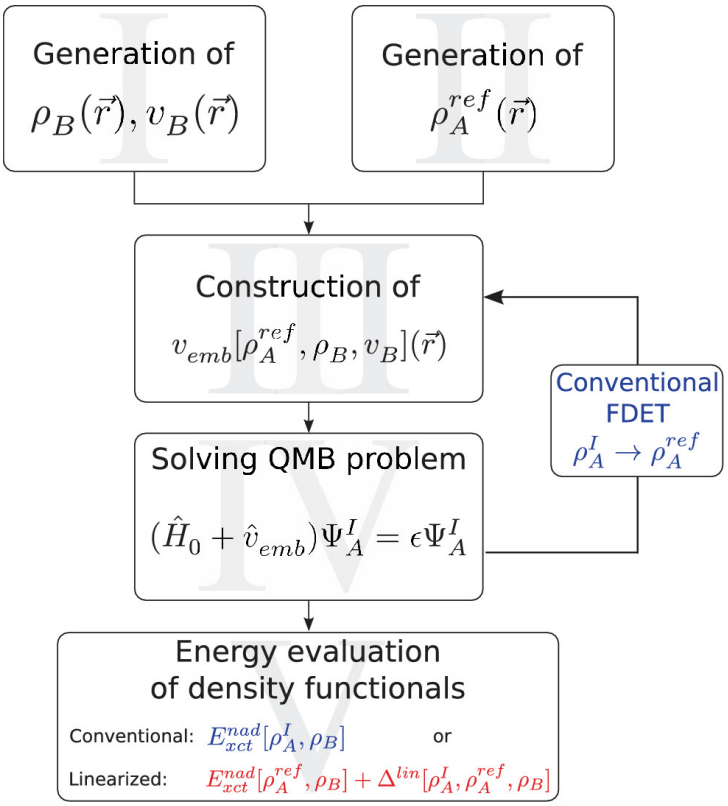

Figure 2.10: Procedure of conventional and linearized FDET. Reprinted from *Zech et.al,*[154] with the permission of AIP Publishing.

Chapter 3

Photochemistry of Tetrathia-[7]Heterohelicenes

"No amount of experimentation can ever prove me right;
a single experiment can prove me wrong."
Albert Einstein

Tetrathia-heterohelicenes belong to the class of molecules known as *helicenes*. Helicenes are generally characterized by several *ortho* annelated aromatic rings forming an open macrocycle.[160–164] Since both ends of the macrocycle are not connected the helicene forms a helical structure due to steric repulsion. The first helicenes were synthesized by *M. Newman et al.* in the 1950s.[165–167] In all-benzene-helicenes, the name of the compound is formed by an arabic number in square brackets indicating the number of annelated rings followed by the name "helicene".[160] For example [6]helicene consists of six annelated benzene rings and represents the most famous helicene. The helix introduces a chiral axis inducing chirality in all helicenes even without containing an asymmetric carbon atom or other chiral centers. Following the nomeclature of *Cahn, Ingold and Prelog*[168] from 1966, the left-handed helix is referred to as "minus", indicated by the letter "M" while the right-handed helix is denoted "plus", indicated by the letter "P".[164] Helicenes can generally be synthesized by photocyclization of the corresponding subunits (e.g. stilbene) followed by oxidation.[169] Helicenes exhibit a strong circular dichroism and high optical rotation values which were studied both experimentally and theoretically.[170–172]

The first heterohelicenes were synthesized by *Wynberg et al.*[173] by replacing some of the benzene rings with thiophene rings. If in [7]helicene four benzene

rings are substituted by thiophene, one obtains tetrathia-[7]heterohelicene. It was analyzed using X-ray crystallography by *Nakagawa et al.*.[174] It was found that the racemate does not only form enantiopure crystals but also a crystal in which the molecules are stacked in columns of alternating chirality. The synthesis of tetrathia-[7]heterohelicene is similar to the synthesis of the all-carbon helicenes: The subunits can be connected by a Wittig reaction[175,176] followed by a photocyclization and oxidation to obtain the aromatic helical structure (Scheme 3.1).[177–179] Tetrathia-

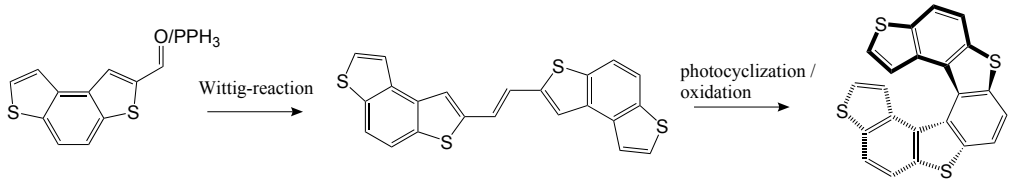

Scheme 3.1: Synthesis of tetrathia-[7]heterohelicene via Wittig reaction and photocyclization.

[7]heterohelicenes are known to be easily functionalizable[180–182] and are suited for application in optoelectronics,[183–186] biomolecular recognition,[187,188] and asymmetric catalysis.[189–192] A selective functionalization at the α-position of the terminal thiophene ring allows the use of tetrathia-[7]heterohelicenes as chiral ligands for transition metal complexes. Especially phosphorus derivatives of tetrathia-[7]heterohelicenes are of particular interest since phosphines are known for their ability to bind transition metals like gold(I). Hence, organophosphorus-gold(1) complexes have received increasing attention in the last years as efficient and selective homogeneous catalysts in organic transformations.[193–197] The functionalization can be carried out according to Scheme 3.2. Instead of *n*-butyl groups

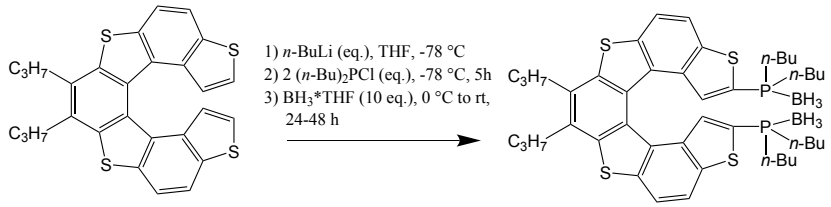

Scheme 3.2: Synthesis of tetrathia-[7]heterohelicene-dialkylphosphane-borane.

analogously cyclohexane, phenyl, *t*-butyl or ethyl groups can be used as substituens at the phosphorus atom.[31] Synthesis of the gold(I)-complex can be achieved by adding a weakly coordinated gold-tetrahydrothiophene-chlorine complex (Scheme 3.3).[29] These compounds can be used as catalysts for cycloisomerization reactions.

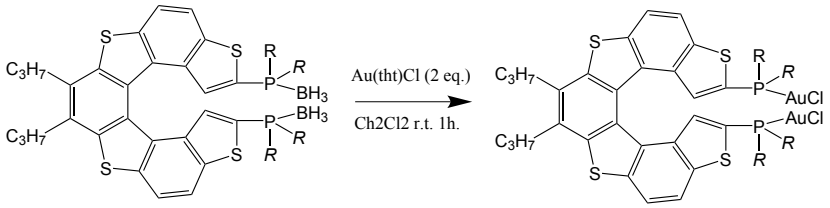

Scheme 3.3: Synthesis of tetrathia-[7]heterohelicene-dialkylphosphane-gold(I).

In this scope, it is important to investigate the electronically excited states of tetrathia-[7]heterohelicene derivatives and the influence of phosphorus substituents on properties of both excited and ionized states. This is essential for the further development of phosphorus derivatives of tetrathia-[7]heterohelicenes in the aforementioned research fields.

In the first part of my dissertation I have investigated electronically excited states and ionizations of various tetrathia-[7]heterohelicene derivatives using state-of-the-art quantum chemical methods and compared the results to experimental data. I will present and discuss the results in detail in this chapter. [1]

[1] Parts of Chapter 3 have already been published in
Gold(I) Complexes of Tetrathiaheterohelicene Phosphanes
Silvia Cauteruccio, Annette Loos, Alberto Bossi, Maria C. Blanco Jaimes, Davide Dova, Frank Rominger, Stefan Prager, Andreas Dreuw, Emanuela Licandro and A. Stephen K. Hashmi
Inorganic Chemistry, 52 (2013), pages 7995-8004
and
Chiral Thiahelicene-Based Alkyl Phosphine-Borane Complexes: Synthesis, X-ray Characterization, and Theoretical and Experimental Investigations of Optical Properties
Davide Dova, Silvia Cauteruccio, Stefan Prager, Andreas Dreuw, Claudia Graiff and Emanuela Licandro
The Journal of Organic Chemistry, 80 (2015), pages 3921-3928.
and
Tetrathia[7]helicene Phosphorus Derivatives: Experimental and Theoretical Investigations of Electronic Properties, and Preliminary Applications as Organocatalysts
Davide Dova, Lucia Viglianti, Patrizia R. Mussini, Stefan Prager, Andreas Dreuw, Arnaud Voituriez, Emanuela Licandro and Silvia Cauteruccio
Asian Journal of Organic Chemistry, 5 (2016), pages 537-549

3.1 Excited state analyses

In the first section of this chapter, I would like to present excited state analyses of various tetrathia-[7]heterohelicene (TTH) derivatives. The analyses involve the calculation of vertical excitations, vibrationally resolved absorption spectra and circular dichroism (CD) spectra.

3.1.1 Investigated systems

The investigated systems are phosphorus derivatives of TTH. The first system, tetrathia-[7]heterohelicene-dialkylphosphane-borane (TTH-DAPB), is substituted on the α-position of both terminal thiophene rings by a di-n-butylphosphane-borane. Lewis structure and geometry of TTH-DAPB is shown in Fig 3.1. The second

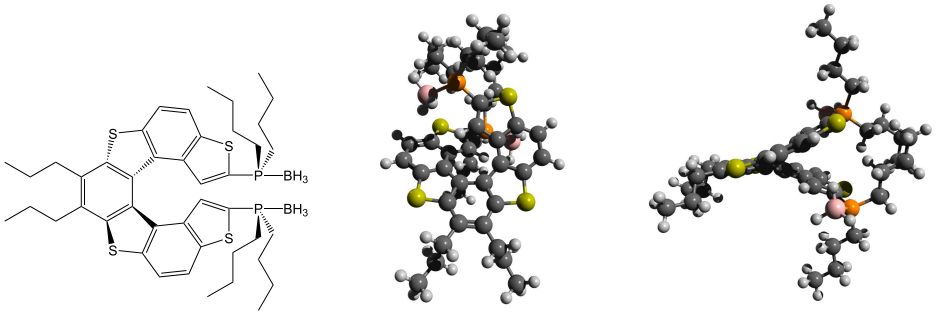

Figure 3.1: Lewis structure (left) and optimized geometry of one enantiomer of TTH-DAPB presented from two different perspectives (middle and right).

investigated system is based on tetrathia-[7]heterohelicene-diphenylphosphane-borane (TTH-DPPB). It differs from TTH-DAPB by incorporating phenyl groups instead on n-butyl groups at the phosphorus atom (Fig 3.2). Complexation

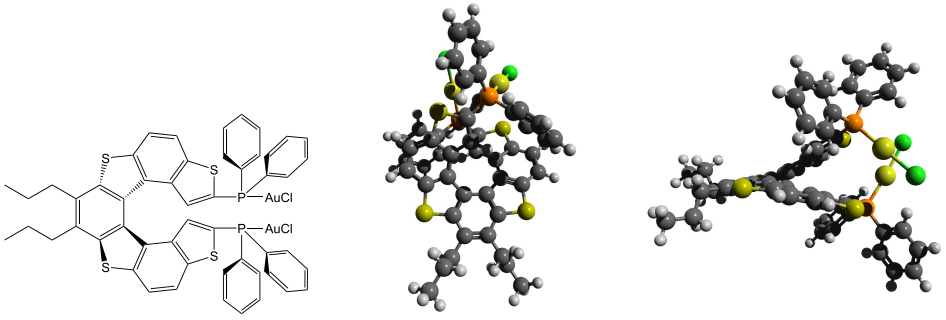

Figure 3.2: Lewis structure (left) and optimized geometry of TTH-DPP-Au(I) presented from two different perspectives (middle and right).

with gold(I)-chloride yields the investigated system tetrathia-[7]heterohelicene-diphenylphosphane-gold(I)-chloride (TTH-DPP-Au(I), Fig 3.2). In this case, each borane (BH_3) of TTH-DPPB is replaced by a gold(I) chloride (AuCl).

3.1.2 Computational methodology

From a quantum chemical point of view the investigated TTH derivatives are rather large systems possessing more than 100 atoms. Hence, computationally demanding methods can, if at all, only be used for specific calculations or as reference for a benchmark of computationally cheaper density based methods. Especially calculation of vibrationally resolved absorption spectra is computationally very demanding since it involves computation of the second derivative of an excited state i with respect to all nuclear coordinates i.e. the Hessian matrix of state i.

For the theoretical investigation of optical properties of the two enantiomers of TTH-DAPB, time-dependent density functional theory (TD-DFT) and approximate coupled cluster theory of second-order (CC2) in combination with the cc-pVDZ basis set have been employed. In addition, for CC2, the resolution of the identity (RI) approximation[198,199] has been applied with the corresponding auxiliary basis set aux-cc-pVDZ. For the investigation on TTH-DPP-Au(I), the 6-31G* basis set has been employed for the first, second and third-row elements while the LANL2DZ effective core potential has been used for the gold atoms. For the ground-state DFT and excited-state TD-DFT calculations of both molecules TTH-DAPB and TTH-DPP-Au(I) the range-separated exchange-correlation (xc)-functional ωB97XD[200] has been used.

An evaluation of xc-functionals with varying amounts of nonlocal Hartree-Fock (HF) exchange has demonstrated that at least 50 % of HF exchange are required to avoid occurrence of spurious low-lying charge-transfer excited states and to achieve a reasonable agreement with experimental spectra. Here, ωB97X has turned out to yield the most reliable results and can also be used for reliable excited state geometry optimizations.[201]

For the RI-CC2 calculations, Turbomole 6.3.1[202] has been employed, while for DFT and TD-DFT calculations, the Gaussian 09 Rev. D.01[203] program package was used.

3.1.3 Results for TTH-DAPB

3.1.3.1 Ground state properties

The ground-state structures of (P)-TTH-DAPB and (M)-TTH-DAPB have been separately optimized at DFT/ωB97XD/cc-pVDZ level of theory. An overview of calculated values for several important internal coordinates is given in Tab. 3.1 and Fig. 3.3. Comparison with experimental data determined by X-ray crystallography shows a very favorable agreement. Bond lengths differ by less than 0.03 Å. The only discrepancy can be determined in the incline of the helix. Both layers of the helix approach each other a bit closer in the calculated structures than in the experimental ones. This can be seen in the smaller P-P distance or in the decreased S_{23}-S_{16}-S_7-S_{24} dihedral angle, which are 6.377 Å and 43.6° in the crystal structure, respectively. As a result the pitch of the helix is slightly reduced in the calculated geometry. This may originate from the applied DFT methodology, which tends to planarize large delocalized π-systems. Also crystal-packing effects might play a role in the X-ray structures, which are not included in the calculations.

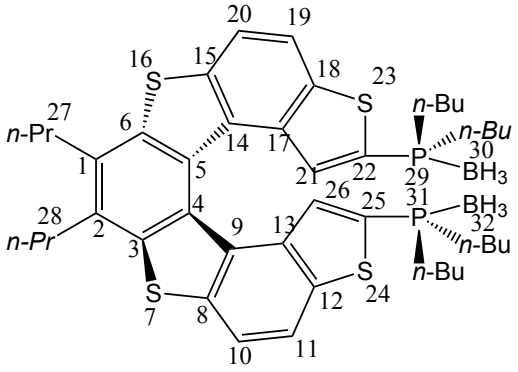

Figure 3.3: Atom numbering scheme for TTH-DAPB.

Table 3.1: Most relevant calculated geometrical parameters (d: dihedral angle, r: bond length, a: angle) of (P/M)-TTH-DAPB.

Geom. Parameter	Value
d(C_6-C_1-C_2-C_3)	±9.6°
d(C_{14}-C_5-C_4-C_9)	±22.9°
d(C_{17}-C_{14}-C_5-C_4)	±19.3°
d(C_{21}-C_{17}-C_{14}-C_5)	±5.4°
d(C_5-C_4-C_9-C_3)	±18.0°
d(C_4-C_9-C_{13}-C_{26})	±5.5°
d(C_{20}-C_1-C_2-C_{10})	±25.0°
d(C_{22}-C_6-C_3-C_{25})	±42.2°
d(S_{23}-S_{16}-S_7-S_{24})	±38.6°
r(C_1-C_2)	1.398 Å
r(C_5-C_4)	1.419 Å
r(C_5-C_{14})	1.456 Å
r(C_{14}-C_{17})	1.422 Å
r(C_{17}-C_{21})	1.439 Å
r(C_{20}-C_{19})	1.379 Å
r(C_{21}-C_{26})	3.103 Å
r(P_{29}-P_{31})	6.051 Å
r(B_{30}-B_{32})	7.825 Å
a(C_{22}-C_4-C_{25})	±52.9°

The six frontier orbitals HOMO−2 (HOMO = highest occupied molecular orbital) to LUMO+2 (LUMO = lowest unoccupied molecular orbital) were plotted and analyzed. They are delocalized over the TTH moiety but have no contributions on the side chains, i.e. the *n*-butyl groups or the boranes. They exhibit typical π character. The orbital energies [hartree] for HOMO−2 to LUMO+2 are: -0.300, -0.272, -0.270, -0.012, 0.022, 0.032, respectively, indicating a slight bonding character of the LUMO. It is especially remarkable that the LUMO has a bonding character between the two layers of the helix. The frontier orbitals are shown in Fig 3.4. The orbitals obtained at Hartree-Fock level of theory are qualitatively identical. Hence, these orbitals serve for the subsequent characterization of both RI-CC2 and TD-DFT results.

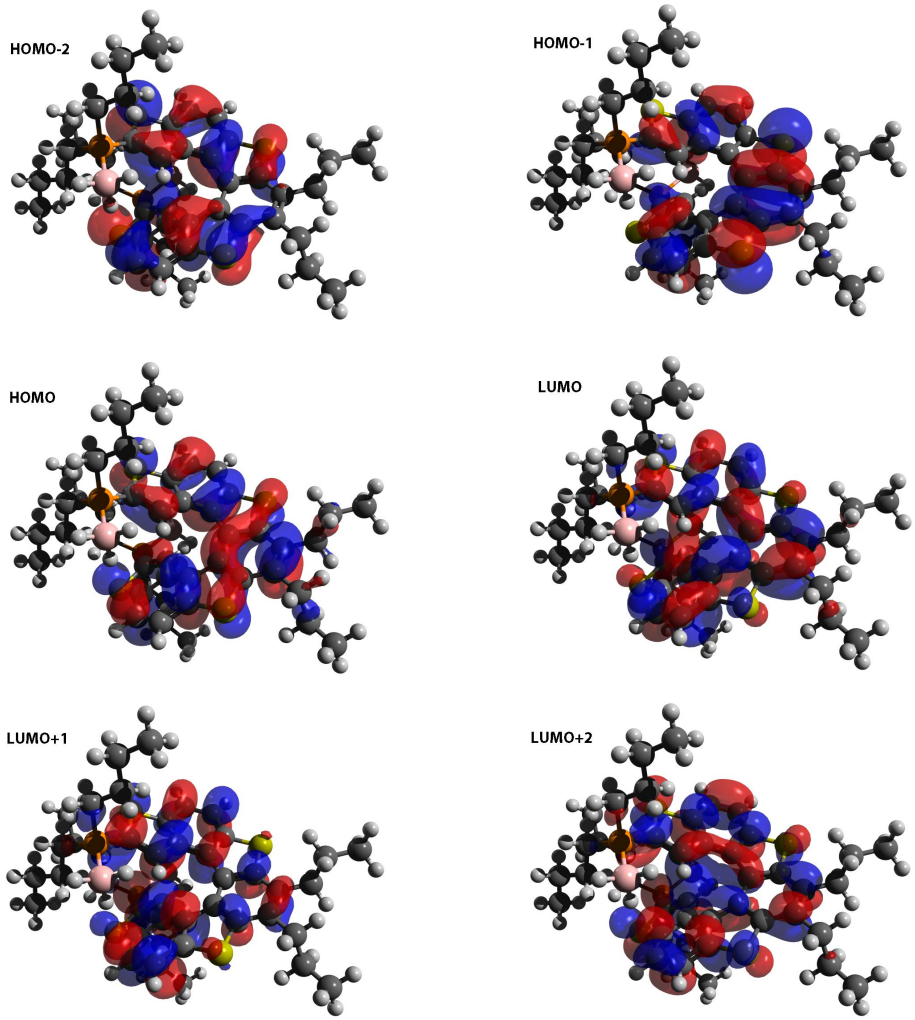

Figure 3.4: Frontier orbitals HOMO−2 (top left), HOMO−1 (top right), HOMO (middle left), LUMO (middle right), LUMO+1 (bottom left) and LUMO+2 (bottom right) of (P)-TTH-DAPB. The orbitals of (M)-TTH-DAPB are identical mirror images.

3.1.3.2 Excited state properties

The eight energetically lowest electronically excited singlet states of TTH-DAPB were calculated both at RI-CC2/cc-pVDZ and TD-DFT/ωB97XD/cc-pVDZ levels of theory. All calculated excited states exhibit a local ($\pi \mapsto \pi^*$) transition character on the TTH moiety. A more detailed analysis of the excited states and their orbital transitions is given in Tab. 3.2 for the RI-CC2 results and in Tab. 3.3 for the TD-DFT results. As can be seen, only the first and second excited state

can be characterized sufficiently in the molecular orbital basis. The higher lying states exhibit more low-contributing orbital transitions indicating the insufficient representation of the excitation in the molecular orbital picture. This exacerbates the characterization of an excited state.

However, it can be seen, that the state characterized by a HOMO-to-LUMO transition is the S_1 state in the results obtained at TD-DFT level of theory but occurs as the second excited state in the RI-CC2 results. The same can be observed for the S_1 state obtained at RI-CC2 level of theory and the S_2 state obtained at TD-DFT. This means, that the energetic order of the first two excited states is interchanged for TD-DFT as compared to RI-CC2. However, their character, this means the orbital transitions, the transition dipole moment

Table 3.2: Excitation energies, oscillator strengths and orbital transitions (> 5 %) for the energetically lowest eight excited states of TTH-DAPB calculated at RI-CC2/cc-pVDZ level of theory.

State	Exci. Energ. [eV]	Osc. Str.	Orb Trans.[a]	Weight [%]
S_1	3.41	0.16	-1 $\mapsto$ 0 ($\pi \mapsto \pi^*$)	80.3
S_2	3.46	0.17	0 $\mapsto$ 0 ($\pi \mapsto \pi^*$)	89.6
S_3	4.11	0.23	-2 $\mapsto$ 0 ($\pi \mapsto \pi^*$)	57.4
			0 $\mapsto$ 1 ($\pi \mapsto \pi^*$)	12.3
			-1 $\mapsto$ 0 ($\pi \mapsto \pi^*$)	6.0
S_4	4.12	0.07	-3 $\mapsto$ 0 ($\pi \mapsto \pi^*$)	57.3
			-1 $\mapsto$ 1 ($\pi \mapsto \pi^*$)	15.4
			0 $\mapsto$ 2 ($\pi \mapsto \pi^*$)	8.3
S_5	4.31	0.06	0 $\mapsto$ 1 ($\pi \mapsto \pi^*$)	60.9
			-2 $\mapsto$ 0 ($\pi \mapsto \pi^*$)	20.9
			-1 $\mapsto$ 2 ($\pi \mapsto \pi^*$)	7.4
S_6	4.46	0.00	-1 $\mapsto$ 1 ($\pi \mapsto \pi^*$)	63.3
			-1 $\mapsto$ 1 ($\pi \mapsto \pi^*$)	21.1
S_7	4.54	0.11	0 $\mapsto$ 2 ($\pi \mapsto \pi^*$)	58.7
			-1 $\mapsto$ 2 ($\pi \mapsto \pi^*$)	10.0
			-1 $\mapsto$ 1 ($\pi \mapsto \pi^*$)	8.3
S_8	4.55	0.02	-1 $\mapsto$ 2 ($\pi \mapsto \pi^*$)	54.1
			0 $\mapsto$ 3 ($\pi \mapsto \pi^*$)	8.1
			0 $\mapsto$ 2 ($\pi \mapsto \pi^*$)	6.5

[a] HOMO+x $\mapsto$ LUMO+y

Table 3.3: Excitation energies, oscillator strengths and orbital transitions (> 5 %) for the energetically lowest eight excited states of TTH-DAPB calculated at DFT/ωB97XD/cc-pVDZ level of theory.

State	Exci. Energ. [eV]	Osc. Str.	Orb Trans.[a]	Weight [%]
S_1	3.65	0.16	$0 \mapsto 0$ ($\pi \mapsto \pi^*$)	89.9
S_2	3.72	0.19	$-1 \mapsto 0$ ($\pi \mapsto \pi^*$)	82.5
S_3	4.30	0.08	$-3 \mapsto 0$ ($\pi \mapsto \pi^*$)	52.8
			$-1 \mapsto 1$ ($\pi \mapsto \pi^*$)	20.6
			$0 \mapsto 2$ ($\pi \mapsto \pi^*$)	6.9
S_4	4.35	0.38	$-2 \mapsto 0$ ($\pi \mapsto \pi^*$)	51.3
			$0 \mapsto 1$ ($\pi \mapsto \pi^*$)	27.4
S_5	4.76	0.06	$-5 \mapsto 0$ ($\pi \mapsto \pi^*$)	22.3
			$-1 \mapsto 2$ ($\pi \mapsto \pi^*$)	19.6
			$0 \mapsto 3$ ($\pi \mapsto \pi^*$)	12.9
			$-3 \mapsto 1$ ($\pi \mapsto \pi^*$)	12.3
			$0 \mapsto 1$ ($\pi \mapsto \pi^*$)	6.7
S_6	4.83	0.19	$0 \mapsto 2$ ($\pi \mapsto \pi^*$)	43.6
			$-4 \mapsto 0$ ($\pi \mapsto \pi^*$)	15.3
			$-3 \mapsto 0$ ($\pi \mapsto \pi^*$)	15.2
			$-2 \mapsto 1$ ($\pi \mapsto \pi^*$)	5.4
S_7	4.90	0.04	$0 \mapsto 1$ ($\pi \mapsto \pi^*$)	40.9
			$-2 \mapsto 0$ ($\pi \mapsto \pi^*$)	31.8
			$-5 \mapsto 0$ ($\pi \mapsto \pi^*$)	10.5
			$-2 \mapsto 2$ ($\pi \mapsto \pi^*$)	5.2
S_8	5.03	0.07	$-1 \mapsto 1$ ($\pi \mapsto \pi^*$)	61.2
			$-3 \mapsto 0$ ($\pi \mapsto \pi^*$)	14.3
			$-4 \mapsto 0$ ($\pi \mapsto \pi^*$)	6.5

[a] HOMO+x $\mapsto$ LUMO+y

vectors and the oscillator strengths are retained. The same holds for the S_3- and S_4 state, which also change their energetic order at TD-DFT level of theory with respect to the RI-CC2 results. For comparison of the calculated excitation energies with the experimentally determined absorption spectrum, the calculated excitation energies obtained with RI-CC2 are shifted to lower energies by -0.325 eV, accounting for systematic errors in the calculation stemming from the approximate level of computation and the lack of solvation effects. The energy shift has been chosen such that the first excitation energy matches the first absorption

band at 400 nm wavelengths. Applying this shift yields a very good agreement between calculated excited states obtained at the RI-CC2 level of theory and the experimental absorption spectrum. An overlay of the experimental spectrum with the calculated line spectrum is shown in Fig. 3.5. Both the S_1 and S_2 state

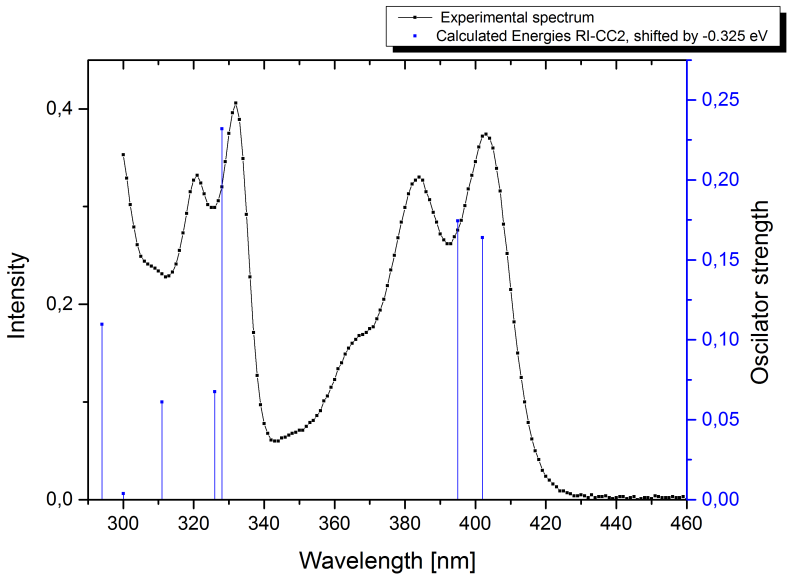

Figure 3.5: Overlay of experimental absorption spectrum and calculated excited states for TTH-DAPB. Excitation energies (shifted by 0.325 eV, see text) and oscillator strengths of the eight lowest electronically excited states calculated at the RI-CC2/cc-pVDZ level of theory.

could contribute to the first experimental absorption band at 400 nm wavelengths. The third excited state S_3 most probably corresponds to the absorption band at 330 nm wavelengths. Even the beginning of the last absorption band at 300 nm wavelengths is visible. It corresponds probably to the S_8 state.

Additionally, rotatory strengths have been calculated at the RI-CC2/ccpVDZ level of theory, which are required for the simulation of CD spectra. The rotatory strengths of the eight energetically lowest excited singlet states are compared to the oscillator strengths in Tab. 3.4. Comparison of the calculated rotatory strength with the experimental CD spectrum of TTH-DAPB shows, like for the absorption spectrum, very good agreement after applying the same energetic shift as done for the absorption spectrum. An overlay of the calculated excitation energies and rotatory strengths with the experimental CD spectrum is shown in Fig 3.6. As can be readily seen from Tab 3.4, the rotatory strengths of the first and second

Table 3.4: Comparison of rotatory strengths and oscillaotr strengths for TTH-DAPB calculated at RI-CC2/cc-pVDZ level of theory

State	Exci Energ. [eV]	Osc. Str.	Rot. Str. $[10^{-40} * erg * cm^3]$
S_1	3.41	0.16	-127.80
S_2	3.46	0.17	113.06
S_3	4.11	0.23	-18.10
S_4	4.12	0.07	353.94
S_5	4.31	0.06	-47.53
S_6	4.46	0.00	1.86
S_7	4.54	0.11	173.63
S_8	4.55	0.02	47.52

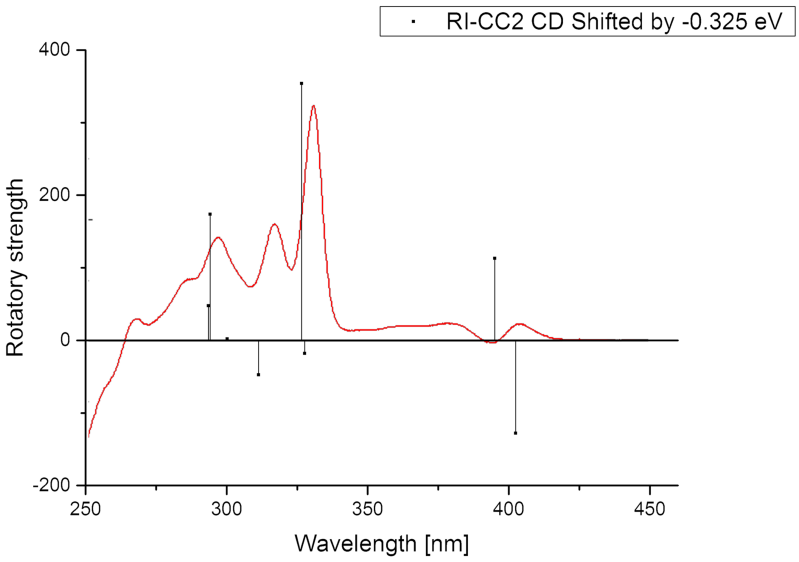

Figure 3.6: Overlay of experimental CD spectrum (red line) and calculated excitation energies (shifted by 0.325 eV, see text) and rotatory strengths (black lines) of the eight lowest electronically excited states calculated at the RI-CC2/cc-pVDZ level of theory for TTH-DAPB.

excited state exhibit different sign. This nicely explains the flat area from 250 to 420 nm wavelengths in the experimental spectrum. The first and second excited state almost cancel each other. Only the small bump at 390 nm wavelengths indicates the presence of a second excited state. It is also remarkable that the state exhibiting the largest oscillator strength (S_3) does not show a large rotatory strength. The S_4 state exhibits the largest rotatory strength. As expected, the M-enantiomer shows the exact inverse rotatory strengths.

Since the S_1 and S_2 state change their energetic order at the TD-DFT level compared to the RI-CC2 level of theory but remain their their character and the corresponding orbital contributions, a label referring to the character rather than the energetic order will be used in the following. Therefore, the state mainly characterized by a HOMO−1-to-LUMO transition (S_1 at RI-CC2, S_2 at TD-DFT level of theory) will be named S_A and the state mainly characterized by a HOMO to LUMO transition (S_2 at RI-CC2, S_1 at TD-DFT level of theory) will be referred to as S_B state. Excited state geometry optimizations of these states have been performed at the TD-DFT level of theory. They yield fluorescence wavelengths of 406 nm (3.06 eV) for the S_B state, and 365 nm (3.39 eV) for the S_A state at TDDFT/ωB97XD/SVP level. The corresponding equilibrium structures of S_A and S_B are almost identical to the ground state equilibrium structure. The most apparent change is that the pitch of the helix is slightly reduced in the excited states due to an attractive orbital interaction of the LUMO in the overlapping region of the 7-TH moiety. This will be discussed in more detail in the analysis of the very similar TTH-DPP-Au(I) system in Sec. 3.1.4.

However, it remains unclear whether the second experimental band at 380 nm wavelengths corresponds to the second excited state or to vibrational progression of the S_1 state. To elaborate this question, vibrationally resolved absorption spectra of the ($S_0 \mapsto S_A$) and the ($S_0 \mapsto S_B$) transitions were calculated. Therefore, analyses of the harmonic frequencies of the equilibrium structures of S_0, S_A and S_B have been performed using TD-DFT/ωB97XD/SVP level of theory due to computational cost. The obtained vibrationally resolved absorption spectra have been shifted to match the excitation energy difference of the states as calculated at the RI-CC2/cc-pVDZ level of theory. Thereby, vibrationally resolved absorption spectra are obtained, for which the electronic contributions are calculated at RI-CC2 level of theory and the vibrational contributions stem from lowerlevel TD-DFT calculations. For comparison with the experimental absorption spectrum, the computed vibrationally resolved spectra of S_A and S_B have been added (Fig. 3.7).

As can be readily seen, the vibrationally resolved spectrum of state S_B exhibits a much weaker intensity than the spectrum of state S_A, although both have similar oscillator strengths. Analysis of their corresponding shift vectors and Duschinsky matrices reveals that much more normal modes contribute to the excitation to state S_B than to S_A leading to a much broader absorption spectrum of S_B. As a consequence a large number of very small contributions is neglected in the

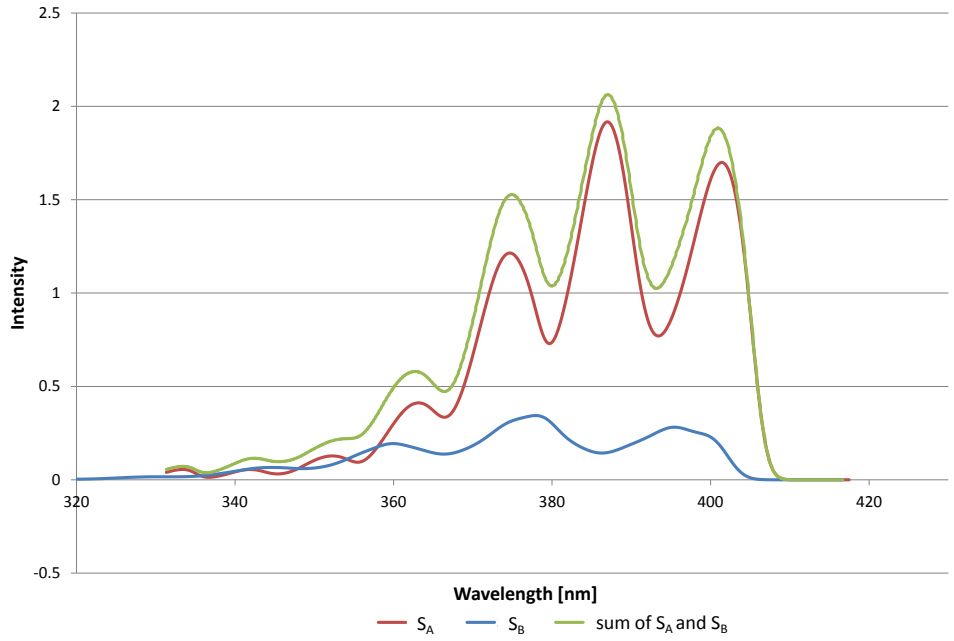

Figure 3.7: Calculated vibrationally resolved absorption spectrum for the states S_A and S_B of TTH-DAPB as well as the sum of both spectra.

numerical computation of the spectrum of the ($S_0 \mapsto S_B$) transition resulting in a seemingly too small peak. For the calculation of vibrationally resolved absorption spectra, both the Herzberg-Teller and the Franck-Condon approximations have been employed, showing that the latter is sufficient here. The normal modes were individually calculated at the relaxed geometries of the ground state, first and second excited state, respectively.

It is clear now that S_A dominates the first band of the spectrum, while S_B contributes only marginally. The vibrational progression of the sum of the ($S_0 \mapsto S_A$) and ($S_0 \mapsto S_B$) transitions (Fig 3.7) corresponds to the observed peaks at 405 nm, 385 nm, and 365 nm absorption wavelength in the experimental spectrum (for comparison see Fig. 3.5). A vibrational analysis of the peaks around 320 nm has not been performed, since the main interest here lies on the investigation of the states from which fluorescence can occur.

3.1.4 Results for TTH-DPP-Au(I)

3.1.4.1 Ground state properties

In addition to the isolated ligand TTH-DAPB the gold(I)-complex TTH-DPP-Au(I) has been investigated theoretically and compared to experimental results. The ground state structure of both enantiomers of TTH-DPP-Au(I) has been optimized both in the gas phase and using a polarizable continuum model (PCM). For the PCM calculation, the C-PCM approach was employed and the parameters of dichloromethane (DCM) were used for the solvent model. The energy difference between the gas phase equilibrium structure and the one obtained using PCM is 1.22 eV where the PCM structure refers to the energetically more stable one. However, the geometric differences due to the solvent are qualitatively negligible for TTH-DPP-Au(I). Since the equilibrium structures of (P)-TTH-DPP-Au(I) and (M)-TTH-DPP-Au(I) are identical mirror images, from here on only the (M)-enantiomer is considered. The ground state equilibrium structure and the corresponding Lewis structure indicating the atom labeling are shown in Fig. 3.8. The calculated

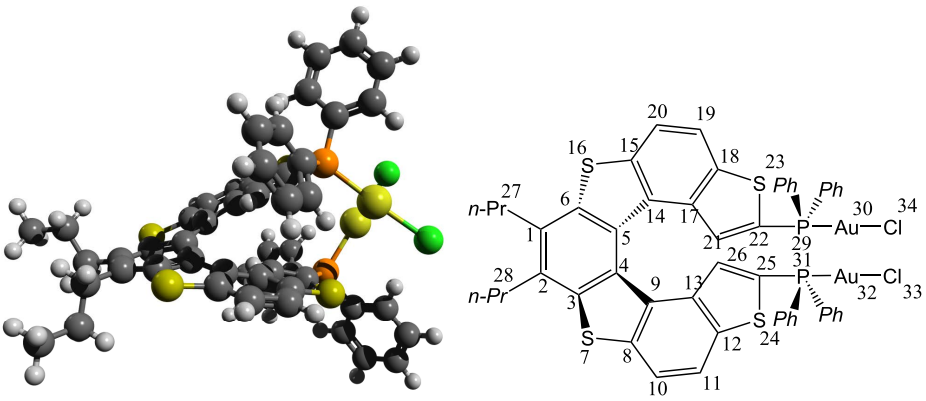

Figure 3.8: Optimized geometry of TTH-DPP-Au(I) at DFT/ωB97XD/6-31G* level of theory (left) and Lewis structure of TTH-DPP-Au(I) with atom labeling (right).

equilibrium structure is in good agreement with the structure determined by X-ray analysis (see Tab. 3.5). The largest deviations of approximately 0.1 Å are observed for bonds where the gold atoms are involved. In particular, the computed Au-Au distance is found to be slightly larger with 3.32 Å as compared to the experimental value of 3.18 Å. Most likely this deviation is due to the use of a rather small basis set and an effective core potential for the gold atoms. All other bond lengths deviate by less than 0.1 Å. The largest deviations in the bond angles are found for

Table 3.5: Selected computed bond lengths and angles for TTH-DPP-Au(I) optimized in the electronic ground state S_0, first and second excited state S_1 and S_2 and in the lowest triplet state T_1. The experimentally determined values of the electronic ground state structure are given for comparison.

Distances [Å]	S_0	S_1	S_2	T_1	Exp.
Au_{32}-P_{31}	2.305	2.308	2.307	2.306	2.244
Au_{30}-P_{29}	2.307	2.310	2.309	2.308	2.232
Au_{32}-Cl_{33}	2.389	2.393	2.392	2.391	2.308
Au_{30}-Cl_{34}	2.391	2.394	2.394	2.391	2.287
Au_{30}-Au_{32}	3.320	3.309	3.312	3.322	3.183
C_{21}-C_{17}	1.440	1.422	1.431	1.428	1.430
C_{17}-C_{14}	1.422	1.438	1.423	1.443	1.419
C_{19}-C_{20}	1.376	1.397	1.398	1.395	1.361
C_{14}-C_5	1.463	1.408	1.434	1.390	1.450
C_1-C_2	1.391	1.449	1.409	1.489	1.397
C_9-C_{13}	1.425	1.439	1.424	1.434	1.424
C_{10}-C_{11}	1.376	1.394	1.397	1.382	1.365
C_{13}-C_{26}	1.440	1.424	1.431	1.435	1.437
C_5-C_4	1.423	1.454	1.417	1.478	1.429
Angles [°]					
P_{31}-Au_{32}-Cl_{33}	176.4	176.6	176.3	176.6	175.4
P_{29}-Au_{30}-Cl_{34}	176.6	176.2	176.3	176.2	172.4
P_{29}-Au_{30}-Au_{32}	98.1	96.8	97.9	97.8	93.8
Cl_{34}-Au_{30}-Au_{32}	85.2	86.8	85.7	85.9	93.8
C_{25}-P_{31}-Au_{32}	112.6	113.6	113.4	112.9	112.9
C_{22}-P_{29}-Au_{30}	113.3	114.7	114.2	114	115.3

the P_{29}-Au_{30}-Au_{32} and Cl_{34}-Au_{30}-Au_{32} angles. Here, in addition to the limited basis set size also crystal packing effects may play a role, which are not included in the calculations.

The frontier orbitals HOMO−4 to LUMO+2 have been plotted. They are quite similar to the ones for TTH-DAPB shown in Fig. 3.4 but some include spacial contribution on the gold atoms or on the phenyl groups. The main parts of all orbitals exhibit π symmetry localized on the TTH backbone. The orbital energies in hartree for the HOMO−4 to LUMO+2 are: -0.334, -0.321, -0.318, -0.292, -0.287, -0.012, 0.022, 0.027, 0.030, 0.033, respectively. Again, the LUMO is slightly bonding. The HOMO−LUMO gap amounts to 0.27527 hartree (7,4905 eV). The frontier orbitals are plotted in Fig 3.9.

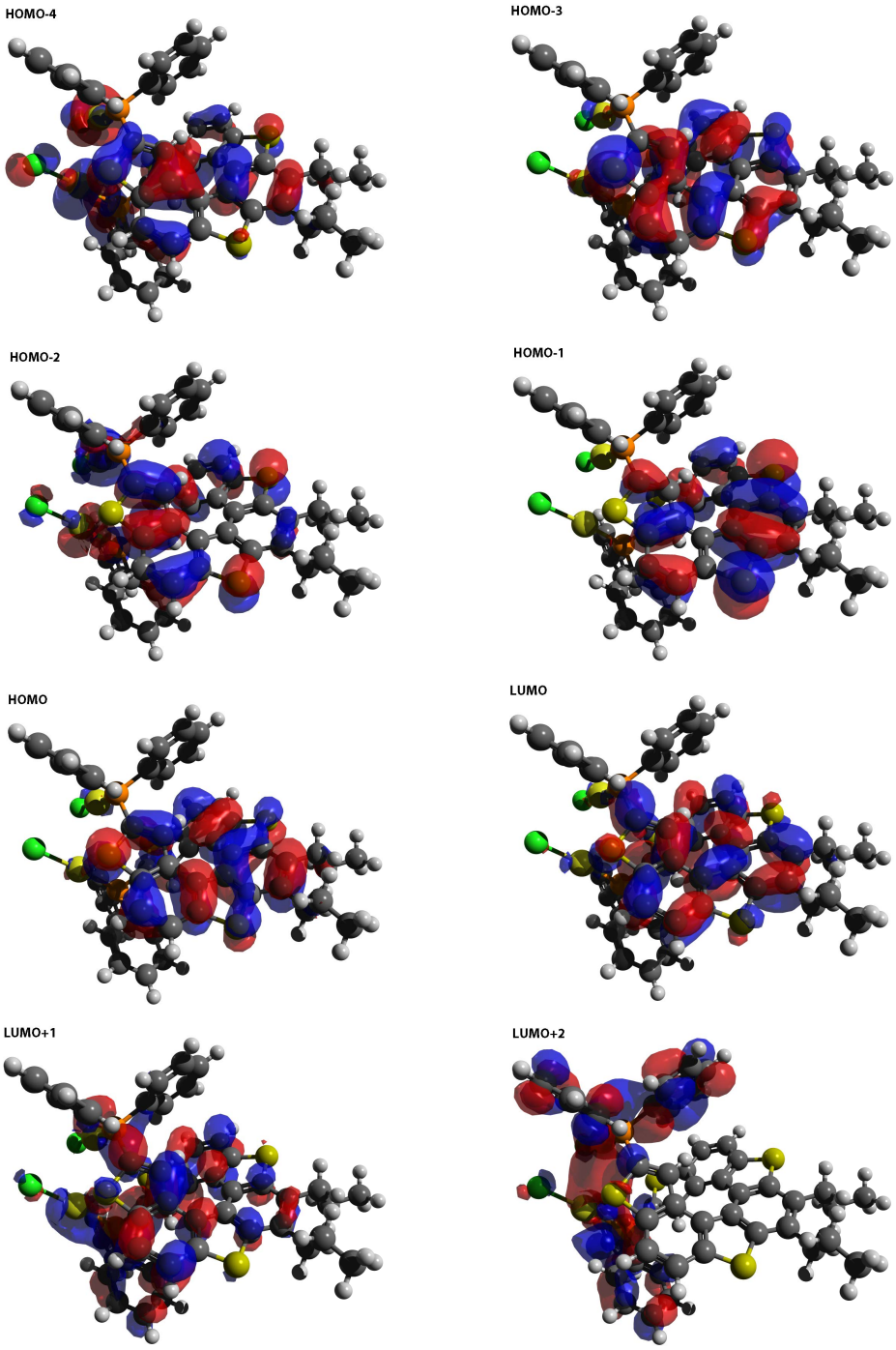

Figure 3.9: Frontier orbitals HOMO−4 (top left) to LUMO+2 (bottom right) of TTH-DPP-Au(I).

3.1.4.2 Excited state properties

The six energetically lowest electronically excited singlet states of TTH-DPP-Au(I) have been calculated at TD-DFT/ωB97XD/6-31G* level of theory at the optimized ground state equilibrium geometry using non-equilibrium solvation in the PCM and an ECP for the gold atoms. A detailed overview of the states and their corresponding orbital transitions is given in Tab. 3.6. The excited states were also calculated without solvation but the influence of the solvent DCM modeled using PCM remains negligible. The excited states are quite similar to the ones

Table 3.6: Excitation energies, oscillator strengths and orbital transitions (> 5 %) for the energetically lowest six excited states of TTH-DPP-Au(I) calculated at TD-DFT/ωB97XD/6-31G* level of theory.

State	Exci. Energ. [eV]	Osc. Str.	Orb Trans.[a]	Weight [%]
S_1	3.81	0.22	$0 \mapsto 0$ ($\pi \mapsto \pi^*$)	84.3
S_2	3.94	0.38	$-1 \mapsto 0$ ($\pi \mapsto \pi^*$)	75.3
S_3	4.45	0.22	$-2 \mapsto 0$ ($\pi \mapsto \pi^*$)	41.6
			$-1 \mapsto 1$ ($\pi \mapsto \pi^*$)	19.2
			$-4 \mapsto 0$ ($\pi \mapsto \pi^*$)	11.5
S_4	4.50	0.68	$-3 \mapsto 0$ ($\pi \mapsto \pi^*$)	43.9
			$0 \mapsto 1$ ($\pi \mapsto \pi^*$)	31.7
S_5	4.83	0.15	$-5 \mapsto 0$ ($\pi \mapsto \pi^*$)	19.1
			$-1 \mapsto 3$ ($\pi \mapsto \pi^*$)	10.8
			$-2 \mapsto 1$ ($\pi \mapsto \pi^*$)	8.8
			$0 \mapsto 3$ ($\pi \mapsto \pi^*$)	6.1
S_6	4.85	0.25	$0 \mapsto 3$ ($\pi \mapsto \pi^*$)	27.8
			$-2 \mapsto 0$ ($\pi \mapsto \pi^*$)	12.4
			$-6 \mapsto 0$ ($\pi \mapsto \pi^*$)	8.7
			$-4 \mapsto 0$ ($\pi \mapsto \pi^*$)	7.7

[a] HOMO+x $\mapsto$ LUMO+y

obtained for TTH-DAPB (Sec. 3.1.3.2). All of the calculated excited states are mostly characterized by ($\pi \mapsto \pi^*$) transitions localized in the TTH backbone. Comparison with the experimental spectra (Fig. 3.10) shows a good agreement if a constant shift of the excitation energies is applied accounting for solvation effects beyond the polarizable continuum model and systematic errors in the calculation caused by the applied level of theory and the choice of the used functional. As can be seen in the experimental spectra, the excitation and emission spectra

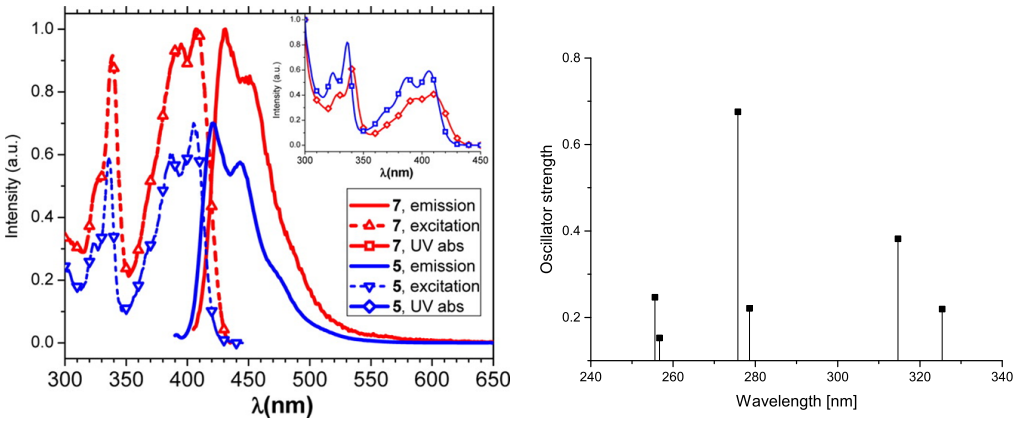

Figure 3.10: Experimental absorption, excitation and emission spectra (left) and calculated absorption stick spectrum (right) of TTH-DPP-Au(I). In the experimental spectra, TTH-DPP-Au(I) is indicated as **7**.

are almost perfect mirror images while the excitation spectra also resembles the first absorption band in the absorption spectrum quite well. This indicates that this first absorption band corresponds to a single excited state with the second peak as an vibrational overtone. The only possible second explanation for this behavior would be a dual fluorescence from S_1 and S_2. However, the experimental absorption spectrum is very similar to the one observed for TTH-DAPB which further supports the explanation of vibrational broadening. This shall be verified by calculation of vibrationally resolved absorption spectra for the first two excited states as already performed for TTH-DAPB. In fact, the S_1 and S_2 state are represented by the same dominating orbital transitions HOMO-to-LUMO and HOMO-1-to-LUMO, respectively, as it was found for TTH-DAPB. Accordingly to the previously introduces scheme, the S_1 state will be referred to as S_B while the S_2 state will be referred to as S_A. The vibrationally resolved absorption spectra have been calculated using both Franck-Condon and Herzberg-Teller approximation while the normal modes have been calculated individually at the relaxed geometries of the of the ground state, first and second excited state, respectively. This ensures a correct description of all normal modes although it is computationally very demanding.

The vibrationally resolved absorption spectra for the ($S_0 \mapsto S_A$) and the ($S_0 \mapsto S_B$) transitions are plotted in Fig. 3.11. They are in very good agreement to the results obtained for TTH-DAPB showing the dominance of the S_A state in the first absorption band, thus explaining the mirror-like image of the excitation and emission spectra. As before, the spectrum of the ($S_0 \mapsto S_B$) transition is

very broad due to many low-contributing vibrational transitions. The artificially low intensity is due to numerical restrictions in the calculation of the spectrum.

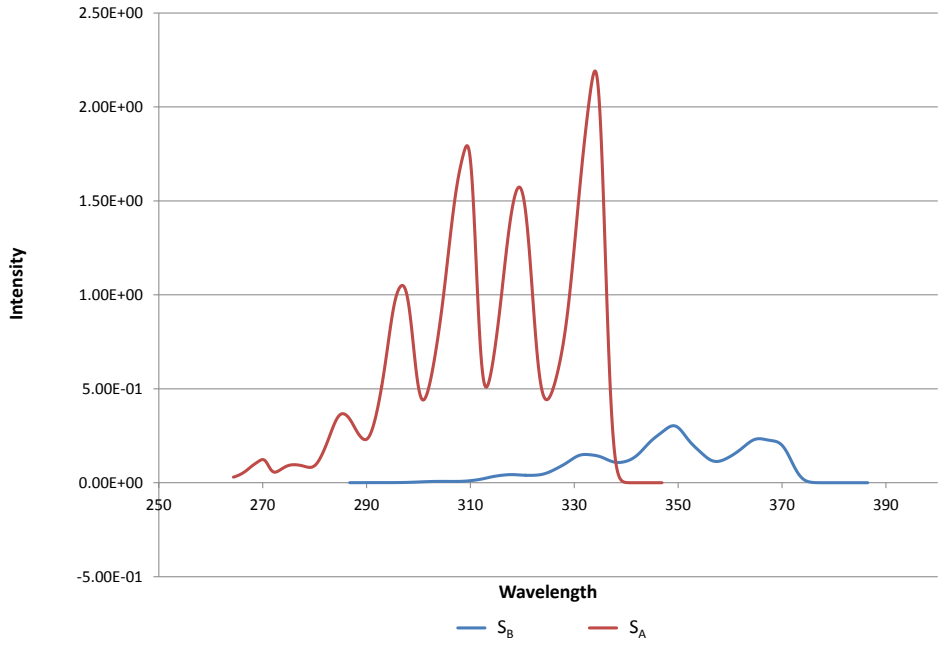

Figure 3.11: Calculated vibrationally resolved absorption spectrum for the states S_A and S_B of TTH-DPP-Au(I).

gold(I) atoms. However, these states are characterized by lots of orbital transitions which prevents a sufficient characterization of the states. To verify contribution of the gold atom to these states, different characterization techniques not based on molecular orbitals have to be employed. A good alternative to characterize excited states is the analysis of the transition density matrix and the calculation of natural transition orbitals (NTOs). These are a state-specific set of orbitals describing the electron transition itself (see Sec. 2.3.6). Although it is mathematically not fully correct, for the sake of simplicity, the nomenclature used for molecular orbitals is also applied here for NTOs. Therefore, the hole NTO exhibiting the highest eigenvalue is labeled "highest occupied natural transition orbital" (HONTO) and the corresponding particle NTO sharing the same eigenvalue is labeled "lowest unoccupied natural transition orbital" (LUNTO). The NTO pairs exhibiting lower eigenvalues follow the same scheme (HONTO−1, LUNTO+1,...). The NTOs for the S_3 and S_4 state have been calculated at TD-DFT/ωB97XD/6-31G* level

of theory. The NTOs for the S_3 state are shown in Fig 3.12 with each line corresponding to one pair of NTOs. The contributions of the HONTO $\mapsto$ LUNTO and HONTO$-1 \mapsto$ LUNTO$+1$ transitions to the total excitation of the S_3 state are 56.0 % and 29.9 %, respectively. The NTOs for the S_4 state are shown in

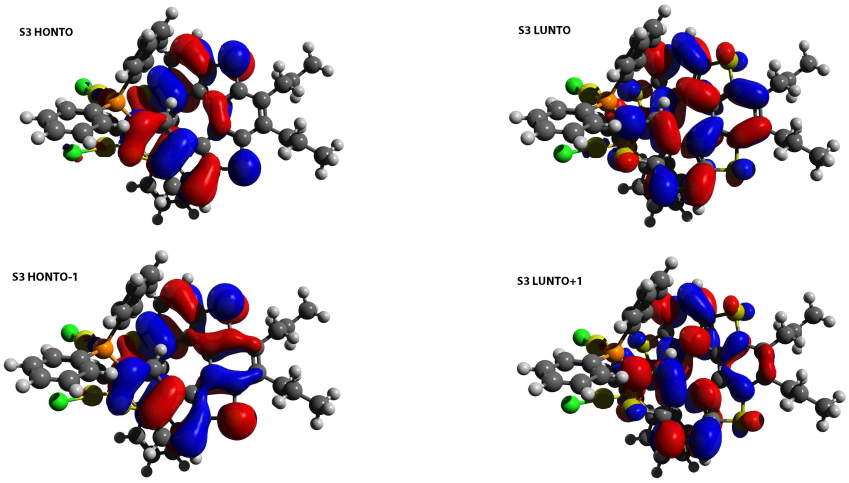

Figure 3.12: Natural transition orbitals (NTOs) ($>$ 5 % contribution) of the ($S_0 \mapsto S_3$) transition of TTH-DPP-Au(I). Each line corresponds to a NTO pair.

Fig 3.13 with contributions of 53.4 % and 35.1 % for the HONTO $\mapsto$ LUNTO and HONTO$-1 \mapsto$ LUNTO$+1$ transitions, respectively.

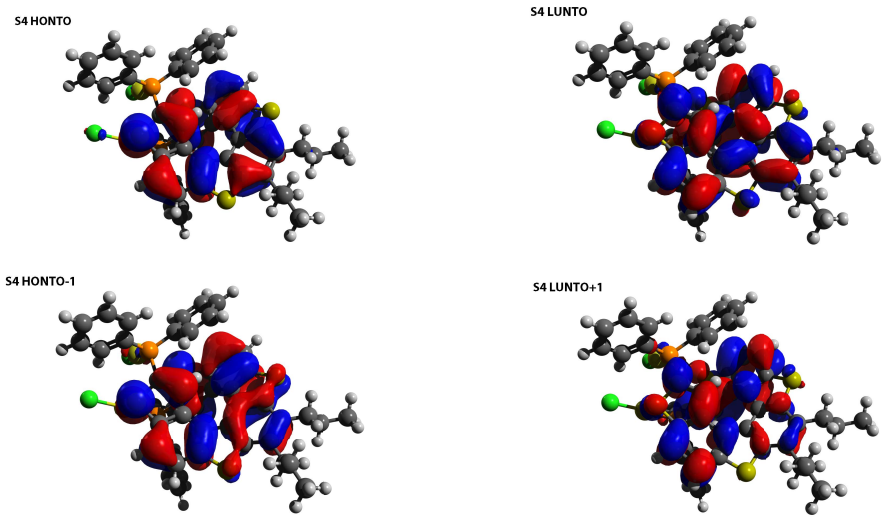

Figure 3.13: Natural transition orbitals (NTOs) ($>$ 5 % contribution) of the ($S_0 \mapsto S_4$) transition of TTH-DPP-Au(I). Each line corresponds to a NTO pair.

Analysis of these NTOs shows pure ($\pi \mapsto \pi^*$) transition character for the states S_3 and S_4. Neither do any *d*-orbitals localized on the gold(I) atoms nor *n*-orbitals localized at the chlorine atoms contribute to the excitation of these states. The contribution of these type of molecules indicated by the MOs cancel by other complementary orbital transitions. Only the typical ($\pi \mapsto \pi^*$) orbital transitions remain.

The equilibrium structures of the excited states S_1, S_2 and T_1 have been optimized as well. A comparison of important distances and angles is given in Tab. 3.5. By analyzing the geometrical parameters, only marginal differences can be identified between ground state, first and second excited state. Most strikingly, for all considered states, the geometrical parameters in the vicinity of the gold atoms do hardly change upon excitation. However, the analysis shows a slight decrease of the incline of the helix in the excited state. This is more pronounced in the first excited state than in the second. A superposition of the three equilibrium structures is given in Fig. 3.14. Most likely, this decrease of the incline of the helix

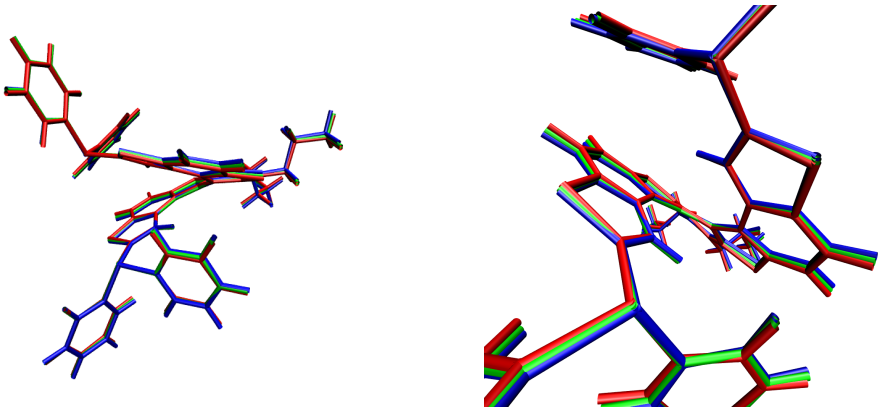

Figure 3.14: Superposition of the equilibrium structures of S_0 (blue), S_1 (red) and S_2 (green) of TTH-DPP-Au(I). The gold and chlorine atoms are omitted. Overview (left) and detail (right).

is caused by a bonding interaction of part of the LUMO between the two layers of the helix in the terminal region. This leads to a slight contraction once this orbital gets occupied.

The calculated fluorescence wavelength and oscillator strength corresponding to the excitation energy of the first excited state in the S_1 equilibrium geometry (S_1@S_1) is 3.03 eV (409.2 nm) and 0.38, respectively. This is in good agreement with the experimental result of the fluorescence wavelength of 430 nm. The same holds for the phosphorescence wavelength which can be computed as energy

difference between the total energies of the optimized S_0 structure and optimized T_1 structure. Here an energy difference of 2.58 eV compared to the experimental phosphorescence wavelength of 545 nm (2.27 eV) is found.

Finally, it is to conclude that *a)* in TTH-phosphane derivatives the TTH backbone dominates the photochemical properties and *b)* gold(I) shows no influence on the photochemical properties beyond a heavy-atom effect which slightly shifts the excitation energies.

3.2 Investigations on ionization of TTH derivatives

In this section the electrochemical properties of various TTH derivatives are analyzed. This involves the calculation of ionization energies (IEs), corresponding to oxidation and electron affinities (EAs), corresponding to a reduction process. Ionization processes can either be caused by absorption of high-energy photons like in X-ray radiation or electronically. Understanding these oxidation and reduction processes is very important for application of TTH-derivatives in optoelectronics.

3.2.1 Investigated systems and computational methodology

The electrochemical properties of different TTH-phosphine-oxides and TTH-phosphine-selenides have been investigated. For the phosphine-oxides, both *n*-butyl (TTH-(PO(*n*−Bu)$_2$)$_2$)and phenyl (TTH-(PO(Ph)$_2$)$_2$) substituted phosphines were considered. While the alkyl-substituted TTH-phosphine was investigated using only the double-substituted derivative, the phenyl substituted TTH-phosphine was investigated using both mono- and disubstituted derivatives, i.e. TTH-(PO(Ph)$_2$)$_2$ and TTH-PO(Ph)$_2$. The Lewis structures of the three investigated TTH-phosphine-oxides are given in Fig. 3.15. As phosphine-selenides, the mono- and disubstituted

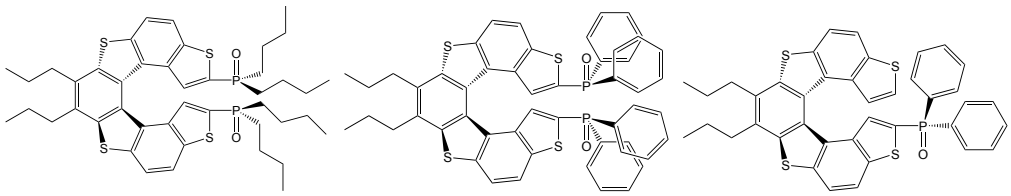

Figure 3.15: Lewis structures of the investigated TTH-PO derivatives: TTH-(PO(*n*−Bu)$_2$)$_2$ (left), TTH-(PO(Ph)$_2$)$_2$ (middle) and TTH-PO(Ph)$_2$ (right).

TTH-phosphine-diphenly-selenides TTH-(PSe(Ph)$_2$)$_2$ and TTH-PSe(Ph)$_2$ have been investigated (Fig. 3.16)

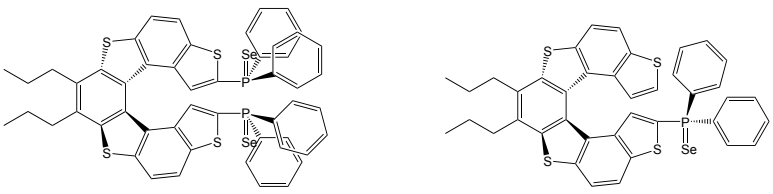

Figure 3.16: Lewis structures of the investigated TTH-PSe derivatives: TTH-(PSe(Ph)$_2$)$_2$ (left) and TTH-PSe(Ph)$_2$ (right).

All calculations were carried out at DFT/ωB97XD/cc-pVDZ level of theory. The functional ωB97XD was chosen, since it is known, that for calculating IEs or electronic excitations with a large charge-transfer character a pure DFT functional is insufficient and an increasing amount of Hartree-Fock exchange improves the results significantly.[99,100] A polarizable continuum model (PCM) using the integral equation formalism variant (IEFPCM) was applied to consider solvation effects. The parameters of dichloromethane (DCM) and water (H_2O) were chosen for the solvent model. The unrelaxed IEs and EAs have been calculated at the optimized ground state structures as the difference between neutral and anionic or cationic system. Relaxed IEs and EAs have been calculated after geometric relaxation in the cationic or anionic form, respectively, as the difference to the neutral system at the equilibrium geometry. For all calculations, the program package Gaussian 09 Rev. D.01 was used.[203]

3.2.2 TTH-phosphine-oxides

The ground state structures of the three systems TTH-$(PO(n\text{–}Bu)_2)_2$, TTH-$(PO(Ph)_2)_2$ and TTH-$PO(Ph)_2$ have been optimized for the neutral systems. All

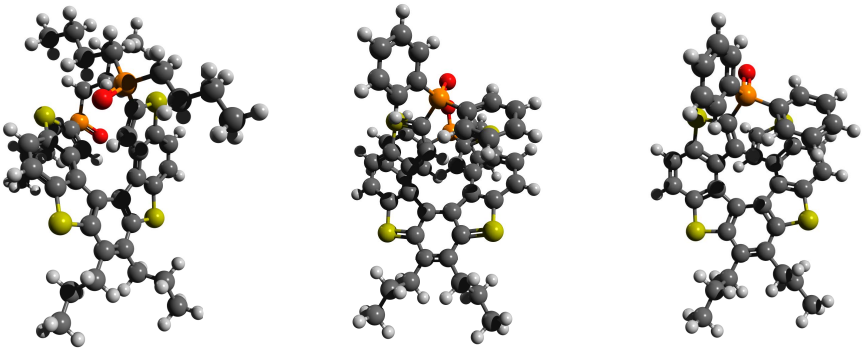

Figure 3.17: Optimized geometric structures of TTH-$(PO(n\text{–}Bu)_2)_2$ (left), TTH-$(PO(Ph)_2)_2$ (middle) and TTH-$PO(Ph)_2$ (right). Optimization including PCM with water as solvent.

structures are very similar. However, the most noticable difference is the direction the oxygen atoms are pointing. In the case of the phenyl-substituted phosphines, the oxygen atoms point to the outer region while in the case of the *n*-butyl-phosphines the oxygen atoms point more towards the TTH-moiety. The frontier orbitals, namely HOMO, HOMO−1, LUMO and LUMO+1 for the neutral systems are qualitatively identical for all PO systems independent of the inclusion of PCM or the solvent. All of them are located at the TTH-ring and are hardly influenced

by the substituents. This is in perfect agreement with previous investigations on TTH derivatives (see Sec. 3.1.3 and 3.1.4). None of the frontier orbitals exhibit any contribution on the phosphine oxide or the alky side-chains or phenyl rings. The frontier orbitals of TTH-(PO(n–Bu)$_2$)$_2$ are shown representatively in Fig. 3.18. The orbitals are labeled based on their structure from ϕ to ω. The

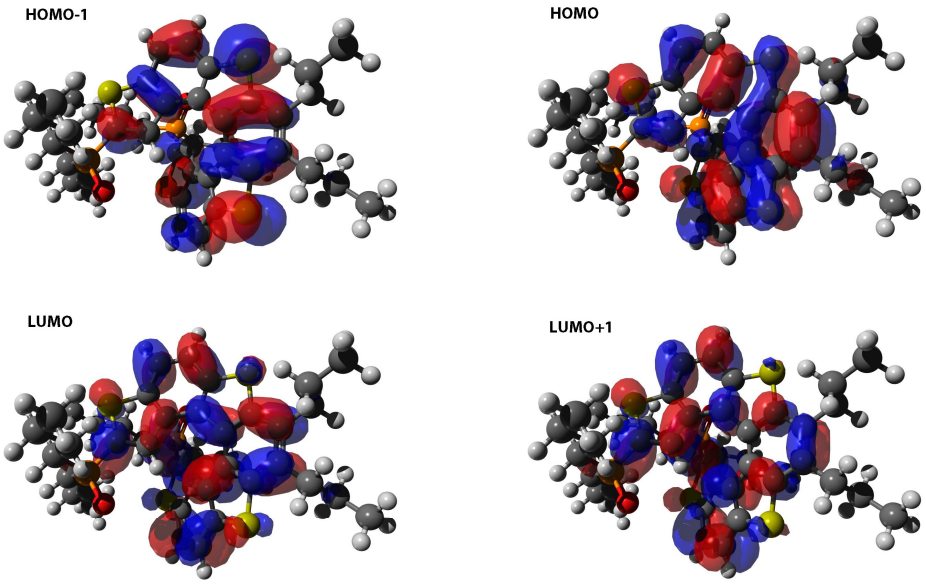

Figure 3.18: Frontier orbitals HOMO−1 (ϕ) (top left), HOMO (χ) (top right), LUMO (ψ) (bottom left) and LUMO+1 (ω) (bottom right) of neutral TTH-(PO(n–Bu)$_2$)$_2$.

investigated TTH-phosphine-oxides exhibit a general first EA of about 2 eV and a general first IE of about 6 eV in solution. Analyzing the IEs and EAs, after adding the solvent model shows that, the IEs are decreased and the EAs are increased owing to stabilization of the charged molecule in the environment. This stabilizing effect is more pronounced in the polar solvent water, in which the EAs are about 0.2 eV higher than in DCM. The unrelaxed first IEs and EAs for the three TTH-phosphine-oxides in the gas phase as well as in water and DCM solution are listed in Tab. 3.7.

To analyze the region of the reduction and oxidation processes, difference densities of the neutral and charged species were calculated. The anionic difference density is defined as the total density of the neutral system minus the total density of the anionic system. This holds for the cationic system accordingly. Generally, difference densities can be described in terms of particle and hole interactions.

Table 3.7: First ionization energies (IE) and first electron affinities (EA) in eV for TTH-(PO(n–Bu)$_2$)$_2$, TTH-(PO(Ph)$_2$)$_2$ and TTH-PO(Ph)$_2$ in the gas phase, in aqueous solution and in DCM calculated at DFT/ωB97XD/cc-pVDZ level of theory using a polarizable continuum model for the solvent.

	TTH-(PO(n–Bu)$_2$)$_2$	TTH-(PO(Ph)$_2$)$_2$	TTH-PO(Ph)$_2$
1st IE (vac.)	7.10	6.00	6.18
1st IE (DCM)	6.13	6.09	6.02
1st IE (H_2O)	6.06	5.97	5.9
1st EA (vac.)	0.53	1.83	1.47
1st EA (DCM)	1.83	1.94	1.86
1st EA (H_2O)	2.06	2.14	2.05

In the case of an oxidation, an electron is annihilated and a hole is created. In these densities, positive (green) and negative (red) values indicate the position of the hole and particle, respectively. The small areas with a negative difference density in the cationic form or positive difference density in the anionic form are due to orbital relaxation and electron reorientation effects in the oxidation and reduction process, respectively. Mathematically, they can be described as two-particle-one-hole or one-particle-two-hole terms (see also Sec. 2.3.6). The cationic and anionic difference densities of TTH-(PO(Ph)$_2$)$_2$ and TTH-PO(Ph)$_2$ are shown in Fig 3.19. Both the electron detachment (oxidation) as well as the electron attachment (reduction) are localized on the TTH scaffold and do not include the phenyl or alkyl moieties or the P=O group. They corresponds to the form of the frontier orbitals, which exhibit also almost no localization on these parts. The pattern of the cationic and anionic difference density match the HOMO and LUMO pattern, respectively, resulting from a strong dependence of the electron attachment and detachment of these orbitals. In the monosubstituted TTH derivate TTH-PO(Ph)$_2$ the cationic difference density is slightly shifted to the unsubstituted end of the TTH ring while the anionic difference density is shifted towards the phosphine-oxide. However, this still matches the pattern of the also slightly shifted frontier orbitals.

In contrast, TTH-(PO(n–Bu)$_2$)$_2$ has a different pattern in the difference density of the cationic form compared to the two-phenyl-substituted molecules, although the frontier orbitals remain unchanged. In this case, the electron detachment is driven by the HOMO−1, which has a similar pattern as the difference density. The anionic difference density is similar to the ones of TTH-(PO(Ph)$_2$)$_2$ and

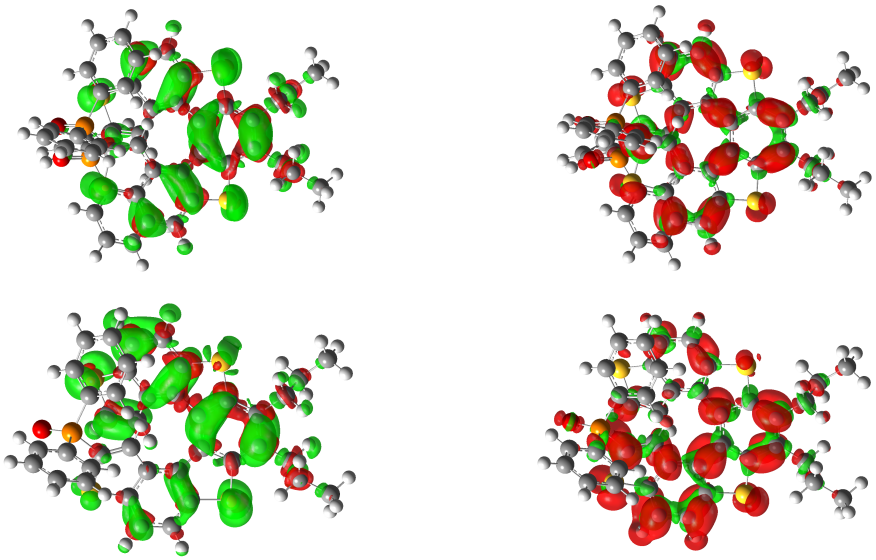

Figure 3.19: Difference density plots for cationic (left) and anionic (right) TTH-$(PO(Ph)_2)_2$ (top) and TTH-$PO(Ph)_2$ (bottom) in aqueous solution.

TTH-$PO(Ph)_2$ (Fig. 3.20). In all three molecules, the solvent affects the difference densities and the frontier orbitals only marginally.

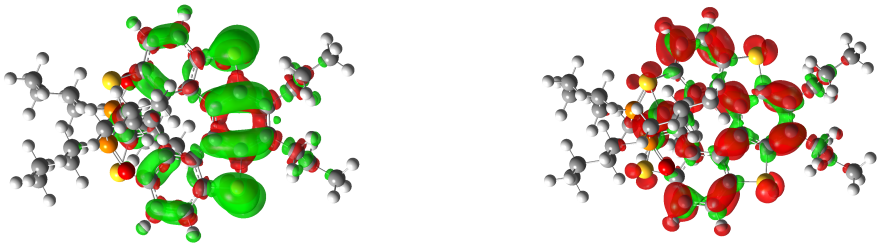

Figure 3.20: Difference density plots for cationic (left) and anionic (right) TTH-$(PO(n\text{–}Bu)_2)_2$ in aqueous solution.

The relaxed first IE and EA of TTH-$(PO(n\text{–}Bu)_2)_2$ were calculated by relaxing the geometry of the anionic and cationic form in the gas phase, in aqueous solution and in DCM. This is in particular important for comparison with experimental results like those obtained by cyclovoltammetry. This is because there a voltage is applied for a long time in terms of molecular timescale. Therefore, the molecule has time to adapt geometrically to the new electronic configuration of the anionic or cationic form.[204] The IEs and EAs are 6.46 eV, 5.90 eV, 5.98 eV, 0.73 eV, 2.22 eV and 2.05 eV, respectively. In both cases, the structure relaxes and adapts

to the new electronic configurations, which are still stable, by releasing thermal energy of about 0.16 eV (15.44 kJ/mol)

For investigation of higher order oxidation and reduction processes the second and third unrelaxed IEs and EAs of TTH-$(PO(Ph)_2)_2$ in DCM solution have been calculated as well. The corresponding energies are given in Tab. 3.8. The

Table 3.8: First three unrelaxed ionization energies (IE) and first three unrelaxed electron affinities (EA) in eV of TTH-$(PO(Ph)_2)_2$ in DCM solution calculated at DFT/ωB97XD/cc-pVDZ level of theory using PCM.

	TTH-$(PO(Ph)_2)_2$
1^{st} IE (DCM)	6.09
2^{nd} IE (DCM)	13.21
3^{rd} IE (DCM)	21.57
1^{st} EA (DCM)	1.94
2^{nd} EA (DCM)	2.86
3^{rd} EA (DCM)	2.88

difference density of the double-cationic form to the neutral form ($2+ \mapsto$ N) shows a different pattern than that exhibited by the mono-cationic form. Visualizing the difference density of the double-cationic form to the mono-cationic form ($2+ \mapsto 1+$) reveals that the second electron detachment has a pattern similar as the ϕ-orbital (HOMO-1 in the neutral form). In combination, the difference density of the mono-cationic form to the neutral form ($1+ \mapsto$ N) and the difference density of the double-cationic form to the mono-cationic form ($2+ \mapsto 1+$) build the pattern observed in the double-cationic difference density ($2+ \mapsto$ N). This is in particular interesting, since one would assume that both electron detachments of a double ionization occur in the same orbital. To elaborate this, the orbital energies of the alpha and beta frontier orbitals were calculated for the neutral and for all ionized forms. In the neutral form, the HOMO and HOMO-1 are separated by only 0.13 eV. In the first ionization process, the beta electron of the HOMO (χ) is removed leading to a rise of the orbital energy from -7.49 eV in the neutral form to -4.66 eV in the mono-cationic form. Accordingly, the energy of the alpha χ is lowered from -7.49 eV in the neutral form to -8.61 eV in the mono-cationic form, while the energy of the alpha ϕ changes from -7.62 eV to -8.51 eV. The alpha χ is now energetically lower than the alpha ϕ. Both orbitals are still occupied. This is due to a stronger Coulomb interaction between alpha χ and beta χ than between alpha ϕ and beta χ. This interaction is missing in the case of the mono-cationic

system since the beta χ is now unoccupied leading to a changed energetic order of the alpha orbitals. The beta ϕ exhibits a similar energy as the alpha ϕ of -8.48 eV. In the second ionization process, the electron of the alpha ϕ is removed, since it is the highest occupied orbital. This would lead to a configuration with an occupied alpha ϕ and alpha χ and unoccupied beta ϕ and beta χ, resulting in a non-closed-shell electron distribution and a $S^2 \neq 0$. In singlet multiplicity, this is avoided by building new orbitals. In this case, however, a triplet configuration is also possible. Calculations on the double-cationic triplet state (T_1^{2+}) along with the results of an unrestricted open shell wave function stability analysis reveal that this triplet state is indeed the energetically most stable electron configuration with a total energy of 0.1 eV below the singlet ground state (S_0^{2+}). In contrast, the double-anionic difference density to the neutral ($2- \mapsto$ N) form shows the same pattern as the mono-anionic difference density to the neutral form ($1- \mapsto$ N) (Fig 3.19 top right), which is comparable to the LUMO of the neutral form (ψ) (Fig. 3.21). This leads to the same pattern in the difference density of the double-anionic form to the mono-anionic form ($2- \mapsto 1-$).

In summary, the difference density of the mono-anionic ($\widehat{=} \psi$) (mono-cationic ($\widehat{=} \chi$)) form to the neutral form ($1- \mapsto$ N) / ($1+ \mapsto$ N) (Fig 3.19 top) and the difference density of the double-anionic (double-cationic) form to the mono-anionic ($\widehat{=} \psi$) (mono-cationic ($\widehat{=} \phi$)) form ($2- \mapsto 1-$) / ($2+ \mapsto 1+$) (Fig 3.21 right) build the difference density of the double-anionic (double-cationic) form to the neutral form ($2- \mapsto$ N) / ($2+ \mapsto$ N) (Fig. 3.21 left).

This is similar for the triple-anionic form. The difference densities of the triple-anionic form to the neutral form ($3- \mapsto$ N) exhibits further contributions compared to the difference densities of the double-anionic form to the neutral form ($2- \mapsto$ N), which can be described by the difference density of the triple-anionic form to the double-anionic form ($3- \mapsto 2-$). This corresponds to the ω-orbital (the LUMO+1 in the neutral form). In contrast, in the triple-cationic form, new orbitals are formed due to the large contraction of the electron density caused by the high charge. In this case, one cannot relate the difference density of the triple-cationic form to the double-cationic form ($3+ \mapsto 2+$) to an orbital of the neutral form. However, these further contributions to the difference density of the triple-cationic form to the neutral form ($3+ \mapsto$ N) are still located on the TTH-ring and show no contributions of the phosphane-oxide groups to the ionization.

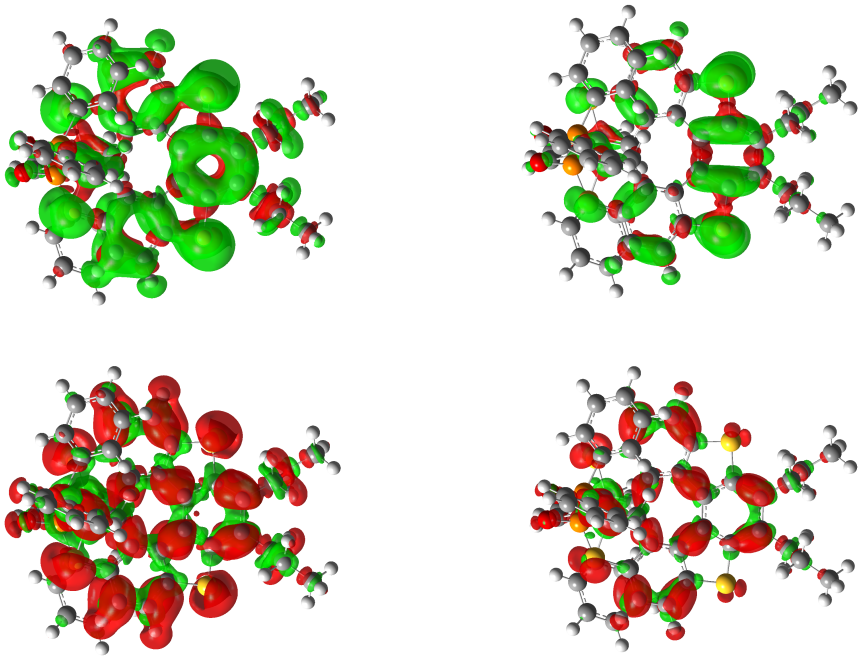

Figure 3.21: Difference densities of the double-cationic form of TTH-$(PO(Ph)_2)_2$ to the neutral form ($2+ \mapsto$ N) (top left) and to the mono-cationic form ($2+ \mapsto 1+$) (top right) as well as the difference densities of the double-anionic form to the neutral form ($2- \mapsto$ N) (bottom left) and to the mono-anionic form ($2- \mapsto 1-$) (bottom right).

To conclude these results, both the oxidation and reduction process are localized on the TTH backbone of the investigated TTH-phosphine-oxides. The results differ only marginally between the phenly- or *n*-butyl substituted phoshpines and between the mono- and disubstituted TTH, thus indicating only marginal influences of the phosphine-groups on the electrochemical properties. The oxidations and reductions, even of higher order, depend strongly on the form of the frontier orbitals. However, it can be observed that the phenyl substituted phosphine-oxides exhibit lower IEs and higher EAs than the alkyl-substituted ones. This result of easier reduction and oxidation of aryl phosphorus derivatives is in agreement with experimental results.

3.2.3 TTH-phosphine-selenides

As done for the TTH-phosphine-oxides, the TTH-phosphine-selenides TTH-$(PSe(Ph)_2)_2$ and TTH-$PSe(Ph)_2$ have been optimized in the electronic ground state in neutral form in the gas phase and in solvation using PCM with both DCM and water as solvent. The obtained equilibrium structures are qualitatively identical. Analysis of the orbitals in different solvents reveals a higher dependence

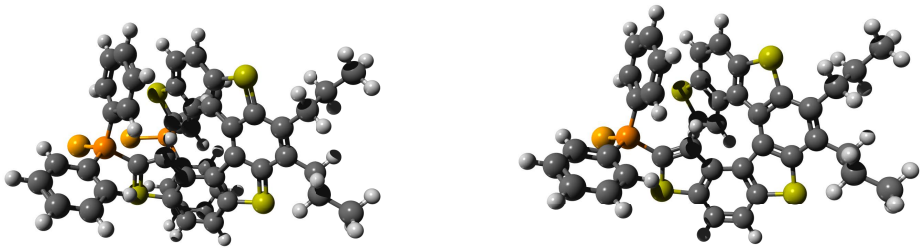

Figure 3.22: Optimized geometric structures of TTH-$(PSe(Ph)_2)_2$ (left) and TTH-$PSe(Ph)_2$ (right). Optimization including PCM with water as solvent.

of the TTH-phosphine-selenides on an environment than the TTH-phosphine-oxides. Without a solvent, the lone-pair orbitals of selenium are shifted to higher energies such that they even enter the energetic region of the frontier orbitals. For example, in the case of TTH-$(PSe(Ph)_2)_2$ the HOMO is a n-type orbital localized at a selenium atom. However, when PCM is employed, the energies of the n-type orbitals are reduced due to stabilizing interactions with the solvent. Now, the frontier orbitals of TTH-$(PSe(Ph)_2)_2$ and TTH-$PSe(Ph)_2$ in solution are qualitatively identical to the frontier orbitals of the TTH-phosphine-oxides as shown in Fig. 3.18. The frontier orbitals HOMO-1 to LUMO$+1$ of TTH-$(PSe(Ph)_2)_2$ calculated in the gas phase are shown in Fig. 3.23.

The first IE and EA have been calculated in the gas phase and in solution modeled by PCM using the parameters of water and DCM. The IE and EA exhibit a large difference of about 1 eV between the gas phase calculations and in solution. In solution, the IEs and EAs are comparable to the ones obtained for the TTH-phosphine-oxides in Sec. 3.2.2. The calculated IEs and EAs of TTH-$(PSe(Ph)_2)_2$ and TTH-$PSe(Ph)_2$ are listed in Tab. 3.9.

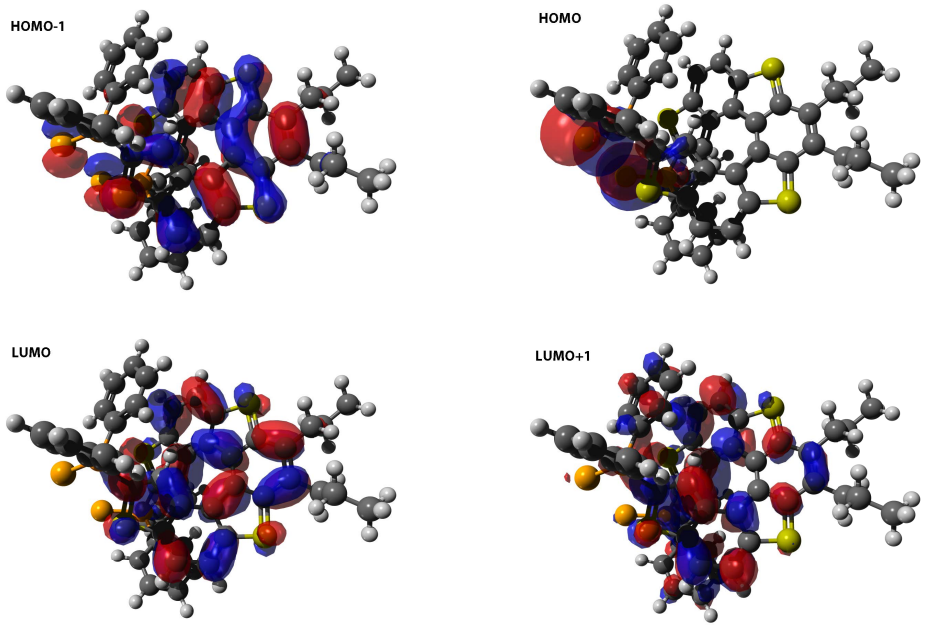

Figure 3.23: Frontier orbitals HOMO−1 (top left), HOMO (top right), LUMO (bottom left) and LUMO+1 (bottom right) of TTH-$(PSe(Ph)_2)_2$ in the gas phase.

Table 3.9: First ionization energies (IE) and first electron affinities (EA) in eV for TTH-$(PSe(Ph)_2)_2$ and TTH-$PSe(Ph)_2$ in the gas phase, in aqueous solution and in DCM calculated at DFT/ωB97XD/cc-pVDZ level of theory using a polarizable continuum model for the solvent.

	TTH-$(PSe(Ph)_2)_2$	TTH-$PSe(Ph)_2$
1^{st} IE (vac.)	6.83	7.08
1^{st} IE (DCM)	6.12	6.03
1^{st} IE (H_2O)	6.00	5.91
1^{st} EA (vac.)	0.80	0.64
1^{st} EA (DCM)	1.99	1.90
1^{st} EA (H_2O)	2.18	2.09

The oxidation and reduction were analyzed using difference densities. The difference in IEs and EAs in the gas phase compared to the results in solution can be explained by the aforementioned stabilization of the *n*-orbitals localized at the selenium atoms. The difference density of the cationic form of TTH-$(PSe(Ph)_2)_2$ in the gas phase exhibits the largest contribution localized at the selenium atoms (Fig 3.24). The difference density of the anionic form is delocalized over the TTH ring without any contributions of the phenylrings or the phosphine-selenides. The calculated difference densities match perfectly the form of the LUMO for the gas phase and in solution. As a result, different oxidations can be observed. However, the solvated TTH-phosphine-selenides exhibit difference densities for the anionic and cationic form which are qualitatively identical to the difference densities of the solvated TTH phosphane oxides. Hence, the energy difference of the IE and EA of TTH-$(PSe(Ph)_2)_2$ and TTH-$(PO(Ph)_2)_2$ in aqueous solution are only 0.03 eV and 0.04 eV, respectively. In general, the effect of the selenium on the first ionizations is marginal.

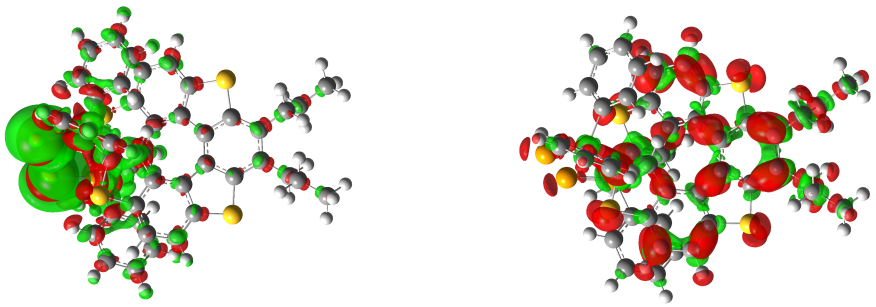

Figure 3.24: Difference density plots for cationic (left) and anionic (right) TTH-$(PSe(Ph)_2)_2$ in the gas phase.

In both TTH-phosphine-oxides and TTH-phosphine-selenides, it has been found that the electrochemical properties are strongly determined by the TTH backbone. The oxidation and reduction is closely related to the frontier orbitals and the P=Se group influences the these properties only marginally.

3.3 Summary and conclusion

In this chapter, I investigated the photochemical and electrochemical properties of various tetrathia-[7]heterohelicene (TTH) derivatives. The investigated systems contain a phosphorus-based functionalization of TTH in the α-position of both termnial thiophene rings.

The spectroscopic properties of tetrathia-[7]heterohelicene-dialkylphosphane-borane and tetrathia-[7]heterohelicene-diphenylphospane-gold(I)-chloride have been investigated using DFT and TD-DFT in combination with the functional ωB97XD and the basis sets cc-pVDZ and 6-31G* as well as at RI-CC2/cc-pVDZ level of theory. Solvation effects have been included via a polarizable continuum model.

The eight energetically lowest excited singlet states of both molecules have been calculated. They are all characterized by ($\pi \mapsto \pi^*$) transitions localized on the TTH-backbone. None of the analyzed states exhibits significant contributions of orbitals localized on the phosphorus atom, the gold(I) atom or any side-group. In both molecules, the first two excited states are close in energy and could both contribute equally to the experimentally observed first absorption band. Calculation of vibrationally resolved absorption spectra for the first two excited states of both molecules shows a clear dominance of the S_1 state, since lots of low-contributing vibrational transitions contribute to the vibronic spectrum of the S_2 state resulting in a very broad band with low intensity. The calculation of rotatory strengths explains the flat area observed in the experimental circular dichroism spectrum around the wavelengths of the first absorption band. The first and second excited state exhibit similar rotatory strengths with opposite sign resulting in a mutual canceling. Besides small shifts of excitation energies, no major influence of the phosphane-groups or the gold(I) atoms could be identified. The spectroscopic properties are determined by the TTH moiety.

The electrochemical properties of tetrathia-[7]heterohelicene-phosphine-oxides and TTH-phosphine-selenides have been investigated. Ionization energies, corresponding to oxidation and electron affinities, corresponding to reduction, have been calculated at DFT/ωB97XD/cc-pVDZ level of theory. These were analyzed using difference densities. A close correlation between the form of an oxidation and reduction and the form of the frontier orbitals has been found. This holds also for higher ionized species. As for the photochemical properties, also the electrochemical properties are determined by the TTH-ring with only slight modulating effects of the phosphine-oxide- or phosphine-selenide-groups.

Chapter 4

Development and Implementation of FDE-ADC

"The important thing in science is not so much to obtain new facts as to discover new ways of thinking about them."
Sir William Bragg

In recent years, the inclusion of environment effects on excited state calculations became more and more important to achieve chemical and physical properties that can be compared with experimental data. These interactions can be modeled using intrinsic solvation models like PCM if only dispersion and Coulombic interaction play a role. However, if more specific interactions start to play a role, these models exhibit known deficits.[205,206] In these cases, an explicit model for the environment, such as *frozen density embedding theory* (FDET), is needed. In the early formulation of FDET, the embedded system A is treated on the DFT level of theory,[71,207,208] but can also, as shown recently, be calculated using wavefunction based methods.[142,145–149] The density of the environment is usually obtained from lower level quantum chemical calculations[142] but can also be obtained from theories for ensembles,[209] or even from experiment.[143]

In this second part of my dissertation, I combined the wavefunction based method ADC with linearized FDET. The development of this new method *FDE-ADC* and its implementation into the quantum chemical program package `Q-Chem` in the module `fdeman` is described in this chapter. `fdeman` has been developed in cooperation with the research group of Prof. Dr. Tomasz. A. Wesolowski from the University of Geneva. So far, including environmental

effects into an ADC calculation has been accomplished by means of a polarizable continuum model (PCM)[210,211] and through QM/MM calculations.[212]

Generally, linearized FDET is employed to maintain the orthogonality of the excited states. Therefore, an MP(2) density is used for the reference density $\rho_A^{ref}(\vec{r})$. A more detailed description will be given in Sec. 4.1.

The electron density ρ is represented by a density matrix. During a calculation, density matrices instead of full electron densities are used. For the sake of simplicity, the electron density and the density matrix are used analogously here.

The procedure of an FDE-ADC calculation comprises four steps: ***a)*** generation of $\rho_A(\vec{r})$, ***b)*** generation of $\rho_B(\vec{r})$, ***c)*** calculation of $v_{emb}^{lin}(\vec{r})$ and finally ***d)*** applying $v_{emb}^{lin}(\vec{r})$ in an FDE-ADC calculation. In the first step, fragment A is initialized and an MP(2) density matrix in the basis of atomic orbitals is computed employing the `adcman`[24] module in Q-Chem. This density matrix ($\rho_A^{ref}(\vec{r})$) is stored and in the next step the environment fragment B is initialized, and either an HF or DFT calculation can be performed to obtain the density matrix $\rho_B(\vec{r})$. In a third step, the two density matrices of A and B are used to evaluate the four state-independent parts of the embedding potential, which are the nuclear attraction potential, the coulombic repulsion potential and the exchange-correlation and kinetic energy non-additive bifunctional potentials. The sum of these individual parts resembles $v_{emb}^{lin}(\vec{r})$. In the last step, an FDE-ADC calculation is performed. For this purpose, system A is initialized again and the previously generated embedding potential is added to the Fock-Matrix $\mathbf{F}$ in the SCF procedure of the ADC underlying HF calculation. This way, an ADC calculation is performed with inclusion of the environment interaction via the orbitals and integrals. This is described in detail in Sec. 4.2. After this, the user control of `fdeman` is outlined in Sec. 4.3. In the end of this chapter, a summary and overview of the features of FDE-ADC in the module `fdeman` is given in Sec. 4.4. [1] [2]

[1] Parts of Chapter 4 have already been published in
First time combination of frozen density embedding theory with the algebraic diagrammatic construction scheme for the polarization propagator of second order
Stefan Prager, Alexander Zech, Francesco Aquilante, Andreas Dreuw and Tomasz A. Wesolowski
The Journal of Chemical Physics, 144 (2016,) page 204103
and
Implementation and application of the frozen density embedding theory with the algebraic diagrammatic construction scheme for the polarization propagator up to third order
Stefan Prager, Alexander Zech, Tomasz A. Wesolowski and Andreas Dreuw
submitted for publication, (2017)

[2] All C++ source code snippets are printed with the written permission of the Board of Directors of Q-Chem, Inc.

4.1 Expansions of the embedding potential

I would like to start with the representation of the embedding potential. Once a basis is introduced, the embedding potential is represented as a matrix of coefficients in the basis of atomic orbitals. Since the embedding potential acts on system A, it has to be expressed in the basis of A as well. However, the embedding potential depends both on the electron densities of the isolated systems A and B. Thus, for creation of the embedding potential a different basis is needed than for the application of the embedding potential. To overcome this issue, three different techniques are possible. The most straightforward variant is the *supermolecular expansion*. An approximation to this is the by myself newly developed *re-assembling of density matrix* variant. An alternative approach is referred to as *monomer expansion*. I will elaborate these variants in this section.

4.1.1 Supermolecular expansion

The first approach to overcome the inconsistency between bases required for creation of the embedding potential and applying is the supermolecular expansion (SE). In this approach, both individual densities of A and B required for the embedding potential are expressed in a supermolecular basis of A and B. In the calculation of A, part B is treated as ghost atoms and vice versa. Both the MP(2) density matrix for $\rho_A(\vec{r})$ and the HF/DFT density matrix for $\rho_B(\vec{r})$ exhibit the same size. Thus, the embedding potential is also created in the supermolecular basis. Consequently, the final FDE-ADC calculation is also performed in the basis of A and B. A scheme of the SE approach is shown in Fig. 4.1.

However, SE is not very efficient, since it provides no computational savings compared to a supermolecular ADC calculation. Instead, it is intended as a benchmark method for FDE-ADC and can be used for analyses of the embedding theory itself, since SE contains by construction no basis-set superposition error (BSSE).

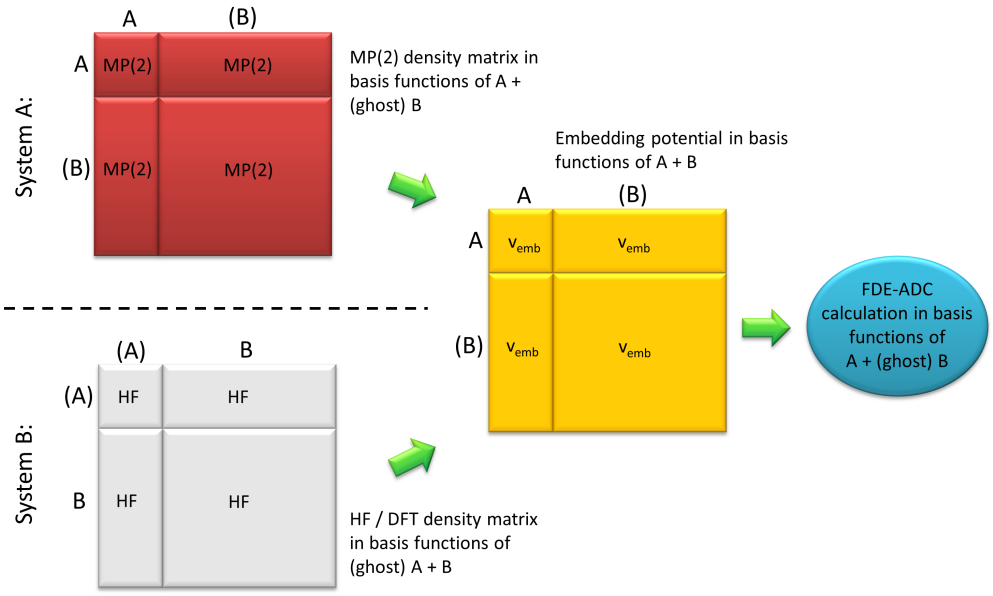

Figure 4.1: Schematic representation of the supermolecular expansion. The MP(2) (red) density matrix of system a as well as the HF or DFT (grey) density matrix of system B are both expressed in the supermolecular basis A + B. Hence, the generation of the embedding potential as well as the FDE-ADC calculation are carried out in the supermolecular basis.

4.1.2 Re-assembling of density matrix

To overcome the limitations of SE as not being applicable for modeling, I developed the re-assembling of density matrix (RADM) approach as an approximation to SE. In RADM, the calculation of A is split. A is calculated at first in the supermolecular basis A + B on HF level of theory, obtaining the HF density matrix. This density matrix contains 4 blocks: AA, AB, BA and BB. After this, it is calculated again, now in the basis of A only on MP(2) level of theory and a separate HF-to-MP(2) difference density matrix in the basis of A is generated. The HF-to-MP(2) difference density matrix is in a following step added to the AA block of the HF density matrix of the previous calculation, thus building a density matrix in the basis of A+B on MP(2) level of theory in the AA block and on HF level of theory on the remaining AB, BA and BB blocks. This mixed density matrix is called the *reassembled density matrix*.

The environment system B is, as in SE, calculated in the supermolecular basis A+B. The subsequent calculation of the embedding potential is performed in the supermolecular basis as well. But after the embedding potential is complete, it

is truncated to the AA block only. A schematic representation of the RADM approach is shown in Fig. 4.2.

This approximation is valid, since, in the supermolecular basis, the values of the embedding potential in the off-diagonal AB and BA blocks and the values

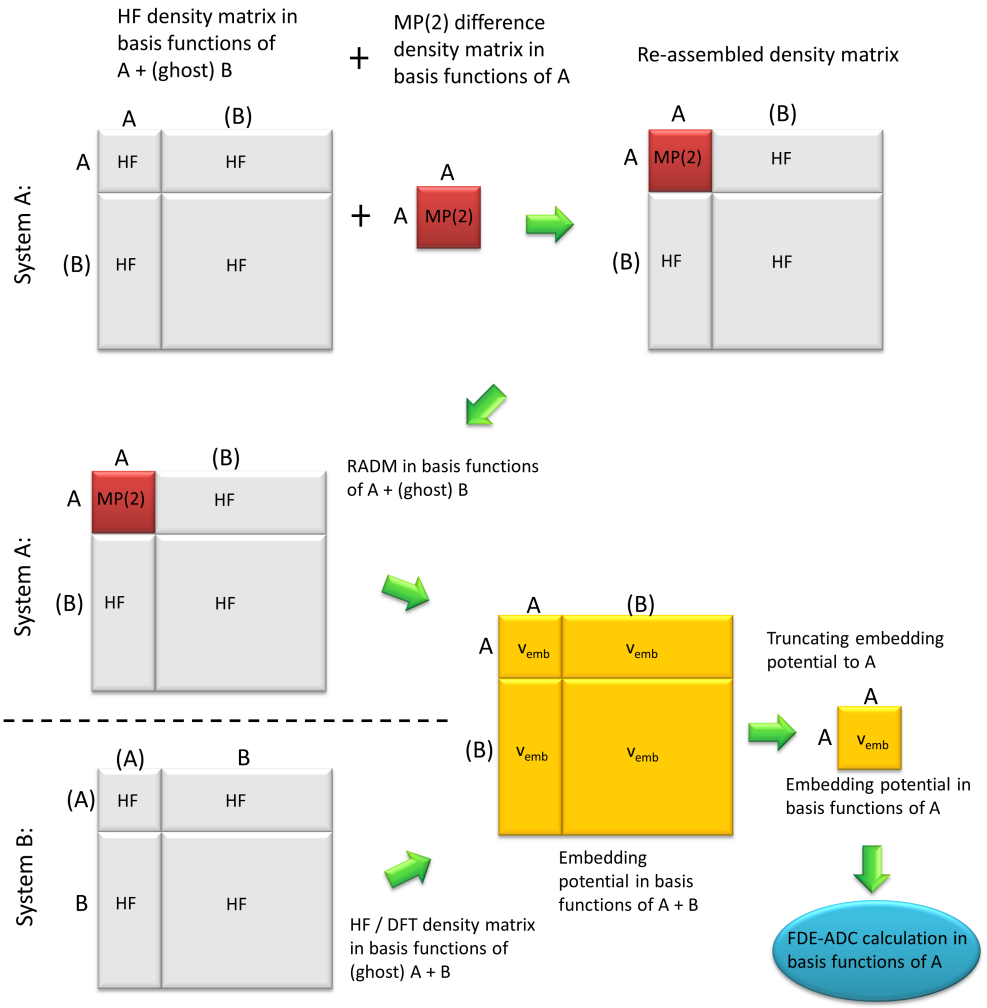

Figure 4.2: Schematic representation of the re-assembling of density matrix approach. In the upper line, the isolated system A is calculated forming the reassembled density matrix by combining the HF (grey) density matrix on the basis functions of A and B with the HF/MP(2) (red) difference density matrix on the basis functions of A. This is used with the isolated system B in a supermolecular basis to create the embedding potential (yellow). After truncation to the elements in the basis of A only, it is applied in the subsequent FDE-ADC calculation (blue) in the basis of A only as well.

of the density matrix of A in the BB block are almost zero (see example in Fig. 4.3). Hence, in a contraction of the density matrix of A with the embedding potential, the values in these three blocks vanish and can therefore be neglected. Consequently, the FDE-ADC calculation (step *d)*), which is the computationally

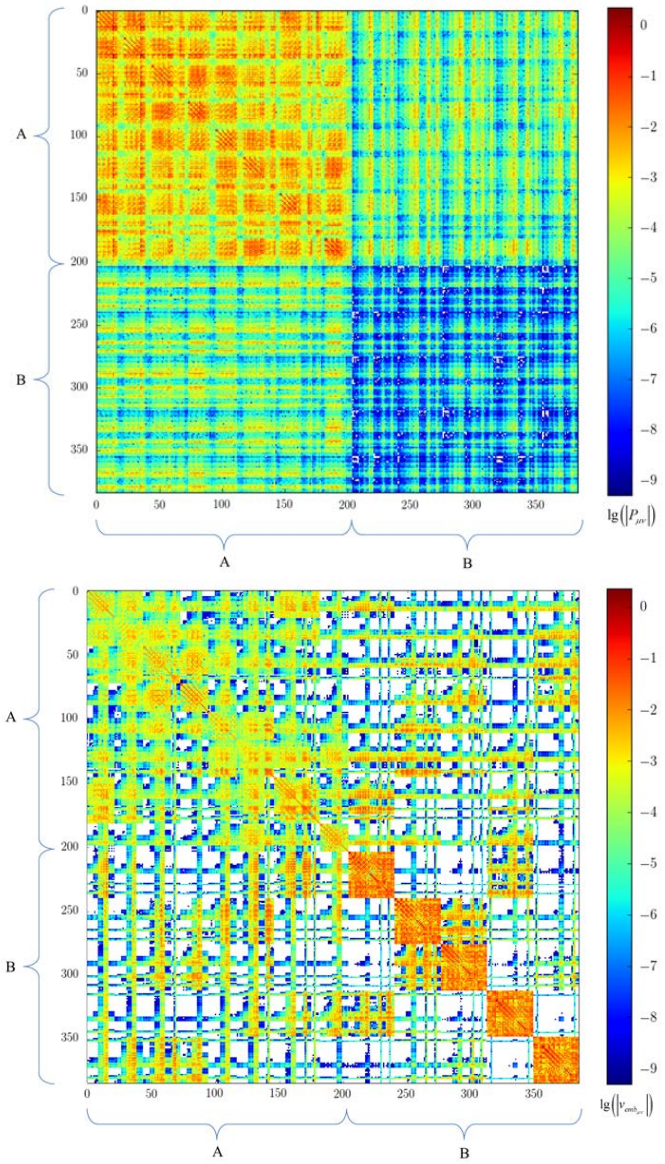

Figure 4.3: Graphical representation of the values of the re-assembled density matrix (top) and the total embedding potential (bottom) of the example system uracil (A) and five water molecules (B) in the basis of both subsystems (A+B). For better visibility, the decadic logarithm of the values is shown. Values below 10^{-10} are treated as zero and displayed as white in the diagram.

most demanding step, can be performed in the basis of A only. In summary, the RADM approximation consists of an assembling of a density matrix and the truncation of the calculated embedding potential.

4.1.3 Monomer expansion

In the monomer expansion (ME) the embedding potential is calculated directly in the basis of A from the MP(2) density matrix of A in the basis of A and the HF / DFT density matrix of B in the basis of B. The subsequent FDE-ADC calculation can be carried out without any truncation of the embedding potential. This approach is illustrated in Fig. 4.4.

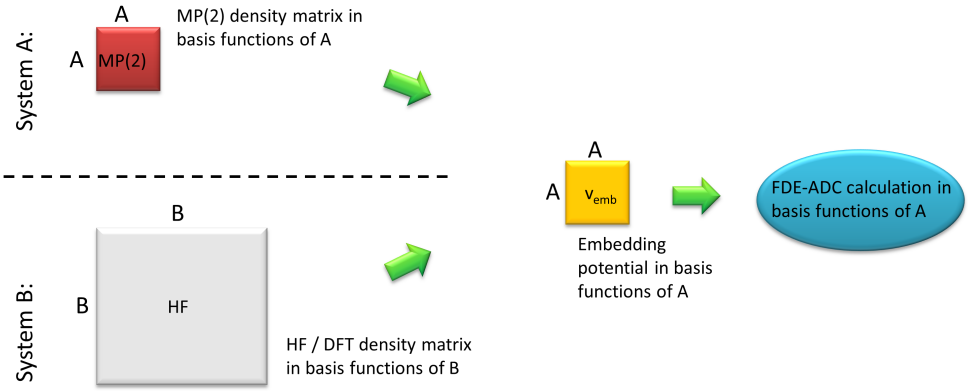

Figure 4.4: Schematic representation of the monomer expansion. The density matrices of A and B are created in their respective monomer basis and the embedding potential is directly calculated in the basis of A for the subsequent FDE-ADC calculation.

To overcome the mixed basis sets, a basis set transformation is needed during the calculation of the embedding potential. However, the development of the monomer expansion for FDE-ADC is not part of my dissertation. Hence, I will not go into more detail here.

4.2 Implementation of fdeman

In this section, I would like to elaborate in detail on the implementation of the FDE-ADC method in the program package Q-Chem. For the management of the complete FDE-ADC calculation, a module was implemented called fdeman. This module controls all related subtasks needed for the calculation. fdeman takes advantage of available functions in Q-Chem to achieve various tasks. fdeman is written in the object-oriented C++ programming language but also accesses existing Fortran based code in Q-Chem. fdeman is fully parallelized using OpenMP and will be publicly available in the next official release of Q-Chem.

At first, I would like to introduce the structure of fdeman. After this I will describe the creation of the individual densities $\rho_A(\vec{r})$ and $\rho_B(\vec{r})$ and then discuss the calculation of the embedding potential itself.

4.2.1 General structure of fdeman

fdeman is implemented in Q-Chem to manage, as its name already says, FDE-ADC calculations. In Q-Chem, the several tasks like the SCF procedure or ADC calculations are performed by specific managers. For example, the mentioned SCF is performed by the module scfman and ADC by the module adcman. For a typical ADC calculation, after the initialization at first to load the geometry, generate the atomic basis, manage the memory, etc. the modules scfman and adcman are called by the Q-Chem scheduler. After the ADC calculation is finished, the program is closed properly, which includes for example releasing the allocated memory or printing final statements in the output. For an FDE-ADC calculation, fdeman is called from the Q-Chem scheduler directly after the initialization and fdeman itself takes care of calling all necessary subtasks. After the FDE-ADC calculation is finished, fdeman passes over to the final routine of Q-Chem to close the program (Fig 4.5). In the flowcharts used within this chapter, the blue boxes

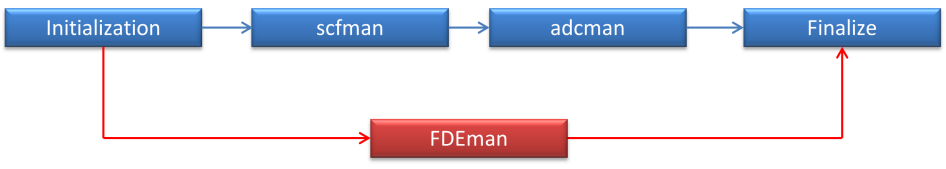

Figure 4.5: Flowchart of a ADC calculation vs. fdeman in Q-Chem.

indicate modules or functions from Q-Chem, while fdeman and its subroutines are indicated by red boxes.

fdeman is implemented mainly as one class. This facilitates the communication between all functions of fdeman by using class-global variables for specific information like the amount of basis functions in one of the fragments. When fdeman gets called from the Q-Chem scheduler Qinks the *FDE* class is initialized.

Source Code 4.1: Snippet of the initialization of the FDE class.

```
1  class FDE{
2    private:
3      int GlobalNAts;
4      int *jAtomIndex;
5      int NFrag;
6      int fde_basis; // internal expansion definition
7      double  *jCartsGlobal;
8      double  **jjCartsFrag;
9      ⋮
10     void make_frag(int);
11     void make_basis(int);
12     void compute_density(int, int, int);
13     void compute_coulomb_potential(int);
14     void compute_nuclear_potential(int);
15     void compute_xct_potential(int);
16     ⋮
17   public:
18     FDE();
19     ~FDE();
20     void fde_control(int);
21 }
```

The constructor of the *FDE* class then sets up everything needed in fdeman. The geometries of both fragments are loaded, the coordinates and the atomic indices are stored in memory. This is done by the two member-functions make_frag and make_basis. From there on, each fragment can be initialized, i.e. loading the geometries and creating basis functions on this fragment at any point within fdeman. This is important since the fragments have to be changed several times during the whole process. During the construction, also the function to read in user-specific information is called. This will be discussed in Sec. 4.3.1. After the construction is completed fde_control, the main routine in fdeman, is called. A flowchart of the initialization of fdeman is shown in Fig. 4.6. Data like density matrices or potentials are generally stored on disk so they can easily be accessed by both functions of fdeman and other modules in Q-Chem if needed.

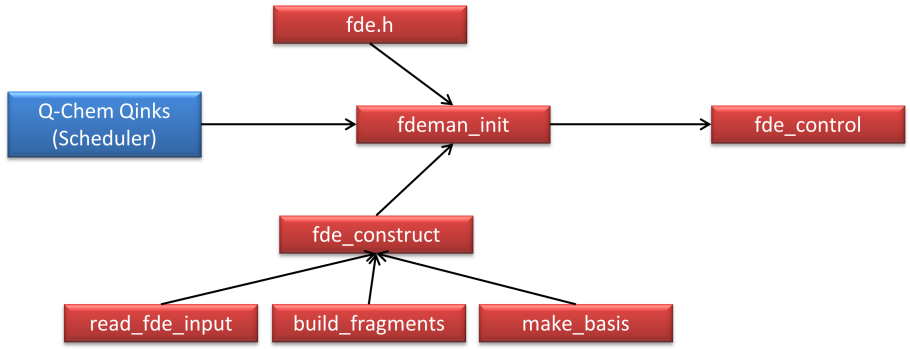

Figure 4.6: Flowchart of the initialization of `fdeman`. The constructor `fde_construct` handles the fragments, the creation of basis functions and the user input and calls the main routine `fde_control`.

In the main function of `fdeman`, called `fde_control`, the whole FDE-ADC calculation is orchestrated. It mainly distinguishes the work-flow for the applied expansion (SE or RADM). Based on this, one of the two instruction sets will be called. As can be seen from the flowchart diagram of the function `fde_control` in Fig. 4.7, the same routines are called for specific tasks independent of the chosen expansion. So, for example, the function `compute_density` is called for both the fragments A and B in both expansions. Three additional control variables are introduced in `fde_control` to pass on information to the subroutines and to call specific variants of these subroutines. The variable *level* controls the level of theory applied at that specific part. The second control variable is *curr_frag* which gives information whether fragment A or B should be loaded for calculation. The variable *fde_basis* controls the internally applied expansion i.e. applying the supermolecular basis or not. I would like to illustrate and explain this in an example which is also shown as a C++ code snippet in Code 4.2. The expansion RADM has been chosen. At first, $\rho_A(\vec{r})$ in the basis of A and B on HF level of theory should be calculated. Therefore, the variable *fde_basis* is set to supermolecular basis, *curr_frag* is set to 0, which corresponds to fragment A, and *level* is HF. Then, the routine `compute_density` is called with the parameters for fragment, expansion and level. This routine will be described in detail in Sec. 4.2.2. Once the calculation is finished, the MP(2) density matrix of A in the basis of A only will be calculated for the construction of the reassembled density matrix. Hence, *fde_basis* is set to monomer basis and *level* is set to ADC. Since later in the final FDE-ADC calculation excited states shall be calculated using `adcman` but now only a ground state MP(2) calculation using also `adcman` shall be performed, the

user-specific settings for ADC like the amount of excited states, is backed up and now `adcman` is called with different parameters requesting an MP(2) calculation only. Again, the function `compute_density` is responsible for the calculation of the MP(2) density matrix. Now, both density matrices are available to build the reassembled density matrix, which is done by the function `build_radm`. Fragment A has now been initialized in the supermolecular basis done by using the functions `make_frag`, `make_shells`, `make_basis` and `make_ghosts`.

Now we turn to fragment B. The variables *fde_basis*, *level* and *curr_frag* are set to supermolecular basis, HF and 1 for fragment B, respectively. The variable *expansion* has to be set temporarily to SE, since no reassembled density matrix shall be calculated for fragment B. Again, the function `compute_density` handles the calculation of $\rho_B(\vec{r})$. Now, everything is available for the calculation of the embedding potential. This is done in three steps. The nuclear attraction potential is calculated by the function `compute_nuclear_potential`, while the electronic Coulomb repulsion is calculated by `compute_coulomb_potential`. The non-

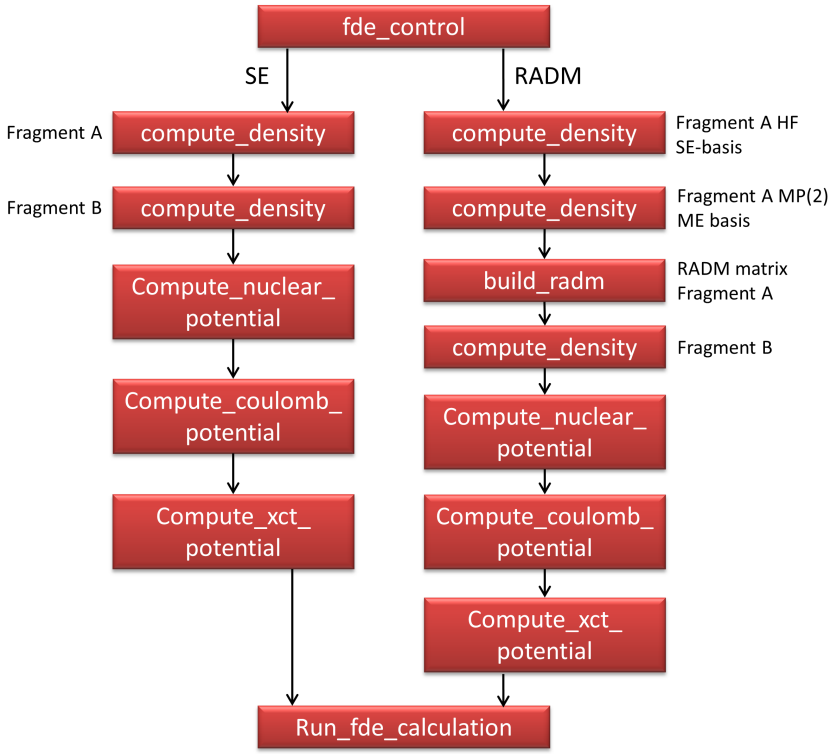

Figure 4.7: Flowchart of the main control unit `fde_control` of `fdeman` with the most important functions.

classical non-additive exchange-correlation energy and kinetic energy potential is calculated by calling the function `compute_xct_potential`. These functions will be explained in Sec. 4.2.3.

Source Code 4.2: Snippet of the function `fde_control` for an RADM-FDE-ADC calculation. For further details, see text.

```
1  void FDE::fde_control(int expansion){
2    int level;
3    int curr_frag;
4    switch (expansion){
5      case FDE_RADM:{
6        // Density for fragment A
7        fde_basis = SUPERMOL_BASIS;
8        level = LEVEL_HF;
9        curr_frag = 0;
10       compute_density(curr_frag, level, expansion);
11       fde_basis = MONOMER_BASIS;
12       curr_frag = 0;
13       level = LEVEL_ADC;
14       mod_adc_params();
15       compute_density(curr_frag, level, expansion);
16       build_radm(curr_frag);
17       //reset A to SE basis. Needed for calc of emb.
18       fde_basis = SUPERMOL_BASIS;
19       curr_frag = 0;
20       make_frag(curr_frag);
21       make_shells();
22       make_basis(curr_frag);
23       make_ghosts(curr_frag);
24       // Density for fragment B
25       fde_basis = SUPERMOL_BASIS;
26       level = rhoB_level;  // read in level for B
27       curr_frag = 1;
28       expansion = FDE_SE;
29       compute_density(curr_frag, level, expansion);
30       //calculate the potentials
31       curr_frag = 1;
32       compute_nuclear_potential(curr_frag);
33       compute_coulomb_potential(curr_frag);
34       curr_frag = 0;
35       compute_xct_potential(curr_frag);
36       //Configure for main Task
37       expansion = FDE_RADM;
38       fde_basis = MONOMER_BASIS;
39       run_fde_calculation(expansion); // pass on to main
             calculation
40       break;
41     }
42   }
43 }
```

After the embedding potential is calculated, `fde_control` sets up the actual FDE-ADC calculation. The variable *expansion* is set back to RADM and *fde_basis* is set to monomer basis as the FDE-ADC calculation in RADM is performed on A in the basis of A only. Finally, the function `run_fde_calculation` performs the FDE-ADC calculation, which includes adding the embedding potential to the Fock matrix during the SCF. This is also explained in more detail in Sec. 4.2.3.

After `fde_control` is finished, `fdeman` is closed, the class FDE is destructed and `Q-Chem` is finished.

4.2.2 Obtaining the isolated densities

The function `compute_density` is responsible for obtaining all one-particle electron density matrices needed for the construction of the embedding potentials. It takes the parameters *expansion*, *level* and *curr_frag* to specifiy which density is requested. Once specified, `compute_density` calls the specific module in `Q-Chem` with the respective parameters or presets to perform the calculation of the requested density, e.g. `scfman` for an HF density matrix or `scfman` followed by `adcman` for a MP(2) density matrix. This process is illustrated in the flowchart in Fig. 4.8. Additionally, the function `comp_frag_nuc_rep` calculates

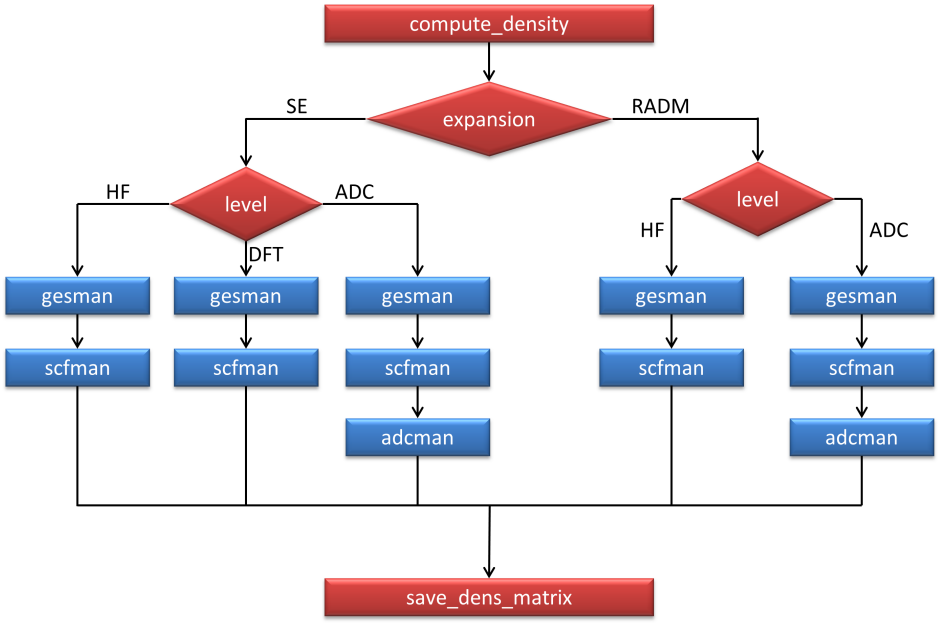

Figure 4.8: Flowchart of the function `compute_density` of `fdeman`. Functions are indicated by rectangles, diamonds represent decisions.

the constant nuclear repulsion before an electron density is calculated.

In SE, there are the three options HF, DFT and ADC based density. However, since in RADM a DFT-based density is not needed, this option is omitted. Note that, for the calculation of $\rho_B(\vec{r})$ in RADM, *expansion* is temporarily set to SE. A snipped of the C++ source code of the function `compute_density` is shown in Code 4.3. In the beginning of `compute_density`, the fragment is initialized by the functions `make_frag`, `make_shells`, `make_basis` and `make_ghosts`. After this, the nuclear repulsion is calculated as mentioned before. Then, the

Source Code 4.3: Snippet of the function `compute_density` for the case of supermolecular expansion. In the case of RADC, a similar block of code is executed.

```
1  make_frag(curr_frag);
2  make_shells();
3  make_basis(curr_frag);
4  if (fde_basis == SUPERMOL_BASIS){
5    make_ghosts(curr_frag);
6  }
7  frag_nuc_rep(curr_frag);
8  if (expansion == FDE_SE){
9    switch (level){
10     case LEVEL_HF:{
11       gesman_main();
12       scfman_main();
13       save_dens_mat(curr_frag);
14       break;
15     }
16     case LEVEL_DFT:{
17       gesman_main();
18       XCFunctional xcFuncSCF_B(X_Func_B, C_Func_B);
19       SCFman(XCFunctional(xcFuncSCF_B), ...);
20       save_dens_mat(curr_frag);
21       break;
22     }
23     case LEVEL_ADC:{
24       gesman_main();
25       scfman_main();
26       adcman_main();
27       save_dens_mat(curr_frag);
28       break;
29     }
30   }
31 }
32 else if (expansion == FDE_RADM){
33   ⋮
34 }
```

initial guess for the SCF is generated by calling `gesman`. After this, `scfman` can perform an HF or DFT calculation. After the SCF is converged, `adcman` is called to calculate the MP(2) density if needed.

For a DFT calculation, the `Q-Chem` class `XCFunctional` is initialized with the requested exchange- and correlation functionals *X_Func_B* and *C_Func_B*, which can be defined by the user (see Sec. 4.3.1). This is subsequently used as a parameter for `scfman`.

To obtain the MP(2) and ADC density matrices, new functions have been added to `adcman` to export the total and difference MP(2) density matrix and the total, difference, and transition ADC density matrix of excited states. While the former is needed directly for the construction of the embedding potential, the latter will be needed later after the FDE-ADC calculation. It is used to evaluate the total state-specific energy according to Eq. 2.254. The export of the density matrices out of `adcman` is realized with the class `prop_fde`, which includes several member functions. To obtain the references of the density matrices, the namespaces `adcman`, `libctx` and `libtensor` have to be used.[24,213] The module `libctx` is a context manager using keywords for data objects and `libtensor` is a tensor contraction library. The class `prop_fde` is called several times during a full MP and ADC calculation. Since it is able to export difference, transition and total density matrices, differentiation criteria are needed. Here, the presence of a density itself is the criterion. If a ground state density (here called *dm0...*) is available, the corresponding correlated density matrix corresponds to the difference density matrix, whereas it corresponds to a transition density matrix if no *dm0...* is present. This can be done since transition and difference density properties are calculated separately in `adcman`. A C++ source code snippet of this is shown in Code 4.4.

Source Code 4.4: Snippet of the function in `adcman` to obtain MP(2) and ADC density matrices. Part 1: requesting the data

```
1  void prop_fde::perform(libctx::context &octx)
2  {
3    bool has_dm0 = m_dmctx.key_exists("dm0_bb_a");
4    bool has_dm = m_dmctx.key_exists("dm_bb_a");
5    if (has_dm && has_dm0 == false) {
6      ctx_ref< btensor_i<2, double> > dm_bb_a(m_dmctx, "dm_bb_a");
7      ctx_ref< btensor_i<2, double> > dm_bb_b(m_dmctx, "dm_bb_b");
8      calc_transdensmat(dm_bb_a, dm_bb_b);
9    }
10   if (has_dm0 && has_dm) {
11     ctx_ref<double> ene(m_stctx, "energy");
12     ctx_ref< btensor_i<2, double> > dm_bb_a(m_dmctx, "dm_bb_a");
           //alpha diff density
13     ctx_ref< btensor_i<2, double> > dm_bb_b(m_dmctx, "dm_bb_b");
           //beta diff density
14     ctx_ref< btensor_i<2, double> > dm0_bb_a(m_dmctx, "dm0_bb_a");
            //ground-state alpha density
15     ctx_ref< btensor_i<2, double> > dm0_bb_b(m_dmctx, "dm0_bb_b");
            // ground-state beta density
16     calc_diffdensmat(dm_bb_a, dm_bb_b);
17     calc_densmat(dm_bb_a, dm_bb_b, dm0_bb_a, dm0_bb_b);
18     print_energy(m_name, ene);
19   }
20 }
```

The α and β density matrices are processed separately. The further conversion of the data, the calculation of the total density matrix and the export to files on disk for the usage in `fdeman` are done in the functions `calc_transdensmat`, `calc_diffdensmat` and `calc_densmat`. Since also the energies of all excited states are needed, they are exported by the function `print_energy` as well.

Fortunately, the further processing of the density matrices in `libtensor` is very straightforward using block tensors and the `libtensor` interface. For the calculation of the total density matrix, the ground state density matrix and the difference density matrix have to be added. Using `libtensor` this can be done in a single line of C++ code as shown in Code 4.5. As can be seen in line 9 of Code 4.5, the individual values μ and ν of both density matrices are added to build the total density matrix. The same holds for β in line 13.

Finally, the routine `convert_densmat` converts the data into a format usable for `fdeman` and exports it to disk.

Note that currently the algebraic expressions for the ISR in third order are not implemented. Therefore, the density matrices are obtained using the ADC vectors

Source Code 4.5: Snippet of the function in `adcman` to obtain MP(2) and ADC density matrices. Part 2: calculation of the the total density matrix

```
1  void prop_fde::calc_densmat(btensor_i<2, double> &dm_bb_a,
       btensor_i<2, double> &dm_bb_b, btensor_i<2, double> &dm0_bb_a,
        btensor_i<2, double> &dm0_bb_b)
2  {
3    string type = "Total";
4    const size_t tens_dims = 2;
5    btensor<tens_dims, double> tot_dm_bb_a(dm_bb_a.get_bis());
6    btensor<tens_dims, double> tot_dm_bb_b(dm_bb_b.get_bis());
7    {
8      letter mu, nu;
9      tot_dm_bb_a(mu|nu) = dm_bb_a(mu|nu) + dm0_bb_a(mu|nu);  //
           total alpha density matrix
10   }
11   {
12     letter mu, nu;
13     tot_dm_bb_b(mu|nu) = dm_bb_b(mu|nu) + dm0_bb_b(mu|nu);  //
           total beta density matrix
14   }
15   convert_densmat(m_name, type, tot_dm_bb_a, tot_dm_bb_b);
16 }
```

at third order with the ISR at second order. Hence, the embedding potential for FDE-ADC(3) is calculated using the MP(2) density for $\rho_A^{ref}(\vec{r})$.

4.2.3 Calculating the embedding potential and running an FDE-ADC calculation

From the previously calculated electron densities the embedding potential can be calculated. The embedding potential contains four individually calculated potentials: the nuclear attraction potential, the electron Coulomb repulsion potential, the exchange-correlation energy potential and the kinetic energy potential. The first two parts constitute the electrostatic part of the embedding potential while the latter two comprise the non-electrostatic part.

4.2.3.1 Calculation of the electrostatic parts

The nuclear attraction can straightforwardly be calculated using the atomic nuclear charge (i.e. the atomic number) and the corresponding Cartesian coordinates. The potential is expressed as a matrix in the basis of the atomic orbitals.

The electron repulsion potential of fragment B is calculated from the electron density matrix of B in atomic orbitals by integration using standard quantum

chemical integration techniques as described in the literature.[214–216] For the integration, the existing integral code `AOInts` of `Q-Chem` has been employed. Here it is crucial to maintain the correct basis, since the integration is not performed in function pairs, which is the standard for the elements of a density matrix or a potential, but instead in shell-pair functions. A shell is defined as functions sharing common exponents and centers. For example taking a Pople basis set (see Sec. 2.1.4.2) the four basis functions on the same atomic center sharing the same principle quantum number are considered a shell. In shell-pair functions, in contrast to normal function pairs where all possible combinations of functions are considered resulting in a dense matrix, only one of the two possible combinations of functions is built (which would lead to a triangular matrix), except for combinations with same principal and azimutal quantum numbers but different magnetic quantum number. This results in a nearly triangular matrix but contains square blocks on the diagonal. In the case of a single carbon atom calculated using the cc-pVDZ basis set, the following numbers occur:

- 6 basis shells: 3*s, 2*p and 1*d, namely 1s, 2s, 3s, 2p, 3p, 3d.
- 14 basis functions: 3*1 (s) + 2*3 (p) + 1*5 (d).
- 196 basis function pairs: all combinations of the 14*14 basis functions. This is the typical basis of a density matrix or a potential.
- 21 shell-pairs: 6 ss shell-pairs, 6 sp shell-pairs, 3 sd shell-pairs, 3 pp shell-pairs, 2 pd shell-pairs and 1 dd shell-pair.
- 121 shell-pair functions: 6*1 (ss) + 6*3 (sp) + 3*1*1*5 (sd) + 3*3*3 (pp) + 2*3*1*5 (pd) + 1*1*5*5 (dd).

The corresponding density matrix in shell-pair functions is shown in Fig. 4.9

Before creating the Coulomb embedding potential, the used density matrix has to be converted to the shell-pair function format. Since the generated potential is also in shell-pair functions, it has to be back-converted to the function pair format. However, it should be noted that both formats contain the same information and also the same numbers. Only some redundant combinations are omitted. Using shell-pairs in the SCF routine exhibits the big advantage that combinations of shells with very low overlap can be neglected. This can reduce the formal scaling of the integral calculations in the SCF procedure.

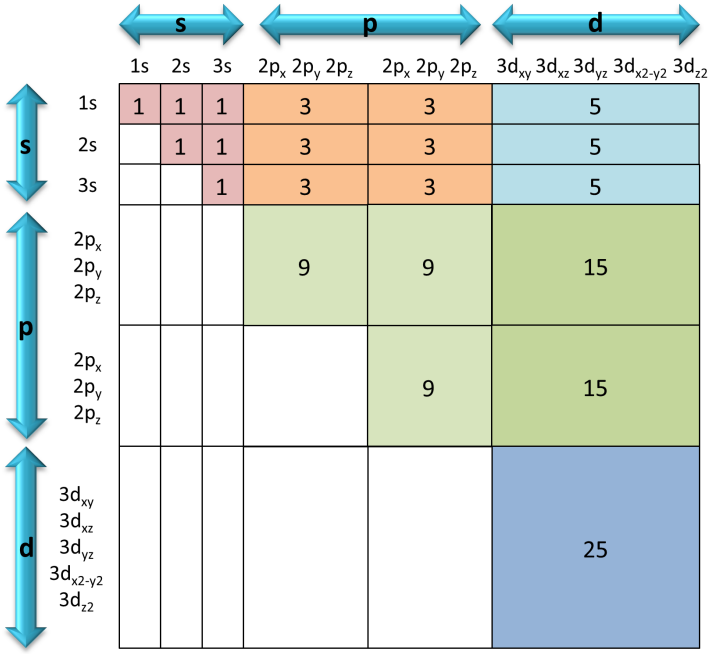

Figure 4.9: Illustration of a density matrix for one carbon atom in the basis cc-pVDZ in shell-pair functions. The numbers in the blocks indicate the amount of matrix elements in each block.

4.2.3.2 Calculation of the non-electrostatic parts

The two parts of the non-classical embedding potential, i.e. the exchange-correlation energy potential and the kinetic energy potential, are calculated separately. The function `compute_xct_potential` is responsible for the whole process, collecting the data and exporting the potentials. For the actual calculation, the sub-function `make_dft_potential` is employed, which is called from within `compute_xct_potential`. The expectation value as well as the derivative of the non-additive functionals are calculated using integration on a standard quadrature grid SG-1.[217] The parameter of the derivation with respect to which functional derivative is built is defined by the active fragment *curr_frag*. Whether the exchange-correlation or the kinetic energy potential is calculated is determined by the employed functional. A C++ source code snipped of the function `make_dft_potential` is shown in Code 4.6, which will be used to describe the calculation of the non-electrostatic embedding potential.

Source Code 4.6: Snippet of the function `make_dft_potential` within `compute_xct_potential` to calculate the non-classical parts of the embedding potential (both exchange-correlation and kinetic).

```
1  void FDE::make_dft_potential(double *Exc, double *pFxc, double*
       pDen_AB, double* pDen_A, double* pDen_B, XCFunctional& Func,
       int grdTyp){
2    ⋮
3    int jobID0 = 0;   // request exchange-correlation energy and
         matrix
4    XCAtoms xcatom;   // get atomic coordinate information
5    XCJobPara xcpara(Func, xcatom, jobID0);
6    XCBasisSet basDen(IBCode, nAtoms, thresh);
7    xcatom.setSize(basDen);
8    MoleGrid mgrid(xcatom, grdTyp, xcpara.nDrvNuc, thresh);   //
         setting up integration grid
9    XCOrderedMat denMat_AB(basDen, pDen_AB, xcpara.nDen, useMatrix,
         true);
10   denMat_AB.toXCMat();
11   XCOrderedMat denMat_A(basDen, pDen_A, xcpara.nDen, useMatrix,
         true);
12   denMat_A.toXCMat();
13   XCOrderedMat denMat_B(basDen, pDen_B, xcpara.nDen, useMatrix,
         true);
14   denMat_B.toXCMat();
15   XCOrderedMat fxcMat(basDen, pFxc, xcpara.nDen, useMatrix, true);
16   // finished set-up
17
18   #pragma omp parallel reduction(+:excTot,eleTot,totalgrid){
19     while ( true ) {
20       #pragma omp critical (XCCOUNTER){
21         ibat = GPI_DLB_next()-1;
22       }
23       if (ibat >= nBatch) break;
24
25       // initialize grid
26       BatchGrid grid(mgrid, ibat);
27       totalgrid+=grid.getNGrid();
28
29       // express significant shells and basis on the current grid
30       BatchShl  sigs1(grid, xcatom, basDen);
31       grid.updateDrv(sigs1);
32       BatchBas  bbas(basDen, xcpara, grid, xcatom, sigs1);
33
```

```
34        // compute variables such as density and density gradients
35        BatchVar  bvar_AB(xcpara, bbas, grid, sigs1, denMat_AB); //
              A+B
36        BatchVar  bvar_A(xcpara, bbas, grid, sigs1, denMat_A); // A
              only
37        BatchVar  bvar_B(xcpara, bbas, grid, sigs1, denMat_B); // B
              only
38        eleTot += bvar_AB.eleSum;
39
40        // compute functional values and update energy
41        BatchFnlX  bfnlX_AB(xcpara, grid, Func, bvar_AB); // A+B
42        BatchFnlX  bfnlX_A(xcpara, grid, Func, bvar_A);  // A only
43        BatchFnlX  bfnlX_B(xcpara, grid, Func, bvar_B);  // B only
44        excTot += bfnlX_AB.exSum + bfnlX_AB.ecSum;
45        excTot -= bfnlX_A.exSum + bfnlX_A.ecSum;
46        excTot -= bfnlX_B.exSum + bfnlX_B.ecSum;
47
48        //build difference of functional derivatives on the grid
49        VRsub(bfnlX_AB.pD1FX, bfnlX_AB.pD1FX, bfnlX_A.pD1FX, lenD1F)
              ;
50
51        // functional derivative: update xc matrix
52        BatchXCMat xcmatx(xcpara, grid, sigs1, bbas);
53        xcmatx.updateMat(fxcMat, bvar_AB, bfnlX_AB);
54      }
55    }
56    (*Exc)=excTot;
57    // convert back to normal format
58    fxcMat.toHFMat();
59    #ifdef PARALLEL
60    GlobalSum(Exc, 1, true);
61    GlobalSum(pFxc, nBas*nBas*xcpara.nDen, true);
62    GlobalSum(&eleTot, 1, true);
63    #endif
64    ⋮
65  }
```

The function `make_dft_potential` takes the density matrices of fragment A, fragment B and the sum of both density matrices representing the supersystem AB, the requested functional and the grid type as input parameters.

At first, the grid itself has to be initialized (Line 4 - 8). This is done by loading the atomic coordinates of both fragments (Line 4) and then specifying the type of calculation to perform on the grid (Line 5). In this case, the energy of an

exchange-correlation functional and the calculation of its derivative, represented as a matrix, shall be calculated. After gathering information about the basis set (Line 6) the integration grid can be built (Line 8). For the processing on the grid, the input density matrices have to be in a special ordered from. This is done in Lines 9 to 14 for the density matrices of fragment A, fragment B and the sum of both density matrices, referred to as AB. The later created potential will also be created using the special ordered format. Thus, its container, i.e. the data class is also created here (Line 15) and will be filled with the actual potential later.

At this point, the initial setup is complete. All calculations on the grid (Lines 18 - 55) are performed in parallel with OpenMP using batch processing. This is done until all integration points are finished. Therefore, the total grid is divided into sub-grids (Line 26) on which the significant shells (Line 30) and basis functions (Line 32) are initialized. Next, the important variables like densities and density-gradients on that specific sub-grid are calculated on Lines 35 to 37. The number of electrons of all sub-grids is added and has to resemble the total number of electrons for both systems (Line 38). The energy of the functional can now be evaluated. This is done for fragment A, fragment B and for the supersystem AB in Lines 41 to 43. The corresponding energy is calculated as the sum of all resulting energies (Lines 44 - 46). Finally, the potential is calculated as the functional derivative. Instead of subtracting the matrix elements of individually calculated potentials to form the non-additive potential according to Eq. 2.245, it is possible to build the difference of the functional derivative on the grid beforehand and calculate the potential by integration of the latter. This exhibits the advantage that only one integration has to be performed. It is referred to as *integration after subtraction* and is done in Line 49. The actual derivative is calculated in Line 52. In the end, all results of the parallel running sub-tasks have to be added to the final resuls (Line 59 - 63).

4.2.3.3 Applying the embedding potential

In the last step of the total process, the embedding potential is applied and the FDE-ADC calculation is performed. This is done by the function `run_fde_calculation`, which is called from the main control function `fde_control`. Based on the chosen expansion, fragment A is initialized either in the supermolecular basis for an SE-FDE-ADC calculation or in the monomer basis for an RADM-FDE-ADC run. This is accomplished by the already introduced functions `make_frag`, `make_shells` and `make_basis`. If the RADM expansion is requested, the

function `cut_potential` cuts the embedding potential, which was generated in SE, to the matrix elements of the AA block only. While in SE the ghost atoms are again initialized using `make_ghosts`, in RADM all remaining ghost definitions are removed by the function `make_ghost_buster`. After initialization, the previously backed up and then modified ADC parameters (see Sec. 4.2.1) are now restored and the nuclear repulsion is calculated. After this, the `Q-Chem` functions `gesman`, `scfman`, `adcman` and `anlman` are called to perform the FDE-ADC calculation. A flowchart of the function `run_fde_calculation` is shown in Fig. 4.10. As

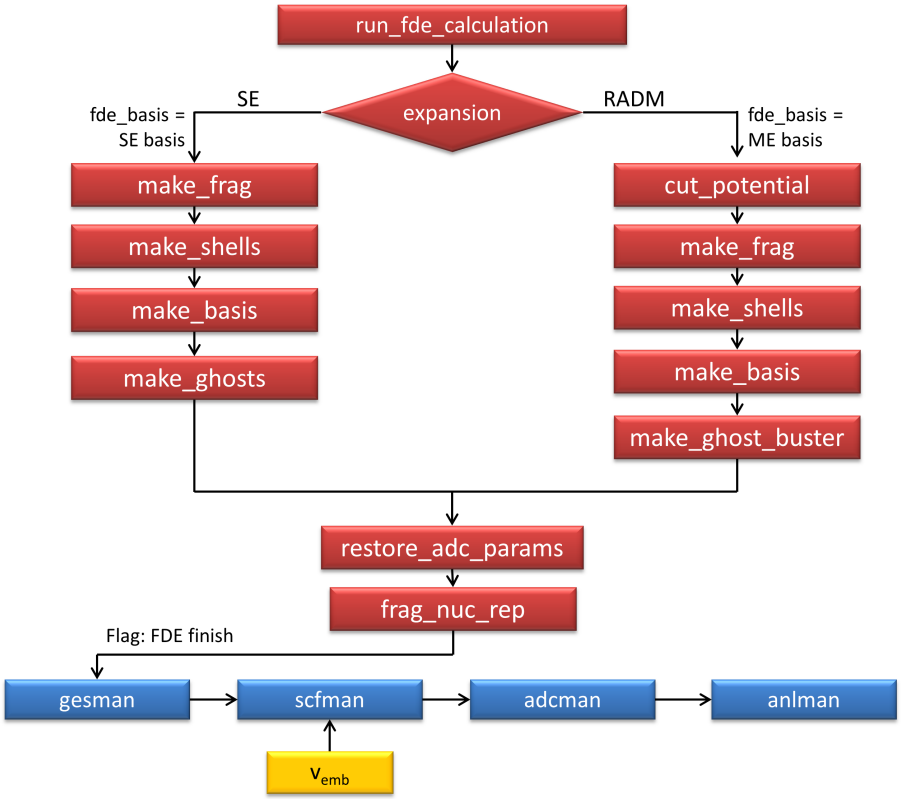

Figure 4.10: Flowchart of the function `run_fde_calculation` of `fdeman`. Functions are indicated by rectangles, diamonds represent decisions.

indicated in the flowchart, a flag is set which activates the import of the embedding potentials during the SCF cycle in `scfman`. Since the four parts of the embedding potential are kept separate, they are individually read in and added to the Fock matrix. This enables a direct evaluation of the interaction energies by contraction of one part of the embedding potential with the electron density of A in the current iteration of the SCF. This can be controlled by the print level (see Sec. 4.3). Also, the total interaction energy obviously has to be added to the total energy. This

process of contraction and addition of the embedding potential is shown in the C++ source code snippet 4.7. The generated orbitals and integrals intrinsically

Source Code 4.7: Snippet of the addition of the embedding potential to the Fock matrix and contraction with the electron density of fragment A.

```
1  if (ADC_FDE_finish) {
2    ⋮
3    //read potentials from file
4    ⋮
5    if (details >= 1){
6      if (details >= 2){
7        VRdot(&E_J,jPA,jJ,N2); //contraction of Coulomb part with
             density matrix
8        cout << " Integrated Coulomb potential: " << E_J << endl;
9        VRdot(&E_V,jPA,jV,N2); //contraction of nuclear part with
             density matrix
10       cout << " Integrated nuclear potential: " << E_V << endl;
11     }
12     VRadd(jv_elstat,jV,jJ,N2); //addition electrostatic parts
13     VRdot(&E_elstat,jPA,jv_elstat,N2);
14     cout << " Integrated electrostatic embedding potential: " <<
           E_elstat << endl;
15     if (details >= 2){
16       VRdot(&E_xc,jPA,jFxc,N2);
17       cout << " Integrated non-add. XC potential: " << E_xc <<
             endl;
18       VRdot(&E_ts,jPA,jFt,N2);
19       cout << " Integrated non-add. kinetic potential: " << E_ts
             << endl;
20     }
21     VRadd(jv_nonel,jFxc,jFt,N2); //addition non-electrostatic
         parts
22     VRdot(&E_nonel,jPA,jv_nonel,N2);
23     cout << " Integrated non-electrostatic embedding potential: "
           << E_nonel << endl;
24   }
25   VRadd(jv_tot,jv_tot,jFt,N2);
26   VRadd(jv_tot,jv_tot,jFxc,N2);
27   VRadd(jv_tot,jv_tot,jJ,N2);
28   VRadd(jv_tot,jv_tot,jV,N2);
29   VRdot(&E_embed,jPA,jv_tot,N2); //contraction of total embedding
       potential with density matrix
30   cout << " Integrated total embedding potential: " << E_embed <<
       endl;
31   ETot += E_embed;
32
33   VRadd(jFA,jv_tot,N2); //adding embedding potential to Fock-
       matrix
34 }
```

include the effect of the environment. They are used by the following `adcman` run, which thus leads to embedded excited states. After the ADC calculation, the routine `anlman` is called, which typically closes a `Q-Chem` run by calculating standard properties of the investigated system such as multipole moments or charge distributions.

4.3 Program control of FDE-ADC

Generally, Q-Chem is controlled using a so-called *input file*, which contains all information necessary for the requested calculation like method, basis set or additional requests like population analysis. It contains also the spatial coordinates of the molecule that shall be calculated. For an FDE-ADC calculation, various user-defined options are available. In this section, I will describe the user-defined options and their implementation.

4.3.1 User-defined input

In the Q-Chem input file the so-called *$rem* section contains all the keywords to control a quantum mechanical calculation. For example, the method and basis set is defined here using specific keywords. To request an FDE-ADC calculation, the new keyword *"FDE"* has been added. It is used as a Boolean data type, which means taht it accepts only the values *true* or *false*. Hence, an FDE-ADC calculation will be performed when *FDE = true* is set in the input file.

However, beyond this keyword for activation, fdeman needs further specifications. A separate input section in the input file named *$fde* has been introduced. This way, all FDE-related keywords can be specified without interfering with other keywords of the *$rem* section. Additionally, it is much more convenient for the user to specify all parameters in one block. The parameters can be divided into mandatory parameters and optional parameters. While the mandatory parameters will be discussed here, most of the optional parameters will be introduced in Chapter 7. The important parameters are:

- Specification of the expansion: Using the keyword *expansion*, one of the two available expansions SE or RADM can be selected.

- Specification of the exchange-correlation functional for the calculation of the corresponding part of the potential. Here, all available pure DFT functionals of Q-Chem can be employed. Since in Q-Chem both so-called *canned* xc-functionals, which consist of an inseparable combination of exchange and correlation functionals, and individual exchange and correlation functionals are included, the former one can be selected with the keyword *XC_Func* while the latter ones are specified with the two keywords *X_Func* and *C_Func*.

- Specification of the kinetic energy functional for the calculation of the second non-electrostatic part of the embedding potential. This is selected with

the keyword *T_Func*. Although in principle all kinetic energy functionals in Q-Chem can be employed, however, the only included kinetic energy functional currently is the Thomas-Fermi functional.

- Specification of the method used to calculate $\rho_B(\vec{r})$. This is controlled by the keyword *rhoB_method*. It takes as arguments either HF or DFT. If a DFT calculation for the environment is requested, additionally the keywords *XC_Func_B* for canned xc-functionals or *X_Func_B* and *C_Func_B* for individual functionals have to be specified. Note that the functional used to calculate $\rho_B(\vec{r})$ does not need to correspond to the employed xc-functional in the calculation of the embedding potential.

- Specification of the print level of `fdeman`. This is an optional parameter. It controls the level of output in three stages. At level 0, only minimal information is printed. Level 1 represents the standard output level with the most usefull information. At the extended output level 2, all additional information, which might be useful during an FDE-ADC run, are printed. Level 3 is identical to level 2 but additionally prints text files of important matrices like density matrices or the parts of the embedding potential. These can be used for visualization after the calculation.

All these parameters are gathered by the `fdeman` function `read_fde_input`.

4.3.2 Verification of input parameters

The user-defined input is checked in `fdeman` directly after initialization to verify that all parameters are set correctly. The first level of input check is to control if all mandatory parameters for `fdeman` are set in the *$fde* input section. This is done by a checklist. `fdeman` will only proceed if all points on this checklist are marked positive. If anything is missing, the program will stop and tell the user which parameter is missing. To avoid unintentional calculations using wrong methods, no defaults are set. The user has to specify the aforementioned parameters.

The second check level is to verify that no contradicting parameters have been set. For example, requesting an HF calculation for the generation of $\rho_B(\vec{r})$ and specifying an xc-functional for the environment calculation will lead to an abort of the program. Additionally, it will ask the user to choose either a functional or the method HF. Since currently `fdeman` is implemented only to perform FDE-ADC calculations, a similar check prevents activating FDE in combination with a non-ADC method.

The third check controls if the requested xc- and t-functionals are appropriate. For the calculation of $\rho_B(\vec{r})$ both pure and hybrid xc-functionals can be employed, while for the calculation of the embedding potential only pure xc-functionals are allowed. However, no meta-GGA functionals can be used due to the included kinetic energy correction (see Sec. 2.2.5).

After all checks are passed successfully, the user-defined input is printed in a summary in the output file. This ensures the correct processing of the user input.

4.4 Summary and overview of features of FDE-ADC

In this chapter, I describe the development of FDE-ADC and its implementation in the module `fdeman` in the quantum chemical program package `Q-Chem`. In an FDE-ADC calculation, the embedded system (A) is calculated on the ADC level of theory while the environment (B) is calculated on the HF or DFT level of theory. The two subsystems have to be clearly separated, i.e. may not be connected by a covalent bond. An FDE-ADC calculation can be carried out in two ways, referred to as expansions. In the *supermolecular expansion*, all density matrices and the embedding potential are expressed in the basis of A and B together. However, this variant is only useful for benchmark calculations, since it provides no computational savings compared to a supermolecular ADC calculation. In the second variant, *re-assembling of density matrix*, an approximation is introduced reducing the embedding potential to the basis of A only. This allows productive calculations, since the subsequent FDE-ADC calculation is performed in the basis of the embedded system.

In the implementation of FDE-ADC, the module `fdeman` organizes all required parts of the full run. It is called directly by the `Q-Chem` scheduler. It generates the electron densities $\rho_A^{ref}(\vec{r})$ and $\rho_B(\vec{r})$, calculates the embedding potential and performs the FDE-ADC calculation by adding the potential to the Fock matrix during the SCF, which also directly influences the ADC calculation.

`fdeman` can easily be controlled by the user via the separate *$fde* section in the `Q-Chem` input file. For the calculation of the environment density, either HF or DFT in combination with all available pure and global-hybrid xc-functionals of `Q-Chem` can be used. Also all available pure xc-functionals can be employed to calculate the non-electrostatic part of the embedding potential.

FDE-ADC is available for all variants of ADC[24,108] and core-valence separated ADC (CVS-ADC) up to third order.[218–221] Using this approach, it is also possible to employ other features of ADC, e.g. the wavefunction and density analysis utility `libwfa`,[114,115,222] or the calculation of spin-orbit coupling elements,[223] which are also implemented in `Q-Chem`. With these tools, the direct influence of an environment on the excitations of the embedded system can be visualized via difference and transition density analysis, attachment and detachment density plots or generation of excited state natural orbitals.[115,221] This will be demonstrated in Chapter 6.

Chapter 5

Benchmarking FDE-ADC up to Third Order

"What we observe is not nature itself, but nature exposed to our method of questioning."
Werner Heisenberg

In this chapter, I will present a thorough testing of the combination of frozen density embedding (FDE) with the algebraic-diagrammatic construction scheme for the polarization propagator (ADC) up to third order, yielding the method FDE-ADC. For these tests, supermolecular calculations of test systems consisting of an embedded species and an environment are calculated as reference. To determine the influence of the environment, the core systems are calculated alone as well. FDE-ADC calculations are then benchmarked against the supermolecular results. In the benchmark, the excitation energies (Ω), oscillator strengths and excitation characters determined by the orbital transitions are analyzed. The accuracy is determined as the energy or oscillator strength difference between FDE-ADC and supermolecular ADC results of states exhibiting the same character. If changes in the energetic order occur, they are mentioned explicitly.

Note that in all benchmark calculations, the supersystem calculation is always taken as reference for both isolated and FDE-ADC results. Hence, solvatochromic shifts and deviations of FDE-ADC from the supersystem results are calculated as $\Omega_{isol} - \Omega_{sup}$ and $\Omega_{FDE-ADC} - \Omega_{sup}$, respectively. As a consequence, a negative value indicates a larger excitation energy in the supersystem (blue shift). The same holds for oscillator strengths.

At first, FDE-ADC(2) using supermolecular expansion is tested followed by FDE-ADC(2) employing the RADM approach. The basis set dependence is tested next followed by an investigation of the influence of the method used to calculate $\rho_B(\vec{r})$ and the influence of the employed xc-functional used in the calculation of the embedding potential. Subsequently, a benchmark of RADM-FDE-ADC(3) is performed. The chapter ends with a summary and conclusion of the benchmark results.[1]

[1] Parts of Chapter 5 have already been published in
First time combination of frozen density embedding theory with the algebraic diagrammatic construction scheme for the polarization propagator of second order
Stefan Prager, Alexander Zech, Francesco Aquilante, Andreas Dreuw and Tomasz A. Wesolowski
The Journal of Chemical Physics, 144 (2016,) page 204103
and
Implementation and application of the frozen density embedding theory with the algebraic diagrammatic construction scheme for the polarization propagator up to third order
Stefan Prager, Alexander Zech, Tomasz A. Wesolowski and Andreas Dreuw
submitted for publication, (2017)

5.1 The benchmark systems

For this benchmark, three representative model systems were created. All three benchmark systems are shown in Fig. 5.1. The first model system consists of a benzene molecule as system A and a hydrogen fluoride (HF) molecule placed side-on and in-plane with the benzene ring as the environment (B) ([BZ · HF]). For the second model system, a benzaldehyde molecule was used as embedded system and two water molecules forming a dimer and building a hydrogen bond to the oxygen atom of the benzaldehyde as the environment ([BA · 2 H_2O]). Because of the hydrogen bond within the water dimer, the strength of the hydrogen bond from the water dimer to benzaldehyde is increased. The last model system consists of a uracil molecule for A and five water molecules as B ([UC · 5 H_2O]). Uracil was chosen as a test system because it has an aromatic π-system and in addition two hydrogen bond donors (B and D in Fig. 5.1 and two oxygen atoms as hydrogen bond acceptors (A and C), thus providing a large variety of environment interactions. The water molecules exhibit various hydrogen bonds both among themselves and to the uracil molecule. This set of systems accounts for various interaction strengths

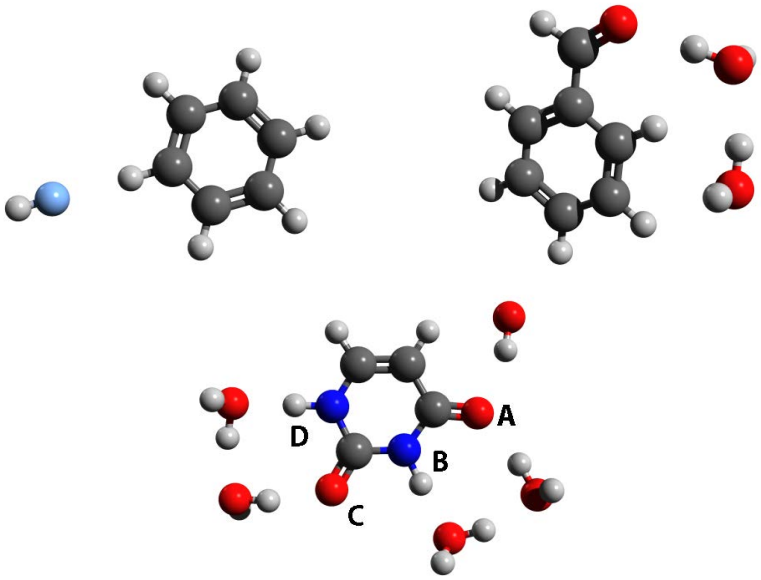

Figure 5.1: Molecular structures of the three test systems: benzene with a hydrogen fluoride molecule ([BZ · HF]) (top left), benzaldehyde with two water molecules ([BA · 2 H_2O]) (top right) and uracil with five water molecules ([UC · 5 H_2O]) (bottom).

between embedded system and environment as well as different kinds of excited states. While the first system (benzene and HF) shows only weak and polarization based interactions, the benzaldehyde is more influenced by the environment due to the hydrogen bond in addition to the polarization of the π-system. The uracil system shows intense interactions between the core system and the environment including various hydrogen bonds.

For all investigations, the three supersystem are optimized at the MP(2)/cc-pVDZ level of theory. This ensures that no geometrical changes influence the comparison between the FDE approach and the supersystem calculation.

5.2 Benchmark of FDE-ADC(2) using supmermolecular expansion

In this section, the method FDE-ADC of second order, FDE-ADC(2), is benchmarked. In the first test, FDE-ADC(2) employing the supermolecular expansion was tested. This approach is the mathematically exact implementation of FDE-ADC without any further approximation and without restrictions to the basis set. Although no benefit in computational cost with respect to the supersystem calculation can be achieved, this serves as a benchmark for further approximate FDE-ADC approaches.

The five energetically lowest electronically excited singlet states of the supersystems are calculated at ADC(2)/cc-pVDZ level of theory. Additionally, the five energetically lowest excited singlet states of the isolated system A have been calculated at ADC(2)/cc-pVDZ level of theory without re-optimizing the geometry. In this way, the electronic interactions between core system and environment can be analyzed directly without influences of geometry changes due to environment interactions. The FDE-ADC(2) calculations were carried out using the same optimized geometries for system A and B as in the supersystem calculation. For all investigations, the singlet multiplicity and neutral charge was conserved. The HF method was chosen for the calculation of the environment density $\rho_B(\vec{r})$ and the PBE xc-functional for the non-electrostatic part of the embedding potential.

5.2.1 Benzene with one hydrogen fluoride molecule

At first, the system [BZ · HF] was tested. The frontier orbitals of benzene, i.e. the highest occupied molecular orbital (HOMO), HOMO−1, the lowest unoccupied molecular orbital (LUMO) and LUMO+1 are the typical π orbitals. The lower lying occupied orbitals (HOMO−2 and HOMO−3) show σ-character while the higher unoccupied orbitals (LUMO+2 and LUMO+3) can be described as Rydberg-orbitals. The analysis of the five lowest electronically excited states of isolated benzene shows four locally excited states characterized by ($\pi \mapsto \pi^*$) transitions and an energetically higher lying Rydberg state. The five lowest excited states and their character are given in Tab. 5.1.

Calculating the supersystem, the frontier orbitals of benzene are almost identical to the frontier orbitals of the isolated benzene and only slightly distorted by the hydrogen fluoride. Only the LUMO+2, which is a Rydberg orbital in the case of the isolated benzene, is now localized on the hydrogen fluoride and the original

Table 5.1: Excitation energies, oscillator strengths and orbital transitions (> 5 %) for the five energetically lowest electronically excited singlet states of isolated benzene, the supersystem and the SE-FDE-ADC(2) calculations of [BZ · HF].

	Excitation Energies [eV]			Oscillator Strengths			Orb. Trans.	Weight [%]		
state	isol.	supersys.	FDE-ADC	isol.	supersys.	FDE-ADC	H+x ↦ L+y[a]	isol.	supersys.	FDE-ADC
S_1	5.287	5.323	5.328	0.0000	0.0001	0.0001	$0 \mapsto 0$ ($\pi \mapsto \pi^*$)	8.3	45.2	45.1
							$0 \mapsto 1$ ($\pi \mapsto \pi^*$)	36.6	-	-
							$-1 \mapsto 0$ ($\pi \mapsto \pi^*$)	36.6	-	-
							$-1 \mapsto 1$ ($\pi \mapsto \pi^*$)	8.2	43.6	43.5
S_2	6.677	6.692	6.704	0.0000	0.0000	0.0000	$0 \mapsto 0$ ($\pi \mapsto \pi^*$)	37.9	-	-
							$0 \mapsto 1$ ($\pi \mapsto \pi^*$)	8.5	45.0	45.6
							$-1 \mapsto 0$ ($\pi \mapsto \pi^*$)	8.2	46.2	45.4
							$-1 \mapsto 1$ ($\pi \mapsto \pi^*$)	37.2	-	-
S_3	7.520	7.500	7.530	0.7155	0.6810	0.7000	$0 \mapsto 0$ ($\pi \mapsto \pi^*$)	18.3	-	-
							$0 \mapsto 1$ ($\pi \mapsto \pi^*$)	25.8	44.1	43.4
							$-1 \mapsto 0$ ($\pi \mapsto \pi^*$)	25.7	43.0	43.6
							$-1 \mapsto 1$ ($\pi \mapsto \pi^*$)	18.5	-	-
S_4	7.522	7.527	7.548	0.7162	0.6867	0.7057	$0 \mapsto 0$ ($\pi \mapsto \pi^*$)	25.5	42.6	42.6
							$0 \mapsto 1$ ($\pi \mapsto \pi^*$)	18.3	-	-
							$-1 \mapsto 0$ ($\pi \mapsto \pi^*$)	18.4	-	-
							$-1 \mapsto 1$ ($\pi \mapsto \pi^*$)	26.0	44.3	44.3
S_5	8.131	8.298	8.317	0.0000	0.0005	0.0003	$0 \mapsto 2$ ($\pi \mapsto R$)	90.2	-	-
							$-2 \mapsto 0$ ($\sigma \mapsto \pi^*$)	-	69.4	64.7[e]
							$-3 \mapsto 1$ ($\sigma \mapsto \pi^*$)	-	14.3	18.3[e]

[a] H = HOMO, L = LUMO, R = Rydberg-type orbital
[b] Occurs as S_6 in the original FDE-ADC(2) calculation.

Rydberg orbital located at the benzene is the LUMO+3. The S_1 to S_4 states are characterized as local ($\pi \mapsto \pi^*$) transitions on the benzene while the S_5 state is a mixed Rydberg state delocalized over benzene and hydrogen fluoride.

In the FDE-ADC calculation, a higher lying virtual Rydberg orbital is lowered inenergy and becomes the LUMO, but this orbital does not contribute to any local ($\pi \mapsto \pi^*$) transition. Since the energy of the higher lying unoccupied orbitals (LUMO+1 to LUMO+10) are practically identical to the supersystem calculation, the character of the excited states remains the same even if the number of the electron accepting orbital is increased by 1. The excited states S_3 and S_4 are, like in the supersystem calculation, degenerate. The excited states of the supersystem and the isolated benzene as well as the FDE-ADC calculations are characterized in detail in Tab. 5.1.

The influence of the hydrogen fluoride molecule onto the benzene while it is located in-plane with the benzene-ring is reproduced almost exactly by the FDE-ADC(2) calculations. The largest deviation in the excitation energies is lower than 0.02 eV for the Rydberg state and lower than 0.005 eV for the ($\pi \mapsto \pi^*$) transitions. The mean absolute error (MAE) averaged over all calculated excited states is 0.004 eV for excitation energies and 0.0039 for oscillator strengths. The differences in the excitation energies and oscillator strengths between isolated benzene and the FDE-ADC(2) calculation to the supersystem calculation are shown in Fig. 5.2.

5.2.2 Benzaldehyde with two water molecules

The [BA $\cdot$ 2 H_2O] system was tested next. The frontier orbitals of isolated benzaldehyde optimized as supersystem are characterized as follows: HOMO$-$3: π, HOMO$-$2: n, HOMO$-$1: π, HOMO: π, LUMO: π^*, LUMO+1: π^*, LUMO+2: Rydberg, LUMO+3: Rydberg, LUMO+4: π^*. Analysis of the five energetically lowest electronically excited states shows two states with ($n \mapsto \pi^*$) character (S_1 and S_4) and three ($\pi \mapsto \pi^*$) transitions. A detailed characterization is given in Tab. 5.2.

Going to the supersystem, the frontier orbitals are hardly changed but the HOMO and HOMO$-$1 change their energetic order. Since these two orbitals are almost degenerate it can be neglected from an energetic point of view. However, this change has to be considered in the characterization of the excited states. In contrast, the excited states are influenced significantly by the water environment. As expected, the hydrogen-bonded water molecule stabilizes the n-orbitals leading

Table 5.2: Excitation energies, oscillator strengths and orbital transitions (> 5 %) for the five energetically lowest electronically excited singlet states of isolated benzaldehyde, the supersystem and the SE-FDE-ADC(2) calculations of [BA · 2 H_2O].

	Excitation Energies [eV]			Oscillator Strengths			Orb. Trans.	Weight [%]		
state	isol.	supersys.	FDE-ADC	isol.	supersys.	FDE-ADC	H+x ↦ L+y[a]	isol.	supersys.	FDE-ADC
S_1	3.692	3.897	3.891	0.0001	0.0001	0.0001	-2 ↦ 0 ($n \mapsto \pi^*$)	73.9	74.3	73.9
							-2 ↦ 4 ($n \mapsto \pi^*$)	13.2	9.1	-
							-2 ↦ 5 ($n \mapsto R$)	-	-	6.9
S_2	4.933	4.813	4.837	0.0104	0.0197	0.0174	0 ↦ 0 ($\pi \mapsto \pi^*$)	18.5	61.9	59.1
							0 ↦ 1 ($\pi \mapsto \pi^*$)	20.5	-	-
							-1 ↦ 0 ($\pi \mapsto \pi^*$)	41.0	4.3	6.0
							-1 ↦ 1 ($\pi \mapsto \pi^*$)	46.1	19.8	19.1
S_3	5.771	5.554	5.595	0.3258	0.3444	0.3519	0 ↦ 0 ($\pi \mapsto \pi^*$)	60.9	7.3	9.8
							-1 ↦ 0 ($\pi \mapsto \pi^*$)	43.2	76.1	73.5
S_4	6.272	6.751	6.742	0.0000	0.0059	0.0001	-2 ↦ 1 ($n \mapsto \pi^*$)	83.6	82.1	81.4
S_5	6.884	6.753	6.784	0.3684	0.2942	0.2908	0 ↦ 0 ($\pi \mapsto \pi^*$)	5.3	17.7	18.4
							0 ↦ 1 ($\pi \mapsto \pi^*$)	41.9	5.6	7.1
							-1 ↦ 0 ($\pi \mapsto \pi^*$)	23.5	-	-
							-1 ↦ 1 ($\pi \mapsto \pi^*$)	12.4	50.3	47.7
							0 ↦ 4 ($\pi \mapsto \pi^*$)	-	6.0	-

[a] H = HOMO, L = LUMO, R = Rydberg-type orbital

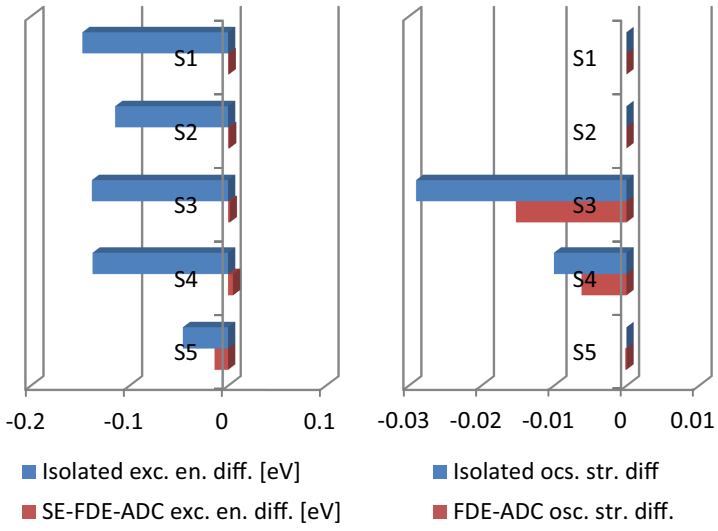

Figure 5.2: Excitation energy difference (left) and oscillator strength difference (right) of the isolated benzene (blue) to the supersystem [BZ · HF] and the FDE-ADC(2) calculation (red) to the supersystem. The blue bars correspond to the influence of the environment on the excitation energies and oscillator strengths (solvatochromic shift) while the red bars indicate the accuracy of the FDE-ADC(2) calculation in comparison with the ADC(2) calculation of the full system.

to a large increase of the excitation energies of the corresponding ($n \mapsto \pi^*$) states. Simultaneously, the excitation energies of the ($\pi \mapsto \pi^*$) states are reduced. However, the energetic order and the character of the states are not changed by the environment (Tab. 5.2).

In the FDE-ADC(2) calculation, the interactions of the hydrogen bonds are simulated almost quantitatively. The degeneracy of the HOMO and HOMO-1 is retained and also the n-orbitals are correctly described. The excited states in the FDE-ADC(2) calculation show the same influence of the environment on the ($n \mapsto \pi^*$) as well as on the ($\pi \mapsto \pi^*$) states as seen in the supersystem calculation. The full characterization is given in Tab. 5.2.

In this example, the largest deviation in the excitation energies is lower than 0.01 eV for the ($n \mapsto \pi^*$) states and lower than 0.05 eV for the ($\pi \mapsto \pi^*$) transitions. The MAE is 0.022 eV for excitation energies and 0.0033 for oscillator strengths. Especially the reproduction of the influence of the hydrogen bonds on the excited states is remarkable, since hydrogen bonds have larger orbital interactions compared to dispersion interaction or polarization. The difference in excitation energies and oscillator strengths of the isolated benzaldehyde and

the FDE-ADC(2) calculation to the supersystem calculation are summarized in Fig. 5.3.

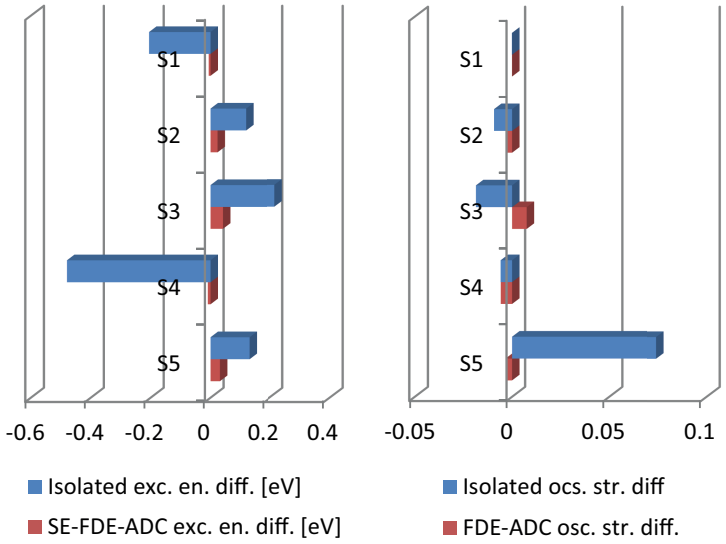

Figure 5.3: Excitation energy difference (left) and oscillator strength difference (right) of the isolated benzene (blue) to the supersystem [BA · 2 H_2O] and the FDE-ADC(2) calculation (red) to the supersystem. The blue bars correspond to the influence of the environment on the excitation energies and oscillator strengths (solvatochromic shift) while the red bars indicate the accuracy of the FDE-ADC(2) calculation in comparison with the ADC(2) calculation of the full system.

5.2.3 Uracil with five water molecules

The frontier orbitals of uracil, optimized in the supersystem, show π character for the HOMO−1 and HOMO, while the HOMO−2 and HOMO−3 are n-orbitals localized mainly at the oxygen atom O_A and O_C, respectively. The LUMO and LUMO+2 exhibit π^* character, whereas the LUMO+1 is a Rydberg orbital. Analyzing the five lowest electronically excited states of the isolated uracil, optimized in the supersystem structure, ($n \mapsto \pi^*$) transitions are observed as the S_1, S_3 and S_5 states. The S_2 and S_4 states are local ($\pi \mapsto \pi^*$) transitions. The detailed characterization of the five lowest excited states is given in Tab. 5.3.

In the supersystem structure, the water molecules interact strongly with the uracil by forming hydrogen bonds. Two water molecules act as hydrogen bond donors for the O_A, one as an acceptor for N_B, forming a hydrogen bond chain over one of the previously mentioned water molecules to O_A. Another hydrogen

Table 5.3: Excitation energies, oscillator strengths and orbital transitions (> 5 %) for the five energetically lowest electronically excited singlet states of isolated benzaldehyde, the supersystem and the SE-FDE-ADC(2) calculations of [UC · 5 H_2O].

	Excitation Energies [eV]			Oscillator Strengths			Orb. Trans.	Weight [%]		
state	isol.	supersys.	FDE-ADC	isol.	supersys.	FDE-ADC	H+x $\mapsto$ L+y[a]	isol.	supersys.	FDE-ADC
S_1	4.440	5.143	5.108	0.0001	0.0016	0.0007	-2 $\mapsto$ 0 ($n \mapsto \pi^*$)	77.2	72.2	72.9
							-3 $\mapsto$ 0 ($n \mapsto \pi^*$)	-	-	5.8
							-4 $\mapsto$ 0 ($n \mapsto \pi^*$)	-	4.6	-
S_2	5.439	5.215	5.291	0.2261	0.2371	0.2162	0 $\mapsto$ 0 ($\pi \mapsto \pi^*$)	81.3	80.7	80.1
S_3	5.866	6.211	6.221	0.0000	0.0001	0.0002	-2 $\mapsto$ 0 ($n \mapsto \pi^*$)	4.6	-	5.8
							-2 $\mapsto$ 1 ($n \mapsto \pi^*$)	35.7[b]	20.0	-
							-3 $\mapsto$ 0 ($n \mapsto \pi^*$)	28.3	17.4	31.0
							-3 $\mapsto$ 1 ($n \mapsto \pi^*$)	16.4[b]	10.8	-
							-4 $\mapsto$ 0 ($n \mapsto \pi^*$)	-	20.2	-
							-4 $\mapsto$ 1 ($n \mapsto \pi^*$)	-	5.6	-
							-2 $\mapsto$ 6 ($n \mapsto R$)	-	-	24.8
							-3 $\mapsto$ 6 ($n \mapsto R$)	-	-	13.6
S_4	6.194	6.292	6.320	0.0311	0.0963	0.0850	-1 $\mapsto$ 0 ($\pi \mapsto \pi^*$)	85.9	84.4	84.1
S_5	6.468	6.657	6.749	0.0001	0.0005	0.0021	-2 $\mapsto$ 1 ($n \mapsto \pi^*$)	38.0[b]	22.8	-
							-3 $\mapsto$ 0 ($n \mapsto \pi^*$)	44.6	15.3	45.9
							-3 $\mapsto$ 1 ($n \mapsto \pi^*$)	-	12.4	-
							-4 $\mapsto$ 0 ($n \mapsto \pi^*$)	-	20.4	-
							-4 $\mapsto$ 1 ($n \mapsto \pi^*$)	-	6.6	-
							-2 $\mapsto$ 6 ($n \mapsto R$)	-	-	19.1
							-3 $\mapsto$ 6 ($n \mapsto R$)	-	-	9.2

[a] H = HOMO, L = LUMO, R = Rydberg-type orbital

[b] Orbital index for LUMO+1 and LUMO+2 interchanged

bond chain is formed from N_D over two water molecules to O_C. These hydrogen bonds will influence the n-orbitals and hence also the ($n \mapsto \pi^*$) excitations but will do so differently for each state since the interaction is more pronounced at the O_A than at the O_C atom. The rest of the frontier orbitals are qualitatively unchanged except for the LUMO+1 and LUMO+2, which change their energetic order. Analyzing the five lowest electronically excited states of the supersystem, the excitation energy of the S_1 state is, as expected, largely increased due to the stabilizing effects of the environment on the n-orbitals. Accordingly, the influence on the two other ($n \mapsto \pi^*$) transitions is weaker but still significant. However, some orbitals delocalized over uracil and one or more water molecules contribute only slightly to the excitation. A detailed description of the excited states is given in Tab. 5.3.

In the FDE-ADC calculations, the uracil was considered as system A while all 5 water molecules are used as the environment B. As in the supersystem calculation, the energetic order of the LUMO+1 and LUMO+2 is changed compared to the isolated uracil calculation. The remaining frontier orbitals are essentially identical to the orbitals of isolated uracil, but higher lying virtual orbitals are largely distorted accounting for the effect of the environment. The results of the FDE-ADC calculations are in very good agreement with the supersystem benchmark. The largest shift in excitation energy (S_1) and the largest shift in oscillator strength (S_4) are well reproduced. Also, the different influence of the hydrogen bonds on the excited states is included in the FDE-ADC(2) calculation. The characterization of the excited states is given in Tab. 5.3.

For this system, the largest error is 0.09 eV for the excitation energies and 0.02 for the oscillator strengths, which is slightly higher than in the previous systems. The MAE is 0.048 eV for excitation energies and 0.0059 for oscillator strengths. Still, considering the strong interaction between uracil and the water environment, this error is acceptable for this approximate treatment of the environment. The slightly larger error arises because some orbitals, localized on the water molecules of the environment, contribute slightly to the excitations in the supersystem but are not considered in the FDE-ADC calculation. Comparison of the FDE-ADC calculation and the isolated uracil calculation to the supersystem is presented in Fig. 5.4.

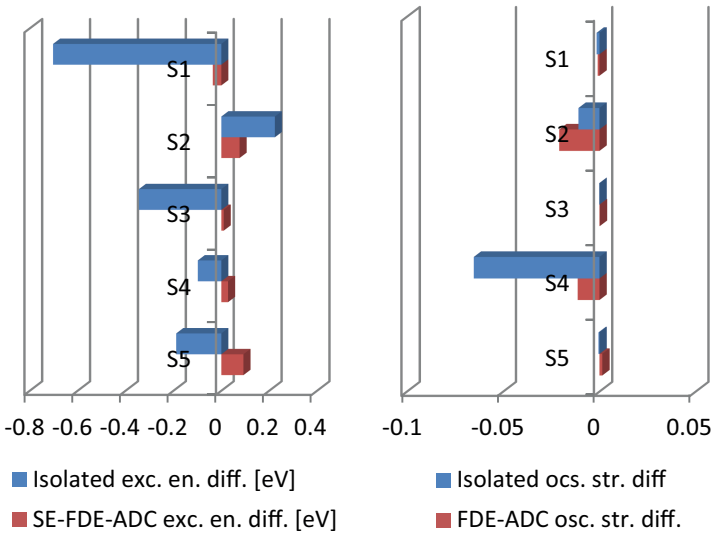

Figure 5.4: Excitation energy difference (left) and oscillator strength difference (right) of the isolated benzene (blue) to the supersystem [UC · 5 H_2O] and the FDE-ADC(2) calculation (red) to the supersystem. The blue bars correspond to the influence of the environment on the excitation energies and oscillator strengths (solvatochromic shift) while the red bars indicate the accuracy of the FDE-ADC(2) calculation in comparison with the ADC(2) calculation of the full system.

5.3 Benchmark of FDE-ADC(2) using the re-assembling of density matrix approach

In this chapter, the newly developed re-assembling of density matrix (RADM) approach was used within the FDE-ADC calculations. Using RADM, the density matrix for the FDE-ADC(2) calculation is conducted within the basis functions of A only, leading to a substantial decrease of the computational costs. The neglect of the embedding potential on the basis functions on B induces, however, an additional error, which is also discussed in this section.

As in the previous chapters, the FDE-ADC calculation is tested against the supersystem calculation and the isolated system A. All settings of the calculations are identical to the ones employed in Sec. 5.2. Also, the supermolecular as well as the isolated benzene, benzaldehyde and uracil calculation results of Sec. 5.2 are taken as reference.

5.3.1 Benzene with one hydrogen fluoride molecule

The FDE-ADC calculations on [BZ · HF] show almost identical orbitals compared to the isolated benzene. Only the LUMO+2 Rydberg orbital shows a distorted surface in the region pointing towards the hydogenfluoride molecule. In contrast to using the supermolecular expansion for FDE-ADC (SE-FDE-ADC), no higher lying virtual orbital is lowered in energy. HOMO−1, HOMO, LUMO and LUMO+1 exhibit π and π^*-character, respectively. The character of the five lowest electronically excited states is the same as in the supersystem calculation. The S_1 to S_4 are local ($\pi \mapsto \pi^*$) transitions, and the S_5 is a Rydberg state. Like in the supersystem, the S_3 and S_4 states are almost degenerate. In this case, the state corresponding to the S_4 of the supersystem calculation shows a slightly lower excitation energy and becomes the S_3 state (Tab. 5.4).

Using RADM, the excited states are in very good agreement to the supersystem calculation and almost identical to the SE-results. The differences of RADM-FDE-ADC(2) to the supersystem are below 0.006 eV for the local ($\pi \mapsto \pi^*$) transitions and below 0.03 eV for the Rydberg state (MAE 0.006 eV (0.038)). In comparison to the SE-FDE-ADC(2) results, the error of the RADM approximation alone is smaller than 0.04 eV for the excitation energy of the Rydberg state and almost zero (0.0001 eV) for the local ($\pi \mapsto \pi^*$) excitation energies. In summary, the differences of SE-FDE-ADC, RADM-FDE-ADC and the isolated benzene calculations to the supersystem calculation are collected in Fig. 5.5.

Table 5.4: Excitation energies, oscillator strengths and orbital transitions for the FDE-ADC(2) calculation using the RADM approach for [BZ · HF].

State	Excitation Energies [eV]			Oscillator Strengths			Orb. Trans.	Weight [%]
	RADM	$\Delta\Omega^a$	$\Delta\Omega^b$	f	Δf^a	Δf^b	H+x $\mapsto$ L+y^c	
S_1	5.436	0.001	0.001	0.0001	0.0000	0.0000	0 $\mapsto$ 0 ($\pi \mapsto \pi^*$)	46.0
							-1 $\mapsto$ 1 ($\pi \mapsto \pi^*$)	43.8
S_2	6.792	0.001	0.000	0.0000	0.0000	0.0000	-1 $\mapsto$ 0 ($\pi \mapsto \pi^*$)	46.2
							0 $\mapsto$ 1 ($\pi \mapsto \pi^*$)	46.0
S_3	7.661	0.002	0.001	0.7298	-0.0149	0.0003	0 $\mapsto$ 0 ($\pi \mapsto \pi^*$)	43.2
							-1 $\mapsto$ 1 ($\pi \mapsto \pi^*$)	45.3
S_4	7.665	0.006	0.001	0.7184	-0.0079	-0.0016	0 $\mapsto$ 1 ($\pi \mapsto \pi^*$)	44.4
							-1 $\mapsto$ 0 ($\pi \mapsto \pi^*$)	44.1
S_5	8.199	0.022	0.036	0.0006	0.0001	0.0003	0 $\mapsto$ 2 ($\pi \mapsto R$)	90.3

[a] Referenced to the supersystem calculation
[b] Referenced to the SE-FDE-ADC(2) calculation
[c] H = HOMO, L = LUMO, R = Rydberg-type orbital

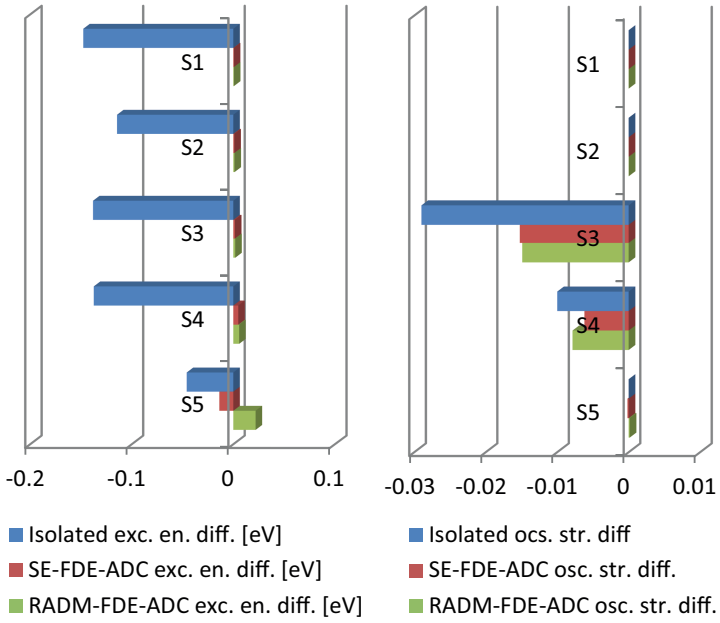

Figure 5.5: Excitation energy difference (left) and oscillator strength difference (right) of the isolated benzene (blue) to the supersystem [BZ · HF], the SE-FDE-ADC(2) calculation (red) to the supersystem and the RADM-FDE-ADC(2) calculation (green) to the supersystem. The blue bars correspond to the influence of the environment on the excitation energies and oscillator strengths (solvatochromic shift) while the red and green bars indicate the accuracy of the SE-FDE-ADC(2) and RADM-FDE-ADC(2) calculations in comparison with the supermolecular ADC(2) calculation. The SE-FDE-ADC(2) results are taken from Sec. 5.2.1.

5.3.2 Benzaldehyde with two water molecules

Analogous to the SE calculations, benzaldehyde was used as system A. The orbitals obtained in the RADM-FDE-ADC(2) calculation are very similar to the orbitals of the isolated benzaldehyde and only slightly distorted. The frontier orbitals HOMO−1 to LUMO+1 and LUMO+4 show π-and π^*-symmetry, respectively. The HOMO−2 is a n-orbital localized at the oxygen and the LUMO+2 and LUMO+3 are Rydberg orbitals. The five lowest electronically excited states are closely related to the excited states of the supersystem exhibiting a local ($\pi \mapsto \pi^*$) transition in the excited states S_2, S_3 and S_5 and a ($n \mapsto \pi^*$) transition in the excited states S_1 and S_4 (Tab. 5.5)

Also for this test, the agreement of the RADM-FDE-ADC calculation with the supersystem calculation is very good, but it shows, as expected, slightly

Table 5.5: Excitation energies, oscillator strengths and orbital transitions for the FDE-ADC(2) calculation using the RADM approach for [BA · 2 H_2O].

	Excitation Energies [eV]			Oscillator Strengths			Orb. Trans.	Weight [%]
	RADM	$\Delta\Omega^a$	$\Delta\Omega^b$	f	Δf^a	Δf^b	H+x $\mapsto$ L+y^c	
S_1	3.877	-0.020	0.014	0.0001	0.0000	0.0000	-2 $\mapsto$ 0 ($n \mapsto \pi^*$)	74.1
							-2 $\mapsto$ 4 ($n \mapsto \pi^*$)	12.2
S_2	4.851	0.038	0.014	0.0164	-0.0033	-0.0010	0 $\mapsto$ 0 ($\pi \mapsto \pi^*$)	58.0
							-1 $\mapsto$ 0 ($\pi \mapsto \pi^*$)	6.6
							-1 $\mapsto$ 1 ($\pi \mapsto \pi^*$)	20.4
S_3	5.628	0.075	0.033	0.3490	0.0046	-0.0029	0 $\mapsto$ 0 ($\pi \mapsto \pi^*$)	10.8
							-1 $\mapsto$ 0 ($\pi \mapsto \pi^*$)	72.6
S_4	6.731	-0.020	-0.011	0.0001	-0.0058	0.0000	-2 $\mapsto$ 1 ($n \mapsto \pi^*$)	83.9
S_5	6.803	0.050	0.019	0.2979	0.0037	0.0071	0 $\mapsto$ 0 ($\pi \mapsto \pi^*$)	18.6
							0 $\mapsto$ 1 ($\pi \mapsto \pi^*$)	8.1
							-1 $\mapsto$ 1 ($\pi \mapsto \pi^*$)	48.4

[a] Referenced to the supersystem calculation
[b] Referenced to the SE-FDE-ADC(2) calculation
[c] H = HOMO, L = LUMO

larger differences than the SE calculation. The difference in the excitation energies compared to the supersystem calculation is below 0.08 eV for the calculated excited states (MAE 0.040 eV (0.0029)). The error induced by the RADM approximation alone compared to the SE-FDE-ADC(2) results is smaller than 0.04 eV in excitation energies. A graphical comparison is presented in Fig. 5.6.

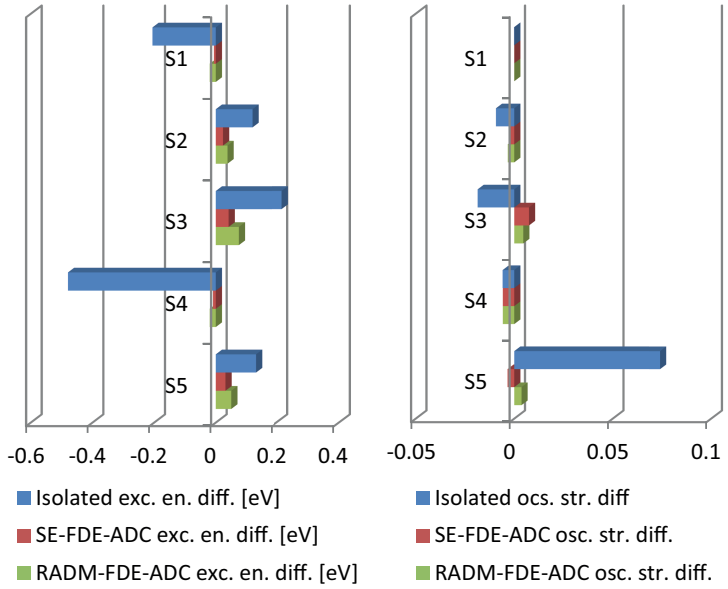

Figure 5.6: Excitation energy difference (left) and oscillator strength difference (right) of the isolated benzene (blue) to the supersystem [BA · 2 H_2O], the SE-FDE-ADC(2) calculation (red) to the supersystem and the RADM-FDE-ADC(2) calculation (green) to the supersystem. The blue bars correspond to the influence of the environment on the excitation energies and oscillator strengths (solvatochromic shift) while the red and green bars indicate the accuracy of the SE-FDE-ADC(2) and RADM-FDE-ADC(2) calculations in comparison with the supermolecular ADC(2) calculation. The SE-FDE-ADC(2) results are taken from Sec. 5.2.2.

5.3.3 Uracil with five water molecules

In the strongly interacting system [UC · 5 H_2O], the orbitals are again hardly perturbed. HOMO−2 and HOMO−3 are of n-type symmetry while the frontier orbitals from HOMO−1 to LUMO+1 are π-and π^*-type orbitals, respectively. The character of the five lowest excited states is conserved with respect to the supersystem calculation. Local ($\pi \mapsto \pi^*$) transitions can be observed in the S_2 and S_4 state while the remaining excited states show ($n \mapsto \pi^*$) transition

character (Tab. 5.6).

Like in the SE-FDE-ADC calculation, the difference to the supersystem calculation is slightly larger than in the previous examples due to the neglected contributions localized on the environment, i.e. the five water molecules. The largest difference in excitation energies is about 0.1 eV (MAE 0.072 eV (0.0074)). The error induced by the RADM approximation alone compared to the SE-FDE-ADC(2) results is smaller than 0.07 eV in the excitation energies. Considering the large shift of the excitation energies with up to 0.7 eV due to the environment, this difference is in excellent agreement with the reference calculation (Fig. 5.7).

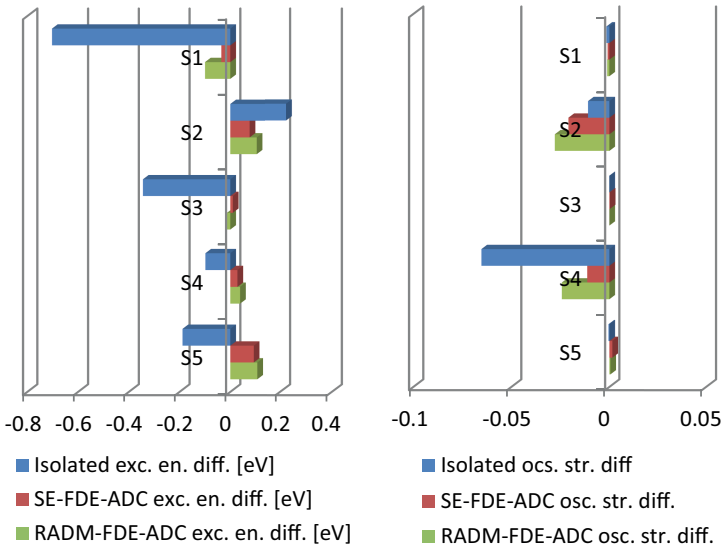

Figure 5.7: Excitation energy difference (left) and oscillator strength difference (right) of the isolated benzene (blue) to the supersystem [UC · 5 H_2O], the SE-FDE-ADC(2) calculation (red) to the supersystem and the RADM-FDE-ADC(2) calculation (green) to the supersystem. The blue bars correspond to the influence of the environment on the excitation energies and oscillator strengths (solvatochromic shift) while the red and green bars indicate the accuracy of the SE-FDE-ADC(2) and RADM-FDE-ADC(2) calculations in comparison with the supermolecular ADC(2) calculation. The SE-FDE-ADC(2) results are taken from Sec. 5.2.3.

Table 5.6: Excitation energies, oscillator strengths and orbital transitions for the FDE-ADC(2) calculation using the RADM approach for $[UC \cdot 5\,H_2O]$.

	Excitation Energies [eV]			Oscillator Strengths			Orb. Trans.	Weight [%]
	RADM	$\Delta\Omega^a$	$\Delta\Omega^b$	f	Δf^a	Δf^b	H+x $\mapsto$ L+y	
S_1	5.043	-0.100	-0.065	0.0004	-0.0011	-0.0003	-2 $\mapsto$ 0 ($n \mapsto \pi^*$)	73.8
							-3 $\mapsto$ 0 ($n \mapsto \pi^*$)	5.9
S_2	5.319	0.104	0.028	0.2092	-0.0279	0.0070	0 $\mapsto$ 0 ($\pi \mapsto \pi^*$)	81.4
S_3	6.198	-0.013	-0.023	0.0001	0.0000	-0.0001	-2 $\mapsto$ 0 ($n \mapsto \pi^*$)	6.0
							-2 $\mapsto$ 1 ($n \mapsto \pi^*$)	31.8
							-3 $\mapsto$ 0 ($n \mapsto \pi^*$)	30.2
							-3 $\mapsto$ 1 ($n \mapsto \pi^*$)	16.9
S_4	6.331	0.039	0.011	0.0720	-0.0243	0.0130	-1 $\mapsto$ 0 ($\pi \mapsto \pi^*$)	85.7
S_5	6.763	0.106	0.014	0.0010	0.0005	-0.0011	-2 $\mapsto$ 1 ($n \mapsto \pi^*$)	24.6
							-3 $\mapsto$ 0 ($n \mapsto \pi^*$)	48.4
							-3 $\mapsto$ 1 ($n \mapsto \pi^*$)	10.0

[a] Referenced to the supersystem calculation
[b] Referenced to the SE-FDE-ADC(2) calculation
[c] H = HOMO, L = LUMO

5.4 Basis-set study

A study of the basis-set dependence of FDE-ADC has been performed using the supermolecular expansion. For this test, the [BA · 2 H_2O] system was employed. The same calculations as described in Sec 5.2.2 have been carried out using the cc-pVTZ basis set instead of the cc-pVDZ one. Generally, the excitation energies are lowered due to the larger basis set. This is observed consistently in the supersystem calculation as well as in the FDE-ADC calculation. Both in the supersystem calculation and the FDE-ADC calculation, the S_4 and S_5 state change their energetic order with respect to the isolated benzaldehyde. This change is reproduced very nicely in the FDE approach (see Tab. 5.7).

Table 5.7: Excitation energies and oscillator strengths for the FDE-ADC(2)/cc-pVTZ calculation in the SE approach for the [BA · 2 H_2O] system.

	Exc. Energies [eV]			Osc. Strength		
state	isol.	supersys.	FDE-ADC	isol.	supersys.	FDE-ADC
S_1	3.623	3.827	3.820	0.0001	0.0002	0.0001
S_2	4.810	4.685	4.715	0.0127	0.0220	0.0188
S_3	5.549	5.350	5.399	0.3260	0.3378	0.3474
S_4	6.129	6.530	6.565	0.0000	0.2975	0.2876
S_5	6.645	6.599	6.587	0.3583	0.0001	0.0001

The basis set dependence is determined by calculating the difference of the deviation in excitation energies obtained with FDE-ADC and the supersystem calculation in the two basis sets according to

$$\Delta\Omega_{basis} = \left|\left(\Omega^{cc\text{-}pVDZ}_{FDE\text{-}ADC} - \Omega^{cc\text{-}pVDZ}_{supersystem}\right) - \left(\Omega^{cc\text{-}pVTZ}_{FDE\text{-}ADC} - \Omega^{cc\text{-}pVTZ}_{supersystem}\right)\right| \tag{5.1}$$

with Ω as the excitation energy. $\Delta\Omega_{basis}$ exhibits values smaller than 0.008 eV in all investigated electronically excited states. Hence, the deviation of FDE-ADC(2) from the supersystem calculation does not vary significantly with the larger basis set. While the results of the ADC(2) and FDE-ADC(2) calculations are in general affected by different basis sets, it appears that the error introduced by employing the FDE approximation does not depend that much on the size of the basis set.

Additionally, the influence of diffuse basis functions on FDE-ADC(2) employing the RADM approximation has been investigated. Again, the [BA · 2 H_2O] system

was chosen using the basis set aug-cc-pVDZ which contains diffuse basis functions that can better describe the peripheral regions of the systems in which the densities overlap. This results in a better description of the embedding potential and therefore in even smaller errors in excitation energies. Since diffuse basis functions are included, the orbitals as well as the orbital transitions of the excited states differ both for the supersystem calculation and the RADM-FDE-ADC(2) calculation compared to the results obtained with the cc-pVDZ basis set. Applying the aug-cc-pVDZ basis set, the error of the RADM-FDE-ADC(2) calculation compared to the supersystem calculation is smaller for all excitation energies in this system compared to the results obtained with the cc-pVDZ basis set (see Tab. 5.8).

Table 5.8: Excitation energies and oscillator strengths for the FDE-ADC(2)/aug-cc-pVDZ calculation in the RADM approach for the [BA $\cdot$ 2 H_2O] system.

	Exc. Energies [eV]			Osc. Strength		
state	isol.	supersys.	FDE-ADC	isol.	supersys.	FDE-ADC
S_1	3.562	3.765	3.761	0.0001	0.0002	0.0002
S_2	4.812	4.682	4.716	0.0132	0.0234	0.0194
S_3	5.486	5.282	5.338	0.3308	0.3393	0.3534
S_4	5.943	6.351	6.350	0.0001	0.0154	0.0019
S_5	6.042	6.403	6.397	0.0115	0.0002	0.0001

Using the basis set aug-cc-pVDZ the mean absolute error (MAE) is reduced from 0.041 eV to 0.016 eV. This clearly shows the advantage of basis sets containing diffuse functions in combination with FDE-ADC.

5.5 Influence of the method and functional on the embedding potential

The dependence of the FDE-ADC results on the choice of the method to calculate $\rho_B(\vec{r})$ and on the employed exchange-correlation functional used for the calculation of the non-electrostatic part of the embedding potential has been investigated and will be discussed in this section. A large variety of methods used to calculate the environment was chosen including HF, generalized gradient approximation (GGA)-DFT (BLYP,[74,75] PBE,[76] BP86[74,77] and PW91[78]) and hybrid-DFT functionals (B3LYP,[82] BHLYP,[74,75] B5050LYP,[224] PBE0[83] and SOGGA11-X[225]). For the evaluation of the non-additive bifunctional in the embedding potential, only explicit density functionals are considered. Hence, the following GGA-DFT functionals were used for the calculation of the non-additive exchange-correlation contribution to the embedding potential: PBE,[76] BLYP,[74,75] BP86,[74,77] $G96_{corr}$[226]-$P86_{ex}$[77], GAM,[227] PW91[78] and SOGGA11.[79] In all calculations, the Thomas-Fermi kinetic energy functional[228] was used for the kinetic energy contribution to the FDET energy and embedding potential. For all calculations, the cc-pVDZ[54] basis set was used.

Again, the three test systems *1)* [BZ · HF], *2)* [BA · 2 H_2O] and *3)* [UC · 5 H_2O] were employed. For all systems, the five energetically lowest electronically excited states of the supersystem were calculated as reference at ADC(2)/cc-pVDZ level of theory. The RADM-FDE-ADC(2)/cc-pVDZ calculations were performed employing all possible combinations of the aforementioned methods for the calculation of the environment with xc-functionals for the calculation of the embedding potential.

5.5.1 Benzene with one hydrogen fluoride molecule

In the supersystem [BZ · HF], the four lowest excited states exhibit typical ($\pi \mapsto \pi^*$) character. The S_5, however, shows a ($\pi \mapsto$ *Rydberg*) character and is therefore characterized as a Rydberg state. An absorbance shift due to the hydrogen fluoride is mainly observed in the ($\pi \mapsto \pi^*$) excitations and varies for the four states from -0.1 to -0.15 eV. Using the FDE approach, the benchmark results of the supersystem calculation can be reproduced in almost perfect agreement. The mean absolute errors (MAEs) for all five states compared to the supersystem calculation have been calculated for all tested methods and functionals and are summarized in Table 5.9.

All MAEs are below 0.01 eV. For this system with only weak interactions, the

Table 5.9: Mean absolute errors for the comparison of RADM-FDE-ADC(2) with the supersystem calculation of [BZ · HF]. The columns represent the applied exchange-correlation functional for the non-electrostatic part of the embedding potential and the rows represent the method used for the calculation of the environment electron density $\rho_B(\vec{r})$.

	PBE	BLYP	BP86	G96-P86	GAM	PW91	S11[a]
HF	0.0064	0.0069	0.0066	0.0074	0.0059	0.0064	0.0026
BLYP	0.0065	0.0070	0.0065	0.0070	0.0057	0.0066	0.0041
B3LYP	0.0064	0.0070	0.0065	0.0098	0.0058	0.0065	0.0034
BHLYP	0.0064	0.0069	0.0065	0.0072	0.0058	0.0065	0.0028
B5050LYP	0.0064	0.0069	0.0065	0.0072	0.0058	0.0064	0.0028
PBE	0.0066	0.0072	0.0066	0.0072	0.0059	0.0067	0.0036
PBE0	0.0066	0.0071	0.0067	0.0100	0.0060	0.0066	0.0029
BP86	0.0066	0.0072	0.0067	0.0099	0.0060	0.0067	0.0033
PW91	0.0065	0.0071	0.0066	0.0072	0.0058	0.0066	0.0037
SOGGA11-X	0.0066	0.0072	0.0067	0.0100	0.0060	0.0067	0.0037

[a] SOGGA11

choice of the xc-functional used to evaluate the non-additive exchange-correlation part of the embedding potential does hardly influence the accuracy of the calculation. Only the SOGGA11 functional performs slightly better and reduces the MAE by half. Also the method used to generate $\rho_B(\vec{r})$ does hardly influence the results. Even the largest deviation, which occurs between the combinations PBE_B - $G96P86_{pot.}$ and $PBE0_B$ - $G96P86_{pot.}$ are smaller than 0.003 eV, much smaller than the inherent error of ADC(2).

5.5.2 Benzaldehyde with two water molecules

The second benchmark system [BA · $2\,H_2O$] exhibits a more intense interaction with the environment as the previous system. Hence, variations in the description of the exchange and correlation interaction by the embedding potential might lead to larger deviations between the used functionals. In benzaldehyde, the five energetically lowest excited states characterize as follows: The S_2, S_3 and S_5 states are delocalized ($\pi \mapsto \pi^*$) excitations. In contrast, the S_1 and S_4 are ($n \mapsto \pi^*$) excitations, localized at the oxygen atom. As described in Sec. 5.2.2, the ($n \mapsto \pi^*$) states are shifted towards higher excitation energies in the supersystem (blue shifted) while the ($\pi \mapsto \pi^*$) states are shifted towards lower energies (red shifted) due to the environment. The energetically shift is about -0.2 eV and

-0.48 eV for the S_1 and S_4 state and 0.12 eV, 0.22 eV and 0.13 eV for the S_2, S_3 and S_5 states, respectively.

In all RADM-FDE-ADC(2) calculations, the excited states are reproduced in very good agreement with the supersystem calculation regarding energy, character and oscillator strength. In all tested combinations of method for B and functional for the embedding potential, the MAE lies between 0.04 eV (e.g. for the combination HF_B - $PBE_{pot.}$) and 0.053 eV (e.g. for the combination GAM_B - $BLYP_{pot.}$). The full list of all MAEs is given in Table. 5.10. However, varying the applied functional in the computation of the embedding potential hardly influences the results. The largest difference is in general about 0.002 eV. Instead, methods including Hartree-Fock exchange for the calculation of $\rho_B(\vec{r})$ increase the accuracy of the calculation. Comparing the functionals BLYP, B3LYP and BHLYP/B5050LYP, the MAE is reduced by about 0.0035 eV from BLYP to B3LYP and additionally reduced by about 0.004 eV from B3LYP to BHLYP. The difference between BHLYP and B5050LYP is with 0.0005 eV not considerable. However, pure HF performs best in this comparison. The MAEs using HF are additionally about 0.004 eV lower compared to using the BHLYP functional (see Tab 5.10). In this case, using

Table 5.10: Mean absolute errors for the comparison of RADM-FDE-ADC(2) with the supersystem calculation of [BA·2 H_2O]. The columns represent the applied exchange-correlation functional for the non-electrostatic part of the embedding potential and the rows represent the method used for the calculation of the environment electron density $\rho_B(\vec{r})$.

	PBE	BLYP	BP86	G96-P86	GAM	PW91	S11[a]
HF	0.0402	0.0410	0.0402	0.0399	0.0416	0.0398	0.0418
BLYP	0.0510	0.0520	0.0511	0.0509	0.0529	0.0506	0.0517
B3LYP	0.0476	0.0486	0.0477	0.0475	0.0495	0.0473	0.0486
BHLYP	0.0439	0.0448	0.0439	0.0437	0.0456	0.0435	0.0451
B5050LYP	0.0434	0.0443	0.0434	0.0432	0.0450	0.0430	0.0447
PBE	0.0492	0.0502	0.0494	0.0491	0.0511	0.0489	0.0501
PBE0	0.0459	0.0468	0.0460	0.0457	0.0476	0.0455	0.0470
BP86	0.0491	0.0501	0.0492	0.0490	0.0510	0.0488	0.0500
PW91	0.0494	0.0504	0.0496	0.0493	0.0513	0.0491	0.0503
SOGGA11-X	0.0458	0.0468	0.0459	0.0456	0.0475	0.0455	0.0503

[a] SOGGA11

HF for the calculation of $\rho_B(\vec{r})$ yields the best agreement with the supermolecular calculation with any xc-functional used for v_{emb}^{lin}.

5.5.3 Uracil with five water molecules

In this last test, the interaction between Uracil (A) and five water molecules as environment (B) ($[UC \cdot 5\,H_2O]$) is even more intense. The five energetically lowest electronically excited state comprise two ($\pi \mapsto \pi^*$) transitions (S_2 and S_4) and three ($n \mapsto \pi^*$) states (S_1, S_3 and S_5) as described in detail in Sec. 5.2.3. Thus, the excitation energies of the S_1, S_3 and S_5 state are again blue shifted in the supersystem calculation by about -0.7 eV, -0.34 eV and -0.19 eV, respectively. Also the S_4 state, although it exhibits a ($\pi \mapsto \pi^*$) transition character, is blue shifted by about -0.1 eV. The second ($\pi \mapsto \pi^*$) state, the S_2 state, is red shifted by about 0.22 eV. The RADM-FDE-ADC(2) calculations, although exhibiting a slightly larger error as in the examples before, again all reproduce the results of the supersystem calculation in very good agreement. Applying the previous combinations of methods and functionals, the mean absolute errors range from 0.071 eV to 0.084 eV. Again, the applied functional for the computation of the embedding potential does not affect the results significantly. However, as observed before, increasing the amount of HF exchange in the method used to calculate $\rho_B(\vec{r})$ improves the accuracy of the FDE-ADC calculation. A reduction of the MAE by up to 0.013 eV can be achieved when using HF for the calculation of $\rho_B(\vec{r})$. All MAEs are shown in Table. 5.11.

Table 5.11: Mean absolute errors for the comparison of RADM-FDE-ADC(2) with the supersystem calculation of $[UC{\cdot}5\,H_2O]$. The columns represent the applied exchange-correlation functional for the non-electrostatic part of the embedding potential and the rows represent the method used for the calculation of the environment electron density $\rho_B(\vec{r})$.

	PBE	BLYP	BP86	G96-P86	GAM	PW91	S11[a]
HF	0.0718	0.0735	0.0719	0.0719	0.0734	0.0715	0.0735
BLYP	0.0823	0.0843	0.0825	0.0823	0.0843	0.0821	0.0829
B3LYP	0.0793	0.0811	0.0794	0.0793	0.0811	0.0790	0.0802
BHLYP	0.0758	0.0775	0.0759	0.0758	0.0775	0.0754	0.0770
B5050LYP	0.0754	0.0772	0.0755	0.0754	0.0771	0.0751	0.0767
PBE	0.0816	0.0835	0.0817	0.0815	0.0835	0.0813	0.0824
PBE0	0.0782	0.0800	0.0783	0.0782	0.0800	0.0779	0.0793
BP86	0.0810	0.0829	0.0811	0.0810	0.0829	0.0807	0.0818
PW91	0.0818	0.0838	0.0820	0.0818	0.0837	0.0815	0.0826
SOGGA11-X	0.0769	0.0787	0.0770	0.0769	0.0786	0.0766	0.0783

[a] SOGGA11

5.5.4 Summary of the results

To summarize the key results, the test of three different systems with environment interactions ranging from weak polarization up to multiple hydrogen bonds shows only marginal dependence of the accuracy on the choice of the functional used to calculate $v_{emb}^{lin}(\vec{r})$. The MAEs for all investigated combinations of the method to calculate $\rho_B(\vec{r})$ and xc-functional used in the embedding potential are summarized in Fig. 5.8. Despite the very small differences in the MAEs, some functionals can be identified to perform generally better than others in combination with ADC. The most accurate functionals used for the embedding potentials are the PBE and the PW91 functionals. The least accurate ones are the BLYP and GAM functionals. However, overall the differences are negligible and presumably not relevant in practical calculations.

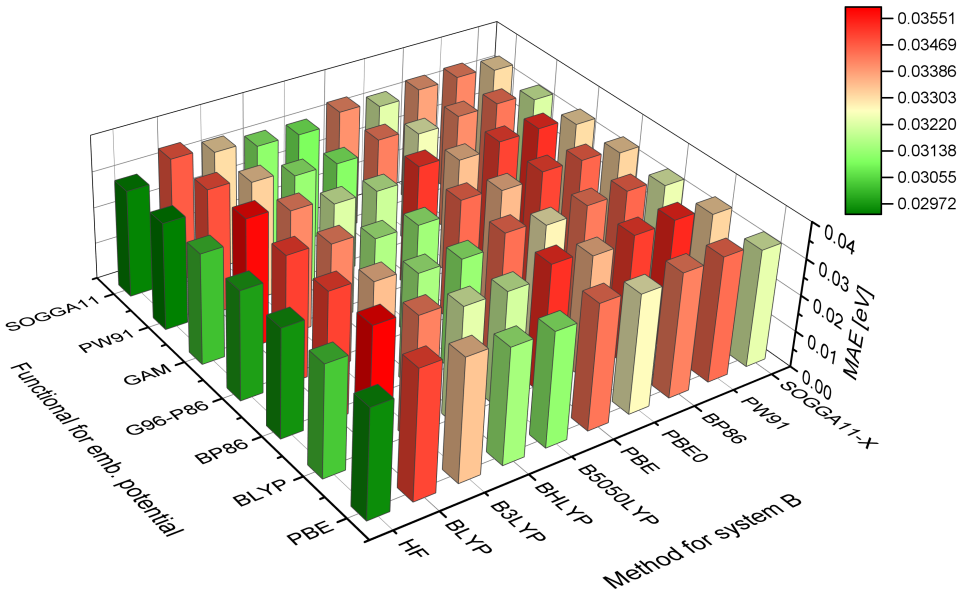

Figure 5.8: Mean absolute errors (MAE) of the environment induced excitation energy shifts of the computed states of all three investigated system ([BZ · HF], [BA · 2 H_2O] and [UC · 5 H_2O]) for all investigated combinations of the method to calculate the environment density and the functional to calculate the non-electrostatic part of the embedding potential.

Regarding the theoretical method used to calculate the environment density $\rho_B(\vec{r})$, the differences in accuracy are more significant. In general, hybrid functionals and HF itself perform better than functionals without exact exchange.

This tendency becomes particularly visible when strong interactions between the embedded system and the environment play a role. In these cases, the accuracy depends clearly on the amount of HF exchange, the more the better. Additionally, it seems not advantageous to apply the same xc-functional for the calculation of $\rho_B(\vec{r})$ and for the embedding potential. In fact, it turns out HF has the smallest MAE when ADC is used for the embedded system. A possible explanation for the observed trend is, that also the density of the embedded system, which is calculated using MP(2) level of theory, is largely based on HF theory. This is also the case in the supermolecular reference calculation. Hence, both densities "match" best, when both are calculated using the same underlying theoretical model, i.e. HF, as in the supermolecular approach.

5.6 Benchmark of FDE-ADC(3) using the re-assembling of density matrix approach

In this section, the combination of frozen density embedding (FDE) with the algebraic-diagrammatic construction scheme of the polarization propagator of third order FDE-ADC(3) is tested. Accordingly to the benchmark of FDE-ADC(2) (see Sec. 5.2 and 5.3), the same test set of *1)* [BZ · HF], *2)* [BA · 2 H_2O] and *3)* [UC · 5 H_2O] will be employed (Fig. 5.1). The supersystems and the isolated core systems (A) were investigated at ADC(3)/6-311++G**[47–49] level of theory. For the FDE-ADC(3) calculations, the reassembling of density matrix approximation (RADM) and the same basis set (6-311++G**) was used, since the basis set study (Sec. 5.4) showed an improved accuracy for FDE-ADC when basis sets with diffuse functions are employed. Only in [BA·2 H_2O], the aug-cc-pVDZ basis set was chosen due to convergence issues in the supersystem calculation using the 6-311++G** basis set. The RADM approach was chosen, since this is the variant capable of performing productive calculations of larger systems. The HF method was chosen for the calculation of the environment density $\rho_B(\vec{r})$ and the PBE functional for the non-electrostatic part of the embedding potential. As demonstrated in Sec. 5.5, this combination exhibits the smallest error for FDE-ADC in the tested systems.

5.6.1 Benzene with one hydrogen fluoride molecule

Let me start again with the weakly interacting system [BZ · HF]. At first, the supersystem and isolated benzene are calculated. Next, an FDE-ADC(3) calculation is performed and the results are compared to the supermolecular calculation.

While the occupied frontier orbitals of [BZ·HF], i.e. HOMO and HOMO−1 are typical π orbitals, the corresponding unoccupied frontier orbitals, i.e. LUMO and LUMO+1, are not necessarily the corresponding π^* orbitals. Due to the diffuse basis functions, Rydberg and various other types of virtual orbitals are present in contrast to calculations using basis sets without diffuse basis functions. Therefore, the corresponding π^* to the HOMO and HOMO−1 are LUMO+7 and LUMO+8 in the supermolecular calculation. The LUMO+1 for example is a Rydberg orbital (R) located in the benzene ring plane opposite to the hydrogen fluoride. The four energetically lowest electronically excited states of [BZ · HF] were calculated. Here, the S_1 and S_4 states are ($\pi \mapsto \pi^*$) transitions, while S_2 and S_3 are Rydberg states. A detailed analysis of the excitations is given in Table 5.12.

Table 5.12: Excitation energies, oscillator strengths and orbital transitions (> 10 %) for the four energetically lowest electronically excited singlet states of isolated benzene, the supersystem and the RADM-FDE-ADC(3) calculations of [BZ · HF].

	Excitation Energies [eV]			Oscillator Strengths			Orb. Trans.	Weight [%]		
state	isol.	supersys.	FDE-ADC	isol.	supersys.	FDE-ADC	H+x ↦ L+y[a]	isol.	supersys.	FDE-ADC
S_1	5.049	5.050	5.049	0.0000	0.0001	0.0001	$0 \mapsto 6$ ($\pi \mapsto \pi^*$)	36.8	37.5[b]	37.5
							$-1 \mapsto 7$ ($\pi \mapsto \pi^*$)	36.8	34.8[b]	35.4
S_2	6.369	6.292	6.292	0.0000	0.0008	0.0007	$0 \mapsto 0$ ($\pi \mapsto R$)	79.2	18.0	27.3
							$0 \mapsto 1$ ($\pi \mapsto R$)	-	57.8	51.9
S_3	6.369	6.310	6.312	0.0000	0.0000	0.0000	$-1 \mapsto 0$ ($\pi \mapsto R$)	79.2	18.0	27.5
							$-1 \mapsto 1$ ($\pi \mapsto R$)	-	56.1	50.4
S_4	6.405	6.396	6.397	0.0000	0.0000	0.0001	$-1 \mapsto 6$ ($\pi \mapsto \pi^*$)	42.1	42.0[b]	42.1
							$0 \mapsto 7$ ($\pi \mapsto \pi^*$)	42.1	40.7[b]	41.5

[a] H = HOMO, L = LUMO, R = Rydberg-type orbital

[b] An orbital localized at the hydrogen fluoride is neglected in counting (see text)

In isolated benzene, HOMO and HOMO−1 have π character, whereas LUMO and LUMO+1 are Rydberg orbitals. The energetically lowest π^* orbitals are the LUMO+6 and LUMO+7. For isolated benzene, also the four energetically lowest excitations were calculated. Again, the S_1 and S_4 states show ($\pi \mapsto \pi^*$) character, the S_2 and S_3 states are Rydberg states. A more detailed analysis is given in Table 5.12. However, it is noticeable that in the calculations employing ADC(3)/6-311++G** the solvatochromic shifts differ from the calculations at ADC(2)/cc-pVDZ level. While using the latter a solvatrochromic blue shift due to hydrogen fluoride could be observed for states S_1 to S_4 (($\pi \mapsto \pi^*$) transitions, see Sec. 5.2.1), two ($\pi \mapsto \pi^*$) excited states show a small red shift at ADC(3)/6-311++G** level of theory.

In the RADM-FDE-ADC(3) calculation, the hydrogen fluoride is modeled by virtue of the embedding potential. The resulting orbitals look qualitatively identical to the ones obtained in the isolated benzene calculation. However, since in the supermolecular calculation the orbitals localized at the benzene did not show any difference to the isolated benzene orbitals either, this result is not unexpected. In the supermolecular calculation, additional orbitals located at hydrogen fluoride are included, which are by set-up not included in the other calculations. For ease of comparison, this is taken care of in the orbital numbering and the orbital numbering of the supermolecular calculation is generally adapted.

Overall, the FDE-ADC(3) calculation shows almost quantitative agreement with the supermolecular calculation. The S_1 and S_4 states exhibit ($\pi \mapsto \pi^*$) transition character, the S_2 and S_3 states are identified as Rydberg states (Tab. 5.12). A diagrammatic representation of the absorbance shift induced by the environment, i.e. the difference between supermolecular calculation and isolated benzene as well as an illustration of the accuracy of the FDE-ADC(3) method in comparison with the supermolecular calculation is given in Fig. 5.9.

The largest deviation in excitation energies is smaller than 0.002 eV and about 0.0001 for oscillator strengths when the FDE-ADC(3) calculation is compared to the supermolecular ADC(3) calculation. The mean absolute error (MAE) of all four states in excitation energies is 0.001 eV and 0.0001 for oscillator strengths.

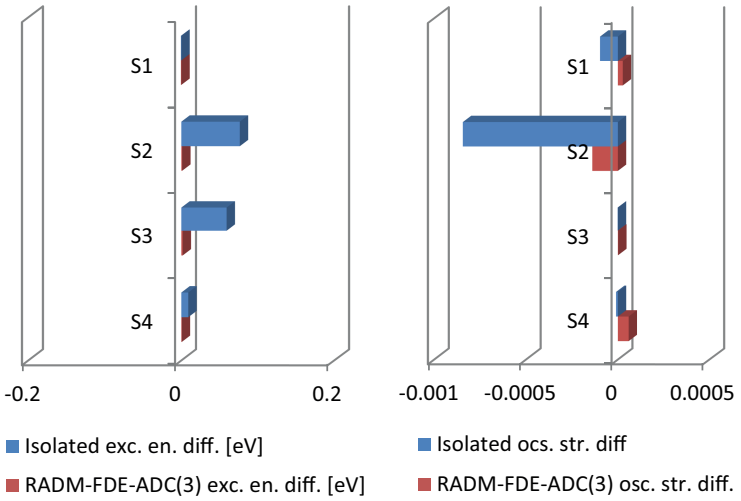

Figure 5.9: Analysis of the accuracy of RADM-FDE-ADC(3) for [BZ · HF]. Excitation energy difference (left) and oscillator strength difference (right) of the isolated benzene to the supersystem (blue) and the FDE-ADC(3) calculation using the RADM approximation to the supersystem (red). The blue bars correspond to the solvatochromic shift while the red bars indicate the accuracy of the FDE-ADC(3) calculation in comparison with the ADC(3) supersystem calculation.

5.6.2 Benzaldehyde with two water molecules

Analogously to the previous system, FDE-ADC(3) has been tested for [BA · 2 H_2O]. In both the supermolecular and the isolated benzaldehyde calculation, the HOMO, HOMO−1 and HOMO−2 exhibit π, π and n character, respectively. However, due to the chosen diffuse basis set, corresponding π^* orbitals can be found as LUMO+3 in [BA · 2 H_2O] and LUMO+4 in the isolated benzaldehyde calculation. Obviously, some orbitals changed their energetic order due to the effect of the two water molecules. Further important π^* orbitals arise as LUMO+7 and LUMO+8 in isolated benzene and as LUMO+9 in [BA · 2 H_2O]. The occupied orbitals HOMO and HOMO−1 are reoriented when including the water molecules (see Fig. 5.10).

The five energetically lowest excited states have been calculated both for [BA · 2 H_2O] and isolated benzaldehyde. However, in none of these systems and independent from the chosen basis set, the calculations of the fourth excited state (S_4) did converge. In both cases, the first excited state exhibits ($n \mapsto \pi^*$) excitation character while the states S_2, S_3 and S_5 exhibit local ($\pi \mapsto \pi^*$) transition character. The solvatochromic shift for benzaldehyde is -0.24 eV for the ($n \mapsto \pi^*$) excitation and between 0.1 eV and 0.18 eV for the ($\pi \mapsto \pi^*$) excitations. A detailed overview

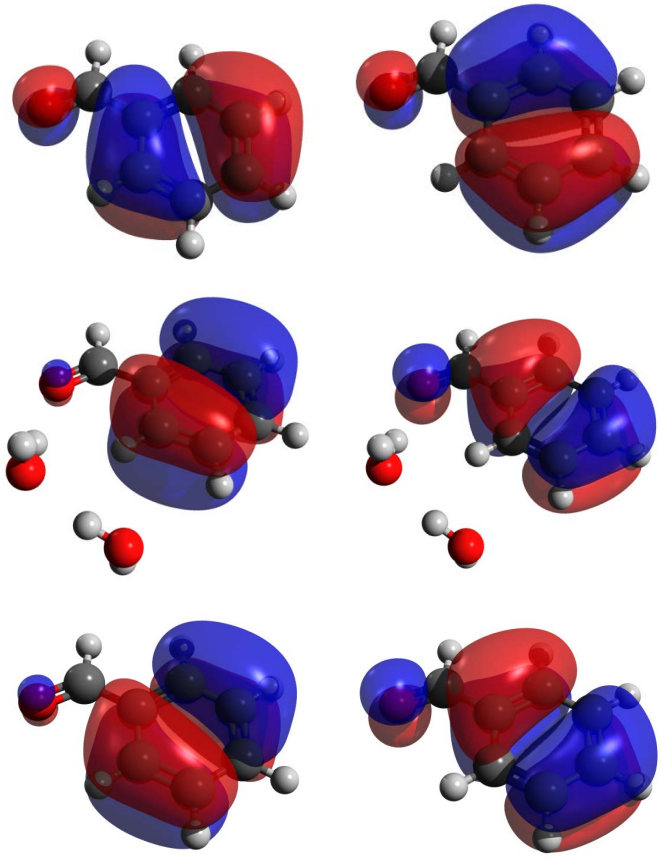

Figure 5.10: HOMO (left side) and HOMO−1 (right side) of isolated benzaldehyde (top), of [BA · 2 H_2O] calculated with supermolecular ADC(3) (middle) and with FDE-ADC(3) (bottom).

of the calculated excited states is given in Table 5.13. The reorientation of the HOMO and HOMO−1 prevents a direct mapping of the corresponding transitions between isolated benzaldehyde and the supermolecular calculation. But since the orbitals are still of the same type and form and also the orbital energies are quite similar, this change does not affect the character of the excited states themselves.

Table 5.13: Excitation energies, oscillator strengths and orbital transitions (> 10 %) for the five energetically lowest electronically excited singlet states[a] of isolated benzaldehyde, the supersystem and the RADM-FDE-ADC(3) calculations of [BA · 2 H_2O].

	Excitation Energies [eV]			Oscillator Strengths			Orb. Trans.	Weight [%]		
state	isol.	supersys.	FDE-ADC	isol.	supersys.	FDE-ADC	H+x ↦ L+y[b]	isol.	supersys.	FDE-ADC
S_1	3.827	4.063	4.038	0.0002	0.0003	0.0002	-2 ↦ 3 ($n \mapsto \pi^*$)	63.4[c]	63.5	65.5
S_2	4.554	4.454	4.476	0.0110	0.0188	0.0157	0 ↦ 3 ($\pi \mapsto \pi^*$)	19.0[c,d]	53.1[d]	52.0
							-1 ↦ 3 ($\pi \mapsto \pi^*$)	36.2[c,d]	5.2[d]	7.6
							-1 ↦ 8 ($\pi \mapsto \pi^*$)	-	-	12.9
S_3	5.334	5.160	5.207	0.2827	0.2878	0.3006	-1 ↦ 3 ($\pi \mapsto \pi^*$)	24.0[c,d]	66.3[d]	66.0
							0 ↦ 3 ($\pi \mapsto \pi^*$)	54.0[c,d]	8.7[d]	12.1
S_5	6.476	6.368	6.399	0.3487	0.3084	0.2874	0 ↦ 8 ($\pi \mapsto \pi^*$)	19.3[d]	-	6.1[e]
							0 ↦ 3 ($\pi \mapsto \pi^*$)	-	16.5[d]	17.1[e]
							-1 ↦ 3 ($\pi \mapsto \pi^*$)	19.0[d,c]	-	4.5[e]
							0 ↦ 7 ($\pi \mapsto \pi^*$)	13.8[d,e]	-	-
							-1 ↦ 8 ($\pi \mapsto \pi^*$)	10.0[d,e]	13.8[d,e]	36.7[e]
							-1 ↦ 12 ($\pi \mapsto \pi^*$)	-	13.5[d,e]	-

[a] Note that the S_4 state did not converge in all calculations.
[b] H = HOMO, L = LUMO
[c] A Rydberg orbital is neglected in counting, i.e. LUMO indices reduced by 1 to match the numbers
[d] Since HOMO and HOMO−1 are differently oriented in isolated benzaldehyde and [BA · 2 H_2O] the energetic numbering might not necessarily match.
[e] Since various Rydberg orbitals change their energetic ordering, orbital indices might not match

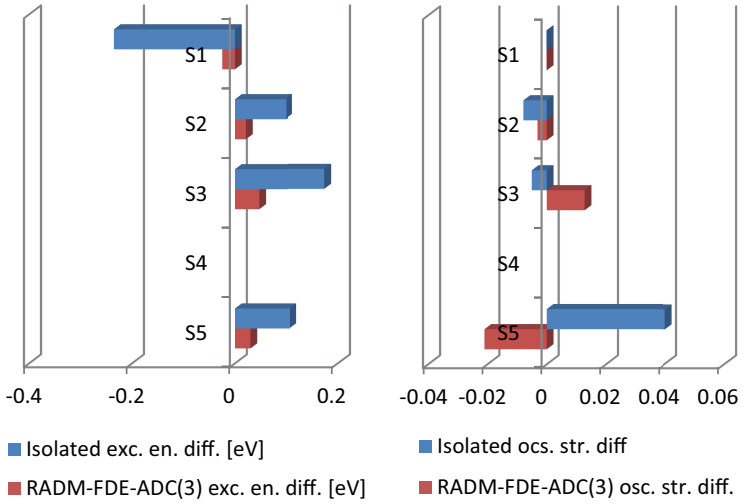

Figure 5.11: Analysis of the accuracy of RADM-FDE-ADC(3) for $[BA \cdot 2\,H_2O]$. Excitation energy difference (left) and oscillator strength difference (right) of the isolated benzaldehyde to the supersystem (blue) and the FDE-ADC(3) calculation using the RADM approximation to the supersystem (red). The blue bars correspond to the solvatochromic shift while the red bars indicate the accuracy of the FDE-ADC(3) calculation in comparison with the ADC(3) supersystem calculation.

5.6.3 Uracil with five water molecules

For the last benchmark system, [UC·5 H_2O], the same analysis has been performed as well. HOMO and HOMO−1 in both the [UC · 5 H_2O] and the isolated uracil exhibit π character. HOMO−2 and HOMO−3 are n orbitals localized at the oxygen atoms of uracil. Calculation of the five energetically lowest excited states of [UC · 5 H_2O] reveals four ($\pi \mapsto \pi^*$) transitions namely the S_1, S_3, S_4, and S_5 states. The S_2 state exhibits ($n \mapsto \pi^*$) transition character. In contrast, in isolated uracil, the S_1 state is an ($n \mapsto \pi^*$) state and the states S_2 to S_4 are ($\pi \mapsto \pi^*$) states. For this system, the molecular orbital picture is insufficient to analyze the character of the excited states properly, since many orbital transitions contribute to the excitation and the orbitals themselves change both in form and energetic order between isolated uracil and [UC · 5 H_2O]. Therefore, natural transition orbitals (NTOs, see Sec 2.3.6.1) have been calculated and analyzed to characterize the excited states. These NTOs reveal the S_1 state of isolated uracil to correspond to the S_2 state of [UC · 5 H_2O] while the S_1 state of the supersystem corresponds to the S_2 state of isolated uracil. The S_3 state is identical in both cases, while the S_4 and S_5 state in [UC · 5 H_2O] exhibit a different character than any of the calculated states of isolated uracil. These states are energetically lowered by the environment. An electronic state of [UC · 5 H_2O] corresponding to the S_4 state of isolated uracil could not be identified. To facilitate comparison of corresponding states, each state is assigned to a Greek letter based on its character and not on its energetic order (see Table 5.14).

Table 5.14: Excitation energies, oscillator strengths and transition character for the five energetically lowest electronically excited singlet states of isolated uracil[a], the supersystem and the RADM-FDE-ADC(3) calculations of $[UC \cdot 5\,H_2O]$.

	Excitation Energies [eV]			Oscillator Strengths			Transition Character		
state	isol.	supersys.	FDE-ADC	isol.	supersys.	FDE-ADC	isol.	supersys.	FDE-ADC
S_1	5.015	5.123	5.199	0.0000	0.2534	0.2235	$(n \mapsto \pi^*)$ (α)	$(\pi \mapsto \pi^*)$ (β)	$(\pi \mapsto \pi^*)$ (β)
S_2	5.299	5.764	5.668	0.2454	0.0000	0.0000	$(\pi \mapsto \pi^*)$ (β)	$(n \mapsto \pi^*)$ (α)	$(n \mapsto \pi^*)$ (α)
S_3	5.716	6.193	6.208	0.0027	0.0130	0.0132	$(\pi \mapsto \pi^*)$ (γ)	$(\pi \mapsto \pi^*)$ (γ)	$(\pi \mapsto \pi^*)$ (γ)
S_4	6.330	6.383	6.456	0.0341	0.1014	0.0957	$(\pi \mapsto \pi^*)$ (δ)	$(\pi \mapsto \pi^*)$ (ϵ)	$(\pi \mapsto \pi^*)$ (ϵ)
S_5	-[a]	6.627	6.631	-[a]	0.2207	0.2069	-[a]	$(\pi \mapsto \pi^*)$ (ζ)	$(\pi \mapsto \pi^*)$ (ζ)

[a] The S_5 state of isolated uracil did not converge.

In the FDE-ADC(3) calculation, the effect of the environment onto the embedded system is generally well reproduced. HOMO and HOMO−1 exhibit π character, the HOMO−2 and HOMO−3 show n character and each is localized on one oxygen atom. The excited states have the same character and energetic order as in the supermolecular calculation. With an MAE of 0.053 eV for excitation

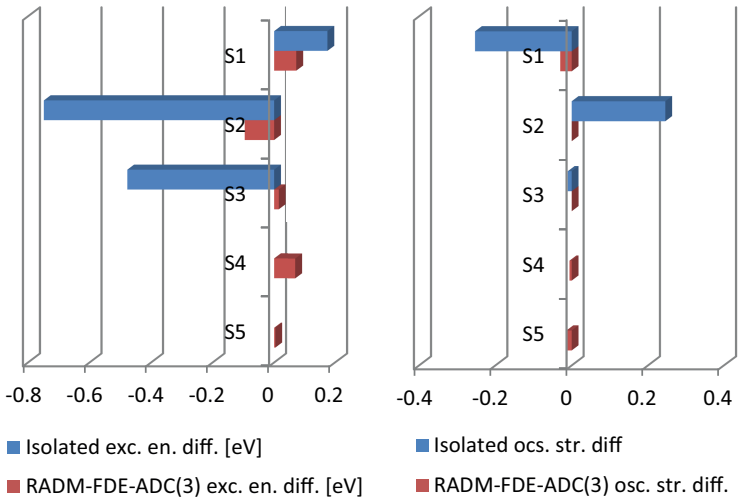

Figure 5.12: Analysis of the accuracy of RADM-FDE-ADC(3) for $[\mathrm{UC} \cdot 5\,\mathrm{H_2O}]$. Excitation energy difference (left) and oscillator strength difference (right) of the isolated uracil to the supersystem (blue) and the FDE-ADC(3) calculation using the RADM approximation to the supersystem (red). The blue bars correspond to the solvatochromic shift while the red bars indicate the accuracy of the FDE-ADC(3) calculation in comparison with the ADC(3) supersystem calculation.

5.7 Summary and conclusion

In this chapter, I presented a benchmark of the new FDE-ADC method up to third order in perturbation theory. For the benchmark, three test systems were created, which were constructed such that an increasing amount of core-environment interaction occurs. In the first system a benzene molecule represents the embedded system (A) and as the environment (B) a hydrogen fluoride molecule placed in plane with the benzene ring was chosen ([BZ · HF]). Here, the interaction consists only of polarization and dispersion effects. In the next system, benzaldehyde (A) with a hydrogen-bonded water-dimer (B) ([BA · 2 H_2O]), the interaction is more intense due to the hydrogen bond between the two subsystems. The last system consists of an Uracil molecule (A) surrounded by 5 water molecules ([UC · 5 H_2O]) which all form a hydrogen bond with uracil. This set of systems was used for all benchmarks. The benchmark was performed in comparison to supermolecular ADC calculations of the three systems. For comparison, also isolated ADC calculations of the embedded systems were performed.

At first FDE-ADC of second order perturbation theory (FDE-ADC(2)) has been investigated employing both the supermolecular expansion and the re-assemilation of density matrix approach. Thus, the accuracy of the FDE-ADC(2) method itself as well as the error induced by the additional approximation of RADM could be determined. After this, FDE-ADC(3) has been tested using the RADM approach. Additionally, a study of the basis set dependence of FDE-ADC as well as a study of the dependence of the choice of the method used to calculate $\rho_B(\vec{r})$ as well as the choice of the xc-functional used for the calculation of the non-electrostatic part of the embedding potential was performed.

In the benchmarks it could be shown that the FDE-ADC method reproduces the results of the supermolecular calculations very well. For SE-FDE-ADC(2) a mean absolute error (MAE) of 0.025 eV for excitation energies was determined. Using the RADM approach, the MAE is slightly higher (0.040 eV). In the RADM-FDE-ADC(3) benchmark, a MAE of 0.029 eV for excitation energies was calculated. The basis set study showed an increasing accuracy when basis sets with diffuse basis functions are used. However, the choice of the method to calculate $\rho_B(\vec{r})$ slightly influences the accuracy while the choice of the employed xc-functional for the embedding potential has practically no influence. It could be seen that HF performs best and that the MAE is reduced with increasing amount of HF exchange. Possibly this behavior is due to the better match of a HF based density for the environment with the HF/MP(2) based density of the embedded system.

Also, the saving of computational time by using FDE-ADC in comparison with supermolecular calculations was considered. The computation time for [UC · 5 H_2O] was calculated for a supermolecular ADC(2) calculation and using the RADM-FDE-ADC(2) method. The calculation of the supersystem takes about 73 hours CPU time on one core keeping all data for the ADC calculation in memory (Intel Xeon E7-4870v2 2.3GHz, software compiled using Intel C++ and Fortran compilers[229] v15.0 in combination with the MKL library[230]). In contrast, the complete FDE-ADC calculations using the RADM aproach which consist of the MP(2) calculation on system A in the basis functions of A, the HF calculation of system A in the basis functions of A and B, the HF calculation of system B in the basis functions of A and B, the creation of the embedding potential and the final FDE-ADC(2) calculations in the basis function of A takes about 3 hours on the same machine. This amounts to a saving of 70 hours or more than 95% of the time needed for the supersystem calculation. For larger systems with even more environment molecules, the percentage of time saved will be drastically larger due to the formal $\mathcal{O}(N^5)$-scaling of the ADC(2) calculation for the supersystem (with N being the number of basis functions). A comparison of the computational time is shown in Fig. 5.13. The size of the environment is successively increased from

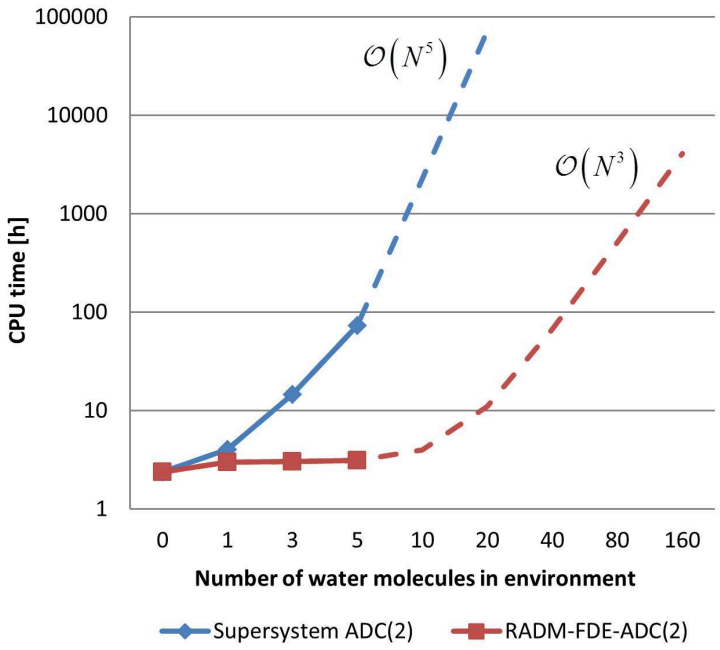

Figure 5.13: Comparison of the computational cost in CPU time of a supermolecular ADC(2) calculation and the RADM-FDE-ADC(2) method.

1 to 5 water molecules. The computational cost of the supersystem calculation increases dramatically already for a small environment due to the $\mathcal{O}(N^5)$ scaling of ADC(2). Hence, the computational cost is dominated by the calculation of the embedded species for a small environment. Of course, this trend holds only for environments up to the same size as system A. The calculation of the environment scales formally as $\mathcal{O}(N^3)$, which will become the most time-consuming step for large environments (e.g. more than 100 water molecules). But for such large systems, a full ADC calculation is no longer feasible.

In total, the FDE-ADC method is a promising approach for considering environmental effects on electronically excited states. The error of this method is lower than the intrinsic error of the used ADC method and using the RADM approximation explicit treatment of extended environments is feasible. This makes FDE-ADC to a reliable "black box" method for the calculation of electronically excited states of embedded systems in extended environments.

Chapter 6

Representative Applications of FDE-ADC

"Erwin with his psi can do
Calculations quite a few.
But one thing has not been seen:
Just what does psi really mean?"
Erich Hückel

After benchmarking FDE-ADC(3) in the previous Chapter, I will demonstrate the potential of the FDE-ADC method on three representative examples, which comprise computations of larger systems. For these, supermolecular calculations at ADC(2) or even ADC(3) level are no longer feasible. Therefore, the method RADM-FDE-ADC is employed. In the first example, the photoswitch spiropyran dissolved in water is analyzed and compared to previous QM- and QM/MM-based investigations performed by myself during my master thesis. In the second example, the excited states of benzoquinone solvated in methanol are investigated. In the third example, the core-excited states of $CO@C_{60}$, a CO molecule caught in a C_{60} fullerene, are calculated using the core-valence separated FDE-CVS-ADC method. The different influence of a C_{60}-cage on the core excitations in carbon monoxide are investigated.[1]

[1] Parts of Chapter 6 have already been published in
Implementation and application of the frozen density embedding theory with the algebraic diagrammatic construction scheme for the polarization propagator up to third order
Stefan Prager, Alexander Zech, Tomasz A. Wesolowski and Andreas Dreuw
submitted for publication, (2017)

6.1 Excited state analysis of spiropyran in water

Spiropyran is a molecular photoswitch, which undergoes a ring-opening and isomerization reaction upon irradiation with UV-light.[231–233] The photoisomerization process has been investigated spectroscopically using femtosecond vis-pump/vis- and IR-probe spectroscopy[234,235].

During my master thesis, I investigated the spiropyran-to-merocyanin photoreaction both in the gas phase and in aqueous solution using a QM/MM. The QM calculations were performed on DFT and TD-DFT level of theory after a thorough benchmark of the applied functional against RI-CC2 and complete active space self-consistent field (CASSCF)[236] / CASSCF with second-order perturbation theory (CASPT2)[237] results. The two energetically lowest excited states of spiropyran have been characterized as "bright" and "dark" state indicating the difference in oscillator strengths. Occupying the bright state leads to a ring-opening reaction to merocyanine. These two important excited states could be identified in the presence of the water environment as well. However, the water environment had only minor influences on the vertical excitations and photochemistry of spiropyran. These results have been published in Ref. 30. In this section, spiropyran in water is investigated using FDE-ADC to verify the previous results.

A supersystem of spiroypran and 100 water molecules arranged in at least two solvation shells around spiropyran was created and fully optimized at DFT/ωB97X-D3/6-31G* level of theory. This structure is used for the calculation of vertical excitation energies of isolated spiropyran as well as of the embedded system using FDE-ADC.

The calculations of the excited states have been performed at ADC(2)/cc-pVDZ and FDE-ADC(2)/cc-pVDZ level of theory. For the FDE-ADC(2) calculation, the environment density $\rho_B(\vec{r})$ was calculated using HF and the non-electrostatic part of the embedding potential was calculated using the PBE functional. The geometry of the supersystem is shown in Fig. 6.1

The two energetically lowest excited states were calculated and analyzed using natural transition orbitals (NTOs). NTOs are orbitals specific for one excitation and describe the electronic transition itself (see Sec. 2.3.6.1). NTOs always come in pairs, one representing the particle, the other representing the hole. Both share the same eigenvalue which corresponds to the contribution of this pair to the total excitation. Although it is mathematically not fully correct, for the sake of simplicity the nomenclature used for molecular orbitals is also applied here. Therefore, the hole NTO exhibiting the highest eigenvalue is labeled "highest

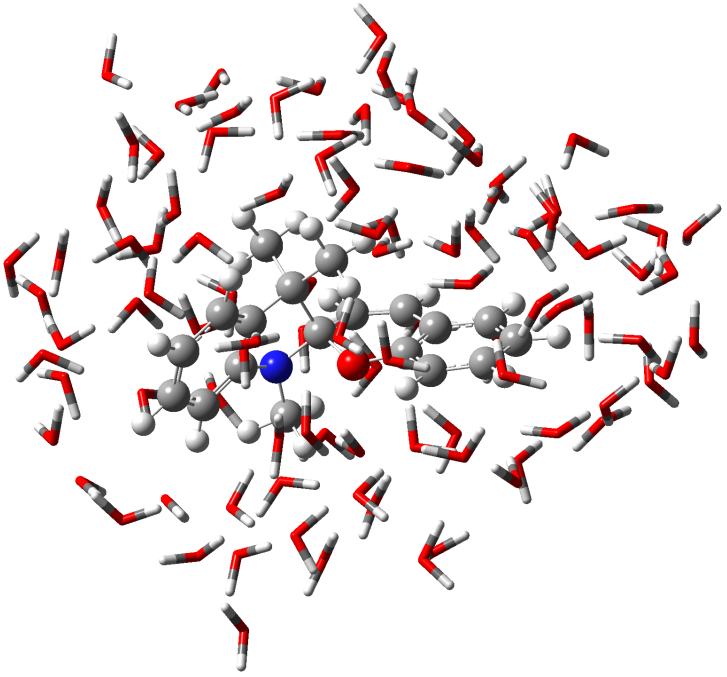

Figure 6.1: Supersystem of spiropyran (balls and sticks, embedded system (A)) surrounded by 100 water molecules (environment (B)).

occupied natural transition orbital" (HONTO) and the corresponding particle NTO sharing the same eigenvalue is labeled "lowest unoccupied natural transition orbital" (LUNTO). The NTO pairs exhibiting lower eigenvalues follow the same scheme (HONTO−1, LUNTO+1,...).

In isolated spiropyran, the S_1 and S_2 states exhibit excitation energies (oscillator strengths) of 4.172 eV (0.0506) and 4.434 eV (0.0084), respectively. Here, the first excited state clearly corresponds to the "bright" state, while the "dark" state is represented by S_2. Analyzing the corresponding NTOs, the S_1 state can be identified as a local ($\pi \mapsto \pi^*$) transition on the benzopyran moiety and the S_2 state as a charge-transfer state from the indoline moiety to the benzopyran side. The leading NTO pairs for both the S_1 and S_2 states are shown Fig. 6.2. Their contribution to the total excitations are 78.1 % and 79.7 % for the S_1 and S_2 state, respectively.

In the FDE-ADC(2) calculation, the excitation energy of the S_1 state is increased while the excitation energy of the S_2 state decreases. The excitation energies (oscillator strengths) of S_1 and S_2 are now 4.222 eV (0.0438) and 4.265 eV (0.0096), respectively. However, their transition character is not changed compared

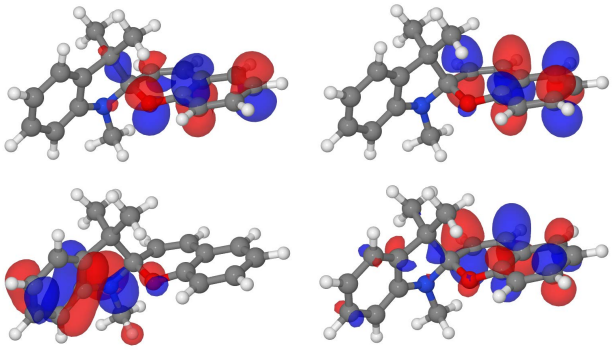

Figure 6.2: HONTO (left) and LUNTO (right) of the S_1 (top) and S_2 (bottom) state of isolated spiropyran.

to isolated spiropyran. Again, the "bright" state is the S_1 state while the S_2 state corresponds to the "dark" state. The leading NTO pairs of the two energetically lowest excited states are given in Fig. 6.3 with contributions of 77.5 % and 79.8 % for S_1 and S_2, respectively.

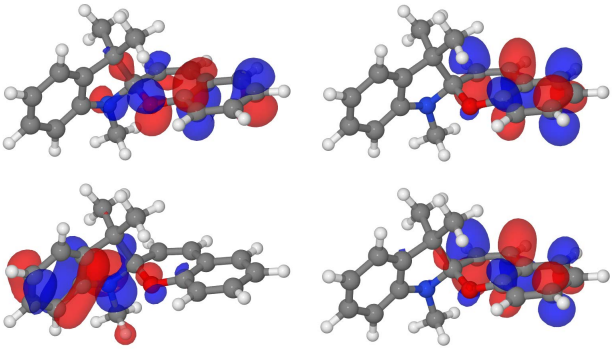

Figure 6.3: HONTO (left) and LUNTO (right) of the S_1 (top) and S_2 (bottom) state of spiropyran calculated with FDE-ADC(2).

These results confirm the previous studies of spiropyran in water on QM/MM level of theory.[30] The water environment shifts the vertical excitation energies slightly but does not affect the photochemistry of spiropyran significantly, it still functions as a photoswitch in water.

6.2 Splitting of excited stats of para-benzoquinone in methanol

To simulate para-benzoquinone in methanol solution, a para-benzoquinone molecule was surrounded by 42 methanol molecules. Benzoquinone was chosen as an example because it is a symmetric molecule of moderate size, has a delocalized π-electron system, can act as hydrogen bond acceptor and exhibits low-lying electronically excited states with both single- and double-excitation character. Therefore, a quantum chemical method including doubly excited configurations in more than zeroth order of perturbation theory, like ADC(3), is needed to describe these excitations properly.[108] Since benzoquinone is soluble in moderately polar solvents, methanol was chosen as environment. The supersystem is shown in Fig. 6.4.

Isolated benzoquinone was optimized at MP(2)/cc-pVTZ level of theory. This geometry serves as the reference for gas phase calculations. Additionally, the supersystem of benzoquinone and 42 methanol molecules placed around the benzoquinone was fully optimized at DFT/ωB97X-D3/6-31G* level of theory. This

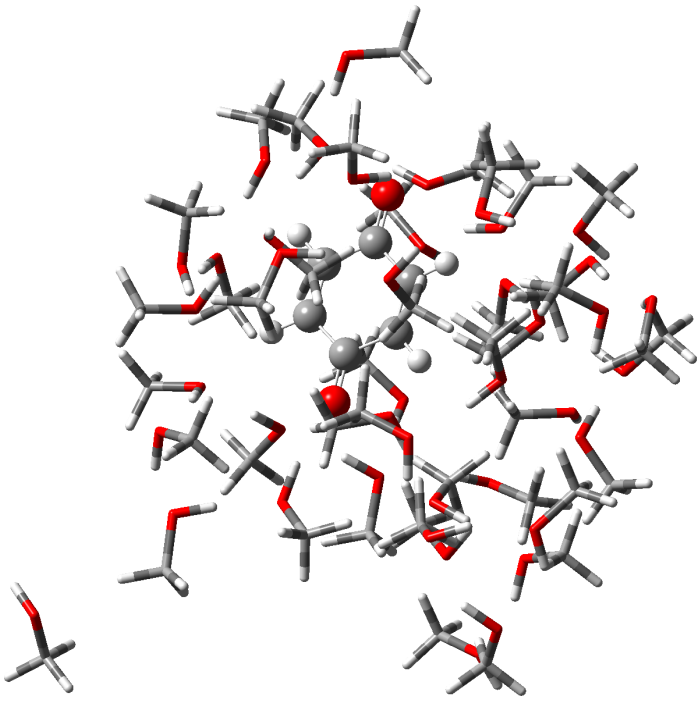

Figure 6.4: Supersystem of para-benzoquinone (balls and sticks, embedded system (A)) and 42 methanol molecules (environment (B)).

structure was used for the investigations of the effects of the environment. The two energetically lowest excited states of p-benzoquinone are investigated at ADC(3)/6-311G** level of theory for the two isolated benzoquinone structures i.e. one optimized at MP(2) level in the gas phase and the other cut out of the methanol environment, and at FDE-ADC(3)/6-311G** level of theory for including the effect of the environment on p-benzoquinone. For the FDE-ADC(3) calculation, the RADM approximation was used, the density of the environment was calculated at HF level of theory and the non-electrostatic part of the embedding potential was calculated employing the PBE functional.

In the gas phase, these states are with excitation energies of 2.840 eV and 2.999 eV close in energy. Both are ($n \mapsto \pi^*$) states each containing transitions from both n orbitals localized at the oxygen atoms. Therefore, both excited states have practically no oscillator strength. The excitation character is visualized by attachment and detachment densities (Fig. 6.5). The detachment density is that part of the total electron density that is removed upon excitation and replaced by the attachment density. In combination, they unambiguously characterize the electronic transition. As can readily be seen, both attach- and detachment densities of both states are delocalized over both oxygen atoms and the central ring.

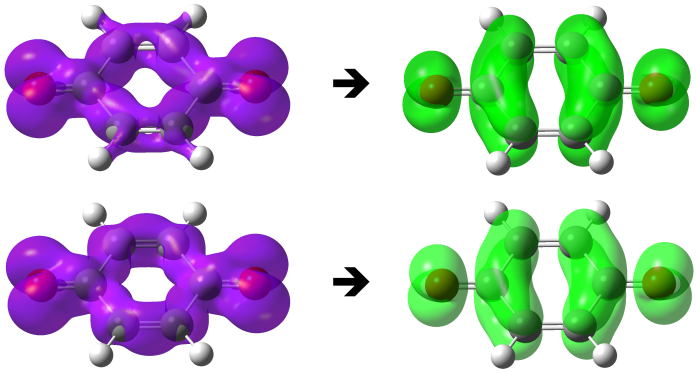

Figure 6.5: Detachment (left) and attachment (right) densities of the S_1 (top) and S_2 state of isolated gas phase p-benzoquinone.

A very similar excitation pattern is obtained for the supersystem-optimized isolated benzoquinone structure. Both S_1 and S_2 exhibit ($n \mapsto \pi^*$) transition character. Since the geometry is somewhat different, also the excitation energies vary slightly and correspond to 2.893 eV and 3.077 eV for S_1 and S_2, respectively. The oscillator strength of both states is still zero, and also the attachment and

detachment densities are practically identical to the gas phase picture. However, they are slightly distorted due to the solvation-induced changes in the geometry. The attachment and detachment densities are shown in Fig. 6.6. Still, the attachment and detachment densities are delocalized as observed in the isolated gas phase results.

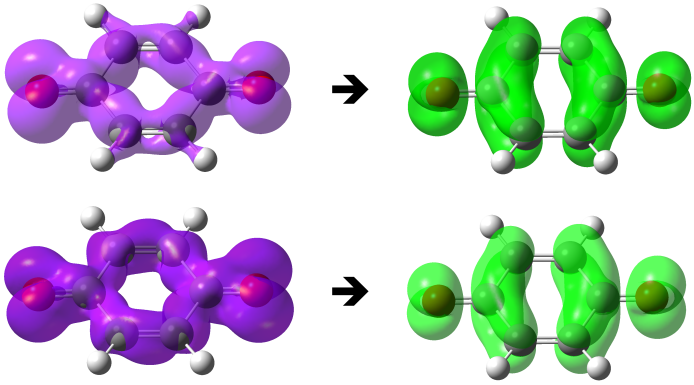

Figure 6.6: Detachment (left) and attachment (right) densities of the S_1 (top) and S_2 state of supersystem-optimized isolated p-benzoquinone.

A different picture is obtained when the environment is included via FDE. While the excitation energy of the first excited state is almost identical to the isolated calculation in the supersystem-optimized geometry, the excitation energy of the second excited state is increased by about 0.23 eV. Although both are still ($n \mapsto \pi^*$) states, they are now localized on one of the oxygen atoms each. Hence, the environment induces a separation and localization of the two excited states. This is nicely seen in the attachment and detachment densities (Fig. 6.7).

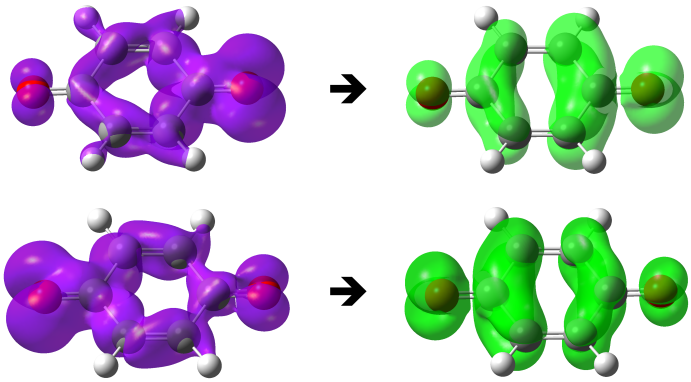

Figure 6.7: Detachment (left) and attachment (right) densities of the S_1 (top) and S_2 state (bottom) of p-benzoquinone embedded in 42 methanol molecules at FDE-ADC(3) level of theory.

6.3 Core excited states of carbon monoxide in fullerene

For the computation of core-excited states, the core-valence separation can be employed within ADC schemes which has recently been implemented in Q-Chem as the CVS-ADC method.[218–221] In CVS-ADC, the coupling terms between core- and valence excitations are neglected. Since the energy difference between these two kinds of excitations is very large, the coupling is very weak and hence this is a good approximation. This facilitates the calculation of energetically high lying core-excited states dramatically.

In this section the influence of a C_{60} cage on the core excitations of a carbon monoxide incorporated in C_{60} are demonstrated. For that purpose, CO@C_{60} was created and fully optimized at DFT/ωB97X-D3/6-31G* level of theory. The system is shown in Fig. 6.8.

For comparison the five energetically lowest (C_{1s})-core excited states were calculated at CVS-ADC(2)-x/6-311++G** level of theory for isolated CO. The core-excited states S_1^c to S_5^c exhibit the following character: ($C_{1s} \mapsto \pi^*$), ($C_{1s} \mapsto \pi^*$),

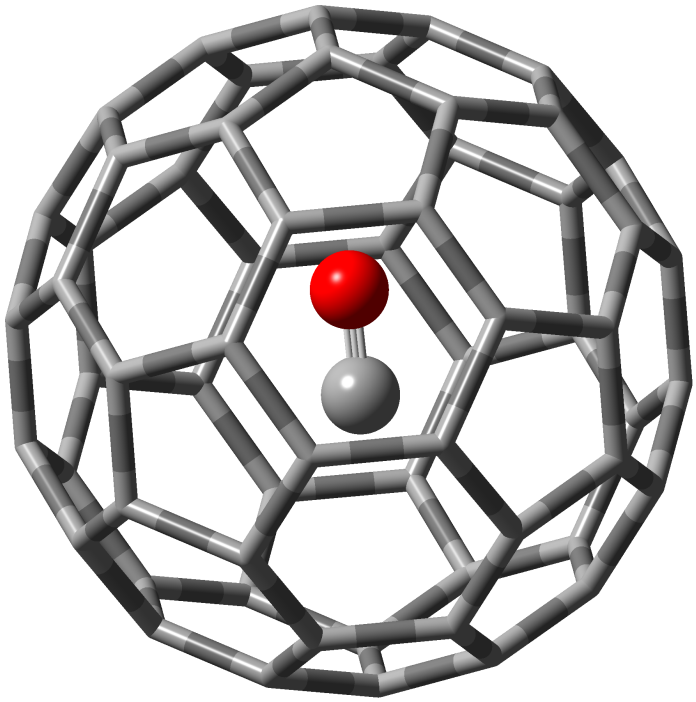

Figure 6.8: CO@C_{60}, drawn as balls and sticks (embedded system (A)) and C_{60} molecule (environment (B)).

($C_{1s} \mapsto \sigma^*$), ($C_{1s} \mapsto \pi^*$) and ($C_{1s} \mapsto \pi^*$) respectively. The corresponding excitation energies are given in Tab. 6.1. S_1^c and S_2^c as well as S_4^c and S_5^c are degenerate.

Employing the FDE-ADC approach for including the effect of C_{60}, the five energetically lowest core excited states were recalculated including the embedding potential obtained from a HF calculation for the electron density of C_{60} and the PBE functional for the non-electrostatic part of $v_{emb}^{lin}(\vec{r})$ using the RADM approximation.

Table 6.1: Excitation energies (in eV) and oscillator strengths (in parentheses) of the five energetically lowest C_{1s}-core excitations of isolated CO and CO@C_{60} using the FDE-CVS-ADC(2)-x method.

	Core excited states C_{1s}	
state	Iso. CVS-ADC(2)-x	FDE-CVS-ADC(2)-x
S_1	287.730 (0.071)	287.656 (0.073)
S_2	287.730 (0.071)	287.659 (0.073)
S_3	293.299 (0.004)	293.493 (0.003)
S_4	294.577 (0.010)	294.593 (0.006)
S_5	294.577 (0.010)	294.628 (0.007)

Including the environment in the calculation of core excited states via FDE-CVS-ADC shows only small influences. All calculated C_{1s}-core excited states are very similar to the results obtained for isolated CO regarding energies as well as properties and characters. This is verified by difference density analyses. The largest energetic shift is observed for the S_3^c state with about 0.2 eV to higher energies in the endohedral case. The excitation character of all five calculated states is retained. However, since C_{60} breaks the symmetry of CO, S_1^c and S_2^c as well as S_4^c and S_5^c are not fully degenerate any more. In Table 6.1, the excitation energies and oscillator strengths for the five energetically lowest C_{1s}-core excitations are given.

The difference density plots for the core excited states of CO@C_{60} obtained using the FDE-CVS-ADC method are qualitatively identical to the ones obtained for isolated CO. Note, that in the core excited difference density plots most of the change in electron density is due to orbital relaxation effects.[221] The difference densities for the five energetically lowest C_{1s}-core excited states S_1^c to S_5^c obtained using FDE-CVS-ADC(2)-x are shown in Fig. 6.9

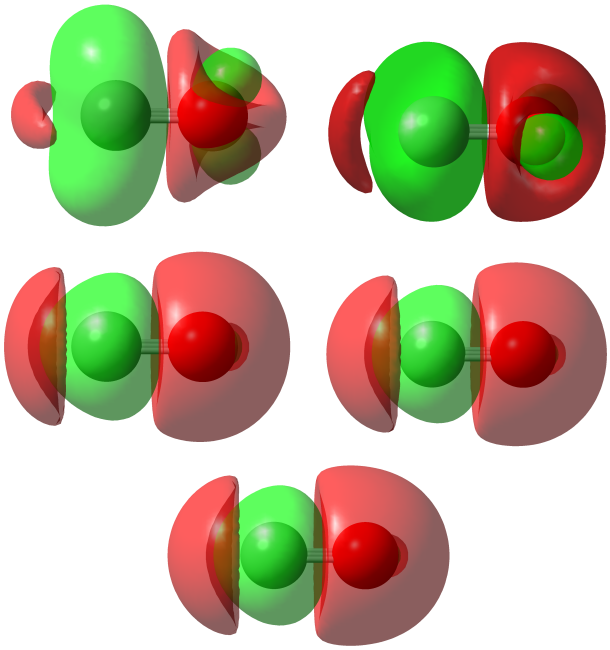

Figure 6.9: C_{1s}-core excited difference density plots of S_1^c (top left), S_2^c (top right), S_3^c (middle left), S_4^c (middle right) and S_5^c (bottom) of $CO@C_{60}$ calculated using FDE-CVS-ADC(2)-x. The difference density plots for isolated CO are practically identical.

Chapter 7

Polarization of the Environment

"The scientist only imposes two things, namely truth and sincerity, imposes them upon himself and upon other scientists."
Erwin Schrödinger

Until now, in FDE-ADC the core system was embedded in the frozen density of the isolated environment, which was accomplished by incorporating the embedding potential in the ground state calculation of the embedded system. Although the tests have shown that this works well also for excited states, it covers only a part (albeit the biggest one) of the total interaction between central system and environment. A more specific and even mutual interaction between the two subsystems is missing. Also, the changed electronic structure due to the excitation of the embedded system is not considered. This mutual interaction, or back-interaction of the embedded system influencing the environment is referred to as *environment polarization*. Note that still only electronic interactions are considered. Neither a geometric adaption of the embedded system nor the environment is included at this point. These will become important when going beyond instantaneous effects like for photoreactions or fluorescence calculations.

In this section, I will go beyond the approximation of a *frozen* environment density and present mainly two different types of environment polarization as well as their implementation in the module `fdeman` in `Q-Chem` and its application in some test calculations. However, I would like to emphasize that this is still in development and all presented results should be considered preliminary. Change of the results due to improvements or bug fixes cannot be excluded.

7.1 Variants of environment polarization

Environment polarization beyond the frozen density approximation can be divided into two important subcategories. In FDET, the two individual systems are initially treated in the gas phase. This means that the environment density $\rho_B(\vec{r})$, in which the central system is embedded, is calculated for an isolated system B without the presence of system A. But in reality, without perturbation, all molecules are fully equilibrated with their environment. This includes a mutual interaction, which is missing here. Thus, the first category of environment polarization is attributed to the ground state interaction between embedded system and environment. This is accomplished by not using a gas phase density of the environment in the calculation of the embedding potential but rather a density which was calculated under the electrostatic influence of the embedded system. Since this affects the environment density directly before the calculation of the embedding potential, it is referred to as *pre-polarization.*[238] As a method to better describe the fully equilibrated condition, it is most beneficial in ground state calculations.

In an excitation process, the embedded system is not equilibrated with the environment anymore due to the absorption of a photon (here we assume that only the central system absorbs a photon and the environment stays in the electronic ground state). The electronic structure changes, it differs from the electronic ground state structure, but also from the structure of other excited states. This change of the electronic structure depends partly on the electronic structure of the environment. This is considered in classical FDET. However, the change of the electronic structure of the embedded system also induces fluctuations in the environment electron density. This leads to a mutual interaction of the embedded system and the environment, which directly influences the absorption properties. The excited state electron density of the embedded system equilibrates with the electron density of the environment, which represents the final point in time in the photon absorption process. This influence of the excited embedded system onto the environment is referred to as *excitation-induced environment polarization.*[239]

Using FDET for describing environment influences, using either (or both) of the mentioned approaches to relax the previously frozen environment and letting it adapt to a given electron structure of the embedded system can improve the description of the system. However, an overestimation of the environment polarization might occur, since always a full self-consistent equilibration of the two subsystems is assumed, which cannot be guaranteed in reality.

7.2 Implementation of environment pre-polarization

As mentioned before, the electron density of the environment, $\rho_B(\vec{r})$, which is used to calculate the embedding potential, is calculated in the gas phase. For inclusion of pre-polarization, it is calculated under the influence of the embedded system A. Therefore, the electron density of system A, $\rho_A^{ref}(\vec{r})$, is typically calculated before $\rho_B(\vec{r})$. This allows the calculation of a potential of A acting on B. This can be accomplished by means of a potential obtained from a charge distribution, e.g. Mulliken charges[240] of A or rather as an electrostatic potential created by the nuclear charges and the electron density according to Eq. 7.1.

$$v_{emb}^{prepol}[\rho_A, v_A](\vec{r}) = v_A(\vec{r'}) + \int \frac{\rho_A(\vec{r'})}{\left|\vec{r} - \vec{r'}\right|} d\vec{r} \tag{7.1}$$

This potential is subsequently added to the Fock matrix of B during the SCF.

The pre-polarization of B is implemented into `Q-Chem` as part of the module `fdeman`. If activated upon user request by the Boolean parameter *prepol* in combination with the specification of the type via the parameter *prepol_type* in combination with the option *"density"* or *"coulombic"*, an FDE-ADC calculation including pre-polarization of B is performed. As indicated by the parameter *prepol_type*, `fdeman` is prepared also for other types of expressing the influence of A on B, e.g. using the aforementioned Mulliken charges.

In `fdeman`, the pre-polarization is performed by the function `make_prepol`, which is called from `fde_control` between the calculation of $\rho_A^{ref}(\vec{r})$ and $\rho_B(\vec{r})$. In principle, it just contains calls of the functions `compute_nuclear_potential` and `compute_coulomb_potential`, which were introduced in Sec. 4.2.3.1. But this time, these functions are called with the parameter for fragment A instructing the functions not to calculate the potential of fragment B but rather of fragment A. This is always performed using supermolecular expansion, since B is always treated in the supermolecular basis. Also, in `make_prepol`, a flag is set instructing `scfman` to read in the previously exported potentials and to add them to the Fock matrix as described in Sec. 4.2.3.3.

If $\rho_A^{ref}(\vec{r})$ is calculated first, the pre-polarization can be performed with only a minor cost of computational time compared to a standard FDE-ADC calculation.

7.3 Implementation of environment polarization due to excitation of the embedded system

In the scope of FDET, excitation-induced environment polarization can be carried out using a similar approach as applied for the pre-polarization. However, it contains some important differences. Since the influence of an excitation of the embedded system on the environment shall be considered, the excited states including the effect of the environment have to be calculated at first. Therefore, the environment polarization is considered after employing the embedding potential instead of before as done in the pre-polarization approach. Additionally, the mutual interaction between the excited state density of the embedded system and the environment has to be calculated iteratively until self-consistency. This is done by exchanging the two subsystems and embedding the environment in the density of the embedded system. After this, the systems are switched again until convergence is reached. This is known as *freeze and thaw* cycles, since both subsystem densities are alternately kept frozen and relaxed.[239] Obviously, this is a state-specific approach which has to be converged for each investigated state separately. Here, an approximation to these freeze and thaw cycles is used. Instead of performing macro-cycles until convergence, here only one cycle consisting of switching twice (*"there and back again"*) without full convergence is applied. This is denoted as *state-specific iteration (SSI)*. This approximation is valid since freeze and thaw cycles converge typically in less than 10 cycles[239] and the first cycle is the dominant one. Fully converging using multiple cycles is not only very demanding in terms of computational time considering the scaling of ADC, it also includes the problematic of changing states. This can be described by two states changing their energetic order due to the environment interaction. The polarization is then calculated for the wrong state in the following cycle.

A completely new approach for including the excitation-induced environment polarization is using a perturbative-like energy correction. In this new approach, a polarization potential is created from the difference density of B embedded in the i^{th} excited state of A minus B embedded in the ground state of A. This potential is subsequently contracted with the i^{th} excited state difference density of A to yield an energy correction for the i^{th} excited state accounting for the environment polarization. This approach is denoted *difference density polarization potential (DDPP)*.

Both variants are implemented as part of `fdeman` in the function `fde_pol-`

`control`. Depending on user request, either polarization via SSI or DDPP is calculated. This can be controlled in the *$fde* input section with the Boolean keyword *polarization_B*. The type of environment polarization is specified with the keyword *polarization_B_type* and the parameters *SSI* or *DDPP* to request the corresponding variant.

7.3.1 Polarization via state-specific iteration

7.3.1.1 Supermolecular expansion

For the calculation of SSI environment polarization, at first a normal FDE-ADC calculation has to be performed. Applying linearized FDET, the applied embedding potential is defined as:

$$v_{emb}^{A}[\rho_A^{ref}, \rho_B, v_B](\vec{r}) = v_B(\vec{r}) + \int \frac{\rho_B(\vec{r}')}{\left|\vec{r} - \vec{r}'\right|} \mathrm{d}\vec{r}' + \frac{\delta E_{xc,T}^{nad}[\rho_A^{ref}, \rho_B]}{\delta \rho_A^{ref}(\vec{r})}. \tag{7.2}$$

After this initial calculation, the state-specific environment polarization is calculated. This can be understood as a macrocycle which has to be performed once for each excited state of A. This is illustrated in Fig. 7.1. The embedding potential in Eq. 7.2 is applied in step 1. After the initial calculation of the excited states including ground state embedding in step 2, the two subsystems are interchanged for the first time. B is now embedded in the total first excited state density of A. This is done in step 3. As always, linearized FDET is applied, but now the linearization is done in $\rho_B(\vec{r})$. The embedding potential for embedding B in the i^{th} excited state total electron density reads:

$$v_{emb}^{B}[\rho_A^{i}, \rho_B^{ref}, v_A](\vec{r}') = v_A(\vec{r}') + \int \frac{\rho_{A_{emb}}^{i}(\vec{r})}{\left|\vec{r} - \vec{r}'\right|} \mathrm{d}\vec{r}' + \frac{\delta E_{xc,T}^{nad}[\rho_{A_{emb}}^{i}, \rho_B^{ref}]}{\delta \rho_B^{ref}(\vec{r})}. \tag{7.3}$$

The embedding potential is created analogously to the embedding potential acting on A by the functions `compute_nuclear_potential`, `compute_coulomb_potential` and `compute_xct_potential` as described in Sec. 4.2.3.1. Then, a ground state calculation of B is performed under the influence of the embedding potential by adding the embedding potential to the Fock matrix of B during the SCF. Therefore, in `fde_polcontrol` a flag is set to enable the read-in of the embedding potential in `scfman`. This new calculation of B represents step 4. Now, a new embedding potential of the polarized $\rho_B(\vec{r})$ acting on A is created (step 5). It depends on the polarized density of B and the already embedded density of A

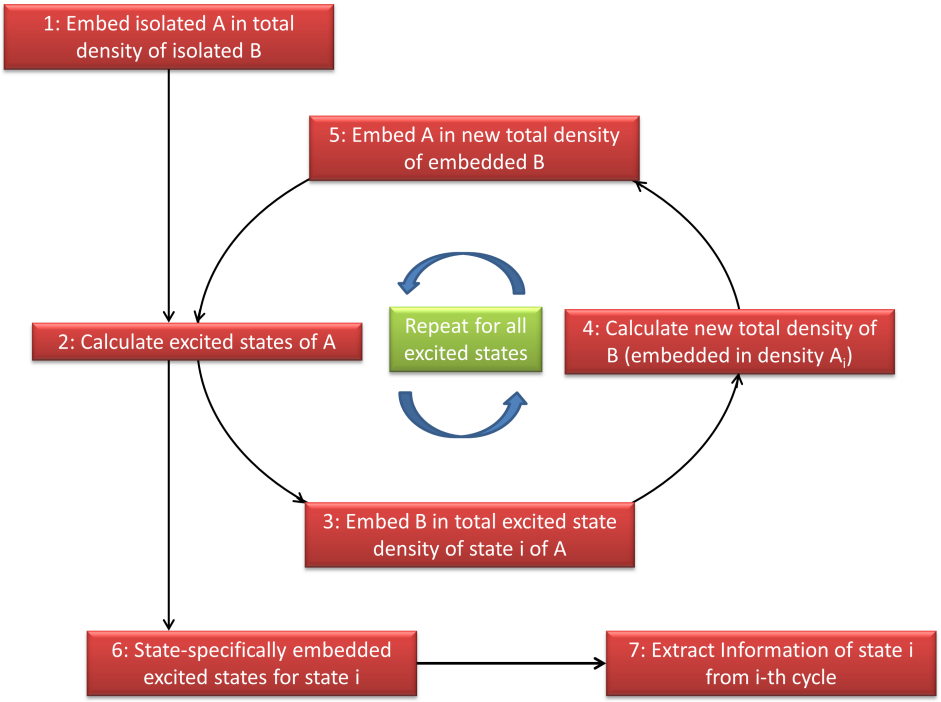

Figure 7.1: Flowchart of excitation-induced environment polarization via state-specific iteration. Implemented in the function `fde_polcontrol` within `fdeman`.

from the initial FDE-ADC calculation. This embedding potential is given as

$$v^A_{emb}[\rho^{ref}_{A^i_{emb}}, \rho_{B_{pol}}, v_B](\vec{r}) = v_B(\vec{r}) + \int \frac{\rho_{B_{pol}}(\vec{r}')}{|\vec{r} - \vec{r}'|} \mathrm{d}\vec{r}' + \frac{\delta E^{nad}_{xc,T}[\rho^{ref}_{A^i_{emb}}, \rho_{B_{pol}}]}{\delta \rho^{ref}_{A^i_{emb}}(\vec{r})}. \quad (7.4)$$

This potential acting on A is again added to the Fock matrix during the SCF. After the ground state calculation, an excited state ADC calculation is performed similarly to the initial FDE-ADC calculation. This yields state-specifically embedded excited states for the i^{th} excited state (step 6).

In summary, for the calculation of the excited states of A embedded in the electron density of B including the excitation-induced environment polarization via SSI, after the initial FDE-ADC calculation with ground-state embedding, for each excited state of A the following tasks are performed: creation of an embedding potential of A acting on B, performing an embedded ground state calculation of B, creating a new embedding potential of B acting on A containing the now polarized environment density and finally performing an excited state calculation of A on ADC level of theory. As a consequence, in each cycle, all requested excited states

are calculated. From these excited states, the state corresponding to each cycle has to be extracted. Since excited states might swap due to the modified influence of the environment interaction, this has to be done by hand. The corresponding excited states have to be chosen based on excitation energy, excitation properties and orbital transitions characterizing the state.

If the presented cycle is repeated from step 2 to 6 until the electron densities of A and B are self-consistent instead of only once as done here, this would represent the full freeze and thaw procedure.

7.3.1.2 Re-assembling of density matrix

In the supermolecular expansion, the implementation is directly realized as described above. Using the RADM approximation, additional steps have to be considered. Since the ADC calculation is performed in the monomer basis yielding density matrices only in the basis functions of A, but an embedding potential acting on B is required, again a re-assembled density matrix has to be created, but this time using the ADC excited state density matrix in the AA block.

After the initial FDE-ADC calculation in step 1 and 2, the original uncut embedding potential is retrieved and used to perform a embedded HF ground state calculation of A embedded in B in the supermolecular basis. This yields the embedded HF density matrix in the basis of A and B. In combination with the previously calculated ADC density matrix of A in the basis of A, the new excited state re-assembled density matrix is built. This can be used to construct the embedding potential on B in step 3. Step 4 is performed as described for the supermolecular expansion. For the state-specific embedding calculation of A in B in steps 5 and 6, the embedding potential is constructed from the polarized supermolecular ground state density matrix of B and the re-assembled excited state density matrix of A and again cut to the basis functions of A only. Then, the SSI FDE-ADC calculation of A can be performed in the monomer basis.

7.3.2 Polarization via difference density polarization potential

7.3.2.1 Supermolecular expansion

In the SSI approach for calculation of the excitation-induced environment polarization, the excited states of A have to be calculated several times. Since ADC calculations are known to be very demanding in computational cost, this might exceed the given timescale. The difference density polarization potential

(DDPP) approach is designed to yield energy corrections for the polarization of the environment without the need of recalculating the excited states of A.

The total process of DDPP is illustrated in Fig. 7.2. At first, a normal FDE-ADC calculation has to be performed to calculate the excited states of A embedded in the isolated density of B (step 1 and 2). The employed linearized embedding potential is given as

$$v_{emb}^{A}[\rho_A^{ref}, \rho_B, v_B](\vec{r}) = v_B(\vec{r}) + \int \frac{\rho_B(\vec{r}\,')}{\left|\vec{r} - \vec{r}\,'\right|} \mathrm{d}\vec{r}\,' + \frac{\delta E_{xc,T}^{nad}[\rho_A^{ref}, \rho_B]}{\delta \rho_A^{ref}(\vec{r})}. \tag{7.5}$$

As a result of this FDE-ADC calculation, a total ground state electron density and N total excited state electron densities are obtained with N being the amount of calculated excited states. Now, the further procedure is split. On the one side, the ground state electron density is used, on the other side the excited state electron densities. Similar to the freeze and thaw approach, the subsystems are interchanged. An embedding potential of the embedded ground state (GS) density onto the environment is created (step 3a). This is done analogously as described in Sec. 4.2.3.1. The calculated embedding potential is defined as:

$$v_{emb}^{B_{GS}}[\rho_A^{GS}, \rho_B^{ref}, v_A](\vec{r}\,') = v_A(\vec{r}\,') + \int \frac{\rho_{A_{emb}}^{GS}(\vec{r})}{\left|\vec{r} - \vec{r}\,'\right|} \mathrm{d}\vec{r}\,' + \frac{\delta E_{xc,T}^{nad}[\rho_{A_{emb}}^{GS}, \rho_B^{ref}]}{\delta \rho_B^{ref}(\vec{r})}. \tag{7.6}$$

This embedding potential is applied in a ground state calculation of B in step 4a. As a result, an embedded ground state electron density of the environment $\rho_{B_{emb-GS}}^{S_0}$ is obtained. On the other side, a similar potential is created but this time using the i$^{\text{th}}$ excited state electron density (step 3b). The embedding potential is given as:

$$v_{emb}^{B_{ES_i}}[\rho_A^{ES_i}, \rho_B^{ref}, v_A](\vec{r}\,') = v_A(\vec{r}\,') + \int \frac{\rho_{A_{emb}}^{ES_i}(\vec{r})}{\left|\vec{r} - \vec{r}\,'\right|} \mathrm{d}\vec{r}\,' + \frac{\delta E_{xc,T}^{nad}[\rho_{A_{emb}}^{ES_i}, \rho_B^{ref}]}{\delta \rho_B^{ref}(\vec{r})}. \tag{7.7}$$

Again, applying the embedding potential in a ground state calculation of B yields a second ground state electron density $\rho_{B_{emb-ES_i}}^{S_0}$ (step 4b). This includes the influence of the i$^{\text{th}}$ excited state of A on B while the electron density $\rho_{B_{emb-GS}}^{S_0}$ of step 4a includes the influence of the ground state of A on B. Subtracting these two densities yields a difference density

$$\Delta\rho_{B_{ES_i-GS}}^{S_0}(\vec{r}) = \rho_{B_{emb-ES_i}}^{S_0}(\vec{r}) - \rho_{B_{emb-GS}}^{S_0}(\vec{r}) \tag{7.8}$$

describing the effect of the excitation of A on the electron density of B (step 5).

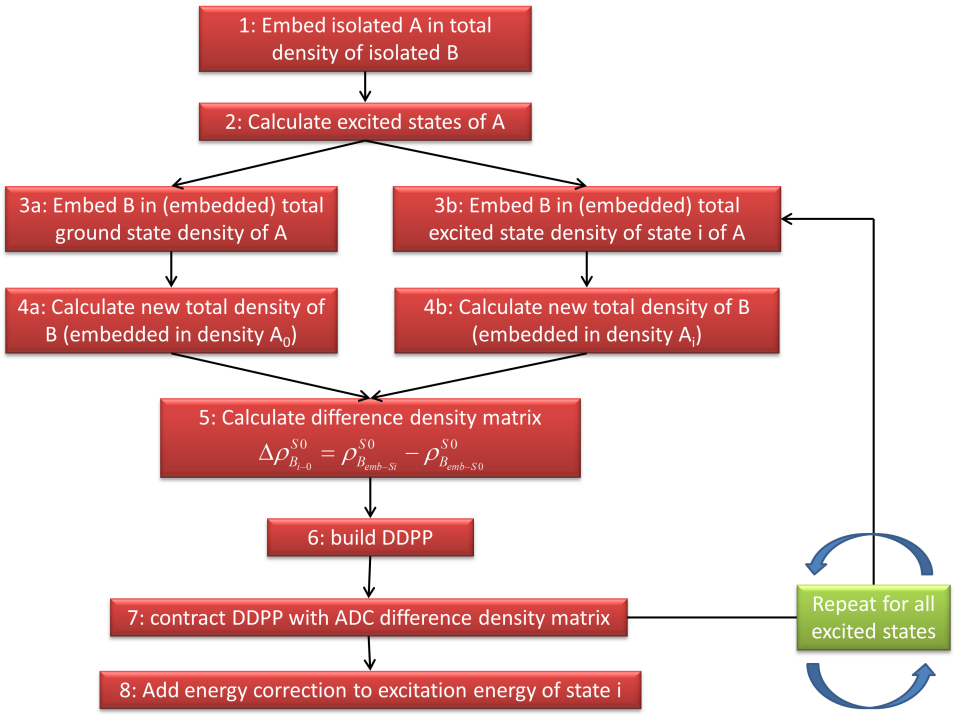

Figure 7.2: Flowchart of excitation-induced environment polarization via difference density polarization potential. Implemented in the function `fde_polcontrol` within `fdeman`.

This difference density is used to create another potential. Because of the used difference density, it is named *difference density polarization potential*. Also, this potential is linear in A. It is defined as

$$v_{DDPP}^{A_{ES_i-GS}}[\rho_{A_{emb}}^{GS_{ref}}, \Delta\rho_{B_{ES_i-GS}}^{S_0}](\vec{r}\,') = \int \frac{\Delta\rho_{B_{ES_i-GS}}^{S_0}(\vec{r}\,')}{|\vec{r}-\vec{r}\,'|}\mathrm{d}\vec{r}\,' + \frac{\delta E_{xc,T}^{nad}[\rho_{A_{emb}}^{GS_{ref}}, \Delta\rho_{B_{ES_i-GS}}^{S_0}]}{\delta\rho_{A_{emb}}^{GS_{ref}}(\vec{r})}. \tag{7.9}$$

It is important to note that no nuclear potential is contained in the DDPP, since this does not depend on the polarization induced in the environment and therefore cancels out. For each i^{th} excited state of A, a potential is obtained. In step 7 this potential is contracted with the corresponding ground to i^{th} excited state electron

difference density of A.

$$\int \Delta\rho_{A_{emb}}^{ES_i-GS}(\vec{r}) \cdot v_{DDPP}^{A_{ES_i-GS}}[\rho_{A_emb}^{GS_{ref}}, \Delta\rho_{B_{ES_i-GS}}^{S_0}](\vec{r}\,') = E_{pol}^{ES_i} \tag{7.10}$$

Addition of this energy correction to the excitation energy of state i yields the final excitation energy including the effect of the excitation-induced environment polarization (step 8).

It should be pointed out that here only a ground state calculation of B for each excited state of A is needed while in SSI, both a ground state calculation of B and an excited state calculation of A for each excited state of A is needed.

7.3.2.2 Re-assembling of density matrix

As in the SSI procedure, additional steps have to be included when the RADM approximation is used. A ground state embedding calculation of A in B in the supermolecular basis has to be performed after the FDE-ADC calculation in steps 1 and 2 using the uncut embedding potential of step 1. Then, as described above, a re-assembled density matrix of A has to be created to build the embedding potentials used in steps 3a and 3b. The AA block used for the construction is either an MP(2) difference density for 3a or an ADC difference density for 3b. The process proceeds similarly as in SE with the embedding of B in both the ground state of A and separately in the i$^{\text{th}}$ excited state of A in steps 4a and 4b, respectively. From these densities, the difference density is built and the difference density polarization potential is calculated according to steps 5 and 6. The used electron density of A is the embedded ground state reference density expressed as the re-assembled density matrix created in the beginning after step 2. For the contraction, the polarization potential is cut to the basis functions of A, since the ADC difference density is also only given in the monomer basis.

7.4 Results

In this section, the aforementioned variants of environment polarization are tested. Although no full comprehensive benchmark is performed, the tests provide insights into the capabilities of the various methods. All tests have been performed on FDE-ADC(2)/cc-pVDZ level of theory and are compared with the supersystem calculations and the FDE-ADC(2) calculations without environment polarization according to the benchmark presented in Secs. 5.2 and 5.3. The tests are performed using one or more of the benchmark molecules presented in Sec. 5.1.

7.4.1 Pre-polarization of the environment

At first, the pre-polarization of the environment has been tested using the system $[\mathrm{BA} \cdot 2\,\mathrm{H_2O}]$. Therefore, an electrostatic embedding potential of A is created before calculation of the environment electron density. This potential is used to calculate $\rho_B(\vec{r})$ under the influence of the nuclei and ground state electron density of A.

The five energetically lowest excited states have been calculated. In this test, the RADM approximation was employed and analogously to the FDE-ADC(2) benchmark, HF was used for the calculation of the environment and the xc-functional PBE was employed for the calculation of the non-electrostatic embedding potential. The excitation energies and oscillator strengths are listed in Tab. 7.1. For comparison, also the unpolarized FDE-ADC(2) results and the supermolecular ADC(2) results are given.

Table 7.1: Excitation energies and oscillator strengths for the pre-polarized FDE-ADC(2)/cc-pVDZ calculation in the RADM approach for the $[\mathrm{BA} \cdot 2\,\mathrm{H_2O}]$ system. For comparison, the results of the supermolecular ADC(2) and unpolarized FDE-ADC(2) calculations are given as well.

	Exc. Energies [eV]			Osc. Strength		
state	supersys.	unpol.	pre-pol.	supersys.	unpol.	pre-pol
S_1	3.897	3.878	3.888	0.0001	0.0001	0.0001
S_2	4.813	4.851	4.847	0.0197	0.0164	0.0167
S_3	5.554	5.628	5.620	0.3444	0.3490	0.3502
S_4	6.751	6.732	6.755	0.0059	0.0001	0.0001
S_5	6.753	6.803	6.799	0.2942	0.2979	0.2943

The inclusion of the pre-polarization in the FDE-ADC(2) calculation slightly

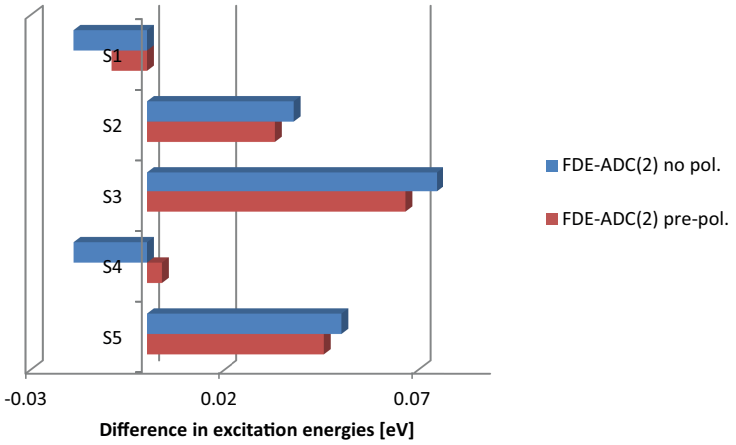

Figure 7.3: Analysis of the accuracy of pre-polarization for RADM-FDE-ADC(2) in [BA · 2 H_2O]. The deviation of excitation energies to the supermolecular ADC(2) calculation is given for unpolarized FDE-ADC(2) (blue) and including pre-polarization (red).

In comparison with the unpolarized calculation, the pre-polarization shows improvement for each state. However, since including the pre-polarization using the coulombic interaction hardly increases the computational cost of an FDE-ADC calculation, it is a promising and efficient improvement over unpolarized FDE-ADC.

7.4.2 Excitation-induced environment polarization via SSI

The state-specific iteration procedure for including excitation-induced environment polarization has been tested employing both the supermolecular expansion as well as the RADM approximation. All other settings of the test are identical to the settings described in the pre-polarization test in the previous section.

7.4.2.1 Supermolecular expansion

At first, the system [BA · 2 H_2O] was used. An SSI cycle has been performed for each of the calculated excited states. The excited states are given in Tab. 7.2. Most of the excited states are clearly better described when the polarization of

Table 7.2: Excitation energies and oscillator strengths for the SSI-polarized FDE-ADC(2)/cc-pVDZ calculation in the supermolecular expansion for the [BA · $2\,H_2O$] system. For comparison, the results of the supermolecular ADC(2) and unpolarized FDE-ADC(2) calculations are given as well.

	Exc. Energies [eV]			Osc. Strength		
state	supersys.	unpol.	SSI-pol.	supersys.	unpol.	SSI-pol
S_1	3.897	3.892	3.907	0.0001	0.0001	0.0001
S_2	4.813	4.837	4.818	0.0197	0.0174	0.0184
S_3	5.554	5.595	5.562	0.3444	0.3518	0.3566
S_4	6.751	6.743	6.731	0.0059	0.0001	0.0001
S_5	6.753	6.784	6.768	0.2942	0.2908	0.2780

the environment is included. Only the S_1 and S_4 states exhibit a slightly larger deviation. This might be due to their ($n \mapsto \pi^*$) excitation character. In contrast, for the ($\pi \mapsto \pi^*$) states, the deviation is more than halved. This is shown in Fig. 7.4 The MAE for excitation energies is reduced from 0.022 eV to 0.012 eV. The

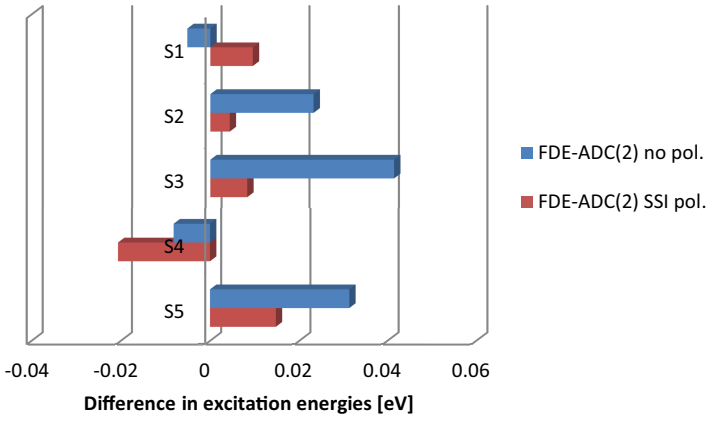

Figure 7.4: Analysis of the accuracy of SSI-polarization for SE-FDE-ADC(2) in [BA·$2\,H_2O$]. The deviation of excitation energies to the supermolecular ADC(2) calculation is given for unpolarized FDE-ADC(2) (blue) and including SSI-polarization (red).

MAE for the oscillator strength is slightly increased from 0.004 to 0.007. However, since now a different potential is employed for each excited state, the excited states are not orthogonal to each other anymore, which prevents a direct comparison of

the properties. Therefore, the oscillator strengths have to be treated with caution.

Next, the [UC · 5 H_2O] system was employed. Again, an SSI cycle has been performed for each calculated excited state. The excitation energies and oscillator strengths are given in Tab. 7.3. Most of the states are now better described.

Table 7.3: Excitation energies and oscillator strengths for the SSI-polarized FDE-ADC(2)/cc-pVDZ calculation in the supermolecular expansion for the [UC · 5 H_2O] system. For comparison, the results of the supermolecular ADC(2) and unpolarized FDE-ADC(2) calculations are given as well.

	Exc. Energies [eV]			Osc. Strength		
state	supersys.	unpol.	SSI-pol.	supersys.	unpol.	SSI-pol
S_1	5.143	5.111	5.175	0.0016	0.0007	0.0020
S_2	5.215	5.291	5.244	0.2371	0.2162	0.2077
S_3	6.211	6.223	6.244	0.0001	0.0003	0.0008
S_4	6.292	6.321	6.327	0.0963	0.0851	0.0915
S_5	6.657	6.751	6.715	0.0005	0.0023	0.0015

However, in this case, no correlation with the type of excitation is noticeable. A comparison is shown in Fig. 7.5. For the S_2 state, the deviation is more than halved,

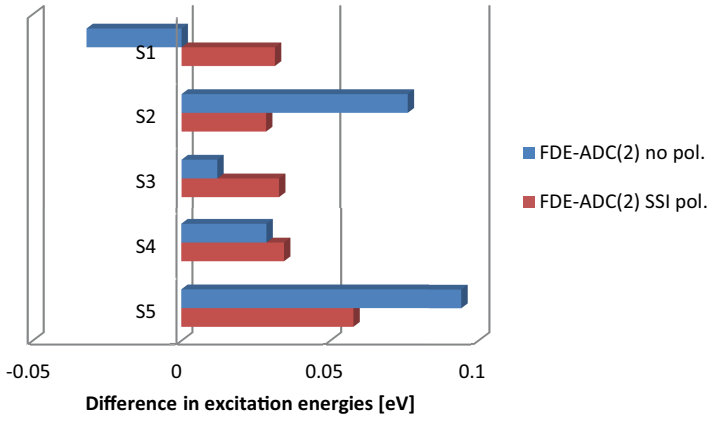

Figure 7.5: Analysis of the accuracy of SSI-polarization for SE-FDE-ADC(2) in [UC·5 H_2O]. The deviation of excitation energies to the supermolecular ADC(2) calculation is given for unpolarized FDE-ADC(2) (blue) and including SSI-polarization (red).

but not for the S_4 state although both are characterized by ($\pi \mapsto \pi^*$) transitions.

The S_5 state shows an improvement despite exhibiting an ($n \mapsto \pi^*$) character. Interestingly, the deviation of the S_1 state changes the sign, while the absolute value hardly varies. Now, the excitation energy is overestimated. The MAE for excitation energies is reduced from 0.049 eV to 0.037 eV. The MAE for the oscillator strengths is unchanged (0.007)

7.4.2.2 Re-assembling of density matrix

The SSI environment polarization scheme was also applied in combination with the RADM approximation. Again, the [BA $\cdot$ 2 H_2O] system was used first. The excitation energies and oscillator strengths are listed in Tab. 7.4. The results are

Table 7.4: Excitation energies and oscillator strengths for the SSI-polarized FDE-ADC(2)/cc-pVDZ calculation employing the RADM approach for the [BA $\cdot$ 2 H_2O] system. For comparison, the results of the supermolecular ADC(2) and unpolarized FDE-ADC(2) calculations are given as well.

	Exc. Energies [eV]			Osc. Strength		
state	supersys.	unpol.	SSI-pol.	supersys.	unpol.	SSI-pol
S_1	3.897	3.878	3.892	0.0001	0.0001	0.0001
S_2	4.813	4.851	4.835	0.0197	0.0164	0.0174
S_3	5.554	5.628	5.599	0.3444	0.3490	0.3530
S_4	6.751	6.732	6.721	0.0059	0.0001	0.0001
S_5	6.753	6.803	6.788	0.2942	0.2979	0.2866

similar to the ones obtained using supermolecular expansion. The deviations for all ($\pi \mapsto \pi^*$) states are reduced and also the S_1 state, which is characterized by an ($n \mapsto \pi^*$) transition, is now better described and exhibits a deviation of only 0.005 eV. Still, the S_4 state exhibits a slightly higher deviation. In total, the MAE for excitation energies is reduced from 0.040 eV to 0.027 eV. The MAE for oscillator strengths is only marginally changed from 0.003 to 0.005. A comparison of the excitation energy deviations is given in Fig 7.6.

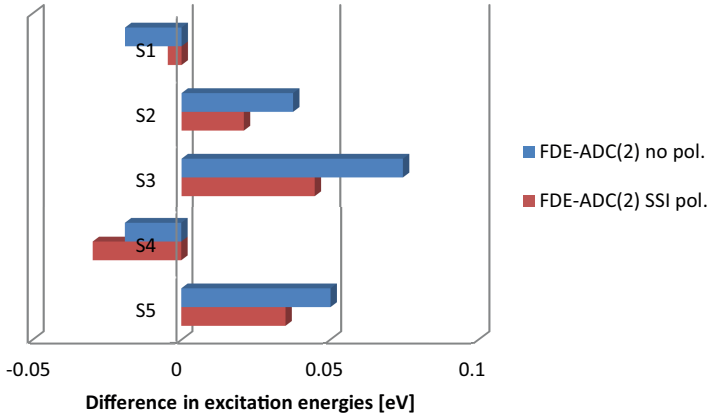

Figure 7.6: Analysis of the accuracy of SSI-polarization for RADM-FDE-ADC(2) in [BA · 2 H_2O]. The deviation of excitation energies to the supermolecular ADC(2) calculation is given for unpolarized FDE-ADC(2) (blue) and including SSI-polarization (red).

Next, the [UC · 5 H_2O] system was used for the test. The excited states are compared to the results of the unpolarized FDE-ADC(2) and supermolecular ADC(2) calculations in Tab. 7.5. The agreement to the supermolecular results

Table 7.5: Excitation energies and oscillator strengths for the SSI-polarized FDE-ADC(2)/cc-pVDZ calculation employing the RADM approach for the [UC · 5 H_2O] system. For comparison, the results of the supermolecular ADC(2) and unpolarized FDE-ADC(2) calculations are given as well.

	Exc. Energies [eV]			Osc. Strength		
state	supersys.	unpol.	SSI-pol.	supersys.	unpol.	SSI-pol
S_1	5.143	5.047	5.109	0.0016	0.0005	0.0008
S_2	5.215	5.319	5.280	0.2371	0.2092	0.1866
S_3	6.211	6.200	6.223	0.0001	0.0001	0.0002
S_4	6.292	6.331	6.335	0.0963	0.0721	0.0809
S_5	6.657	6.765	6.736	0.0005	0.0011	0.0011

are again clearly improved. The largest deviation in the S_5 state is reduced from about 0.108 eV to 0.079 eV. In the case of the first excited state, the improvement is even more pronounced. The deviation is reduced from 0.096 eV to 0.034 eV. In case of the S_3 state, although the absolute value of the deviation stays with

about 0.012 eV rather small, the sing changes. However, since the absolute value of the deviation is so small, the change of the sing is negligible. The deviation to the supermolecular ADC(2) calculation is shown in Fig. 7.7. The total MAE

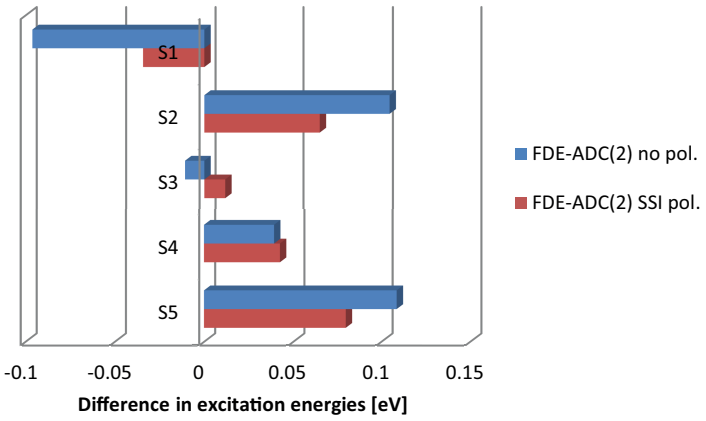

Figure 7.7: Analysis of the accuracy of SSI-polarization for RADM-FDE-ADC(2) in $[UC \cdot 5\,H_2O]$. The deviation of excitation energies to the supermolecular ADC(2) calculation is given for unpolarized FDE-ADC(2) (blue) and including SSI-polarization (red).

for excitation energies is reduced from 0.072 eV for unpolarized FDE-ADC(2) to 0.047 eV using the SSI approach. The MAE for oscillator strengths roughly stays the same with 0.011 for unpolarized compared to 0.013 using SSI.

7.4.3 Excitation-induced environment polarization via DDPP

Next, the new difference density polarization potential approach has been tested to estimate the influence of excitation induced environment polarization on the excitation energies of the embedded system. Again, both the supermolecular expansion as well as the re-assembling of density matrix approach was applied. Like in the SSI test, all other settings were retained. Note that the DDPP approach provides only an energy correction for the excitation energies. Therefore, no oscillator strengths will be given in this section.

7.4.3.1 Supermolecular expansion

We start with the first test system $[BA \cdot 2\,H_2O]$. The excitation energies are given in Tab. 7.6. Again, the unpolarized and supermolecular results are given for comparison as well. The energy correction is already added to the excitation

energies for the polarized FDE-ADC(2) results. The performance of the DDPP

Table 7.6: Excitation energies for the DDPP-polarized FDE-ADC(2)/cc-pVDZ calculation in the supermolecular expansion for the [BA · 2 H_2O] system. For comparison, the results of the supermolecular ADC(2) and unpolarized FDE-ADC(2) calculations are given as well.

	Exc. Energies [eV]		
state	supersys.	unpol.	DDPP-pol.
S_1	3.897	3.892	3.876
S_2	4.813	4.837	4.831
S_3	5.554	5.595	5.599
S_4	6.751	6.743	6.693
S_5	6.753	6.784	6.781

approach is not as good as for SSI. In some cases like in the S_4 state, the deviation to the supermolecular calculation is much higher. This might correlate with the ($n \mapsto \pi^*$) character of this state, since also for S_1 the deviation increases, which is also characterized as an ($n \mapsto \pi^*$) state. As a consequence, the MAE for excitation energies is increased from 0.022 eV to 0.034 eV. A comparison is given in Fig. 7.8.

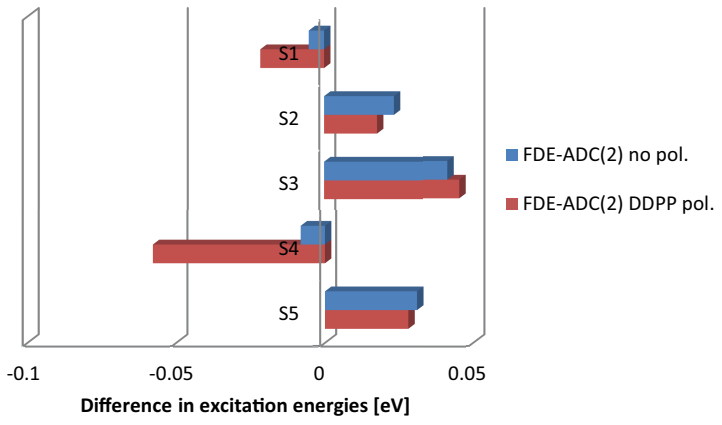

Figure 7.8: Analysis of the accuracy of DDPP-polarization for SE-FDE-ADC(2) in [BA · 2 H_2O]. The deviation of excitation energies to the supermolecular ADC(2) calculation is given for unpolarized FDE-ADC(2) (blue) and including DDPP-polarization (red).

Next, the system [UC · 5 H_2O]was tested. The excitation energies are given in Tab. 7.7. In this system, the same problem arises. In the S_1 state, the deviation to

Table 7.7: Excitation energies for the DDPP-polarized FDE-ADC(2)/cc-pVDZ calculation in the supermolecular expansion for the [UC · 5 H_2O] system. For comparison, the results of the supermolecular ADC(2) and unpolarized FDE-ADC(2) calculations are given as well.

	Exc. Energies [eV]		
state	supersys.	unpol.	DDPP-pol.
S_1	5.143	5.111	5.033
S_2	5.215	5.291	5.271
S_3	6.211	6.223	6.178
S_4	6.292	6.321	6.300
S_5	6.657	6.751	6.688

the supermolecular calculation triples from 0.032 eV to 0.110 eV. Also, in the case of S_3, the deviation increases. In contrast, the deviation is lowered for the states S_4 and S_5. A comparison of the excitation energies is given in Fig. 7.9. Here,

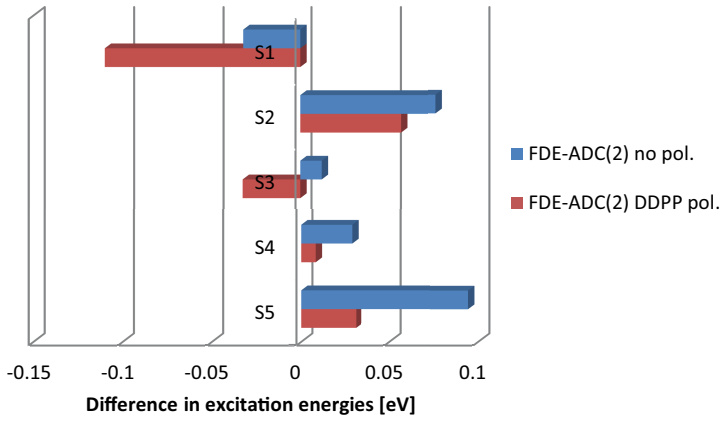

Figure 7.9: Analysis of the accuracy of DDPP-polarization for SE-FDE-ADC(2) in [UC · 5 H_2O]. The deviation of excitation energies to the supermolecular ADC(2) calculation is given for unpolarized FDE-ADC(2) (blue) and including DDPP-polarization (red).

only a partial correlation with the transition character of the state is given. Both the S_1 and S_3 state are characterized as ($n \mapsto \pi^*$) states, but also the S_5 state

exhibits ($n \mapsto \pi^*$) character. The MAE in excitation energies is hardly changed. Without environment polarization, the MAE is 0.049 eV. Including environment polarization using DDPP the MAE is 0.048 eV.

7.4.3.2 Re-assembling of density matrix

The [BA $\cdot$ 2 H_2O] system was tested again employing the RADM approximation in combination with the DDPP approach to include environment polarization. The excited states are listed in Tab. 7.8. Using the RADM approach, a similar result as

Table 7.8: Excitation energies for the DDPP-polarized FDE-ADC(2)/cc-pVDZ calculation using the RADM approach for the [BA $\cdot$ 2 H_2O] system. For comparison, the results of the supermolecular ADC(2) and unpolarized FDE-ADC(2) calculations are given as well.

	Exc. Energies [eV]		
state	supersys.	unpol.	DDPP-pol.
S_1	3.897	3.878	3.849
S_2	4.813	4.851	4.841
S_3	5.554	5.628	5.636
S_4	6.751	6.732	6.638
S_5	6.753	6.803	6.798

for SE can be seen. The two ($n \mapsto \pi^*$) states S_1 and S_4 exhibit a large deviation from the supermolecular results compared to unpolarized FDE-ADC(2). The ($\pi \mapsto \pi^*$) states are more or less described similarly to the FDE-ADC calculation without environment polarization. A comparison is shown in Fig. 7.10. The MAE in excitation energies is increased from 0.040 eV to 0.063 eV.

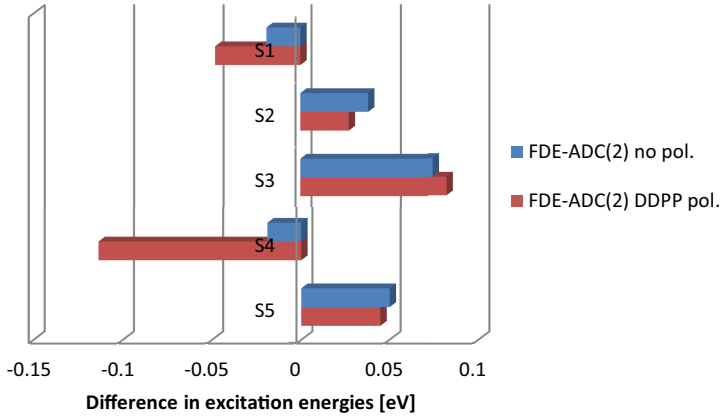

Figure 7.10: Analysis of the accuracy of DDPP-polarization for RADM-FDE-ADC(2) in $[BA \cdot 2\,H_2O]$. The deviation of excitation energies to the supermolecular ADC(2) calculation is given for unpolarized FDE-ADC(2) (blue) and including DDPP-polarization (red).

In the last test, the $[UC \cdot 5\,H_2O]$ system was employed in combination with the RADM approximation and the DDPP approach for environment polarization. The excitation energies are given in Tab. 7.9. Again, a similar result as in the

Table 7.9: Excitation energies for the DDPP-polarized FDE-ADC(2)/cc-pVDZ calculation using the RADM approach for the $[UC \cdot 5\,H_2O]$ system. For comparison, the results of the supermolecular ADC(2) and unpolarized FDE-ADC(2) calculations are given as well.

	Exc. Energies [eV]		
state	supersys.	unpol.	DDPP-pol.
S_1	5.143	5.047	4.902
S_2	5.215	5.319	5.279
S_3	6.211	6.200	6.121
S_4	6.292	6.331	6.289
S_5	6.657	6.765	6.640

SE case can be seen. The S_1 state exhibits a largely increased deviation from the supermolecular result of about 0.24 eV. Also the deviation in the case of S_3 is increased. In contrast, the deviations for the states S_2, S_4 and S_5 are reduced. A comparison is given in Fig. 7.11. The MAE for excitation energies increases from

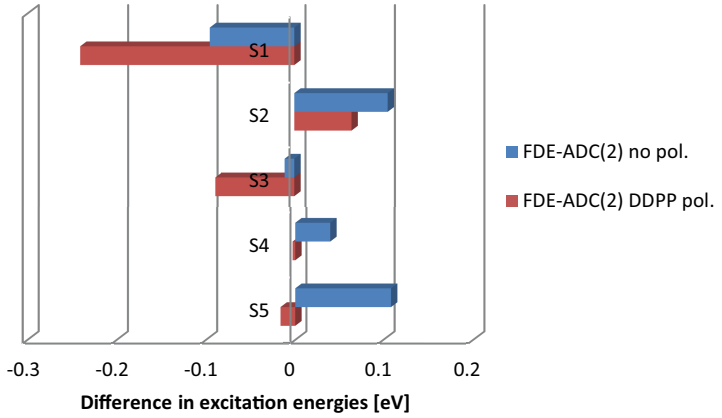

Figure 7.11: Analysis of the accuracy of DDPP-polarization for RADM-FDE-ADC(2) in [UC · 5 H_2O]. The deviation of excitation energies to the supermolecular ADC(2) calculation is given for unpolarized FDE-ADC(2) (blue) and including DDPP-polarization (red).

0.072 eV for unpolarized FDE-ADC(2) to 0.083 eV for FDE-ADC(2) including environment polarization via DDPP.

7.4.4 Pre-polarization in combination with excitation-induced polarization via SSI

In Secs. 7.4.1 and 7.3.1 it has been shown that both the pre-polarization of $\rho_B(\vec{r})$ as well as the SSI approach for including the effect of excitation-induced environment polarization are capable of increasing the accuracy of the FDE-ADC calculation. Since both approaches are based on different theoretical aspects and are implemented independently, they can also be combined. This combination of pre-polarization and SSI is named *dual SSI*. At first, an FDE-ADC(2) calculation including the electrostatic polarization of B due to the nuclei and electron density of A is performed. After this, the SSI cycles for each state are performed.

This has been tested employing the [BA · 2 H_2O] system. The RADM approach has been used. All other settings are identical to the tests performed in the previous sections. The excitation energies are listed in Tab. 7.10. The results for Dual-SSI are very similar to the normal SSI results. However, a slight improvement is noticeable. This is most likely due to the minor influence of the ground state polarized environment density when using state-specific polarized densities during SSI. A comparison of unpolarized, pre-polarized, SSI-polarized and dual-SSI

Table 7.10: Excitation energies for the Dual-SSI-polarized FDE-ADC(2)/cc-pVDZ calculation using the RADM approach for the [BA · 2 H_2O] system. For comparison, the results of the supermolecular ADC(2), unpolarized FDE-ADC(2), pre-polarized FDE-ADC(2) and SSI-polarized FDE-ADC(2) calculations are given as well.

	Exc. Energies [eV]				
state	supersys.	unpol.	pre-pol.	SSI-pol.	Dual-SSI-pol
S_1	3.897	3.878	3.888	3.892	3.893
S_2	4.813	4.851	4.847	4.835	4.835
S_3	5.554	5.628	5.620	5.599	5.598
S_4	6.751	6.732	6.755	6.721	6.723
S_5	6.753	6.803	6.799	6.788	6.788

polarized FDE-ADC(2) is shown in Fig. 7.12. The MAE in excitation energies for dual-SSI is with 0.027 eV approximately identical to the MAE of SSI-RADM-FDE-ADC(2). However, employing the dual-SSI polarization leads to slightly improved results at almost no additional computational cost.

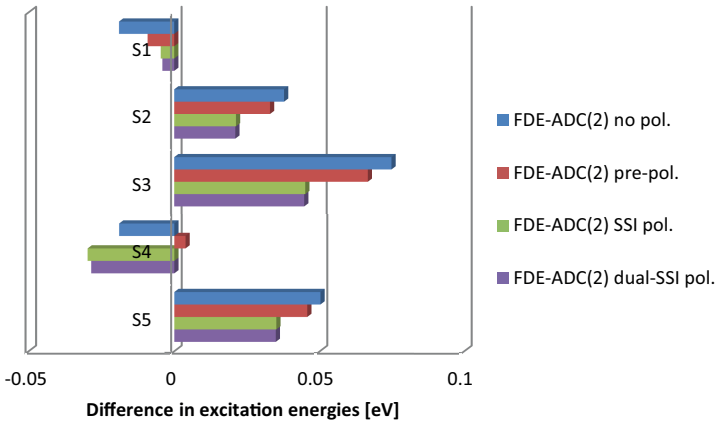

Figure 7.12: Analysis of the accuracy of Dual-SSI-polarization for RADM-FDE-ADC(2) in [BA · 2 H_2O]. The deviation of excitation energies to the supermolecular ADC(2) calculation is given for unpolarized FDE-ADC(2) (blue), with pre-polarization (green), including SSI-polarization (red) and for dual-SSI polarization FDE-ADC(2) (purple).

7.5 Summary and conclusion

I presented in this chapter the extension of FDE-ADC from a frozen environment electron density towards a polarizable density. To include the effect of environment polarization in the calculation of the embedded system, two different theories have to be distinguished. On the one hand, there is the polarization of the environment from the beginning by a ground state electron density and nuclei of the embedded system. In this approach, $\rho_B(\vec{r})$ is not calculated in the gas phase but rather in the presence of system A using an electrostatic potential. This is referred to as *pre-polarization*. A variant of pre-polarization has been implemented into the program package `Q-Chem` in the module `fdeman`.

On the other hand, an excitation of the embedded system can polarize the environment, which is considered after the initial embedding. This is referred to as *excitation-induced environment polarization*. Typically, this can be included using freeze and thaw cycles. In this approach, the two subsystems are interchanged and are alternately embedded into each other until self convergence. Here, I introduced an approximate version named *state-specific iteration (SSI)*, which also switches the subsystems twice to calculate a state-specific embedding. But in contrast to full freeze and thaw, this is not performed until self-convergence but only done once per state. This still includes most of the mutual interaction but prevents calculations of wrong states due to switches in the order which may occur when different embedding potentials for each state are employed.

An approximative approach as an alternative to SSI was also introduced and is referred to as *difference density polarization potential (DDPP)*. In this approach a perturbative-like energy correction for the excitation-induced environment polarization is calculated by building the eponymous potential from an electron difference density of the environment representing the change in the electron density induced by the polarization. Contraction of this potential with the excited state difference density of the corresponding state of the embedded system yields the energy correction for the environment polarization. Both variants to include excitation-induced environment polarization have been implemented into `Q-Chem` as well using the module `fdeman`.

In a first benchmark, the pre-polarization and both SSI and DDPP have been tested. The pre-polarization approach shows small improvements over classical FDE-ADC(2) in comparison to supermolecular ADC(2) calculations. Since pre-polarization can be included with almost no additional computational cost, it can be considered as a promising and efficient improvement with a very good

benefit-cost ratio. In the test of SSI, using both SE and RADM, an improvement of the accuracy could be seen. The MAE for excitation energies for the deviation to supermolecular ADC(2) results is lowered by about 34 % compared to unpolarized FDE-ADC(2). Unfortunately, DDPP does not yet perform as expected. The deviation to the reference values is even increased on average. Especially single states exhibiting ($n \mapsto \pi^*$) character show large deviations. Therefore, the DDPP approach has to be improved. Instead of a contraction with the excited state difference density, a contraction with the excited state transition density could be needed since the latter described the transition itself without inclusion of secondary effects like orbital relaxation.

Since DDPP contains only the influence of the excitation of A on B, but not the static influence (the presence) of A on B, this also might lead to the observed problems. This can be improved in two different ways. Since the pre-polarization includes most of the missing interaction, DDPP could be tested in combination with pre-polarization. This way, the ground state influence of A on B is always included. In the second variant, the difference density is calculated differently. Instead of building the difference of B, embedded in the ground state of A, and B, embedded in the excited state of A, the difference density has to be the difference of isolated B and B, embedded in the excited state of A (see Eq. 7.11). This also includes the ground state influence of A on B.

$$\Delta\rho^{S_0}_{B_{ES_i-vac}}(\vec{r}) = \rho^{S_0}_{B_{emb-ES_i}}(\vec{r}) - \rho^{S_0}_{B_{vac}}(\vec{r}) \tag{7.11}$$

In summary, the SSI approach, although largely increasing the computational cost of an FDE-ADC calculation, improves the accuracy notably. Especially in systems with large shifts of the electron density due to an electronic excitation like in charge-transfer states, which induce a large polarization of the environment, excitation-induced environment polarization should be considered. A further combination of SSI with pre-polarization shows only minor improvements.

Chapter 8

Summary, Conclusion and Outlook

"Because the theory of quantum mechanics could explain all of chemistry and the various properties of substances, it was a tremendous success. But still there was the problem of the interaction of light and matter."
Richard P. Feynman

In my thesis, I have presented various photochemical investigations on tetrathia-[7]heterohelicene-derivatives in comparison with experimental results and the development, implementation and benchmark of the combination of frozen density embedding theory (FDET) with the algebraic diagrammatic construction scheme of the polarization propagator (ADC), resulting in the new method frozen density embedded algebraic diagrammatic construction scheme (FDE-ADC).

Tetrathia-[7]heterohelicenes (TTH) belong to the class of helicenes. TTH molecules exhibit promising chemical properties for application in homogeneous transition metal catalysis, optoelectronics or biochemistry. TTHs consist of 7 ortho-annelated rings (four thiophene rings separated by 3 benzene rings), forming an open macrocycle with a fully delocalized aromatic π-system. Due to the steric repulsion of both ends of the macrocycle, all helicenes form a helical structure. This helical structure induces chirality without the presence of a stereocenter.

The first investigation dealt with the electronically excited states of phosphorus derivatives of TTH with and without complexation with gold(I)-chloride. In particular, the systems tetrathia-[7]heterohelicene-dialkylphosphane-borane (TTH-DAPB) and tetrathia-[7]heterohelicene-diphenylphosphane-gold(I)-chloride (TTH-

DPP-Au(I)) have been investigated theoretically.

The electronic ground state equilibrium structures of both enantiomers of TTH-DAPB have been calculated at the DFT/ωB97XD/cc-pVDZ level of theory and compared to experimental data obtained by X-ray crystallography, showing a good agreement regarding bond lengths and angles. The calculated frontier orbitals, i.e. the highest occupied molecular orbital (HOMO), lowest unoccupied molecular orbital (LUMO), HOMO-1, HOMO-2, LUMO$+1$ and LUMO$+2$, are delocalized over the TTH moiety but do not show any contribution on either the phosphorus atoms or any side chains. The eight energetically lowest electronically excited singlet states of TTH-DAPB were calculated both at the RI-CC2/cc-pVDZ and the TD-DFT/ωB97XD/cc-pVDZ level of theory. All excited states exhibit a ($\pi \mapsto \pi^*$) transition character and are localized on the TTH ring. By applying a constant shift of -0.325 eV to the calculated excitation energies obtained using RI-CC2 to account for environment interactions and intrinsic errors of the employed theoretical model, the calculated spectrum resembles the experimental absorption spectrum very closely. Additionally, the rotatory strengths have been calculated and compared to experimental circular dichroism (CD) spectra. Adding the same constant shift to the calculated excitation energies yields an almost perfect match with the experimental spectrum. To elaborate whether only the first excited state or both S_1 and S_2 contribute to the first absorption band of the experimental absorption spectrum, vibrationally resolved absorption spectra have been calculated for the first and second excited state at the TD-DFT/ωB97XD/SVP level of theory. The vibrationally resolved absorption spectrum of the first excited state resembles the band structure in the experimental spectrum rather closely. However, the second excited state, although exhibiting a similar oscillator strength, yields a vibrationally resolved spectrum with much lower intensity since much more normal modes contribute to the excitation, thus leading to a very broad spectrum. Hence, the first excited state determines the structure of the absorption band.

For the TTH-DPP-Au(I) system, similar investigations have been performed. Calculation of the ground state equilibrium structure both in the gas phase and including the environment model C-PCM using dichloromethane (DCM) as a solvent shows only marginal influence of the solvent on the geometry. Additionally, comparison with experimental data from X-ray crystallography shows a good agreement with deviations lower than 0.1 Å in general. The calculated frontier orbitals are qualitatively identical to the ones obtained for TTH-DAPB. Except for energetically higher lying virtual orbitals like the LUMO+2, which is localized

on the phenyl-groups, the frontier orbitals are localized on the TTH ring system. All of the four energetically lowest electronically excited states are characterized by ($\pi \mapsto \pi^*$) transitions, calculated at the TD-DFT/ωB97XD/6-31G* level of theory, while applying an effective core potential for the gold atoms. These excited states are localized on the TTH ring and share no contribution either from orbitals localized at the phosphorus or at the gold atom. This has been verified by calculation analysis of natural transition orbitals as well as molecular orbital analysis for the states S_1 to S_4. Vibrationally resolved absorption spectra have been calculated for both the S_1 and S_2 state, showing a similar result as obtained for TTH-DAPB. The first excited state dominates the absorption band while the S_2 state shows a very broad absorption band. However, in comparison to RI-CC2 results, the excited states S_1 and S_2 are switched in energetic order but their character is constrained. Therefore, the state numbering of the RI-CC2 results is used.

Next, investigations of the ionizations of three different phosphine-oxide TTH derivatives (TTH-$(PO(n\text{–}Bu)_2)_2$, TTH-$(PO(Ph)_2)_2$ and TTH-$PO(Ph)_2$) and two phosphine-selenide TTH derivatives (TTH-$(PSe(Ph)_2)_2$ and TTH-$PSe(Ph)_2$) have been performed. The localization of both the electron attachment and detachment have been analyzed by electron difference densities. The influence of solvation on the ionizations has been investigated as well, employing the solvation model IEFPCM with water and DCM as solvents. Typical first ionization energies (IE) are between 5.9 and 7.1 eV for all investigated systems with slightly lower energies in solution. The first electron affinities (EA) are between 0.5 and 2.1 eV. In this case, the energies are lower without solvation. All ionizations are localized on the TTH ring with difference densities closely corresponding in form to the frontier orbitals. The results are very similar for all three investigated phosphine-oxide TTH derivatives. For TTH-$(PO(Ph)_2)_2$, also the higher order ionization energies and electron affinities have been calculated. For the second and third IE, the energy rises from 6.1 eV to 13.2 eV and 21.6 eV, respectively, while for the second and third EA the energy rises only slightly from 1.9 eV to 2.86 eV and 2.9 eV, respectively. In the case of higher order ionizations, the orbitals start to mix, which exacerbates the mapping to frontier orbitals.

In the case of the phosphine-selenide TTH derivatives TTH-$(PSe(Ph)_2)_2$ and TTH-$PSe(Ph)_2$, the electron detachment is more prone to environment influences. Without solvation, the lone-pair orbitals of selenium are higher in energy and enter the energetic region of the frontier orbitals. Hence, an oxidation will be

localized at the selenium atoms. This leads to a higher ionization energy in the gas phase of about 7.0 eV for both systems. However, in solution, the results are closely comparable to the results obtained for the phosphine-oxides. Both electron attachment and detachment are localized on the TTH ring with energies for IE of about 6.0 eV and EA of about 2.0 eV for both systems.

In general, the functional groups in the TTH derivatives show only small influences on the photochemical and electrochemical properties, which are clearly dominated by the electronic π-system of the TTH ring.

For the development of FDE-ADC, the environment model FDET has been combined with the excited state method ADC. To maintain the orthogonality of the calculated excited states and to reduce the computational effort, the linearized variant of FDET is employed. In FDE-ADC, the embedded system (A) is calculated in the electronic ground state using Møller-Plesset (MP) perturbation theory to obtain a ground state electron density. The environment (B) is calculated either at the HF or DFT level of theory and a second electron density is obtained. The influence of the environment on the embedded system is expressed via an embedding potential which is a functional of both previously calculated electron densities. This embedding potential is applied during the ADC underlying HF calculation.

FDE-ADC has been implemented in the quantum chemistry program package `Q-Chem` as the new module `fdeman`. It is linked to the `adcman` module responsible for ADC calculations. `fdeman` orchestrates the whole FDE-ADC calculation in a four step process: ***a)*** generation of the electron density of the embedded system $\rho_A(\vec{r})$, ***b)*** generation of the electron density of the environment $\rho_B(\vec{r})$, ***c)*** calculation of the embedding potential $v_{emb}^{lin}(\vec{r})$ and finally ***d)*** applying $v_{emb}^{lin}(\vec{r})$ in an FDE-ADC calculation by adding it to the Fock matrix during the SCF. After calculation of the two individual electron densities expressed in density matrices of system A and B, these are used to evaluate the four state-independent parts of the embedding potential, which are the nuclear attraction potential, the coulombic repulsion potential and the exchange-correlation and kinetic energy non-additive bifunctional potentials. In the last step, the embedding potential is added to the Fock matrix yielding orbitals and integrals that are "perturbed" by the environment, which are subsequently used for the ADC calculation. Thereby, FDE-ADC is directly available for all variants of ADC and core-valence separated ADC (CVS-ADC) up to third order. It is also possible to employ other features of ADC, like the wavefunction and density analysis utility `libwfa`, or the calculation

of spin-orbit coupling elements, which are also implemented in Q-Chem.

Currently, two different approaches are implemented to perform an FDE-ADC calculation: the supermolecular expansion (SE) and the re-assembling of density matrix (RADM) approach. While the first variant is useful only for benchmark calculations, since it provides no computational savings compared to a supersystem calculation, the second variant can be used for production calculations. In SE, all four steps are performed using the supermolecular basis. Thereby, the electron density of A is expressed in basis functions of A and B. The same holds for the electron density of B, the embedding potential and the final FDE-ADC calculation. The RADM approach is an approximation to SE. Using RADM, system A is calculated twice. At first, an HF calculation in the supermolecular basis is performed, followed by a MP(2) calculation in the monomer basis of A. These two density matrices are combined in a patchwork-like manner: The AA block is at the MP(2) level of theory while the other blocks (AB, BA and BB) are at the HF level of theory. This is referred to as re-assembled density matrix. The calculation of $\rho_B(\vec{r})$ and the creation of the embedding potential is performed using the supermolecular basis. The embedding potential is subsequently cut to the basis functions of A only. This approximation is valid, since the values in the off-diagonal blocks AB and BA of the embedding potential as well as the values of the BB block of the density matrix of A are almost zero. The following FDE-ADC calculation, which typically is the time-determining step, is performed in the monomer basis.

FDE-ADC has been benchmarked up to third order perturbation theory employing both the SE and RADM variant. Therefore, three test systems with increasing interaction with the environment have been constructed. The first system consists of benzene (A) with a hydrogen fluoride molecule (B) in plane with the benzene ring ($[\mathrm{BZ} \cdot \mathrm{HF}]$). The second system is a benzaldehyde molecule (A) with a hydrogen-bonded water dimer (B) as environment ($[\mathrm{BA} \cdot 2\,\mathrm{H_2O}]$). The last system contains a uracil molecule (A) surrounded by five hydrogen-bonded water molecules (B) ($[\mathrm{UC} \cdot 5\,\mathrm{H_2O}]$). In the benchmark, the FDE-ADC calculation is compared with supermolecular ADC calculations, which are used as reference. In all cases, the five energetically lowest electronically excited singlet states have been calculated.

The SE-FDE-ADC(2) method, although providing no computational advantage over supermolecular ADC calculations, yields excitation energies very close to the supermolecular results with an MAE averaged over all states and all three systems

of 0.025 eV in excitation energies. The RADM-FDE-ADC(2) variant exhibits slightly larger deviations with an MAE of 0.040 eV for excitation energies. However, both variants exhibit errors still well below the intrinsic error of ADC(2). In the benchmark of RADM-FDE-ADC(3), the overall deviation to the supersystem calculations is only 0.029 eV for excitation energies, which again is smaller than the intrinsic error of ADC(3). Also, the dependence of the accuracy on the choice of method and xc-functional for the calculation of the environment and the non-electrostatic part of the system-environment interaction has been evaluated. While the choice of the xc-functional in the embedding potential practically does not affect the accuracy at all, HF performs best in the choice of the method used to calculate the environment. It could be seen that the MAE is reduced with increasing amount of HF exchange. This is most likely due to the better match of an HF based density for the environment with the HF/MP(2) based density of the embedded system and the agreement with the method used in the supermolecular reference calculations. In a basis set study, it has been shown that basis sets including diffuse basis functions decrease the error of FDE-ADC due to the better description of the overlapping region of the electron densities.

In three representative applications, the performance and capabilities of FDE-ADC have been demonstrated. The splitting of two nearly degenerate ($n \mapsto \pi^*$) excited states of benzoquinone due to a methanol environment has been analyzed. The influence of a water environment onto the excited states of the photoswitch spiropyran has been investigated, and the influence of the C_{60} cage onto the C_{1s}-core excited states of CO in CO@C_{60} has been computed using FDE-CVS-ADC. In all three cases, the specific excitation properties are visualized by transition and difference density analyses.

In FDE-ADC, a frozen environment is used which does not include polarization due to the embedded system. This environment polarization can be divided into two parts. The first part is the influence of the ground state of the embedded system on the environment. This can be included by calculating B not in the gas phase but in the presence of A expressed by an electrostatic potential. This is referred to as pre-polarization. The second type of environment polarization is due to the excitation of A, which changes the electron density. It can be treated by switching the two subsystems and alternatingly embed one system in the other until self-consistence. This is referred to as freeze and thaw cycles. Here, an approximative variant of freeze and thaw has been introduced and implemented in the module `fdeman` named state-specific iteration (SSI), which performs only one

freeze and thaw cycle, thus switching the subsytems twice. As an alternative to SSI, a perturbation-like treatment of the excitation-induced environment polarization has been introduced, which is called difference density polarization potential (DDPP). In this approach, the environment is embedded consecutively in the ground and excited state density of system A. The electron difference density describing the polarization of the environment is used to create a potential which is used to calculate an energy correction for the excitation energy of the excited state of A. All three polarization schemes have been tested. While the pre-polarization shows small improvements in the accuracy of the excitation energies compared to supermolecular calculations, the SSI approach can increase the accuracy by more than 30 % compared to normal FDE-ADC. Unfortunately, the DDPP method does not work as expected yet and shows no improvement. Here, the difference density from ground to excited state of system A is used in combination with the polarization potential to calculate the energy correction. In future developments, the transition density could be used instead, since this density describes the excitation process itself without second order effects like orbital relaxation.

At this point, in `fdeman` only the supermolecular expansion and the RADM approach are implemented. However, the best way expressing the embedding potential is clearly the monomer expansion. In this approach, all densities and the embedding potential are calculated in their own monomer basis. However, this incorporates integration of mixed basis functions (contraction of basis functions of A with basis functions of B), which is not directly possible in `Q-Chem`. Implementation of the monomer expansion would clearly be the next step in the development of `fdeman`.

`fdeman` was designed from scratch and implemented in a way to make it easy to combine FDET also with various other methods for the calculation of the embedded system like coupled cluster, resulting in FDE-CC. Using post-HF ground and excited state methods, this can be done analogously to FDE-ADC by extracting the correlated density matrix and passing it to `fdeman`. The embedding potential is then calculated using this density matrix for system A and can subsequently be added to the Fock matrix. Like in FDE-ADC this generates embedded orbitals and integrals which can be used in the following post-HF calculation.

In summary, the presented FDE-ADC implementation gives access to include explicit environment influences on the excitation process. Exhibiting an error lower than the intrinsic error of the used ADC method makes FDE-ADC a reliable "black box" method for embedded systems in extended environments.

Appendix

Bibliography

[1] P. Klán and J. Wirz. *Photochemistry of organic compounds: From concepts to practice*. Postgraduate chemistry series. Wiley, Chichester and U.K (**2009**).

[2] A. Albini. *Photochemistry*. A specialist periodical report. RSC Publisheing, Cambridge (**2012**).

[3] J. M. Berg, B. Häcker, L. Stryer and J. L. Tymoczko. *Biochemie*. Spektrum Akad. Verl., Heidelberg, 6th edition (**2010**).

[4] H. Zollinger. *Color chemistry: Syntheses, properties, and applications of organic dyes and pigments*. Verlag Helvetica Chimica Acta, Zürich, third, revised edition. edition (**2003**).

[5] H. Hjorth Tønnesen. *Photostability of drugs and drug formulations*. CRC Press, Boca Raton and FL, second edition (**2004**).

[6] K. Thoma and J. T. Piechocki. *Pharmaceutical photostability and stabilization technology*. Informa healthcare, New York (**2007**).

[7] J. C. Bernède. "Organic photovoltaic cells: History, principle and techniques". *Journal of the Chilean Chemical Society*, 53 (2008). doi: 10.4067/S0717-97072008000300001.

[8] A. L. Roes, E. A. Alsema, K. Blok and M. K. Patel. "Ex-ante environmental and economic evaluation of polymer photovoltaics". *Progress in Photovoltaics: Research and Applications*, 17 (2009) pages 372–393. doi: 10.1002/pip.891.

[9] T. M. Clarke and J. R. Durrant. "Charge Photogeneration in Organic Solar Cells". *Chemical Reviews*, 110 (2010) pages 6736–6767. doi: 10.1021/cr900271s.

[10] L. Dou, Y. Liu, Z. Hong, G. Li and Y. Yang. "Low-Bandgap Near-IR Conjugated Polymers/Molecules for Organic Electronics". *Chemical Reviews*, 115 (2015) pages 12633–12665. doi: 10.1021/acs.chemrev.5b00165.

[11] P. W. Atkins, J. d. Paula and M. Baer. *Physikalische Chemie*. Wiley-VCH, Weinheim, fourth edition (**2006**).

[12] G. Wedler. *Lehrbuch der physikalischen Chemie*. Wiley-VCH, Weinheim, fifth edition (**2010**).

[13] P. H. P. Harbach and A. Dreuw. "The Art of Choosing the Right Quantum Chemical Excited-State Method for Large Molecular Systems". In P. Comba, editor, "Modeling of Molecular Properties", chapter 3. Wiley-VCH Verlag GmbH & Co. KGaA (**2011**). pages 29–47. doi: 10.1002/9783527636402.ch3.

[14] A. Dreuw and M. Wormit. "The algebraic diagrammatic construction scheme for the polarization propagator for the calculation of excited states". *WIREs Comput. Mol. Sci.*, 5 (2015) pages 82–95. doi: 10.1002/wcms.1206.

[15] C. Reichardt. "Solvents and Solvent Effects: An Introduction". *Organic Process Research & Development*, 11 (2007) pages 105–113. doi: 10.1021/op0680082.

[16] Aristotle. and C. J. F. Williams. *Aristotle's De generatione et corruptione*. Clarendon Aristotle series. Clarendon Press, Oxford (**2002, ©1982**).

[17] E. Buncel, R. Stairs and H. Wilson. *The role of the solvent in chemical reactions*, volume 6 of *Oxford chemistry masters*. Oxford University Press, New York (**2003**).

[18] C. Reichardt and T. Welton. *Solvents and Solvent Effects in Organic Chemistry*. Wiley-VCH, Weinheim, fourth edition (**2011**).

[19] W. Liptay. "Electrochromism and Solvatochromism". *Angew. Chemie Int. Ed.*, 8 (1969) pages 177–188. doi: 10.1002/anie.196901771.

[20] A. Marini, A. Muñoz Losa, A. Biancardi and B. Mennucci. "What is Solvatochromism?" *The Journal of Physical Chemistry B*, 114 (2010) pages 17128–17135. doi: 10.1021/jp1097487.

[21] T. J. Zuehlsdorff, P. D. Haynes, F. Hanke, M. C. Payne and N. D. M. Hine. "Solvent Effects on Electronic Excitations of an Organic Chromophore". *Journal of Chemical Theory and Computation*, 12 (2016) pages 1853–1861. doi: 10.1021/acs.jctc.5b01014.

[22] Nobelprize.org Nobel Media AB 2014. "The Nobel Prize in Chemistry 2013". `http://www.nobelprize.org/nobel_prizes/chemistry/laureates/2013/` (**2013**). Accessed: 10th Apr 2017.

[23] Y. Shao, Z. Gan, E. Epifanovsky, A. T. Gilbert, M. Wormit, J. Kussmann, A. W. Lange, A. Behn, J. Deng, X. Feng *et al.* "Advances in molecular quantum chemistry contained in the Q-Chem 4 program package". *Molecular Physics*, 113 (2015) pages 184–215. doi: 10.1080/00268976.2014.952696.

[24] M. Wormit, D. R. Rehn, P. H. Harbach, J. Wenzel, C. M. Krauter, E. Epifanovsky and A. Dreuw. "Investigating excited electronic states using the algebraic diagrammatic construction (ADC) approach of the polarisation propagator". *Molecular Physics*, 112 (2014) pages 774–784. doi: 10.1080/00268976.2013.859313.

[25] M. Hanwell, D. Curtis, D. Lonie, T. Vandermeersch, E. Zurek and G. Hutchison. "Avogadro: an advanced semantic chemical editor, visualization, and analysis platform". *Journal of Cheminformatics*, 4 (2012) page 17. doi: 10.1186/1758-2946-4-17.

[26] Persistence of Vision Raytracer Pty. Ltd. "POV-Ray 3.7". `http://www.povray.org`.

[27] E. Willighagen and M. Howard. "Fast and Scriptable Molecular Graphics in Web Browsers without Java3D". *Nature Precedings*, (2007). doi: 10.1038/npre.2007.50.1.

[28] R. Dennington, T. Keith and J. Millam. "GaussView Version 5" (**2009**). Semichem Inc., Shawnee Mission, KS.

[29] S. Cauteruccio, A. Loos, A. Bossi, M. C. Blanco Jaimes, D. Dova, F. Rominger, S. Prager, A. Dreuw, E. Licandro and A. S. K. Hashmi. "Gold(I) Complexes of Tetrathiaheterohelicene Phosphanes". *Inorganic Chemistry*, 52 (2013) pages 7995–8004. doi: 10.1021/ic4005533.

[30] S. Prager, I. Burghardt and A. Dreuw. "Ultrafast C_{Spiro}-O Dissociation via a Conical Intersection Drives Spiropyran to Merocyanine Photoswitching". *The Journal of Physical Chemistry A*, 118 (2014) pages 1339–1349. doi: 10.1021/jp4088942.

[31] D. Dova, S. Cauteruccio, S. Prager, A. Dreuw, C. Graiff and E. Licandro. "Chiral Thiahelicene-Based Alkyl Phosphine–Borane Complexes: Synthesis, X-ray Characterization, and Theoretical and Experimental Investigations of Optical Properties". *The Journal of Organic Chemistry*, 80 (2015) pages 3921–3928. doi: 10.1021/acs.joc.5b00243.

[32] D. Dova, L. Viglianti, P. R. Mussini, S. Prager, A. Dreuw, A. Voituriez, E. Licandro and S. Cauteruccio. "Tetrathia[7]helicene Phosphorus Derivatives: Experimental and Theoretical Investigations of Electronic Properties, and Preliminary Applications as Organocatalysts". *Asian Journal of Organic Chemistry*, 5 (2016) pages 537–549. doi: 10.1002/ajoc.201600025.

[33] S. Prager, A. Zech, F. Aquilante, A. Dreuw and T. A. Wesolowski. "First time combination of frozen density embedding theory with the algebraic diagrammatic construction scheme for the polarization propagator of second order". *The Journal of Chemical Physics*, 144 (2016) page 204103. doi: 10.1063/1.4948741.

[34] S. Prager, A. Zech, T. A. Wesolowski and A. Dreuw. "Implementation and application of the frozen density embedding theory with the algebraic diagrammatic construction scheme for the polarization propagator up to third order". *submitted for publication*, (2017).

[35] M. Olivucci. *Computational photochemistry*. Elsevier Science, Amsterdam and Boston (Mass.) and Paris (**2005**).

[36] Y.-J. Liu, D. Roca-Sanjuán and R. Lindh. "Computational photochemistry and photophysics: the state of the art". In A. Albini, editor, "Photochemistry", volume 40 of *Specialist Periodical Reports: Photochemistry*, chapter 2. Royal Society of Chemistry, Cambridge (**2012**). pages 42–72. doi: 10.1039/1465-1947.

[37] P. G. Szalay, T. Müller, G. Gidofalvi, H. Lischka and R. Shepard. "Multiconfiguration Self-Consistent Field and Multireference Configuration Interaction Methods and Applications". *Chemical Reviews*, 112 (2012) pages 108–181. doi: 10.1021/cr200137a.

[38] W. Thiel. "Semiempirical quantum-chemical methods". *Wiley Interdisciplinary Reviews: Computational Molecular Science*, 4 (2014) pages 145–157. doi: 10.1002/wcms.1161.

[39] A. Szabo and N. S. Ostlund. *Modern quantum chemistry : introduction to advanced electronic structure theory*. Dover Publications, Mineola, N.Y (**1996**).

[40] F. Jensen. *Introduction to computational chemistry*. John Wiley & Sons, Chichester, England Hoboken, NJ (**2007**).

[41] T. Helgaker, J. Olsen and P. Jørgensen. *Molecular Electronic-Structure Theory*. Wiley-Blackwell, Chichester (**2013**).

[42] E. Schrödinger. "Quantisierung als Eigenwertproblem I". *Annalen der Physik*, 79 (1926) pages 361–376. doi: 10.1002/andp.19263840404.

[43] E. Schrödinger. "Quantisierung als Eigenwertproblem II". *Annalen der Physik*, 79 (1926) pages 489–527. doi: 10.1002/andp.19263840602.

[44] E. Schrödinger. "Quantisierung als Eigenwertproblem III". *Annalen der Physik*, 80 (1926) pages 437–490. doi: 10.1002/andp.19263851302.

[45] E. Schrödinger. "Quantisierung als Eigenwertproblem IV". *Annalen der Physik*, 81 (1926) pages 109–139. doi: 10.1002/andp.19263861802.

[46] I. Quilez. "Spherical Harmonics". https://commons.wikimedia.org/w/index.php?curid=32782753.

[47] R. Ditchfield, W. J. Hehre and J. A. Pople. "Self–Consistent Molecular–Orbital Methods. IX. An Extended Gaussian–Type Basis for Molecular–Orbital Studies of Organic Molecules". *The Journal of Chemical Physics*, 54 (1971) pages 724–728. doi: 10.1063/1.1674902.

[48] W. J. Hehre, R. Ditchfield and J. A. Pople. "Self—Consistent Molecular Orbital Methods. XII. Further Extensions of Gaussian—Type Basis Sets for Use in Molecular Orbital Studies of Organic Molecules". *The Journal of Chemical Physics*, 56 (1972) pages 2257–2261. doi: 10.1063/1.1677527.

[49] P. C. Hariharan and J. A. Pople. "The influence of polarization functions on molecular orbital hydrogenation energies". *Theoretica Chimica Acta*, 28 (1973) pages 213–222. doi: 10.1007/BF00533485.

[50] R. Krishnan, J. S. Binkley, R. Seeger and J. A. Pople. "Self–consistent molecular orbital methods. XX. A basis set for correlated wave functions". *The Journal of Chemical Physics*, 72 (1980) pages 650–654. doi: 10.1063/1.438955.

[51] A. D. McLean and G. S. Chandler. "Contracted Gaussian basis sets for molecular calculations. I. Second row atoms, Z =11–18". *The Journal of Chemical Physics*, 72 (1980) pages 5639–5648. doi: 10.1063/1.438980.

[52] T. Clark, J. Chandrasekhar, G. W. Spitznagel and P. V. R. Schleyer. "Efficient diffuse function-augmented basis sets for anion calculations. III. The 3-21+G basis set for first-row elements, Li-F". *Journal of Computational Chemistry*, 4 (1983) pages 294–301. doi: 10.1002/jcc.540040303.

[53] M. J. Frisch, J. A. Pople and J. S. Binkley. "Self–consistent molecular orbital methods 25. Supplementary functions for Gaussian basis sets". *The Journal of Chemical Physics*, 80 (1984) pages 3265–3269. doi: 10.1063/1.447079.

[54] T. H. Dunning. "Gaussian basis sets for use in correlated molecular calculations. I. The atoms boron through neon and hydrogen". *The Journal of Chemical Physics*, 90 (1989) pages 1007–1023. doi: 10.1063/1.456153.

[55] R. A. Kendall, T. H. Dunning and R. J. Harrison. "Electron affinities of the first–row atoms revisited. Systematic basis sets and wave functions". *The Journal of Chemical Physics*, 96 (1992) pages 6796–6806. doi: 10.1063/1.462569.

[56] D. E. Woon and T. H. D. Jr. "Gaussian basis sets for use in correlated molecular calculations. IV. Calculation of static electrical response properties". *The Journal of Chemical Physics*, 100 (1994) pages 2975–2988. doi: 10.1063/1.466439.

[57] F. Weigend and R. Ahlrichs. "Balanced basis sets of split valence, triple zeta valence and quadruple zeta valence quality for H to Rn: Design and assessment of accuracy". *Physical Chemistry Chemical Physics*, 7 (2005) page 3297. doi: 10.1039/B508541A.

[58] D. Rappoport and F. Furche. "Property-optimized Gaussian basis sets for molecular response calculations". *The Journal of Chemical Physics*, 133 (2010) page 134105. doi: 10.1063/1.3484283.

[59] J. Wenzel. *Inaugural-Dissertation: Development and Implementation of Theoretical Methods for the Description of Electronically Core-Excited States*. Ph.D. thesis, University of Heidelberg, Heidelberg (**2015**).

[60] C. J. Cramer. *Essentials of computational chemistry : theories and models*. John Wiley & Sons, Chichester, West Sussex, England Hoboken, NJ (**2004**).

[61] J. D. Watts, J. Gauss and R. J. Bartlett. "Coupled–cluster methods with noniterative triple excitations for restricted open–shell Hartree–Fock and other general single determinant reference functions. Energies and analytical gradients". *The Journal of Chemical Physics*, 98 (1993) pages 8718–8733. doi: 10.1063/1.464480.

[62] R. J. Bartlett. "Coupled-cluster theory and its equation-of-motion extensions". *Wiley Interdisciplinary Reviews: Computational Molecular Science*, 2 (2012) pages 126–138. doi: 10.1002/wcms.76.

[63] O. Christiansen, H. Koch and P. Jørgensen. "The second-order approximate coupled cluster singles and doubles model CC2". *Chemical Physics Letters*, 243 (1995) pages 409–418. doi: 10.1016/0009-2614(95)00841-Q.

[64] H. Koch, O. Christiansen, P. Jørgensen, A. M. Sanchez de Merás and T. Helgaker. "The CC3 model: An iterative coupled cluster approach including connected triples". *The Journal of Chemical Physics*, 106 (1997) pages 1808–1818. doi: 10.1063/1.473322.

[65] C. Møller and M. S. Plesset. "Note on an approximation treatment for many-electron systems". *Physical Review*, 46 (1934) pages 618–622. doi: 10.1103/PhysRev.46.618.

[66] W. Koch and M. C. Holthausen. *A Chemist's Guide to Density Functional Theory*. Wiley-VCH, second edition. edition (**2001**).

[67] L. H. Thomas. "The calculation of atomic fields". *Mathematical Proceedings of the Cambridge Philosophical Society*, 23 (1927) page 542. doi: 10.1017/S0305004100011683.

[68] E. Fermi. "Application of statistical gas methods to electronic systems". *Atti Accad. Naz. Lincei*, 6 (1927) pages 602–607.

[69] P. A. Dirac. "Note on exchange phenomena in the Thomas atom". In "Mathematical Proceedings of the Cambridge Philosophical Society", volume 26. Cambridge Univ Press, pages 376–385.

[70] P. Hohenberg and W. Kohn. "Inhomogeneous Electron Gas". *Phys. Rev.*, 136 (1964) pages B864–B871. doi: 10.1103/PhysRev.136.B864.

[71] W. Kohn and L. J. Sham. "Self-Consistent Equations Including Exchange and Correlation Effects". *Phys. Rev.*, 140 (1965) pages A1133–A1138. doi: 10.1103/PhysRev.140.A1133.

[72] J. P. Perdew, A. Ruzsinszky, J. Tao, V. N. Staroverov, G. E. Scuseria and G. I. Csonka. "Prescription for the design and selection of density functional approximations: More constraint satisfaction with fewer fits". *The Journal of Chemical Physics*, 123 (2005) page 062201. doi: 10.1063/1.1904565.

[73] S. H. Vosko, L. Wilk and M. Nusair. "Accurate spin-dependent electron liquid correlation energies for local spin density calculations: a critical analysis". *Canadian Journal of Physics*, 58 (1980) pages 1200–1211. doi: 10.1139/p80-159.

[74] A. D. Becke. "Density functional calculations of molecular bond energies". *The Journal of Chemical Physics*, 84 (1986) pages 4524–4529. doi: 10.1063/1.450025.

[75] C. Lee, W. Yang and R. G. Parr. "Development of the Colle-Salvetti correlation-energy formula into a functional of the electron density". *Physical Review B*, 37 (1988) pages 785–789. doi: 10.1103/PhysRevB.37.785.

[76] J. P. Perdew, K. Burke and M. Ernzerhof. "Generalized Gradient Approximation Made Simple". *Physical Review Letters*, 77 (1996) pages 3865–3868. doi: 10.1103/PhysRevLett.77.3865.

[77] J. P. Perdew. "Density-functional approximation for the correlation energy of the inhomogeneous electron gas". *Physical Review B*, 33 (1986) pages 8822–8824. doi: 10.1103/PhysRevB.33.8822.

[78] J. P. Perdew, J. A. Chevary, S. H. Vosko, K. A. Jackson, M. R. Pederson, D. J. Singh and C. Fiolhais. "Atoms, molecules, solids, and surfaces: Applications of the generalized gradient approximation for exchange and correlation". *Physical Review B*, 46 (1992) pages 6671–6687. doi: 10.1103/PhysRevB.46.6671.

[79] R. Peverati, Y. Zhao and D. G. Truhlar. "Generalized Gradient Approximation That Recovers the Second-Order Density-Gradient Expansion with Optimized Across-the-Board Performance". *The Journal of Physical Chemistry Letters*, 2 (2011) pages 1991–1997. doi: 10.1021/jz200616w.

[80] Y. Zhao and D. G. Truhlar. "A new local density functional for main-group thermochemistry, transition metal bonding, thermochemical kinetics, and noncovalent interactions". *The Journal of Chemical Physics*, 125 (2006) page 194101. doi: 10.1063/1.2370993.

[81] J. Tao, J. P. Perdew, V. N. Staroverov and G. E. Scuseria. "Climbing the Density Functional Ladder: Nonempirical Meta–Generalized Gradient Approximation Designed for Molecules and Solids". *Physical Review Letters*, 91 (2003). doi: 10.1103/PhysRevLett.91.146401.

[82] A. D. Becke. "Density–functional thermochemistry. III. The role of exact exchange". *The Journal of Chemical Physics*, 98 (1993) pages 5648–5652. doi: 10.1063/1.464913.

[83] C. Adamo and V. Barone. "Toward reliable density functional methods without adjustable parameters: The PBE0 model". *The Journal of Chemical Physics*, 110 (1999) pages 6158–6170. doi: 10.1063/1.478522.

[84] Y. Zhao and D. G. Truhlar. "The M06 suite of density functionals for main group thermochemistry, thermochemical kinetics, noncovalent interactions, excited states, and transition elements: two new functionals and systematic testing of four M06-class functionals and 12 other functionals". *Theoretical Chemistry Accounts*, 120 (2008) pages 215–241. doi: 10.1007/s00214-007-0310-x.

[85] V. N. Staroverov, G. E. Scuseria, J. Tao and J. P. Perdew. "Comparative assessment of a new nonempirical density functional: Molecules and hydrogen-bonded complexes". *The Journal of Chemical Physics*, 119 (2003) pages 12129–12137. doi: 10.1063/1.1626543.

[86] Y.-S. Lin, G.-D. Li, S.-P. Mao and J.-D. Chai. "Long-Range Corrected Hybrid Density Functionals with Improved Dispersion Corrections". *Journal of Chemical Theory and Computation*, 9 (2013) pages 263–272. doi: 10.1021/ct300715s.

[87] R. Peverati and D. G. Truhlar. "Improving the Accuracy of Hybrid Meta-GGA Density Functionals by Range Separation". *The Journal of Physical Chemistry Letters*, 2 (2011) pages 2810–2817. doi: 10.1021/jz201170d.

[88] Y. Zhang, X. Xu and W. A. Goddard. "Doubly hybrid density functional for accurate descriptions of nonbond interactions, thermochemistry, and thermochemical kinetics". *Proceedings of the National Academy of Sciences*, 106 (2009) pages 4963–4968. doi: 10.1073/pnas.0901093106.

[89] S. Grimme. "Semiempirical hybrid density functional with perturbative second-order correlation". *The Journal of Chemical Physics*, 124 (2006) page 034108. doi: 10.1063/1.2148954.

[90] T. Schwabe and S. Grimme. "Double-hybrid density functionals with long-range dispersion corrections: higher accuracy and extended applicability". *Physical Chemistry Chemical Physics*, 9 (2007) page 3397. doi: 10.1039/B704725H.

[91] A. Tarnopolsky, A. Karton, R. Sertchook, D. Vuzman and J. M. L. Martin. "Double-Hybrid Functionals for Thermochemical Kinetics". *The Journal of Physical Chemistry A*, 112 (2008) pages 3–8. doi: 10.1021/jp710179r.

[92] T. Benighaus, R. A. DiStasio, R. C. Lochan, J.-D. Chai and M. Head-Gordon. "Semiempirical Double-Hybrid Density Functional with Improved Description of Long-Range Correlation". *The Journal of Physical Chemistry A*, 112 (2008) pages 2702–2712. doi: 10.1021/jp710439w.

[93] J.-D. Chai and M. Head-Gordon. "Long-range corrected double-hybrid density functionals". *The Journal of Chemical Physics*, 131 (2009) page 174105. doi: 10.1063/1.3244209.

[94] A. Dreuw and M. Head-Gordon. "Single-Reference ab Initio Methods for the Calculation of Excited States of Large Molecules". *Chemical Reviews*, 105 (2005) pages 4009–4037. doi: 10.1021/cr0505627.

[95] E. R. Davidson. "The iterative calculation of a few of the lowest eigenvalues and corresponding eigenvectors of large real-symmetric matrices". *Journal of Computational Physics*, 17 (1975) pages 87 – 94. doi: 10.1016/0021-9991(75)90065-0.

[96] M. Casida and M. Huix-Rotllant. "Progress in Time-Dependent Density-Functional Theory". *Annual Review of Physical Chemistry*, 63 (2012) pages 287–323. doi: 10.1146/annurev-physchem-032511-143803.

[97] Z.-L. Cai, K. Sendt and J. R. Reimers. "Failure of density-functional theory and time-dependent density-functional theory for large extended π systems". *The Journal of Chemical Physics*, 117 (2002) pages 5543–5549. doi: 10.1063/1.1501131.

[98] S. Grimme and M. Parac. "Substantial Errors from Time-Dependent Density Functional Theory for the Calculation of Excited States of Large π Systems". *ChemPhysChem*, 4 (2003) pages 292–295. doi: 10.1002/cphc.200390047.

[99] A. Dreuw, J. L. Weisman and M. Head-Gordon. "Long-range charge-transfer excited states in time-dependent density functional theory require non-local exchange". *The Journal of Chemical Physics*, 119 (2003) pages 2943–2946. doi: 10.1063/1.1590951.

[100] A. Dreuw and M. Head-Gordon. "Failure of Time-Dependent Density Functional Theory for Long-Range Charge-Transfer Excited States: The ZincbacteriochlorinBacteriochlorin and BacteriochlorophyllSpheroidene Complexes". *Journal of the American Chemical Society*, 126 (2004) pages 4007–4016. doi: 10.1021/ja039556n.

[101] A. D. Laurent and D. Jacquemin. "TD-DFT benchmarks: A review". *International Journal of Quantum Chemistry*, 113 (2013) pages 2019–2039. doi: 10.1002/qua.24438.

[102] J. Schirmer. "Beyond the random-phase approximation: A new approximation scheme for the polarization propagator". *Phys. Rev. A*, 26 (1982) pages 2395–2416. doi: 10.1103/PhysRevA.26.2395.

[103] A. B. Trofimov and J. Schirmer. "An efficient polarization propagator approach to valence electron excitation spectra". *Journal of Physics B: Atomic, Molecular and Optical Physics*, 28 (1995) page 2299. doi: 10.1088/0953-4075/28/12/003.

[104] F. Mertins and J. Schirmer. "Algebraic propagator approaches and intermediate-state representations. I. The biorthogonal and unitary coupled-cluster methods". *Phys. Rev. A*, 53 (1996) pages 2140–2152. doi: 10.1103/PhysRevA.53.2140.

[105] J. Schirmer and A. B. Trofimov. "Intermediate state representation approach to physical properties of electronically excited molecules". *J. Chem. Phys.*, 120 (2004) pages 11449–11464. doi: 10.1063/1.1752875.

[106] A. B. Trofimov, G. Stelter and J. Schirmer. "A consistent third-order propagator method for electronic excitation". *The Journal of Chemical Physics*, 111 (1999) pages 9982–9999. doi: 10.1063/1.480352.

[107] M. Wormit. *Inaugural-Dissertation: Development and Application of Reliable Methods for the Calculation of Excited States: From Light-Harvesting Complexes to Medium-Sized Molecules*. Ph.D. thesis, University of Frankfurt am Main, Frankfurt am Main (**2009**).

[108] P. H. P. Harbach, M. Wormit and A. Dreuw. "The third-order algebraic diagrammatic construction method (ADC(3)) for the polarization propagator for closed-shell molecules: Efficient implementation and benchmarking)". *The Journal of Chemical Physics*, 141 (2014) 064113. doi: 10.1063/1.4892418.

[109] J. Franck and E. G. Dymond. "Elementary processes of photochemical reactions". *Transactions of the Faraday Society*, 21 (1926) page 536. doi: 10.1039/TF9262100536.

[110] E. Condon. "A Theory of Intensity Distribution in Band Systems". *Physical Review*, 28 (1926) pages 1182–1201. doi: 10.1103/PhysRev.28.1182.

[111] E. U. Condon. "Nuclear Motions Associated with Electron Transitions in Diatomic Molecules". *Physical Review*, 32 (1928) pages 858–872. doi: 10.1103/PhysRev.32.858.

[112] V. Barone, J. Bloino, M. Biczysko and F. Santoro. "Fully Integrated Approach to Compute Vibrationally Resolved Optical Spectra: From Small Molecules to Macrosystems". *Journal of Chemical Theory and Computation*, 5 (2009) pages 540–554. doi: 10.1021/ct8004744.

[113] F. Duschinsky. "The importance of the electron spectrum in multi atomic molecules. Concerning the Franck-Condon principle". *Acta Physicochim. URSS*, 7 (1937) pages 551–566.

[114] F. Plasser, M. Wormit and A. Dreuw. "New tools for the systematic analysis and visualization of electronic excitations. I. Formalism". *The Journal of Chemical Physics*, 141 (2014) 024106. doi: 10.1063/1.4885819.

[115] F. Plasser, S. A. Baeppler, M. Wormit and A. Dreuw. "New tools for the systematic analysis and visualization of electronic excitations. II. Applications". *The Journal of Chemical Physics*, 141 (2014) 024107. doi: 10.1063/1.4885820.

[116] A. V. Luzanov, A. A. Sukhorukov and V. . Umanskii. "Application of transition density matrix for analysis of excited states". *Theoretical and Experimental Chemistry*, 10 (1976) pages 354–361. doi: 10.1007/BF00526670.

[117] R. L. Martin. "Natural transition orbitals". *The Journal of Chemical Physics*, 118 (2003) pages 4775–4777. doi: 10.1063/1.1558471.

[118] I. Mayer. "Using singular value decomposition for a compact presentation and improved interpretation of the CIS wave functions". *Chemical Physics Letters*, 437 (2007) pages 284–286. doi: 10.1016/j.cplett.2007.02.038.

[119] A. D. Dutoi, L. S. Cederbaum, M. Wormit, J. H. Starcke and A. Dreuw. "Tracing molecular electronic excitation dynamics in real time and space". *The Journal of Chemical Physics*, 132 (2010) page 144302. doi: 10.1063/1.3353161.

[120] S. Miertuš, E. Scrocco and J. Tomasi. "Electrostatic interaction of a solute with a continuum. A direct utilizaion of ab initio molecular potentials for the prevision of solvent effects". *Chemical Physics*, 55 (1981) pages 117 – 129. doi: 10.1016/0301-0104(81)85090-2.

[121] J. M. Herbert and A. W. Lange. "Polarizable continuum models for (bio) molecular electrostatics: Basic theory and recent developments for macromolecules and simulations". In Q. Cui, P. Ren and M. Meuwly, editors, "Many-Body Effects and Electrostatics in Biomolecules", chapter 11. Pan Stanford (**2016**). pages 363–416.

[122] J. Tomasi, B. Mennucci and R. Cammi. "Quantum Mechanical Continuum Solvation Models". *Chem. Rev.*, 105 (2005) pages 2999–3094. doi: 10.1021/cr9904009.

[123] B. Mennucci. "Polarizable continuum model". *Wiley Interdisciplinary Reviews: Computational Molecular Science*, 2 (2012) pages 386–404. doi: 10.1002/wcms.1086.

[124] A. Klamt and G. Schüürmann. "COSMO: a new approach to dielectric screening in solvents with explicit expressions for the screening energy and its gradient". *J. Chem. Soc., Perkin Trans. 2*, (1993) pages 799–805. doi: 10.1039/P29930000799.

[125] T. N. Truong and E. V. Stefanovich. "A new method for incorporating solvent effect into the classical, ab initio molecular orbital and density functional theory frameworks for arbitrary shape cavity". *Chemical Physics Letters*, 240 (1995) pages 253–260. doi: 10.1016/0009-2614(95)00541-B.

[126] V. Barone and M. Cossi. "Quantum Calculation of Molecular Energies and Energy Gradients in Solution by a Conductor Solvent Model". *The Journal of Physical Chemistry A*, 102 (1998) pages 1995–2001. doi: 10.1021/jp9716997.

[127] D. M. Chipman. "Reaction field treatment of charge penetration". *The Journal of Chemical Physics*, 112 (2000) pages 5558–5565. doi: 10.1063/1.481133.

[128] E. Cancès and B. Mennucci. "Comment on "Reaction field treatment of charge penetration" [J. Chem. Phys. 112, 5558 (2000)]". *The Journal of Chemical Physics*, 114 (2001) page 4744. doi: 10.1063/1.1349091.

[129] D. M. Chipman and M. Dupuis. "Implementation of solvent reaction fields for electronic structure". *Theoretical Chemistry Accounts: Theory, Computation, and Modeling (Theoretica Chimica Acta)*, 107 (2002) pages 90–102. doi: 10.1007/s00214-001-0303-0.

[130] J. E. Jones. "On the Determination of Molecular Fields. II. From the Equation of State of a Gas". *Proceedings of the Royal Society A: Mathematical, Physical and Engineering Sciences*, 106 (1924) pages 463–477. doi: 10.1098/rspa.1924.0082.

[131] A. Warshel and M. Levitt. "Theoretical studies of enzymic reactions: Dielectric, electrostatic and steric stabilization of the carbonium ion in the reaction of lysozyme". *J. Mol. Bio.*, 103 (1976) pages 227 – 249. doi: 10.1016/0022-2836(76)90311-9.

[132] S. Faraji, G. Groenhof and A. Dreuw. "Combined QM/MM Investigation on the Light-Driven Electron-Induced Repair of the (6–4) Thymine Dimer Catalyzed by DNA Photolyase". *The Journal of Physical Chemistry B*, 117 (2013) pages 10071–10079. doi: 10.1021/jp401662z.

[133] D. Ghosh, D. Kosenkov, V. Vanovschi, C. F. Williams, J. M. Herbert, M. S. Gordon, M. W. Schmidt, L. V. Slipchenko and A. I. Krylov. "Noncovalent Interactions in Extended Systems Described by the Effective Fragment Potential Method: Theory and Application to Nucleobase Oligomers". *The Journal of Physical Chemistry A*, 114 (2010) pages 12739–12754. doi: 10.1021/jp107557p.

[134] M. S. Gordon, D. G. Fedorov, S. R. Pruitt and L. V. Slipchenko. "Fragmentation Methods: A Route to Accurate Calculations on Large Systems". *Chemical Reviews*, 112 (2012) pages 632–672. doi: 10.1021/cr200093j.

[135] P. N. Day, J. H. Jensen, M. S. Gordon, S. P. Webb, W. J. Stevens, M. Krauss, D. Garmer, H. Basch and D. Cohen. "An effective fragment method for modeling solvent effects in quantum mechanical calculations". *The Journal of Chemical Physics*, 105 (1996) pages 1968–1986. doi: 10.1063/1.472045.

[136] M. S. Gordon, M. A. Freitag, P. Bandyopadhyay, J. H. Jensen, V. Kairys and W. J. Stevens. "The Effective Fragment Potential Method: A QM-Based MM Approach to Modeling Environmental Effects in Chemistry". *The Journal of Physical Chemistry A*, 105 (2001) pages 293–307. doi: 10.1021/jp002747h.

[137] A. Stone and M. Alderton. "Distributed multipole analysis". *Molecular Physics*, 56 (2006) pages 1047–1064. doi: 10.1080/00268978500102891.

[138] D. G. Fedorov and K. Kitaura. "Extending the Power of Quantum Chemistry to Large Systems with the Fragment Molecular Orbital Method". *The Journal of Physical Chemistry A*, 111 (2007) pages 6904–6914. doi: 10.1021/jp0716740.

[139] D. G. Fedorov, T. Nagata and K. Kitaura. "Exploring chemistry with the fragment molecular orbital method". *Physical Chemistry Chemical Physics*, 14 (2012) page 7562. doi: 10.1039/c2cp23784a.

[140] D. Fedorov and K. Kitaura. *The fragment molecular orbital method: Practical applications to large molecular systems*. CRC Press / Taylor & Francis, Boca Raton (**2009**).

[141] T. Nagata, D. G. Fedorov and K. Kitaura. "Mathematical formulation of the fragment molecular orbital method". In R. Zaleśny, M. G. Papadopoulos, P. G. Mezey and J. Leszczynski, editors, "Linear-scaling techniques in computational chemistry and physics: Methods and applications", volume 13 of *Challenges and advances in computational chemistry and physics*, chapter 2. Springer (**2011**). pages 17–64. doi: 10.1007/978-90-481-2853-2.

[142] T. A. Wesolowski. "Embedding a Multideterminantal Wave Function in an Orbital-Free Environment". *Phys. Rev. A*, 77 (2008) page 012504. doi: 10.1103/PhysRevA.77.012504.

[143] T. A. Wesolowski, S. Shedge and X. Zhou. "Frozen-Density Embedding Strategy for Multilevel Simulations of Electronic Structure". *Chemical Reviews*, 115 (2015) pages 5891–5928. doi: 10.1021/cr500502v.

[144] T. A. Wesolowski and A. Warshel. "Frozen Density Functional Approach for Ab Initio Calculations of Solvated Molecules". *J. Phys. Chem.*, 97 (1993) pages 8050–8053. doi: 10.1021/j100132a040.

[145] F. Aquilante and T. a. Wesołowski. "Self-consistency in frozen-density embedding theory based calculations". *The Journal of Chemical Physics*, 135 (2011) page 084120. doi: 10.1063/1.3624888.

[146] C. Daday, C. König, O. Valsson, J. Neugebauer and C. Filippi. "State-specific embedding potentials for excitation-energy calculations". *J. Chem. Theory Comput.*, 9 (2013) pages 2355–2367. doi: 10.1021/ct400086a.

[147] C. Daday, C. König, J. Neugebauer and C. Filippi. "Wavefunction in density functional theory embedding for excited states: which wavefunctions, which densities?" *ChemPhysChem*, 15 (2014) pages 3205–17. doi: 10.1002/cphc.201402459.

[148] N. Govind, Y. A. Wang, A. J. R. da Silva and E. A. Carter. "Accurate ab initio energetics of extended systems via explicit correlation embedded in a density functional environment". *Chem. Phys. Lett.*, 295 (1998) pages 129–134. doi: 10.1016/S0009-2614(98)00939-7.

[149] N. Govind, Y. A. Wang and E. A. Carter. "Electronic-structure calculations by first-principles density-based embedding of explicitly correlated systems". *J. Chem. Phys.*, 110 (1999) page 7677. doi: 10.1063/1.478679.

[150] M. Svensson, S. Humbel, R. D. J. Froese, T. Matsubara, S. Sieber and K. Morokuma. "ONIOM: A Multilayered Integrated MO + MM Method for Geometry Optimizations and Single Point Energy Predictions. A Test for Diels−Alder Reactions and Pt(P(t -Bu) 3) 2 + H 2 Oxidative Addition". *The Journal of Physical Chemistry*, 100 (1996) pages 19357–19363. doi: 10.1021/jp962071j.

[151] L. I. Bendavid and E. A. Carter. "Status in Calculating Electronic Excited States in Transition Metal Oxides from First Principles". In C. Di Valentin, S. Botti and M. Cococcioni, editors, "First Principles Approaches to Spectroscopic Properties of Complex Materials", Springer Berlin Heidelberg, Berlin, Heidelberg (**2014**). pages 47–98. doi: 10.1007/128_2013_503.

[152] F. Aquilante and T. a. Wesołowski. "Self-consistency in frozen-density embedding theory based calculations". *The Journal of Chemical Physics*, 135 (2011) page 084120. doi: 10.1063/1.3624888.

[153] T. A. Wesolowski. "Embedding Potentials for Excited States of Embedded Species". *J. Chem. Phys.*, 140 (2014) page 18A530. doi: 10.1063/1.4870014.

[154] A. Zech, F. Aquilante and T. A. Wesolowski. "Orthogonality of embedded wave functions for different states in frozen-density embedding theory". *J. Chem. Phys.*, 143 (2015) page 164106. doi: 10.1063/1.4933372.

[155] M. Dulak, J. W. Kaminski and T. A. Wesolowski. "Linearized orbital-free embedding potential in self-consistent calculations". *International Journal of Quantum Chemistry*, 109 (2009) pages 1886–1897. doi: 10.1002/qua.22011.

[156] T. Dresselhaus, J. Neugebauer, S. Knecht, S. Keller, Y. Ma and M. Reiher. "Self-consistent embedding of density-matrix renormalization group wavefunctions in a density functional environment". *The Journal of Chemical Physics*, 142 (2015) page 044111. doi: 10.1063/1.4906152.

[157] A. S. P. Gomes, C. R. Jacob and L. Visscher. "Calculation of local excitations in large systems by embedding wave-function theory in density-functional theory". *Physical Chemistry Chemical Physics*, 10 (2008) page 5353. doi: 10.1039/b805739g.

[158] S. Hofener, A. S. P. Gomes and L. Visscher. "Solvatochromic shifts from coupled-cluster theory embedded in density functional theory". *The Journal of Chemical Physics*, 139 (2013) page 104106. doi: 10.1063/1.4820488.

[159] D. K. Kanan, S. Sharifzadeh and E. A. Carter. "Quantum Mechanical Modeling of Electronic Excitations in Metal Oxides: Magnesia as a Prototype". *Chem. Phys. Lett.*, 519 (2012) pages 18–24. doi: 10.1016/j.cplett.2011.11.003.

[160] R. H. Martin. "The Helicenes". *Angewandte Chemie International Edition in English*, 13 (1974) pages 649–660. doi: 10.1002/anie.197406491.

[161] M. Gingras. "One hundred years of helicene chemistry. Part 1: non-stereoselective syntheses of carbohelicenes". *Chem. Soc. Rev.*, 42 (2013) pages 968–1006. doi: 10.1039/C2CS35154D.

[162] M. Gingras, G. Félix and R. Peresutti. "One hundred years of helicene chemistry. Part 2: stereoselective syntheses and chiral separations of carbohelicenes". *Chem. Soc. Rev.*, 42 (2013) pages 1007–1050. doi: 10.1039/C2CS35111K.

[163] M. Gingras. "One hundred years of helicene chemistry. Part 3: applications and properties of carbohelicenes". *Chem. Soc. Rev.*, 42 (2013) pages 1051–1095. doi: 10.1039/C2CS35134J.

[164] Y. Shen and C.-F. Chen. "Helicenes: Synthesis and Applications". *Chemical Reviews*, 112 (2012) pages 1463–1535. doi: 10.1021/cr200087r.

[165] M. S. Newman, W. B. Lutz and D. Lednicer. "A new reagent for resolution by complex formation; the resolution of phenanthro-[3,4-c]phenanthrene 1". *Journal of the American Chemical Society*, 77 (1955) pages 3420–3421. doi: 10.1021/ja01617a097.

[166] M. S. Newman and D. Lednicer. "The Synthesis and Resolution of Hexahelicene 1". *Journal of the American Chemical Society*, 78 (1956) pages 4765–4770. doi: 10.1021/ja01599a060.

[167] M. S. Newman and R. M. Wise. "The Synthesis and Resolution of 1,12-Dimethylbenzo[c]phenanthrene-5-acetic Acid 1". *Journal of the American Chemical Society*, 78 (1956) pages 450–454. doi: 10.1021/ja01583a054.

[168] R. S. Cahn, C. Ingold and V. Prelog. "Specification of Molecular Chirality". *Angewandte Chemie International Edition in English*, 5 (1966) pages 385–415. doi: 10.1002/anie.196603851.

[169] N. Hoffmann. "Photochemical reactions applied to the synthesis of helicenes and helicene-like compounds". *Journal of Photochemistry and Photobiology C: Photochemistry Reviews*, 19 (2014) pages 1–19. doi: 10.1016/j.jphotochemrev.2013.11.001.

[170] Y. Nakai, T. Mori and Y. Inoue. "Theoretical and Experimental Studies on Circular Dichroism of Carbo[n]helicenes". *The Journal of Physical Chemistry A*, 116 (2012) pages 7372–7385. doi: 10.1021/jp304576g.

[171] Y. Nakai, T. Mori and Y. Inoue. "Circular Dichroism of (Di)methyl- and Di-aza[6]helicenes. A Combined Theoretical and Experimental Study". *The Journal of Physical Chemistry A*, 117 (2013) pages 83–93. doi: 10.1021/jp3104084.

[172] D. H. Friese and C. Hättig. "Optical rotation calculations on large molecules using the approximate coupled cluster model CC2 and the resolution-of-the-identity approximation". *Physical Chemistry Chemical Physics*, 16 (2014) page 5942. doi: 10.1039/C3CP54338B.

[173] H. Wynberg. "Some Observations On The Chemical, Photochemical, And Spectral Properties Of Thiophenes". *Accounts of Chemical Research*, 4 (1971) pages 65–73. doi: 10.1021/ar50038a004.

[174] H. Nakagawa, A. Obata, K.-i. Yamada and H. Kawazura. "Crystal and molecular structures of tetrathia[7]heterohelicene: racemate and enantiomer". *Journal of the Chemical Society, Perkin Transactions 2*, (1985) page 1899. doi: 10.1039/P29850001899.

[175] G. Wittig and G. Geissler. "Zur Reaktionsweise des Pentaphenyl-phosphors und einiger Derivate". *Justus Liebigs Annalen der Chemie*, 580 (1953) pages 44–57. doi: 10.1002/jlac.19535800107.

[176] G. Wittig and U. Schöllkopf. "Über Triphenyl-phosphin-methylene als olefinbildende Reagenzien (I. Mitteil". *Chemische Berichte*, 87 (1954) pages 1318–1330. doi: 10.1002/cber.19540870919.

[177] T. Caronna, M. Catellani, S. Luzzati, L. Malpezzi, S. V. Meille, A. Mele, C. Richter and R. Sinisi. "Molecular Crystal Architecture and Optical Properties of a Thiohelicenes Series Containing 5, 7, 9, and 11 Rings Prepared via Photochemical Synthesis". *Chemistry of Materials*, 13 (2001) pages 3906–3914. doi: 10.1021/cm010093z.

[178] H. Nakagawa, J. Yoshino, K.-i. Yamada and M. Shiro. "Helical Assembly Formed by Chiral [11]Thiaheterohelicene Molecules in Crystals. Architecture with Triple Helix". *Chemistry Letters*, 32 (2003) pages 90–91. doi: 10.1246/cl.2003.90.

[179] S. K. Collins and M. P. Vachon. "Unlocking the potential of thiaheterohelicenes: chemical synthesis as the key". *Organic & Biomolecular Chemistry*, 4 (2006) page 2518. doi: 10.1039/B603305A.

[180] S. Maiorana, A. Papagni, E. Licandro, R. Annunziata, P. Paravidino, D. Perdicchia, C. Giannini, M. Bencini, K. Clays and A. Persoons. "A convenient procedure for the synthesis of tetrathia-[7]-helicene and the selective α-functionalisation of terminal thiophene ring". *Tetrahedron*, 59 (2003) pages 6481–6488. doi: 10.1016/S0040-4020(03)01056-1.

[181] E. Licandro, C. Rigamonti, M. Ticozzelli, M. Monteforte, C. Baldoli, C. Giannini and S. Maiorana. "Synthesis and Functionalization of Novel Tetrathia[7]helicenes as New Push-Pull Systems". *Synthesis*, 2006 (2006) pages 3670–3678. doi: 10.1055/s-2006-950222.

[182] D. Waghray, C. d. Vet, K. Karypidou and W. Dehaen. "Oxidative Transformation to Naphthodithiophene and Thia[7]helicenes by Intramolecular Scholl Reaction of Substituted 1,2-Bis(2-thienyl)benzene Precursors". *The Journal of Organic Chemistry*, 78 (2013) pages 11147–11154. doi: 10.1021/jo401807x.

[183] B. Champagne, J.-M. André, E. Botek, E. Licandro, S. Maiorana, A. Bossi, K. Clays and A. Persoons. "Theoretical Design of Substituted Tetrathia-[7]-Helicenes with Large Second-Order Nonlinear Optical Responses". *ChemPhysChem*, 5 (2004) pages 1438–1442. doi: 10.1002/cphc.200400225.

[184] A. Bossi, E. Licandro, S. Maiorana, C. Rigamonti, S. Righetto, G. R. Stephenson, M. Spassova, E. Botek and B. Champagne. "Theoretical and Experimental Investigation of Electric Field Induced Second Harmonic Generation in Tetrathia[7]helicenes †". *The Journal of Physical Chemistry C*, 112 (2008) pages 7900–7907. doi: 10.1021/jp7117554.

[185] C. Kim, T. J. Marks, A. Facchetti, M. Schiavo, A. Bossi, S. Maiorana, E. Licandro, F. Todescato, S. Toffanin, M. Muccini *et al.* "Synthesis, characterization, and transistor response of tetrathia-[7]-helicene precursors and derivatives". *Organic Electronics*, 10 (2009) pages 1511–1520. doi: 10.1016/j.orgel.2009.08.018.

[186] F. Rose-Munch, M. Li, E. Rose, J. C. Daran, A. Bossi, E. Licandro and P. R. Mussini. "Tetrathia[7]helicene-Based Complexes of Ferrocene and (η^5-Cyclohexadienyl)tricarbonylmanganese: Synthesis and Electrochemical Studies". *Organometallics*, 31 (2012) pages 92–104. doi: 10.1021/om200571a.

[187] K.-i. Shinohara, Y. Sannohe, S. Kaieda, K.-i. Tanaka, H. Osuga, H. Tahara, Y. Xu, T. Kawase, T. Bando and H. Sugiyama. "A Chiral Wedge Molecule Inhibits Telomerase Activity". *Journal of the American Chemical Society*, 132 (2010) pages 3778–3782. doi: 10.1021/ja908897j.

[188] S. Cauteruccio, C. Bartoli, C. Carrara, D. Dova, C. Errico, G. Ciampi, D. Dinucci, E. Licandro and F. Chiellini. "A Nanostructured PLGA System for Cell Delivery of a Tetrathiahelicene as a Model for Helical DNA Intercalators". *ChemPlusChem*, 80 (2015) pages 490–493. doi: 10.1002/cplu.201402347.

[189] T. Kawasaki, K. Suzuki, E. Licandro, A. Bossi, S. Maiorana and K. Soai. "Enantioselective synthesis induced by tetrathia-[7]-helicenes in conjunction with asymmetric autocatalysis". *Tetrahedron: Asymmetry*, 17 (2006) pages 2050–2053. doi: 10.1016/j.tetasy.2006.07.015.

[190] M. Monteforte, S. Cauteruccio, S. Maiorana, T. Benincori, A. Forni, L. Raimondi, C. Graiff, A. Tiripicchio, G. R. Stephenson and E. Licandro. "Tetrathiaheterohelicene Phosphanes as Helical-Shaped Chiral Ligands for Catalysis". *European Journal of Organic Chemistry*, 2011 (2011) pages 5649–5658. doi: 10.1002/ejoc.201100726.

[191] S. Cauteruccio, D. Dova, M. Benaglia, A. Genoni, M. Orlandi and E. Licandro. "Synthesis, Characterisation, and Organocatalytic Activity of Chiral Tetrathiahelicene Diphosphine Oxides". *European Journal of Organic Chemistry*, 2014 (2014) pages 2694–2702. doi: 10.1002/ejoc.201301912.

[192] P. Aillard, A. Voituriez, D. Dova, S. Cauteruccio, E. Licandro and A. Marinetti. "Phosphathiahelicenes: Synthesis and Uses in Enantioselective Gold Catalysis". *Chemistry - A European Journal*, 20 (2014) pages 12373–12376. doi: 10.1002/chem.201402822.

[193] A. Börner. *Phosphorus ligands in asymmetric catalysis: Synthesis and applications*. Wiley-VCH, Weinheim ((**2008**)).

[194] A. S. K. Hashmi. "Gold-Catalyzed Organic Reactions". *Chemical Reviews*, 107 (2007) pages 3180–3211. doi: 10.1021/cr000436x.

[195] Z. Li, C. Brouwer and C. He. "Gold-Catalyzed Organic Transformations". *Chemical Reviews*, 108 (2008) pages 3239–3265. doi: 10.1021/cr068434l.

[196] A. Arcadi. "Alternative Synthetic Methods through New Developments in Catalysis by Gold". *Chemical Reviews*, 108 (2008) pages 3266–3325. doi: 10.1021/cr068435d.

[197] D. J. Gorin, B. D. Sherry and F. D. Toste. "Ligand Effects in Homogeneous Au Catalysis". *Chemical Reviews*, 108 (2008) pages 3351–3378. doi: 10.1021/cr068430g.

[198] K. Eichkorn, O. Treutler, H. Öhm, M. Häser and R. Ahlrichs. "Auxiliary basis sets to approximate Coulomb potentials". *Chemical Physics Letters*, 240 (1995) pages 283–290. doi: 10.1016/0009-2614(95)00621-A.

[199] C. Hättig and F. Weigend. "CC2 excitation energy calculations on large molecules using the resolution of the identity approximation". *The Journal of Chemical Physics*, 113 (2000) page 5154. doi: 10.1063/1.1290013.

[200] J.-D. Chai and M. Head-Gordon. "Long-range corrected hybrid density functionals with damped atom–atom dispersion corrections". *Physical Chemistry Chemical Physics*, 10 (2008) page 6615. doi: 10.1039/B810189B.

[201] J. Plötner, D. J. Tozer and A. Dreuw. "Dependence of Excited State Potential Energy Surfaces on the Spatial Overlap of the Kohn−Sham Orbitals and the Amount of Nonlocal Hartree−Fock Exchange in Time-Dependent Density Functional Theory". *Journal of Chemical Theory and Computation*, 6 (2010) pages 2315–2324. doi: 10.1021/ct1001973.

[202] R. Ahlrichs, M. Bär, M. Häser, H. Horn and C. Kölmel. "Electronic structure calculations on workstation computers: The program system turbomole". *Chemical Physics Letters*, 162 (1989) pages 165–169. doi: 10.1016/0009-2614(89)85118-8.

[203] M. J. Frisch, G. W. Trucks, H. B. Schlegel, G. E. Scuseria, M. A. Robb, J. R. Cheeseman, G. Scalmani, V. Barone, B. Mennucci, G. A. Petersson *et al.* "Gaussian 09, Revision D.01" (**2013**). Gaussian, Inc., Wallingford CT.

[204] B. Dandrade, S. Datta, S. Forrest, P. Djurovich, E. Polikarpov and M. Thompson. "Relationship between the ionization and oxidation potentials of molecular organic semiconductors". *Organic Electronics*, 6 (2005) pages 11–20. doi: 10.1016/j.orgel.2005.01.002.

[205] B. Mennucci, J. Tomasi, R. Cammi, J. R. Cheeseman, M. J. Frisch, F. J. Devlin, S. Gabriel and P. J. Stephens. "Polarizable Continuum Model (PCM) Calculations of Solvent Effects on Optical Rotations of Chiral Molecules". *The Journal of Physical Chemistry A*, 106 (2002) pages 6102–6113. doi: 10.1021/jp020124t.

[206] R. A. Klein, B. Mennucci and J. Tomasi. "Ab Initio Calculations of 17O NMR-Chemical Shifts for Water. The Limits of PCM Theory and the Role of Hydrogen-Bond Geometry and Cooperativity". *The Journal of Physical Chemistry A*, 108 (2004) pages 5851–5863. doi: 10.1021/jp0487408.

[207] P. Hohenberg and W. Kohn. "Inhomogeneous Electron Gas". *Phys. Rev.*, 136 (1964) pages B864–B871. doi: 10.1103/PhysRev.136.B864.

[208] R. Parr and W. Yang. *Density-functional theory of atoms and molecules*. Oxford University Press Clarendon Press, New York Oxford England (**1989**).

[209] A. Laktionov, E. Chemineau-Chalaye and T. A. Wesolowski. "Frozen-density embedding theory with average solvent charge densities from explicit atomistic simulations". *Phys. Chem. Chem. Phys.*, 18 (2016) pages 21069–21078. doi: 10.1039/C6CP00497K.

[210] B. Lunkenheimer and A. Köhn. "Solvent Effects on Electronically Excited States Using the Conductor-Like Screening Model and the Second-Order Correlated Method ADC(2)". *Journal of Chemical Theory and Computation*, 9 (2013) pages 977–994. doi: 10.1021/ct300763v.

[211] J.-M. Mewes, Z.-Q. You, M. Wormit, T. Kriesche, J. M. Herbert and A. Dreuw. "Experimental Benchmark Data and Systematic Evaluation of Two a Posteriori, Polarizable-Continuum Corrections for Vertical Excitation Energies in Solution". *J. Phys. Chem. A*, 119 (2015) pages 5446–5464. doi: 10.1021/jp511163y.

[212] A. P. Gamiz-Hernandez, I. N. Angelova, R. Send, D. Sundholm and V. R. I. Kaila. "Protein-Induced Color Shift of Carotenoids in -Crustacyanin". *Angewandte Chemie International Edition*, 54 (2015) pages 11564–11566. doi: 10.1002/anie.201501609.

[213] E. Epifanovsky, M. Wormit, T. Kuś, A. Landau, D. Zuev, K. Khistyaev, P. Manohar, I. Kaliman, A. Dreuw and A. I. Krylov. "New implementation of high-level correlated methods using a general block tensor library for high-performance electronic structure calculations". *Journal of Computational Chemistry*, 34 (2013) pages 2293–2309. doi: 10.1002/jcc.23377.

[214] P. M. W. Gill, M. Head-Gordon and J. A. Pople. "Efficient computation of two-electron - repulsion integrals and their nth-order derivatives using contracted Gaussian basis sets". *The Journal of Physical Chemistry*, 94 (1990) pages 5564–5572. doi: 10.1021/j100377a031.

[215] P. M. W. Gill, B. G. Johnson and J. A. Pople. "Two-electron repulsion integrals over Gaussians functions". *International Journal of Quantum Chemistry*, 40 (1991) pages 745–752. doi: 10.1002/qua.560400604.

[216] P. M. Gill. "Molecular integrals Over Gaussian Basis Functions". *Advances in Quantum Chemistry*, 25 (1994) pages 141–205. doi: 10.1016/S0065-3276(08)60019-2.

[217] P. M. Gill, B. G. Johnson and J. A. Pople. "A standard grid for density functional calculations". *Chemical Physics Letters*, 209 (1993) pages 506 – 512. doi: 10.1016/0009-2614(93)80125-9.

[218] J. Wenzel, M. Wormit and A. Dreuw. "Calculating core-level excitations and x-ray absorption spectra of medium-sized closed-shell molecules with the algebraic-diagrammatic construction scheme for the polarization propagator". *Journal of Computational Chemistry*, 35 (2014) pages 1900–1915. doi: 10.1002/jcc.23703.

[219] J. Wenzel, M. Wormit and A. Dreuw. "Calculating X-ray Absorption Spectra of Open-Shell Molecules with the Unrestricted Algebraic-Diagrammatic Construction Scheme for the Polarization Propagator". *Journal of Chemical Theory and Computation*, 10 (2014) pages 4583–4598. doi: 10.1021/ct5006888.

[220] J. Wenzel, A. Holzer, M. Wormit and A. Dreuw. "Analysis and comparison of CVS-ADC approaches up to third order for the calculation of core-excited states". *The Journal of Chemical Physics*, 142 (2015) page 214104. doi: 10.1063/1.4921841.

[221] J. Wenzel and A. Dreuw. "Physical Properties, Exciton Analysis, and Visualization of Core-Excited States: An Intermediate State Representation Approach". *Journal of Chemical Theory and Computation*, 12 (2016) pages 1314–1330. doi: 10.1021/acs.jctc.5b01161.

[222] F. Plasser, B. Thomitzni, S. A. Bppler, J. Wenzel, D. R. Rehn, M. Wormit and A. Dreuw. "Statistical analysis of electronic excitation processes: Spatial location, compactness, charge transfer, and electron-hole correlation". *Journal of Computational Chemistry*, 36 (2015) pages 1609–1620. doi: 10.1002/jcc.23975.

[223] C. M. Krauter, B. Schimmelpfennig, M. Pernpointner and A. Dreuw. "Algebraic diagrammatic construction for the polarization propagator with spin-orbit coupling". *Chemical Physics*, 482 (2017) pages 286 – 293. doi: 10.1016/j.chemphys.2016.09.018. Electrons and nuclei in motion - correlation and dynamics in molecules (on the occasion of the 70th birthday of Lorenz S. Cederbaum).

[224] Y. Shao, M. Head-Gordon and A. I. Krylov. "The spin–flip approach within time-dependent density functional theory: Theory and applications to diradicals". *The Journal of Chemical Physics*, 118 (2003) pages 4807–4818. doi: 10.1063/1.1545679.

[225] R. Peverati and D. G. Truhlar. "Communication: A global hybrid generalized gradient approximation to the exchange-correlation functional that satisfies the second-order density-gradient constraint and has broad applicability in chemistry". *The Journal of Chemical Physics*, 135 (2011) page 191102. doi: 10.1063/1.3663871.

[226] P. M. W. Gill. "A new gradient-corrected exchange functional". *Molecular Physics*, 89 (2010) pages 433–445. doi: 10.1080/002689796173813.

[227] H. S. Yu, W. Zhang, P. Verma, X. He and D. G. Truhlar. "Nonseparable exchange–correlation functional for molecules, including homogeneous catalysis involving transition metals". *Phys. Chem. Chem. Phys.*, 17 (2015) pages 12146–12160. doi: 10.1039/c5cp01425e.

[228] S. Lundqvist and N. H. March, editors. *Theory of the inhomogeneous electron gas*. Physics of solids and liquids. Plenum press, New York and N.Y and London (**1983**).

[229] "Intel C++ and Fortran Compilers". `https://software.intel.com/en-us/intel-compilers` (**2015**).

[230] "Intel Math Kernel Library (MKL)". `https://software.intel.com/en-us/intel-mkl` (**2015**).

[231] S. Krysanov and M. Alfimov. "Ultrafast formation of transients in spiropyran photochromism". *Chemical Physics Letters*, 91 (1982) pages 77–80. doi: 10.1016/0009-2614(82)87037-1.

[232] N. P. Ernsting. "Transient optical absorption spectroscopy of the photochemical spiropyran-merocyanine conversion". *Chemical Physics Letters*, 159 (1989) pages 526–531. doi: 10.1016/0009-2614(89)87526-8.

[233] N. P. Ernsting, B. Dick and T. Arthen-Engeland. "The primary photochemical reaction step of unsubstituted indolino-spiropyrans". *Pure and Applied Chemistry*, 62 (1990). doi: 10.1351/pac199062081483.

[234] J. Kohl-Landgraf, M. Braun, C. Özçoban, D. P. N. Gonçalves, A. Heckel and J. Wachtveitl. "Ultrafast Dynamics of a Spiropyran in Water". *Journal of the American Chemical Society*, 134 (2012) pages 14070–14077. doi: 10.1021/ja304395k.

[235] J. Kohl-Landgraf, M. Braun, C. Özçoban, D. Goncalves, A. Heckel, J. Wachtveitl, M. Chergui, A. Taylor, S. Cundiff, R. d. Vivie-Riedle *et al.* "Dynamics of a photochromic spiropyran under aqueous conditions". *EPJ Web of Conferences*, 41 (2013) page 05009. doi: 10.1051/epjconf/20134105009.

[236] B. O. Roos. "The Complete Active Space Self-Consistent Field Method and its Applications in Electronic Structure Calculations". In K. P. Lawley, editor, "Advances in Chemical Physics: Ab Initio Methods in Quantum Chemistry Part 2", volume 69 of *Advances in Chemical Physics*. John Wiley & Sons, Inc, Hoboken and NJ and USA (**1987**). pages 399–445. doi: 10.1002/9780470142943.ch7.

[237] K. Andersson, P.-Å. Malmqvist and B. O. Roos. "Second–order perturbation theory with a complete active space self–consistent field reference function". *The Journal of Chemical Physics*, 96 (1992) pages 1218–1226. doi: 10.1063/1.462209.

[238] M. Humbert-Droz, X. Zhou, S. V. Shedge and T. A. Wesolowski. "How to choose the frozen density in Frozen-Density Embedding Theory-based numerical simulations of local excitations?" *Theoretical Chemistry Accounts*, 133 (2014) page 2523. doi: 10.1007/s00214-013-1405-1.

[239] T. A. Wesolowski and J. Weber. "Kohn-Sham equations with constrained electron density: an iterative evaluation of the ground-state electron density of interacting molecules". *Chemical Physics Letters*, 248 (1996) pages 71–76. doi: 10.1016/0009-2614(95)01281-8.

[240] R. S. Mulliken. "Electronic Population Analysis on LCAO-MO Molecular Wave Functions. I". *The Journal of Chemical Physics*, 23 (1955) page 1833. doi: 10.1063/1.1740588.

List of Abbreviations

ADC	Algebraic Diagrammatic Construction scheme
ALDA	Adiabatic Local Density Approximation
AO	Atomic Orbital
BA	BenzAldehyde
BSSE	Basis-Set Superposition Error
BZ	BenZene
CAS	Complete Active Space
CASSCF	Complete Active Space Self-Consistent Field
CC	Coupled Cluster
CI	Configuration Interaction
COSMO	COnductor-like Screening MOdel
CVS	Core-Valence Separation
DDPP	Difference Density Polarization Potential
DFT	Density Functional Theory
ECP	Effective Core Potential
EFP	Effective Fragment Potential
FDET	Frozen Density Embedding Theory
FDE-ADC	Frozen Density Embedded Algebraic Diagrammatic Construction scheme

FMO	Fragment Molecular Orbital
GGA	Generalized Gradient Approximation
GTO	Gaussian-Type Orbital
HF	Hartree-Fock
HOMO	Highest Occupied Molecular Orbital
HONTO	Highest Occupied Natural Transition Orbital
LCAO	Linear Combination of Atomic Orbitals
LSDA	Local Spin-Density Approximation
LUMO	Lowest Unoccupied Molecular Orbital
LUNTO	Lowest Unoccupied Natural Transition Orbital
MAE	Mean Absolute Error
MM	Molecular Mechanics
MO	Molecular Orbital
MP	Møller-Plesset
NDO	Natural Difference Orbital
NO	Natural Orbital
NTO	Natural Transition Orbital
ONIOM	Our own N-layered Integrated molecular Orbital molecular Mechanics method
PCM	Polarizable Continuum Model
QM	Quantum Mechanics
RS	Rayleigh-Schrödinger
RADM	Re-Assembling of Denstiy Matrix
RI	Resolution of the Identity

SCF	Self-Consistent Field
SE	Supermolecular Expansion
SSI	State-Specific Iteration
STO	Slater-Type Orbital
TD	Time-Dependent
UC	UraCil

List of Figures

List of Tables

List of Source Codes

List of Schemes

List of Publications

- **Gold(I) Complexes of Tetrathiaheterohelicene Phosphanes**
  Silvia Cauteruccio, Annette Loos, Alberto Bossi, Maria C. Blanco Jaimes, Davide Dova, Frank Rominger, Stefan Prager, Andreas Dreuw, Emanuela Licandro and A. Stephen K. Hashmi
  Inorganic Chemistry, 52 (2013), pages 7995-8004

- **Ultrafast C_{Spiro}-O Dissociation via a Conical Intersection Drives Spiropyran to Merocyanine Photoswitching**
  Stefan Prager, Irene Burghardt and Andreas Dreuw
  The Journal of Physical Chemistry A, 118 (2014), pages 1339-1349

- **Chiral Thiahelicene-Based Alkyl Phosphine-Borane Complexes: Synthesis, X-ray Characterization, and Theoretical and Experimental Investigations of Optical Properties**
  Davide Dova, Silvia Cauteruccio, Stefan Prager, Andreas Dreuw, Claudia Graiff and Emanuela Licandro
  The Journal of Organic Chemistry, 80 (2015), pages 3921-3928.

- **Tetrathia[7]helicene Phosphorus Derivatives: Experimental and Theoretical Investigations of Electronic Properties, and Preliminary Applications as Organocatalysts**
  Davide Dova, Lucia Viglianti, Patrizia R. Mussini, Stefan Prager, Andreas Dreuw, Arnaud Voituriez, Emanuela Licandro and Silvia Cauteruccio
  Asian Journal of Organic Chemistry, 5 (2016), pages 537-549

- **First time combination of frozen density embedding theory with the algebraic diagrammatic construction scheme for the polarization propagator of second order**
  Stefan Prager, Alexander Zech, Francesco Aquilante, Andreas Dreuw and Tomasz A. Wesolowski
  The Journal of Chemical Physics, 144 (2016,) page 204103

- **Implementation and application of the frozen density embedding theory with the algebraic diagrammatic construction scheme for the polarization propagator up to third order**
  Stefan Prager, Alexander Zech, Tomasz A. Wesolowski and Andreas Dreuw
  submitted for publication, (2017)

Danksagung

Zuallererst möchte ich gerne meinem Doktorvater, Prof. Dr. Andreas Dreuw, für die Betreuung während meiner Dissertation sowie für die Bereitstellung des spannenden und vielseitigen Themas danken. Seit meiner Bachelorarbeit hat er mich immer unterstützt und gefördert. Er hatte immer ein offenes Ohr für Fragen und war immer ein großartiger Betreuer, Mentor und Diskussionspartner, der mir auch die Freiheit ließ, eigene Ideen umzusetzen. Danke für die wunderbare Mischung aus fachlicher Untersttzung und Freundschaft. Ebenfalls einen großen Dank an Prof. Dr. Peter Comba für die Begutachtung meiner Doktorarbeit

Ein ganz besonderer Dank geht an meine gesamte Familie, meine Eltern Irene und Franz und meine Freundin Lea, die ich über alles liebe! Ohne Eure Unterstützung wäre diese Arbeit nicht möglich gewesen. Ihr habt immer zu mir gestanden, mich ermutigt und durch schwierige Zeiten geholfen. Vielen Dank!

Ebenfalls möchte ich mich sehr bei Prof. Dr. Tomasz Wesolowski und Alexander Zech für die großartige Zusammenarbeit bei der Entwicklung von `fdeman` bedanken. Dadurch wurde auch die Zeit, die ich in Genf verbracht habe, zu einem großartigen Erlebnis. Im Zusammenhang mit der Entwicklung von `fdeman` möchte ich mich auch bei Prof. Dr. John Herbert, Prof. Dr. Yihan Shao und Dr. Evgeny Epifanovsky für die hilfreichen Diskussionen bedanken.

Weiterhin möchte ich mich gerne bei der gesamten Arbeitgruppe Dreuw (Mercedes, Tim, Adrian, Georg, Jie, Michael, Manuel, Maximilian, Daniel, Stefanie, Tobias, Chong, Marvin und Nico) sowie den ehemaligen Mitglieder (Jan W., Katie, Dirk, Matthias, Felix, Philipp, Stefan K., Shirin, Jan M., Jürgen und Ben.) und Michael Wormit, dem ich dies leider nicht mehr persönlich sagen kann, für die schöne Zeit

und viele anregende Gespräche und Diskussionen bedanken. Insbesondere danke ich meinen Bürokollegen Katie, Tim, Felix und Manuel für die tolle Atmosphäre im Büro. Auch Danke an Ellen Vogel und Manfred Trunk für die Unterstützung in organisatorischen und technischen Angelegenheiten.

Bei Jan W., Katie, Mercedes, Alexander, Manuel, Tim und meiner Freundin Lea möchte ich mich ganz herzlich für das Korrekturlesen von Teilen dieser Dissertation bedanken. Ebenfalls Danke an Jan W. für das LaTeX Layout.

Ein großer Dank geht auch an alle meine Freunde, die mich ebenfalls bei jeder Gelegenheit unterstützt und zeitweise für die nötige Ablenkung gesorgt haben.

Zuletzt möchte ich der *Heidelberg Graduate School of Mathematical and Computational Methods for the Sciences (HGS MathComp)* für die Unterstützung während meiner Doktorarbeit danken.

Eidesstattliche Versicherung gemäß §8 der Promotionsordnung der Naturwissenschaftlich-Mathematischen Gesamtfakultät der Universität Heidelberg

1. Bei der eingereichten Dissertation zu dem Thema
   "Development of Frozen-Density Embedded Algebraic Diagrammatic Construction Schemes for Excited States and Quantum-Chemical Investigation of Photophysical Properties of Tetrathiaheterohelicenes"
   handelt es sich um meine eigenständig erbrachte Leistung.

2. Ich habe nur die angegebenen Quellen und Hilfsmittel benutzt und mich keiner unzulässigen Hilfe Dritter bedient. Insbesondere habe ich wörtlich oder sinngemäß aus anderen Werken übernommene Inhalte als solche kenntlich gemacht.

3. Die Arbeit oder Teile davon habe ich bislang nicht an einer Hochschule des In- oder Auslands als Bestandteil einer Prüfungs- oder Qualifikationsleistung vorgelegt.

4. Die Richtigkeit der vorstehenden Erklärungen bestätige ich.

5. Die Bedeutung der eidesstattlichen Versicherung und die strafrechtlichen Folgen einer unrichtigen oder unvollständigen eidesstattlichen Versicherung sind mir bekannt.

Ich versichere an Eides statt, dass ich nach bestem Wissen die reine Wahrheit erklärt und nichts verschwiegen habe.

Ort/Datum Unterschrift